INFLUENCE OF STATE OF STRESS ON CREEP FAILURE

by

KHALID DAWOOD AL-FADDAGH, BSc, MSc

A thesis submitted for the degree of

Doctor of Philosophy

of the

University of London

and for the

Diploma of Imperial College

February 1983

Department of Mechanical Engineering
Imperial College of Science & Technology
London SW7 2BX

TO MY

PARENTS

&

SISTERS

ABSTRACT

Two finite element programs have been developed which can be used to calculate the steady-state stress distributions in axi-symmetric and two-dimensional bodies subjected to creep. The numerical method adopted is based on an iterative procedure in which the elastic material properties are up-dated after each iteration until the final steady-state is achieved. Solutions have been obtained for a range of circumferentially notched bar geometries and different values of stress index, n. For each profile, a skeletal point at which the effective stress remained approximately constant, independent of n, was observed. This stress has been used to characterise the overall behaviour of the notch throat region when steady-state is achieved relatively early in life. Other geometries have also been investigated; these were blunt and sharp double notches under remote uniform tension, and compact tension specimens having different circular hole sizes machined in their crack plane.

The finite element steady-state solutions obtained for the notched bars investigated made it possible to carry out a detailed theoretical analysis to predict the lives of these geometries. The equations defining the models in terms of life of notched to unnotched bars and stress strength ratios were derived using either a continuum mechanics approach or Ashby's and co-workers void growth theory. The state of stress parameters required in the calculations were taken from the steady-state solutions at the skeletal point.

In order to check the validity of using the proposed theoretical models as a useful design tool, it was necessary to compare them with real experimental data. Several creep tests were carried out at 538°C on plain and notched bar specimens pulled in tension. The material tested was the ductile 2¼%Cr 1%Mo steel used in the electric power generation industries.

Other creep data were also collected from the literature on the brittle ½%Cr ½%Mo ¼%V steel and a range of high temperature alloys tested by Davis and Manjoine in 1953. The assumptions and limitations associated with interpreting the creep data in terms of notched to unnotched life or stress strength ratios were discussed and focused on. Finally, it has been reported that good agreement was obtained between the proposed models and the available creep data.

ACKNOWLEDGEMENTS

I would like to express my gratitude to Dr G.A. Webster for his continual guidance and interest throughout the course of my research. Thanks are also due to Dr R.T. Fenner for his help and useful advice in solving the many computational problems. The efforts of the technical staff in the Departmental Workshop at Imperial College, and in particular Mr D.K. Willis, is highly appreciated.

I wish to acknowledge the useful suggestions and comments provided by Dr B.F. Dyson during my several visits to the National Physical Laboratories. Thanks are also due to Mr M.S. Loveday and the technical staff at the NPL Workshop for machining the required creep specimens.

My stay at Imperial College was enriched by the help, suggestions of and discussions with my colleagues and post-doctoral workers. These include Mr D.J. Smith, Mr A. Al-Chalabi, Mr L. Mubarek, Mr A. Hadid, Mr D.W. Dean, Dr M.S. Dhillon, and Dr K.M. Nikbin.

I would like to extend my gratitude to my parents and sisters, who have encouraged and offered me all possible support during my studies.

Finally, the diligent typing of Mrs E.A. Hall is very much appreciated.

CONTENTS

NOMENCLATURE

a	:	notch throat radius
a_i, a_j, a_k	:	dimensions of triangular element
b	:	bar radius
b_i, b_j, b_k	:	dimensions of triangular element
$[B]$	:	element dimension matrix
$[D]$	:	element elastic property matrix
$[d]$	:	element dimension matrix
d	:	grain size
E	:	Young's modulus
E'	:	effective modulus
$[F]$	:	vector of overall externally applied forces
F	:	relative stress concentration factor
f_h	:	area fraction of holes on grain boundary
f_i	:	initial area fraction of holes
f_c	:	area fraction of holes at which linkage occurs, taken as 0.25
f_t^d	:	area fraction of voids at transition from growth by boundary diffusion to power-law creep
f_t^s	:	area fraction of voids at transition from growth by surface diffusion to power-law creep
2ℓ	:	centre-to-centre void spacing
n	:	stress index in creep law
P	:	pressure
R	:	notch profile radius
R_1, R_2	:	internal and external radii of a thick-walled cylinder
r_h	:	radius of growing void
S_s	:	notch to unnotched stress strength ratio

S_t : notch to unnotched time strength ratio

t_n : nucleation time

t_{no} : failure time of a notched specimen

t_{un} : failure time of a plain bar specimen

t_R : time to failure

u_i , u_j , u_k : element radial displacement component

w_i , w_j , w_k : element axial displacement component

α : parameter that measures the effect of stress state on void growth rate

α_o : value of α corresponding to simple tension

γ_s : surface free energy

Δ_m : element area

$[\delta]$, $[\delta]_m$: overall and element vector of displacement components

$\dot{\varepsilon}_o$, σ_o : creep constants

ε_R : strain to failure

$\bar{\dot{\varepsilon}}_s$: effective steady-state strain rate

ε_{zz} , $\varepsilon_{\theta\theta}$, ε_{rr} : axial, hoop and radial strains

ε_1 , ε_2 , ε_3 : principal strains

λ : convergence tolerance

ν : Poisson's ratio

$\bar{\sigma}$: effective stress

σ_m : hydrostatic stress

σ_o^{∞} : remote applied stress

σ_n : failure stress of a notched specimen

σ_{un} : failure stress of a plain bar specimen

σ_{zz} , $\sigma_{\theta\theta}$, σ_{rr} : axial, hoop and radial stresses

σ_1 , σ_2 , σ_3 : principal stresses

ϕ_o : dimensionless material quantity which appears in Ashby's boundary diffusion model

ψ_o : dimensionless material quantity which appears in Ashby's surface diffusion model

ω : measure of damage in continuum theory of creep damage

GENERAL INTRODUCTION

The design of components for high temperature applications has become increasingly important in recent years. In power generation plants, nuclear reactors, gas turbines and aircraft frames, there is great economic incentive to run key components under conditions of extreme temperatures and stresses, consistent with reliability and an adequate working life. The economic advantage of obtaining optimum efficiency puts great emphasis on refining design methods. In particular, the prediction of creep behaviour has been the subject of continuing study.

Creep can occur over a wide range of stress and temperature conditions, but it is at temperatures in excess of 0.5 times the absolute melting point of the material that creep deformation or fracture becomes predominant in practical applications. Experience has shown that failure of components subjected to tri-axial states of stress usually initiates in regions of high stress concentration. In order to determine the lives in such circumstances, laws governing creep behaviour under multi-axial stressing are needed.

The most frequent method of introducing a three-dimensional state of stress into a test piece in the laboratory is to subject circumferentially notched bars to an axial tensile load. The constraint of the shank produces a state of tri-axial tension in the notch region which depends upon the notch geometry and creep properties of the material. Several experimental investigations of this kind have revealed that both notch strengthening and notch weakening can be observed, depending upon the notch dimensions and the material examined. To explain this behaviour, a knowledge of how the state of stress parameters across the notch throat vary with notch sharpness and material properties are therefore needed.

Several methods based on slip-line field, approximate plasticity and

finite element analyses have been suggested in the literature for calculating the stress distribution within a notch region. The first two methods make use of non-work hardening plasticity solutions and are, therefore, only relevant when the stress index, n, approaches infinity. This thesis presents a numerical method for determining the steady-state stress distribution in two-dimensional and axi-symmetric problems, rapidly, for any value of n, without the need for calculating how stress redistribution occurs with time. Initially, in the absence of plastic deformation on loading, an elastic stress distribution will be obtained. As time progresses, stress redistribution will take place due to the high sensitivity of creep deformation to stress.

Results of finite element calculations using the present technique and comparisons made with exact, approximate and other finite element solutions are reported. The problems considered were a range of notched bar geometries pulled in tension and some compact tension specimens having different hole sizes machined into their crack plane. Considerable time has been spent in developing the appropriate routines for up-dating the elastic properties after each iteration using either the Von Mises or Tresca criterion, and generating the required finite element grids automatically from a small number of geometric parameters.

The aim of the present investigation, after obtaining the finite element solutions, was to propose some theoretical models which can explain notch strengthening and weakening. These models were derived using either a continuum mechanics or a microstructural approach. The review made prior to the mathematical derivation of these models revealed that detailed information is required on how the state of stress parameters vary with notch sharpness. It is known from previous investigations that the steady-state stress distributions in the notched region for blunt notches are smooth and, for some values of stress index

n, reasonably constant. In contrast, for sharp notches, the stress distributions tend to have peaks in the region nearer to the notch root. However, irrespective of notch shape and value of n, it has been found from the detailed numerical calculations using the present finite element technique that a region of approximately constant effective stress is obtained which can be used to characterise the notch behaviour. The state of stress parameters required in the proposed models were therefore taken from this region.

The experimental part presented in this thesis consists of a series of creep tests carried out at 538°C on notched specimens pulled in tension and having the same throat diameter as the plain tensile bars. The material tested was a ductile 2¼%Cr 1%Mo steel used in the electric power generation industries. The data collected from these tests, together with other information available in the literature, were used to check the validity of the proposed models in assessing component lifetimes.

CHAPTER 1

CONTINUUM CREEP MECHANICS

1.1 CREEP DEFORMATION OF METALS

Creep could be defined as the time-dependent part of the deformation which accompanies the application of stress to a solid. In general, it is described in terms of three different stages, illustrated in Figure 1.1. The first stage in which creep occurs at a decreasing rate is called primary creep; the second, called the secondary stage, proceeds at a nearly constant rate; and the third, or tertiary stage, occurs at an increasing rate and terminates in fracture.

The total strain, ε, at any instant of time in a creep test is represented as the sum of the instantaneous elastic strain, ε_o, and the creep strain, ε_c, which, by nature, is chiefly irrecoverable. The factors influencing the creep deformation, ε_c, are shown in Figure 1.2, and are given by the following equation:

$$\varepsilon_c = f(\sigma, t, T) \tag{1.1}$$

It is clear from Figure 1.2 that creep deformation accelerates with increase in temperature and the applied stress; this causes earlier fracture. Design against creep becomes most important above a critical temperature, $T_c > 0.3T_m$ (T_m = melting temperature), even if the applied stress or combination of stresses are below the macroscopic yield stress of the material.

1.2 UNI-AXIAL CREEP DEFORMATION AND RUPTURE ANALYSES

The phenomenon of creep was observed during the 19th century but never explained. Components in steam boilers and furnaces were often being replaced by new spares because they deformed. The first scientific investigation into this material behaviour was published in 1905 by Phillips. He studied the slow stretch of india rubber, glass and metal wires when subjected to a constant pull. His work was followed in 1910 by a more detailed investigation by De Costa Andrade into the creep of lead wires. Andrade's contribution to the subject was of the highest value. He introduced the terms primary, secondary and tertiary creep, shown in Figure 1.1, and proposed the first creep law as follows:

$$\ell = \ell_o \left(1 + B\, t^{1/3}\right) e^{kt} \tag{1.2}$$

where ℓ_o and ℓ are the initial and current lengths of the specimen, respectively, and B and k are material constants. Since then, various empirical equations have been proposed for the stress, time and temperature dependence of creep of metals based on experimental observations (Chevenard [1919], and Dickenson [1922]). The steady-state region of the creep curve (secondary creep) was studied in great detail. Bailey and Norton [1929] suggested the empirical equation that yielded good agreement with experimental data for steady creep under low stresses:

$$\dot{\varepsilon}_s = C\, \sigma^n \tag{1.3}$$

where C and n are material constants. Equation (1.3) is called the power-law or Norton's creep law.

Long term rupture tests were the main features of the period 1940 to 1958. Creep tests lasting up to 100,000 h were carried out on different

materials (Prager [1945], Johnson [1951], and Richards [1955]). These tests enabled the scientists to establish that when secondary creep dominates, the primary creep may be neglected. However, under large stresses, and especially at high temperatures, primary creep must be taken into account. This, in 1953, led to the publication of the "Theory of Total Creep Deformation", or "Total Creep Strain Theory", by Odqvist, which included the influence of primary creep. The total creep rate was expressed in the form:

$$\frac{d\varepsilon}{dt} = \frac{d}{dt}\left(\frac{\sigma}{\sigma_o}\right)^{n_o} + \left(\frac{\sigma}{\sigma_c}\right)^{n} \tag{1.4}$$

where σ_o, n_o, σ_c and n are material constants.

1.2.1 Robinson's Linear Cumulative Damage Rule

Robinson [1952] proposed a practical solution for estimating life under variable conditions of stress or temperature. It is based on the assumption that the creep strain is a function of stress, temperature and the accumulated creep strain, ε_c:

$$\dot{\varepsilon} = f(\sigma, T, \varepsilon_c) \tag{1.5}$$

In a tensile creep test, if an applied stress, σ_1, is held for time t_1, it will produce damage, D_1, which, under steady conditions, is proportional to the fraction of total life, t_{R_1}:

$$D_1 = \frac{t_1}{t_{R_1}} \tag{1.6}$$

If the stress is changed to σ_2, then the second amount of damage incurred is:

$$\mathcal{D}_2 = \frac{t_2}{t_{R_2}} \tag{1.7}$$

Assuming that the damage resulting from each loading period is independent of all other periods, Robinson's rule should be applicable for an unlimited number of variable temperature on stress conditions. The total damage, $\mathcal{D}$, for all the periods will then be:

$$\mathcal{D} = \sum \left(\frac{t_i}{t_{R_i}}\right) = \int_0^{t_R} \frac{dt}{t_{R_i}} \tag{1.8}$$

At rupture, $\mathcal{D} = 1$.

The advantage of this method is that it could be used to predict rupture times under variable conditions, using steady load rupture data.

1.2.2 Hoff's Theory of Ductile Creep Rupture

In 1953, Hoff presented a theory which can predict creep failure times of uni-axial test specimens failing by geometrical instability or necking. The theory is based on the assumption that the initial cross-sectional area, A_o, of the testpiece will shrink to zero under a constant load, P. Extending Norton's creep law, equation (1.3), to hold for finite deformation and neglecting primary creep, Hoff obtained the following expression for secondary creep rate:

$$\dot{\varepsilon}_s = -\frac{1}{A}\frac{dA}{dt} = C\left(\frac{P}{A}\right)^n \tag{1.9}$$

where A is the cross-sectional area. Equation (1.9) can be integrated, assuming $A = A_o$ at $t = 0$, therefore:

$$A_o^n - A^n = C\, n\, P^n\, t \tag{1.10}$$

Applying the basic assumption that A_o will decrease to $A = 0$ in the finite time, t_h, equation (1.10) becomes:

$$t_h = \frac{1}{C\ n\ \sigma_o^{\,n}} = \frac{1}{n\ \dot{\varepsilon}_s} \tag{1.11}$$

The stress, σ, will increase from its initial value, $\sigma_o = P/A_o$, with time, according to the following equation:

$$\sigma = \sigma_o \left(1 - \frac{t}{t_h}\right)^{-1/n} \tag{1.12}$$

σ will become infinite when $t = t_h$.

Equation (1.11) represents a straight line with a slope $1/n$ in a log/log plot between $\dot{\varepsilon}_s$ and t_h.

1.2.3 Kachanov's and Robotnov's Continuum Damage Theory

An important contribution to creep mechanics was made by Kachanov in 1958. He presented a theory of combined ductile and brittle creep rupture based on: (a) negligible elastic deformation, (b) creep rate, $\dot{\varepsilon}$, at steady-state is dependent on the applied uni-axial stress and temperature, and (c) deterioration with time takes place whenever a metal is subjected to a state of tensile stress. The deterioration or damage represented by the parameter ω increases monotonically from zero at $t = 0$ (damage-free material) to unity at failure; therefore, the strain rate in a standard Norton, equation (1.3), is now written as:

$$\dot{\varepsilon}_s = \frac{C\ \sigma^n}{(1 - \omega)^q} \tag{1.13}$$

and the rate of change of ω is:

$$\dot{\omega} = \frac{B\,\sigma^{m}}{(1-\omega)^{\kappa}} \tag{1.14}$$

where C, n, q, B, m and κ are material constants in equations (1.13) and (1.14).

Robotnov [1969] generalised these concepts to make predictions of creep strain accumulation, local damage and rupture times, assuming negligible primary creep, such as:

$$\frac{\varepsilon}{\varepsilon_R} = 1 - \left(1 - \frac{t}{t_R}\right)^{\frac{1+\kappa-q}{1+\kappa}} \tag{1.15}$$

and:

$$(1-\omega)^{1+\kappa} = 1 - \frac{t}{t_R} \tag{1.16}$$

where the subscript R refers to rupture. Integrating equation (1.16) under the conditions $\omega = 0$, $t = 0$ and $\omega = 1$, $t = t_R$ leads to an expression for uni-axial rupture time:

$$t_R = \frac{1}{B\,\sigma^{m}\,(1+\kappa)} \tag{1.17}$$

Equation (1.17) corresponds to the linear plots of log σ against log t_R, frequently used to present uni-axial creep data.

Penny [1974], in his review on the usefulness of an engineering approach to creep damage, originated by Kachanov, suggested that the inclusion of a damage relationship for use in structural calculations presents no conceptual or computational difficulties under uni-axial stress conditions. He was able to show that a very good agreement (up to $0.95t_R$) exists between equation (1.15) and many experimental data of different alloys. However, McLean, Dyson and Taplin [1977] showed that this agreement is valid only up to $0.9t_R$ for Nimonic 80A.

1.3 MULTI-AXIAL STATE OF STRESS

At an arbitrary point P in a continuum, each force vector, T_i, is associated with a unit normal vector, n_i. This is illustrated in Figure 1.3, in which ΔS is the surface of a small element having P as an interior point. The totality of all possible pairs of such vectors, T_i and n_i, at P defines the state of stress at that point. Fortunately, it is not necessary to specify every pair of stress and normal vectors to completely describe the state of stress at a given point. This may be accomplished by giving the stress vector on each of three mutually perpendicular planes at P. The nine components involved in describing the state of stress constitute a second order Cartesian tensor, σ_{ij}. Coordinate transformation equations then serve to relate the stress vector on any other plane at the point to the given three reference directions.

The nine components of the stress tensor, σ_{ij}, may be displayed in matrix form as follows:

$$\sigma_{ij} = \begin{bmatrix} \sigma_{11} & \sigma_{12} & \sigma_{13} \\ \sigma_{21} & \sigma_{22} & \sigma_{23} \\ \sigma_{31} & \sigma_{32} & \sigma_{33} \end{bmatrix} \tag{1.18}$$

Pictorially, the stress tensor component may be displayed with respect to the coordinate planes, as shown in Figures 1.4(a) and (b). The components perpendicular to the planes are called normal stresses. Those acting tangentially to the planes are called shear stresses.

A particular set of orthogonal planes could be found in which one of the normal stresses is a maximum and one is a minimum with respect to the rotation of coordinates. These normal stresses are the principal stresses, $\sigma_1 > \sigma_2 > \sigma_3$. The shear stresses on the principal stress planes are zero. Similarly, the planes for normal shear stresses could also be found, where

$\tau_1 > \tau_2 > \tau_3$. However, the normal stresses on the principal shear stress planes are not zero.

The stress space shown in Figure 1.5 has coordinate axes associated with the principal stresses. Every point in this space, for example, $P(\sigma_1,\sigma_2,\sigma_3)$, corresponds to a different state of stress. The position vector of any such point may be resolved into a component OA along the line OZ, which makes equal angles with the coordinate axes, and a component OB in the plane known as the π-plane which is perpendicular to OZ and passes through the origin. The component along OZ, for which $\sigma_1 = \sigma_2 = \sigma_3$, represents the hydrostatic stress and the component in the π-plane represents the deviator portion of the stress state. The equation of the π-plane is given by:

$$\sigma_1 + \sigma_2 + \sigma_3 = 0 \tag{1.19}$$

For an isotropic material, the yield condition defines a surface called the "yield surface" which is a function of the principal stresses defined as follows:

$$f(\sigma_1,\sigma_2,\sigma_3) = constant \tag{1.20}$$

Since the yield conditions are independent of the hydrostatic stress, such yield surfaces are general cylinders, having their generators parallel to OZ. Stress points that lie inside the cylindrical yield surface represent elastic stress states; those which lie on the yield surface represent incipient plastic stress states.

In a true view of the π-plane, looking along OZ towards the origin O, the principal stress axes appear symmetrically placed 120° apart, as shown in Figure 1.6. The yield curves proposed by Von Mises and Tresca are

also shown; these will be discussed in the next sections.

1.3.1 The Maximum Shear Stress or Tresca Theory

As a result of extrusion tests on the flow of soft metals through orifices, Tresca concluded that a metal will yield when the greatest algebraic difference between the three principal stresses reaches a constant critical value. Taking $\sigma_1 > \sigma_2 > \sigma_3$, the theory may be expressed as:

$$\sigma_1 - \sigma_3 = 2\tau_{max} = \bar{\sigma} \tag{1.21}$$

The yield locus described by equation (1.21) is a hexagon, as shown in Figure 1.6. Only the maximum stress difference has an influence upon yielding.

Experimental work on various materials tested under combined tension-torsion or compression-tension suggest that some materials tend to approximately follow the Tresca yield function, but none of them showed the discontinuity required by the criterion (Morrison [1940,1948], Taylor and Quinney [1931], and Rogan and Shelton [1969]).

1.3.2 The Shear Strain-Energy or Von Mises Theory

This theory is variously known as Maxwell-Mises or Henckey-Mises. It states that a material will yield when the shear strain-energy stored in the body reaches a critical value. It is not necessary to stipulate $\sigma_1 > \sigma_2 > \sigma_3$, as all three principal stress differences are involved and not just the maximum difference, as in the Tresca theory. It can be expressed as:

$$(\sigma_1 - \sigma_2)^2 + (\sigma_2 - \sigma_3)^2 + (\sigma_3 - \sigma_1)^2 = 2\bar{\sigma}^2 \tag{1.22}$$

The yield locus in the π-plane, described by equation (1.22), is a circle, as shown in Figure 1.6.

Nadai [1950] has also shown that this combination of principal stresses is proportional to the octahedral shear stress, such as:

$$\tau = \{(\sigma_1 - \sigma_2)^2 + (\sigma_2 - \sigma_3)^2 + (\sigma_3 - \sigma_1)^2\}^{\frac{1}{2}} = \frac{\sqrt{2}}{3}\bar{\sigma} \qquad (1.23)$$

Tests carried out on various materials under combined stresses (tension, torsion, internal pressure) revealed that most low alloy steels, aluminium alloys and copper obey the Von Mises criterion (Siebel [1953], Lianis and Ford [1957], Naghdi, Essenberg and Koff [1958], and Holloway and Shelton [1979[). Other material, such as cast iron and mild steels, showed some deviation from the Von Mises criterion (Cook and Robertson [1911], Lode [1926], and Davis [1945]).

1.3.3 Plasticity Theories and the Phenomenon of Creep

It has been shown in previous sections that plastic deformation in metals takes place if a stress in excess of the yield stress is suddenly applied. A strain of a value, say, ε_1, is instantaneously observed. However, if the stress is kept constant, the strain gradually increases with time until it approaches a steady value of, say, ε_2 (Figure 1.7). The value $(\varepsilon_1 - \varepsilon_2)$ is the creep strain.

Metal physicists attribute the deformation of metals, whether it is plastic or creep, to dislocation movement in the shear or slip planes due to the applied stress. The dislocation movements in purely plastic deformation are activated by the applied stress, while under creep conditions they are activated by thermal agitation due to the high temperature, even if the applied stress is lower than the yield stress of the material. This fundamental similarity in the deformation process

means that the well-established theories of plasticity are applicable also to creep.

The first satisfactory theory of isotropic tri-axial secondary creep behaviour was published in 1935 by Odqvist. He generalised Norton's equation (1.3) by employing the Von Mises definition of the second stress invariant, $\bar{\sigma}$ (equation (1.22)), as follows:

$$\dot{\varepsilon}_{ij} = \frac{3}{2} C \bar{\sigma}^{n-1} S_{ij} \tag{1.24}$$

where S_{ij} is the tensor for the stress deviator. Odqvist's theory was based on two assumptions:

(a) Incompressibility, i.e.

$$\dot{\varepsilon}_{11} + \dot{\varepsilon}_{22} + \dot{\varepsilon}_{33} = 0 \tag{1.25}$$

(b) Normality and convexity of preserved surfaces, i.e.

$$\bar{\sigma} = constant \tag{1.26}$$

Other equations for multi-axial creep based on similar principles have also been proposed by Soderberg [1936], Nadai [1937], and Tapsell and Johnson [1940]. These equations showed reasonable agreement with the experimental data collected from different tests on different materials.

The experimental work done by Johnson and co-workers [1962] also confirmed that plasticity theories are applicable for creep. They showed that the primary and secondary creep resistance of a number of pure

metals and engineering alloys in uni-axial tension and under complex stress systems are identical when these results are analysed using plasticity theories. They found that their data were well represented by the following equation:

$$\bar{\dot{\varepsilon}} = A\,\bar{\sigma}^{n}\,f(t) \tag{1.27}$$

where $\bar{\sigma}$ and $\bar{\dot{\varepsilon}}$ are the effective stress and strain rate, respectively, A is the material constant, and $f(t)$ is a time function equal to unity for secondary creep. Equation (1.27) is simply a specific form of the generally acceptable flow theory of Odqvist (equation (1.24)).

1.4 CREEP BEHAVIOUR OF NOTCHED BARS

Equipment which operates over long periods of time at elevated temperatures may suffer excessive deformation or fracture due to creep. Since many components experience tri-axial stress as a result of the applied loading conditions or local sharp changes in section, the laws describing creep behaviour under multi-axial stressing are used in the design. Experience has shown that failure often initiates from sites of stress concentrations where there is a significant hydrostatic tensile stress component.

The most frequently used method of introducing a three-dimensional state of stress into a testpiece in the laboratory is to subject circumferentially notched bars to an axial tensile load. The state of stress in the notch root can be changed systematically by changing the notched section dimensions. This cannot be measured experimentally; therefore, scientists have to rely on various analytical techniques which, together with the uni-axial and notch bar rupture data, can provide useful information for design engineers.

1.4.1 Notch Rupture Strength

The results of experimental uni-axial and notched bar creep tests are usually interpreted in terms of notch to unnotched lives or strength ratios. When time ratios are used in the presentation, the following condition is applied:

$$\frac{\sigma_n}{\sigma_{un}} = 1 \tag{1.28}$$

therefore:

$$\frac{t_{no}}{t_{un}} = S_t \tag{1.29}$$

where t_{no} is failure time of a notched specimen due to an applied nominal

stress, σ_n, on the minimum section, and t_{un} is failure time of a uni-axial specimen under a similar applied stress, $\sigma_n = \sigma_{un}$.

Similarly, when stress ratios are presented, the condition is:

$$\frac{t_{no}}{t_{un}} = 1 \tag{1.30}$$

therefore:

$$\frac{\sigma_n}{\sigma_{un}} = S_\delta \tag{1.31}$$

where σ_n is the stress on the minimum section of a notched bar that fails in a time t_{no}, and σ_{un} is the stress in a uni-axial specimen that fails in the same time, $t_{no} = t_{un}$. Figure 1.8(a) illustrates how the time and stress ratios are estimated for typical uni-axial and notched data under various applied stresses at constant temperature. The materials are said to be notch strengthened if S_t and $S_\delta > 1$, but notch sensitive (weakening) if S_t and $S_\delta < 1$, as shown in Figure 1.8(b).

Previous experimental work has indicated that notch strengthening and notch weakening can both be observed, depending upon the material and test conditions.

Davis and Manjoine [1953], Newman, et al. [1953], and Ng, et al. [1980], in their experimental investigations on different materials, showed that some materials will always notch strengthen with increase in constraint, while others will change from notch strengthening to notch weakening after a certain amount of constraint.

1.4.2 Stress Distributions in Circumferentially Notched Bars

Several methods of calculating the stress distributions within a notch region undergoing creep deformation have been proposed in the literature. Some methods make use of the non-workhardening plasticity solutions and are, therefore, strictly relevant only to values of creep

stress index, $n \to \infty$. Other methods use the finite element techniques with the appropriate equations describing primary, secondary and tertiary creep.

In 1952, Bridgman suggested an approximate method for determining the stress distribution in the necked region of a two-dimensional sheet and a cylindrical bar pulled in tension by a uniform load. Both the stress equation of equilibrium and the general condition of plasticity have to be satisfied in the neck. Bridgman's analysis is only applicable for notches with low constraint.

Slip-line field analyses on rigid perfectly-plastic materials have been performed on various notched geometries to determine the distribution of strain and the constraint factor, P_c, defined as follows:

$$P_c = \frac{\sigma_n}{\bar{\sigma}} \tag{1.32}$$

where σ_n is the axial throat stress, and $\bar{\sigma}$ is the equivalent stress.

The work by Ewing [1967,1968] on plane strain V-notched bars with and without fillet radii led to a mathematical expression that could be used to calculate the ratio of the throat to bar diameters required to achieve localised deformation. Other expressions were also suggested by McClintock [1961], and Neimark [1968], based on slip-line field analyses.

In 1966, Szczepinski, et al., calculated the constraint factor, P_c, for circumferential notches where the radial and the tangential components in the minimum section are equal. They also suggested a method for determining the critical width for these notches.

Bates and Santhanam [1978] used a modified form of slip-line field solution to calculate the stress distributions ahead of notch tips for strain hardening materials. Later, Santhanam and Bates [1979] discussed the influence of notch tip geometry on the distribution of

stress and strain. They suggested a formula for the maximum principal strain in the notch zone and the way it decays throughout the region.

In the last 20 years, great advances have been made in computational techniques and computer power. One numerical technique which benefitted from these advances was the finite element method. Many scientific research studies have been made to solve and improve the quality of solutions of plastic and non-linear problems.

Sutherland [1970] developed an elastic finite element computer code to include non-linearity arising from creep. He obtained solutions for plane strain, plane stress and axi-symmetric problems. The technique used in the code to converge from the elastic to steady-state creep condition was based on Greenbaum and Rubinstein's [1968] incremental procedure.

The first detailed finite element calculations performed to obtain steady-state stress distributions in the throat of notched bar geometries were made by Hayhurst and co-workers [1977a,b,1978]. They produced steady-state solutions in the absence of damage at first, then damage was introduced gradually until failure.

Needleman and Shih [1978] used a finite element method for solving plane strain incompressible material deformation problems. The problems they considered were a beam in pure bending, thick-walled tube subjected to internal pressure, a hole in an infinite plate, and a plane strain notched bar in tension. Later, Kumar, German and Shih [1980] extended this method to deal with axi-symmetric problems and produced some steady-state stress distributions in the throat of a notched bar under tensile loading.

Al-Faddagh, et al. [1982] used a finite element iterative procedure for calculating directly the steady-state stress distributions in axi-symmetric bodies without the need for obtaining solutions at

intermediate time intervals. The solutions obtained for various notched bars showed good agreement with Bridgman's approximate plasticity solutions and other finite element predictions.

1.4.3 Steady-State and Rupture Times Under Multi-Axial State of Stress

A number of theories and methods have been proposed in the literature for estimating the steady-state and rupture times under multi-axial state of stress. Provided that the required material coefficients and the state of stress components are known, they should, therefore, be applicable to notched bars.

Several studies by Calladine [1963-1967] have demonstrated that Hoff's theory of ductile creep rupture (Section 1.2.2) is applicable for a wide range of structural problems, such as beams, plates and shells. Later, in 1969, Calladine proposed a mathematical formula, which takes into consideration multi-axial effects, to estimate the time taken for the stress to relax from the initial elastic value to the steady-state. His estimates showed a satisfactory level of agreement with other numerical predictions of the time to achieve steady-state, made by Marriott and Leckie [1964] and Penny [1967].

A time-iterative numerical method was used by Hayhurst [1973a] to calculate rupture times of plate structures subjected to in-plane tension. The effects of stress redistribution due to primary and tertiary creep were included in the calculations.

A generalised method to that of Martin and Leckie [1972] was used by Hayhurst [1973b] and Hayhurst and Leckie [1973] to include the effects of multi-axial stress rupture. Estimates of rupture times for a number of structures were made. They showed satisfactory agreement with the experimental predictions by Leckie and Hayhurst [1974].

Hayhurst, Dimmer and Chernuka [1975] carried out some numerical calculations using a finite element method to estimate rupture lives of plates containing a circular hole subjected to in-plane tension. They showed good agreement with the experiments performed on copper and aluminium alloys. The same finite element method was used by Hayhurst and co-workers [1977a,b,1978] to solve axi-symmetric problems. Estimates of steady-state and rupture times were given but never proved experimentally.

Cane [1981] published the results of a research programme geared to assess the design and performance of heavy section steam pipe welds operating in the creep range. The materials tested were a selection of brittle and ductile low alloy steels. The creep and rupture data on these materials were used in finite element computations to predict failure strains, times and stresses.

1.5 CONCLUSIONS

Continuum mechanics laws, which describe the behaviour of components undergoing creep deformation leading to rupture, due to an applied uni-axial or multi-axial state of stress, have been discussed in detail. The associated equations describing these laws will be used in coming chapters in experimental and theoretical analyses.

The creep behaviour of notched bars under tensile loading were discussed in general. In particular, the equations describing notch strengthening and weakening in terms of time or stress strength ratios were given. These will be used in future analyses to model real material data.

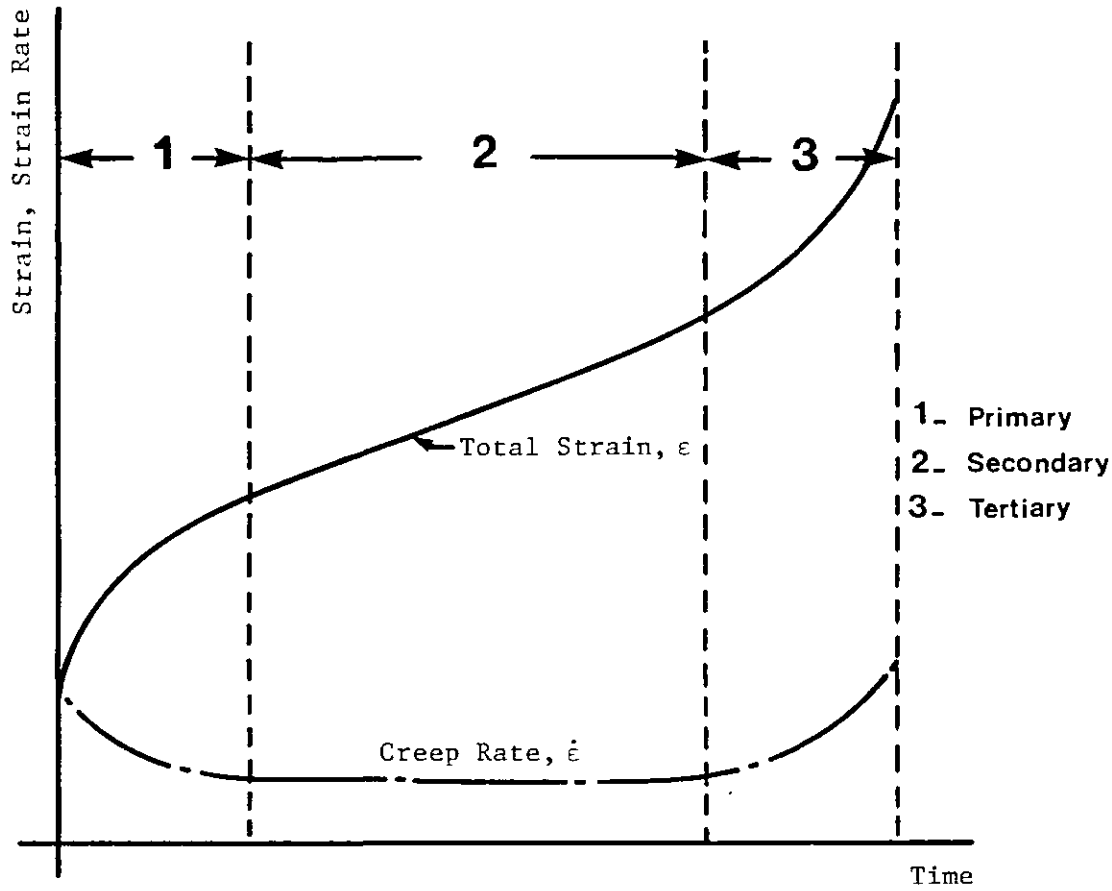

Figure 1.1: Three stages of creep

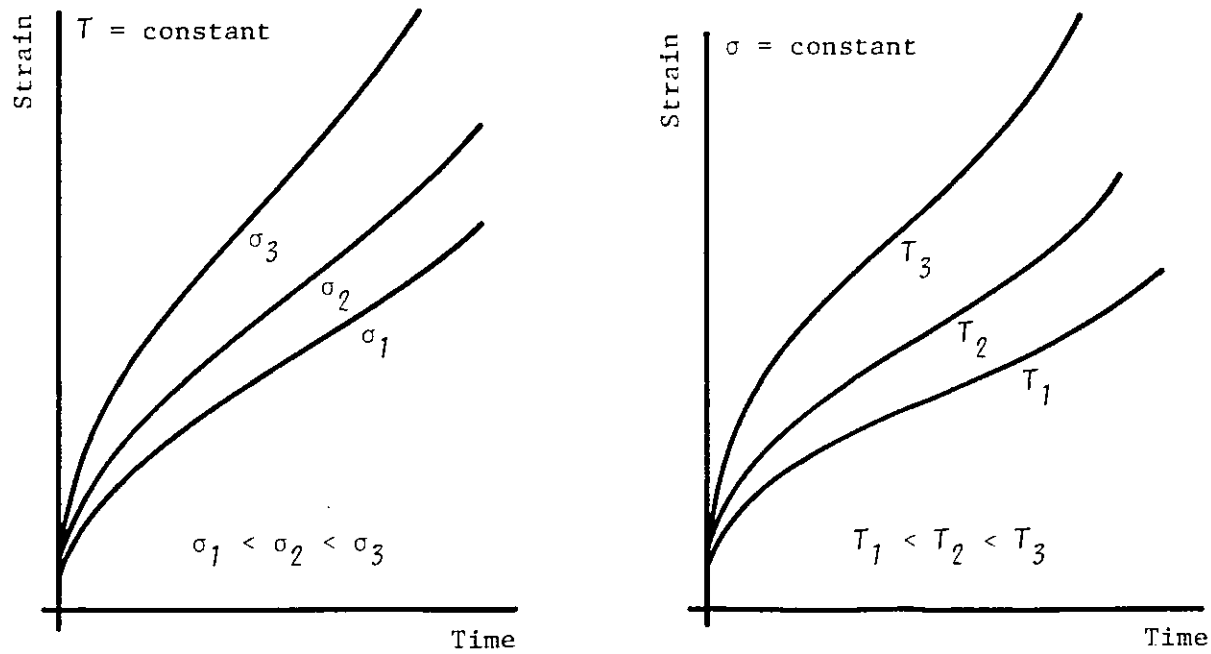

Figure 1.2: Influence of stress and temperature on creep deformation

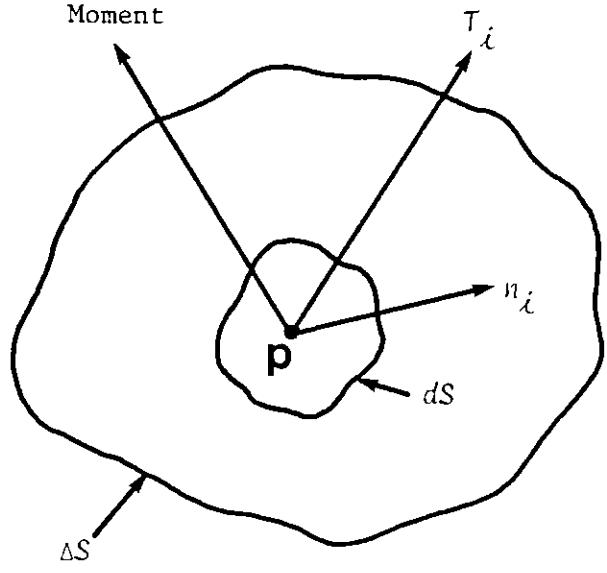

Figure 1.3: State of stress at a point

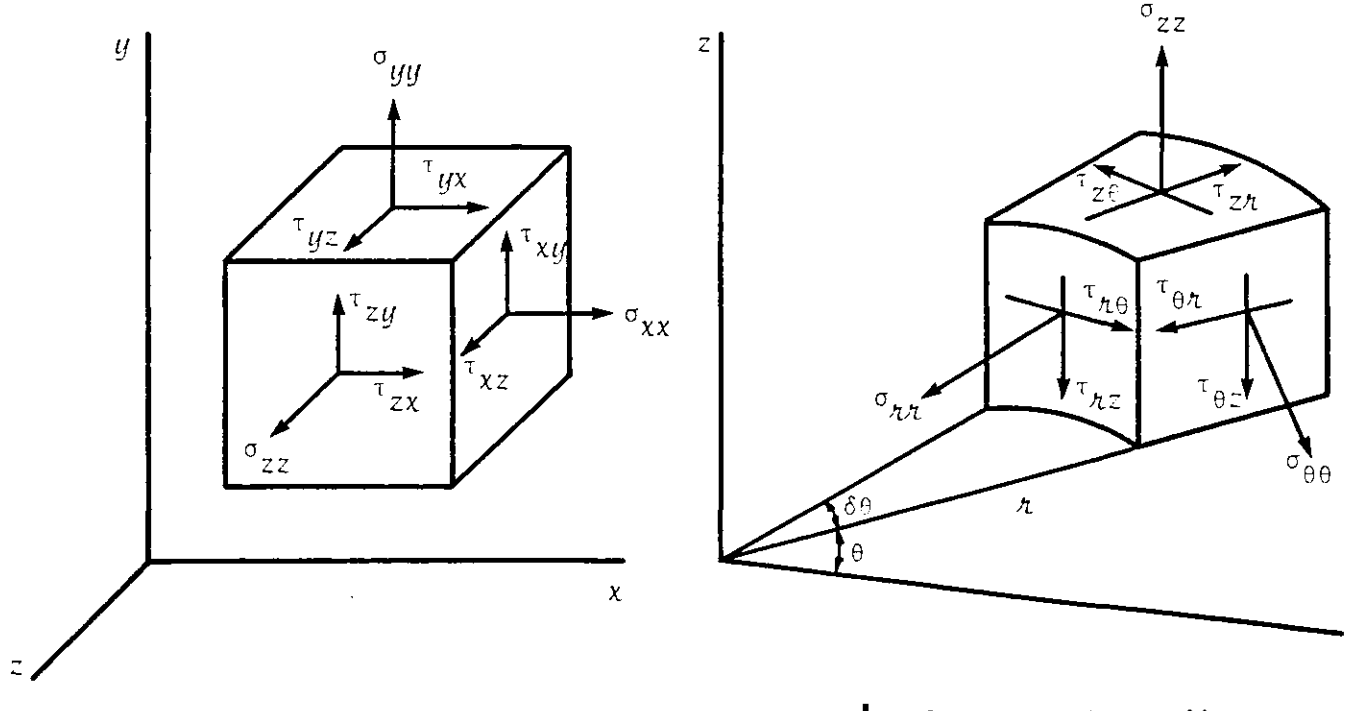

Figure 1.4: Stress components

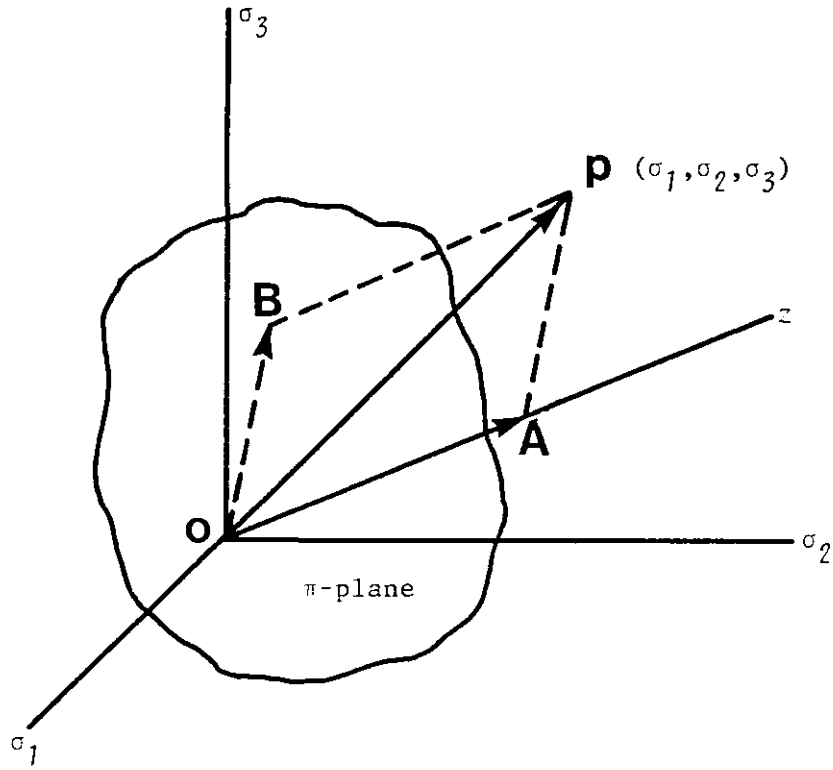

Figure 1.5: Stress space associated with principal stress coordinates

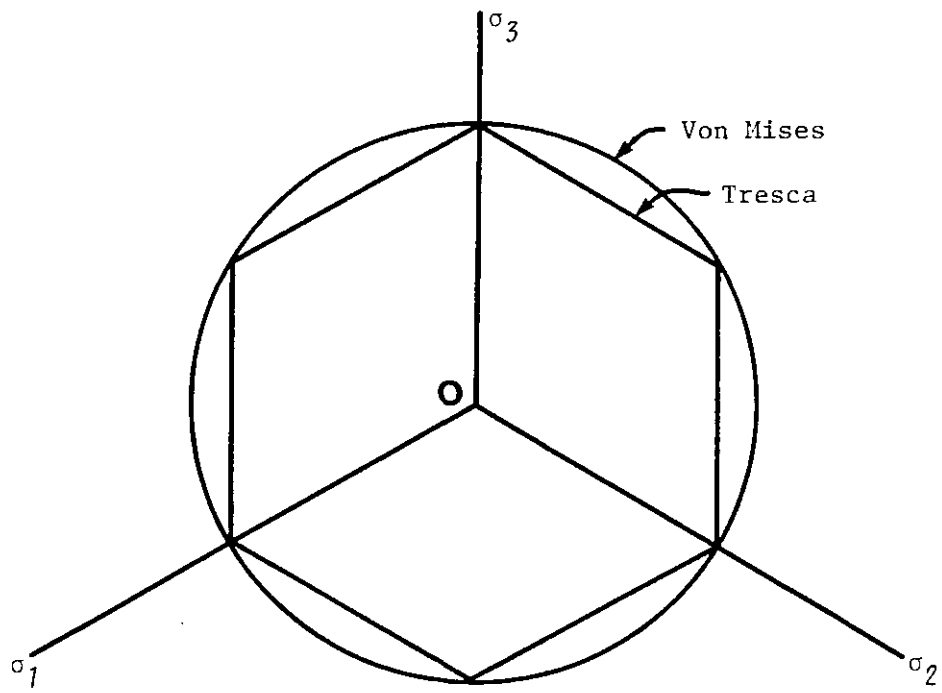

Figure 1.6: Yield curves in the π-plane

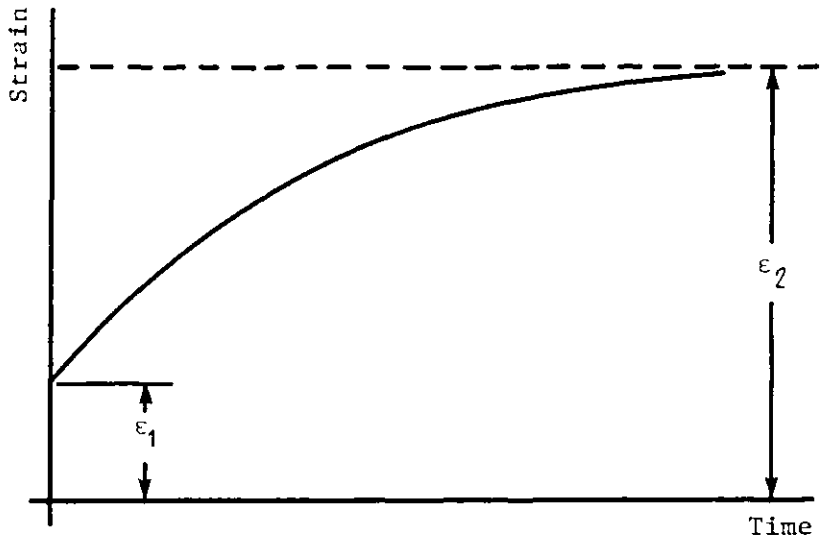

Figure 1.7: Plastic and creep strain

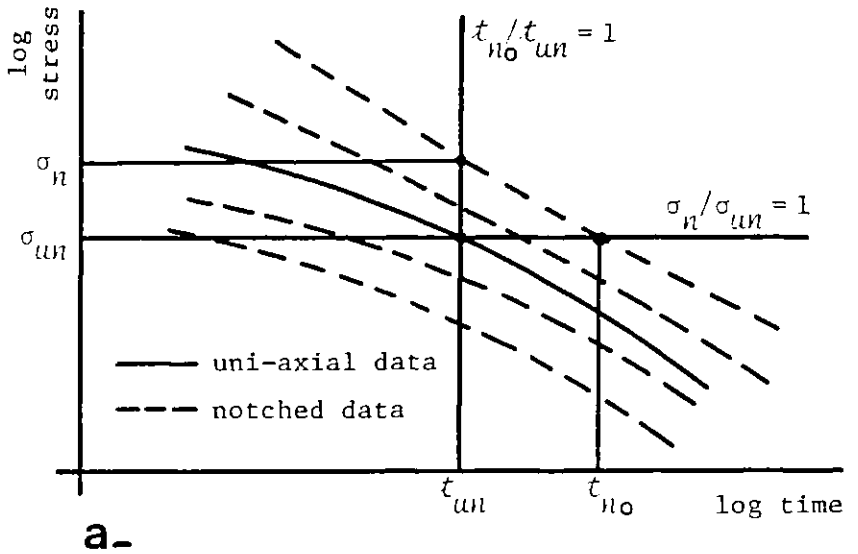

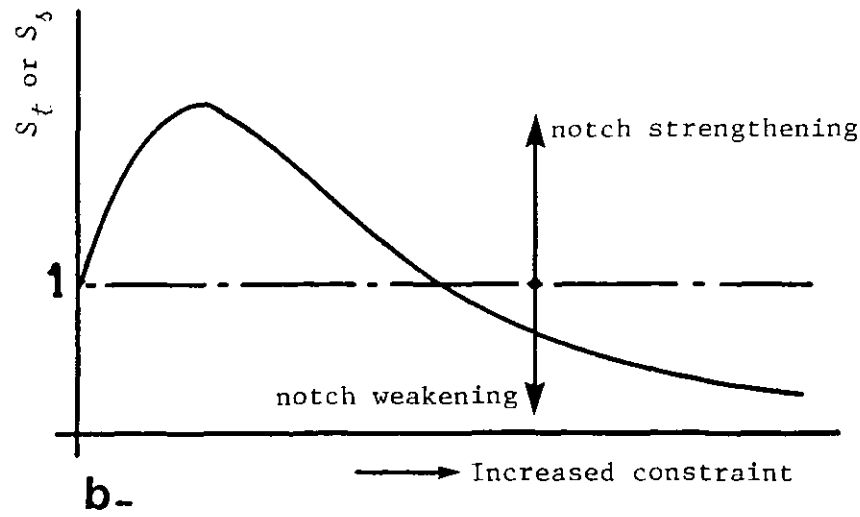

Figure 1.8: Schematic diagrams of notch strengthening and weakening

CHAPTER 2

CREEP RUPTURE BY VOID GROWTH

2.1 INTRODUCTION

Creep damage theories are, in general, classified under two headings:

(a) Engineering creep damage theories.

(b) Metal science creep damage theories.

All theories agree in principle that damage is reponsible for the acceleration in strain rate observed during tertiary creep and therefore causes fracture. The difference is that engineering damage theories use a state parameter in the constitutive equations to describe the damage process responsible for weakening the material (Chapter 1), while metal scientists can identify the damage microscopically. This enables them (the metal scientists) to choose the correct stress component in their constitutive equations to describe the internal damage accumulation. Metal science theories relate intergranular creep fracture to the initiation and growth of grain boundary cavities.

2.2 GRAIN BOUNDARY SLIDING

At high temperatures ($T > 0.3T_m$), intercrystalline fractures, or fractures that run along grain boundaries, are the rule rather than the exception. A metal which at low temperatures fails with a normal transcrystalline failure is inclined to fail by a fracture that passes along the grain boundaries at elevated temperatures. These intercrystalline fractures are closely related to grain boundary shearing or sliding. Figure 2.1 illustrates the various ways in which sliding could be accommodated (Edwards and Ashby [1979]). Elastic deformation is a reversible process; therefore, it has no significant influence on the overall deformation mechanisms. The remaining four methods, in which sliding can be accommodated, form two distinct failure mechanisms. These are diffusion, which is usually responsible for brittle failure, and power-law creep mechanisms associated with ductile failure.

Intercrystalline brittle and ductile failure mechanisms differ in the way the shear stress along the grain boundary is relaxed (Figure 2.2). In a totally brittle failure, the shear stress along the sliding boundary is relaxed by causing a high stress concentration zone at the grain corner. Because the grains do not deform, then the concentration of stress will cause the formation of microcracks and voids which grow until grain separation takes place. However, in a totally ductile failure, the stress concentration at the end of the boundary is relieved by plastic flow or creep. Separation occurs when the cohesive strength of the grain boundary can no longer take the stress. A combination of these two mechanisms can also cause grain separation. The shear stress is relaxed by the formation of voids, mini-cracks and grain deformation.

2.3 INTRODUCTION TO THE CONCEPT OF CREEP RUPTURE BY VOID GROWTH

Before discussing the various growth theories, it is necessary to define some basic terms which will be used frequently in the future. The schematic diagram drawn by Cocks and Ashby [1980a] represents the simplest way of modelling a grain boundary void subjected to the stress field σ_1, σ_2, σ_3, as shown in Figure 2.3. The parameter 2ℓ is the void spacing, d the grain size, and $2r_h$ is the void diameter. Under the above stress field, voids grow by three distinct micromechanisms; these are:

(a) Power-law creep mechanism.

(b) Boundary diffusion mechanism.

(c) Surface diffusion mechanism.

Figure 2.4 shows the simplest way of representing each mechanism in a unit structure.

Void growth by coupled mechanisms is also possible. They control the growth because the volumetric growth rate of a void is dependent upon the following parameters:

$$\dot{V} = f(\dot{\varepsilon}, T, V) \tag{2.1}$$

where $\dot{\varepsilon}$ is the strain rate, T is the temperature, and V is the current volume of a void. One mechanism dominates for a period of time, then a switch to another mechanism will dominate until failure. Three types of coupled mechanisms can control the growth of voids; these are:

(a) Coupled boundary diffusion and power-law creep mechanism.

(b) Coupled surface diffusion and power-law creep mechanism.

(c) Coupled boundary and surface diffusion mechanism.

Figure 2.5 shows a void growing under the influence of a normal stress, σ_1, for each individual coupled mechanism.

To visualise how the switch in failure mechanisms can take place, Ashby, et al. [1979], Svensson and Dunlop [1980], and Cocks and Ashby [1982a], constructed cavity growth mechanism maps for various materials. One example of these maps for copper and for α-brass is shown in Figures 2.6(a) and (b). The diagrams show how the strain rate, stress, temperature, and void dimensions can cause a switch from one failure mechanism to the other.

Dyson and Taplin [1976] also showed how dependent the transition is, from continuum growth (power-law creep) to diffusion-controlled growth, on strain rate, temperature, and void dimensions (Figure 2.7).

2.4 THEORIES OF RUPTURE RELATED TO THE NUCLEATION AND GROWTH OF VOIDS

The creep fracture process in metallic materials involves stages of: cavity nucleation, growth, interlinkage to form cracks, crack propagation, and final fracture. Some of these stages may occupy a small proportion of the total creep life and therefore have little influence on the total rupture time of the material. Metal scientists, through their observations of material behaviour under creep conditions, believe that nucleation, growth, interlinkage, and propagation occur simultaneously during tertiary creep prior to failure.

To develop a theory which includes the effects and interactions of all these stages is extremely difficult. Therefore, creep life is often considered to be dominated by only one or two stages and that the others can be neglected. In this section, metal science theories and their development will be discussed in detail.

In 1954, Greenwood, et al., noted that creep rupture is due to the growth and coalescence of voids at grain boundaries. They also stated that the cavity nucleation at the grain boundaries is predominantly dependent on creep strain and that the growth of these cavities is due to diffusion.

Hull and Rimmer [1959] proposed a theory of void growth controlled by boundary diffusion. Their equation for void growth is:

$$\frac{d\delta_h}{dt} \propto \left[\frac{\sigma}{1-\delta_h} - \frac{\gamma}{\ell}\sqrt{\frac{\pi}{\delta_h}}\right] \tag{2.2}$$

where γ is the surface energy, and:

$$\delta_h = \frac{r_h^2}{\ell^2} \tag{2.3}$$

where r_h is the hole radius, and 2ℓ is their spacing. The cross-

sectional area of voids per unit area parameter δ_h is similar to the state parameter ω in Kachanov's theory. Other theories and models for diffusion-controlled void growth were proposed by Speight and Harris [1967], Weertman [1974], Speight and Beer [1975], Raj and Ashby [1975], Chuang, et al. [1979], and Cocks and Ashby [1982a]. In these theories, expressions for the rate of volumetric change of a void are given, based on the assumptions:

(a) Constancy of cavity density.

(b) Grains do not deform plastically.

(c) Cavities are a perfect vacancy sink and the normal stress is a perfect cavity source.

(d) The applied load remains constant on each cavitated grain facet.

The mechanism of void growth by power-law creep was first introduced by McClintock [1968] when studying a simple model of a hole growth during plastic deformation. His work was followed by many proposed theories for void growth by power-law creep (Rice and Tracey [1969], Hellan [1975], Dyson and Taplin [1976], Edwards and Ashby [1979], Needleman and Rice [1980], and Cocks and Ashby [1980b]). All these theories proposed an expression for calculating the rate of radius growth of a void under the influence of a remote uniform effective strain rate field, $\bar{\dot{\varepsilon}}$, such as:

$$\dot{r} = r K \bar{\dot{\varepsilon}} \tag{2.4}$$

K is the stress state sensitivity parameter dependent on the particular theory adopted.

It was shown in Section 2.3 that the volumetric growth rate of a void is dependent on the three parameters, $\dot{\varepsilon}$, T and V (equation (2.1)). This

makes it necessary to analyse a model in which voids grow by coupled mechanisms. This was done by Beer and Speight [1978], Edwards and Ashby [1979], Chuang, et al. [1979], and Cocks and Ashby [1980a,1982a,b]. One example of a void growth by a coupled diffusion and power-law creep mechanism is shown in Figures 2.8(a) and (b) (Cocks and Ashby [1982a]). It shows the damage rate ($d\delta_h/dt$) dependence on both the stress and the area fraction of holes, δ_h. The interesting thing about this model is the introduction of a transition parameter, δ_t. The diffusion mechanism dominates from the initial area fraction of holes δ_i to δ_t and power-law creep dominates from δ_t until fracture.

Other theories and models are available in the literature which focus on the linkage of separately nucleated grain boundary cracks and their propagation.

Lindborg [1968] derived a relationship which gave the fraction of cracked grain, P, in terms of the number of micro-cracks, n, required for fracture:

$$P = 0.2 \left(\frac{2n}{N}\right)^{\frac{1}{2}} \tag{2.5}$$

where N is the number of grains. He used this equation to predict the percentage of area that had been cracked due to creep prior to fracture and compared it with his experiments. Later, Lindborg [1969] studied the growth rate of sharp intercrystalline cracks and suggested that fracture occurs when one of the cracks reaches a critical size.

Dyson [1976] proposed a theory in which the rate of diffusive cavity growth may be constrained by either the rate of deformation of the surrounding material or the rate of supply of vacancies at the adjacent grain boundary. He proposed an upper bound strain rate equation, similar to Kachanov's equation (1.13), such that:

$$\dot{\varepsilon} = B \left[\frac{\sigma}{1 - A_c}\right]^n \tag{2.6}$$

where A_c is a parameter controlled by strain and can change by continuous cavity nucleation. It is expressed as:

$$A_c = K \varepsilon \quad , \quad K = constant \tag{2.7}$$

therefore:
$$\dot{\varepsilon} = B \left[\frac{\sigma}{1 - K \varepsilon}\right]^n \tag{2.8}$$

or
$$\dot{\varepsilon} = B \sigma^n (1 + n K \varepsilon) \tag{2.9}$$

and for $K\varepsilon << 1$:
$$\dot{\varepsilon} = B \sigma^n \exp^{nK\varepsilon} \tag{2.10}$$

Dyson stated that equation (2.10) can represent the secondary and tertiary creep of many materials.

2.5 ASHBY'S THEORY OF CREEP RUPTURE BY VOID GROWTH

In recent years, Ashby and co-workers published a comprehensive theory for modelling the growth of voids by mechanisms controlled by grain boundary diffusion, by surface diffusion, by power-law creep, and by any combination of the two of these (Figures 2.4 and 2.5) (Raj and Ashby [1975], Edwards and Ashby [1979], Cocks and Ashby [1980a,b,1982a,b]). The theory replaces the classical continuum mechanics damage parameter, ω, responsible for the acceleration in strain rate during tertiary creep, by a new term called the area fraction of holes on grain boundary, δ_h, defined by:

$$\delta_h = \frac{r_h^2}{\ell^2} \tag{2.11}$$

where r_h is the radius of a growing void, and 2ℓ is the centre-to-centre void spacing, as shown in Figure 2.3.

The theory assumes that all voids nucleate at a certain time, t_n, in which δ_h has an initial small value, δ_i. Voids then start to grow under the influence of either stress state or temperature, until δ_h reaches a critical value, δ_c, where failure takes place. According to continuum mechanics theories, $\omega = 1$ at failure, similarly for this theory δ_h should therefore equal one at $t = t_R$. In reality, samples will fail sooner because, as δ_h approaches one, the true stress on the remaining ligament increases rapidly; therefore, either ductile failure, cleavage, or some other fast fracture mechanism will cause failure. Ashby's theory adopts a critical value, $\delta_c = 0.25$, except when there is a non-uniform distribution of voids (constrained cavity growth).

The constitutive law used in Ashby's theory for power-law creep is:

$$\dot{\bar{\varepsilon}}_\Delta = \dot{\varepsilon}_o \left(\frac{\bar{\sigma}}{\sigma_o}\right)^n \tag{2.12}$$

where n, $\dot{\varepsilon}_o$ and σ_o are material constants, and $\bar{\sigma}$ and $\bar{\dot{\varepsilon}}_\delta$ are the Von Mises effective stress and strain rate defined as follows:

$$\bar{\sigma} = \left\{\frac{1}{2}\left|(\sigma_1 - \sigma_2)^2 + (\sigma_2 - \sigma_3)^2 + (\sigma_3 - \sigma_1)^2\right|\right\}^{\frac{1}{2}} \tag{2.13}$$

and:
$$\bar{\dot{\varepsilon}}_\delta = \left\{\frac{2}{9}\left|(\dot{\varepsilon}_1 - \dot{\varepsilon}_2)^2 + (\dot{\varepsilon}_2 - \dot{\varepsilon}_3)^2 + (\dot{\varepsilon}_3 - \dot{\varepsilon}_1)^2\right|\right\}^{\frac{1}{2}} \tag{2.14}$$

The stresses and strains in equations (2.13) and (2.14) are all principal values.

The strain rate at lower stresses is controlled by diffusion across or around grains; therefore:

$$\dot{\varepsilon}_\delta = \frac{12\, \mathcal{D}_v\, \Omega\, \bar{\sigma}}{k\, T\, d^2}\left(1 + \frac{\pi\, \delta\mathcal{D}_b}{d\mathcal{D}_v}\right) \tag{2.15}$$

where $\mathcal{D}_v$ and $\delta\mathcal{D}_b$ describe the rates of lattice and of grain boundary diffusion, Ω is the atomic volume, d is the grain size, T is the absolute temperature, and k is Boltzmann's constant.

In the next sections, a summary of Ashby's analysis is given for the different mechanisms proposed to model the growth of voids.

2.5.1 Void Growth by Boundary Diffusion Alone

When voids grow by boundary diffusion, matter diffuses out of the growing void, which remains spherical, and plates onto the grain boundary, as shown in Figure 2.4(a). The equations to describe damage rate and strain rate are:

$$\frac{1}{\dot{\varepsilon}_o}\frac{d\delta_h}{dt} = \frac{\phi_o}{\delta_h^{\frac{1}{2}}\ln(1/\delta_h)}\left(\frac{\sigma_1}{\sigma_o}\right) \tag{2.16}$$

$$\frac{1}{\dot{\varepsilon}_o}\frac{d\varepsilon}{dt} = \frac{2\phi_o}{\ln(1/\delta_h)}\left(\frac{\ell}{d}\right)\left(\frac{\sigma_1}{\sigma_o}\right) \tag{2.17}$$

where ϕ_o is a material property defined as:

$$\phi_o = \frac{2\, D_b\, \delta_b\, \Omega}{k\, T\, \ell^3} \frac{\sigma_o}{\dot{\varepsilon}_o} \tag{2.18}$$

The constants in equation (2.18) were defined after equation (2.15).

The time to rupture expression was found by integrating equation (2.16) between the following limits:

$$\begin{aligned} \delta_h &= \delta_i \quad \text{at} \quad t = t_n \\ \delta_h &= \delta_c \quad \text{at} \quad t = t_R \end{aligned} \tag{2.19}$$

where δ_i is the initial area fraction of the holes, and t_n is the nucleation time. The result is:

$$t_R = t_n + \frac{2}{3\,\phi_o\,\dot{\varepsilon}_o} \left\{ \delta_c^{3/2} \left[\ln \left(\frac{1}{\delta_c}\right) + \frac{2}{3} \right] - \delta_i^{3/2} \left[\ln \left(\frac{1}{\delta_i}\right) + \frac{2}{3} \right] \right\} \frac{\sigma_o}{\sigma_1}$$

or:
$$t_R \simeq t_n + \frac{0.17}{\phi_o\,\dot{\varepsilon}_o} \left(\frac{\sigma_o}{\sigma_1}\right) \tag{2.20}$$

if $\delta_i < 10^{-2}$ and $\delta_c = 0.25$.

The strain to rupture expression was obtained by integrating equations (2.16) and (2.17) as a coupled set. The result is:

$$\varepsilon_R = \frac{4}{3}\, \delta_c^{3/2}\, \frac{\ell}{d} \simeq 0.2\, \frac{\ell}{d} \tag{2.21}$$

The nucleation strain, ε_n, must be added to rupture strains which are usually small; therefore, rupture times at constant load and stress are expected to be almost equal.

2.5.2 Void Growth by Surface Diffusion Alone

When voids grow by surface diffusion, matter flows out of it at the equator, causing it to become flatter and more crack-like, as shown in Figure 2.4(b). The equations given to describe damage rate and strain rate are:

$$\frac{1}{\dot{\varepsilon}_o}\frac{d\delta_h}{dt} = \frac{\psi_o\,\delta_h^{\frac{1}{2}}}{(1-\delta_h)^3}\left(\frac{\sigma_1}{\sigma_o}\right)^3 \tag{2.22}$$

$$\frac{1}{\dot{\varepsilon}_o}\frac{d\varepsilon}{dt} = \frac{4\,\psi_o\,\delta_h^{\frac{1}{2}}}{(1-\delta_h)^3}\frac{\gamma_s}{d\sigma_o}\left(\frac{\sigma_1}{\sigma_o}\right)^3 \tag{2.23}$$

where ψ_o is a material property defined as:

$$\psi_o = \frac{1}{\sqrt{2}}\frac{D_s\,\delta_s\,\Omega}{k\,T\,\ell\,\gamma_s^2}\frac{\sigma_o^3}{\dot{\varepsilon}_o} \tag{2.24}$$

where γ_s is the surface free energy. The other parameters are similar to those in equation (2.18), but are for surface diffusion.

The time to rupture expression was found by integrating equation (2.22) between the limits of equation (2.19). The result is:

$$t_R = t_n + \frac{2\,(\delta_c^{\frac{1}{2}} - \delta_i^{\frac{1}{2}})}{\dot{\varepsilon}_o\,\psi_o}\left(\frac{\sigma_o}{\sigma_1}\right)^3$$

or:

$$t_R \simeq t_n + \frac{1-2\delta_i}{\dot{\varepsilon}_o\,\psi_o}\left(\frac{\sigma_o}{\sigma_1}\right)^3 \tag{2.25}$$

when δ_i is small, and $\delta_c = 0.25$.

Voids growing by surface diffusion contribute almost no strain as they grow because of their flat crack-like shapes. The times to rupture at constant load and stress are, therefore, expected to be almost equal.

2.5.3 Void Growth by Power-Law Creep Alone

When voids grow by power-law creep alone, the effective stress, $\bar{\sigma}$, determines their rate of expansion. The rest of the matter containing the voids, shown as the shaded area in Figure 2.4(c), extends at a rate determined by the net section stress, $\bar{\sigma}/(1-f_h)$. The equations given to describe damage rate and strain rate are:

$$\frac{1}{\dot{\varepsilon}_o}\frac{df_h}{dt} = \frac{1}{\alpha}\left[\frac{1}{(1-f_h)^n} - (1-f_h)\right]\left(\frac{\bar{\sigma}}{\sigma_o}\right)^n \tag{2.26}$$

$$\frac{1}{\dot{\varepsilon}_o}\frac{d\varepsilon}{dt} = \left\{1 + \frac{2n_h}{\alpha\, d}\left[\frac{1}{(1-f_h)^n} - 1\right]\right\}\left(\frac{\bar{\sigma}}{\sigma_o}\right)^n \tag{2.27}$$

where α is a parameter that measures the effect of stress state on void growth rate. It is defined as:

$$\alpha = \left\{\sinh - \left[2\,\frac{(n-\frac{1}{2})}{(n+\frac{1}{2})}\,\frac{\sigma_m}{\bar{\sigma}}\right]\right\}^{-1} \tag{2.28}$$

where σ_m is the hydrostatic pressure expressed by:

$$\sigma_m = -\frac{\sigma_1 + \sigma_2 + \sigma_3}{3} \tag{2.29}$$

At constant stress, the time to rupture was found by integrating equation (2.26) between the limits of equation (2.19) and assuming that f_i is small and $f_c = 0.25$. The result is:

$$t_R = t_n + \frac{\alpha}{(n+1)\,\dot{\varepsilon}_o}\,\ln\left[\frac{1}{(n+1)\,f_i}\right]\left(\frac{\sigma_o}{\bar{\sigma}}\right)^n \tag{2.30}$$

At constant load, the expression given for rupture time, using the same assumption for constant stress, is:

$$t_R^L = [(n+1)\ \delta_i]^{n/(n+1)}\ t_n + \frac{1 - [(n+1)\ \delta_i]^{n/(n+1)}}{n\ \dot{\varepsilon}_o} \left(\frac{\sigma_o}{\sigma_a}\right)^n \qquad (2.31)$$

where σ_a is the stress at rupture defined by:

$$\sigma_a = \frac{\sigma_i}{(1 - n\ \dot{\varepsilon}_\delta\ t)^{1/n}} \qquad (2.32)$$

σ_i is the initial stress. When δ_i goes to zero, equation (2.31) reduces to Hoff's equation (1.11):

$$t_R^L = \frac{1}{n\ \dot{\varepsilon}_\delta} \qquad (2.33)$$

The rupture strain was found by adding the term responsible for the creep in the specimen ($t_R\ \dot{\varepsilon}_\delta$) to that due to the growing voids (equation (2.21)). The result is:

$$\varepsilon_R = t_R\ \dot{\varepsilon}_o\ \left(\frac{\bar{\sigma}}{\sigma_o}\right)^n + 0.2\ \frac{\ell}{d} \qquad (2.34)$$

where t_R is defined by equation (2.30).

2.5.4 Coupled Boundary Diffusion and Power-Law Creep

A switch from one void growth mechanism to another can take place if the stress field or the temperature vary with time (Figure 2.5(a)). Figure 2.8(a) shows a plot of the damage rate (equations (2.16) and (2.26)) for boundary diffusion and power-law creep against stress. When the stress is low, the voids grow by diffusion, but when high they grow by power-law creep. This also means that when δ_h is small, the voids grow by diffusion, and when large they grow by power-law creep, as the plot of the damage rate against δ_h shows (Figure 2.8(b)). In between, voids grow

by coupling of both mechanisms (full line). The rate of growth by the coupled mechanism is calculated by simply adding the rates of the two mechanisms.

The point where the broken lines intersect in Figures 2.8(a) and (b) was calculated from equations (2.16) and (2.15). The result is:

$$\phi_o = \frac{\delta_h^{\frac{1}{2}}}{\alpha} \ln\left(\frac{1}{\delta_h}\right) \left[\frac{1}{(1-\delta_h)^n} - (1-\delta_h)\right] \left(\frac{\bar{\sigma}}{\sigma_o}\right)^n \left(\frac{\sigma_o}{\sigma_1}\right) \tag{2.35}$$

Void growth by diffusion dominates from δ_i to δ_t^b and power-law creep from δ_t^b to δ_c. The value δ_t^b is found by solving equation (2.35). It represents the critical area fraction at which the change of mechanism occurs. The definition for δ_t^b is:

$$\delta_t^b = \frac{1}{[a\ (\ln a - 1)]^{3/2}} \tag{2.36}$$

where:

$$a = \frac{4\ (n+1)}{3\ \alpha\ \phi_o} \left(\frac{\bar{\sigma}}{\sigma_o}\right)^n \left(\frac{\sigma_o}{\sigma_1}\right) \tag{2.37}$$

The time to rupture was found by combining equations (2.20) and (2.30) with δ_t^b inserted. The result is:

$$t_R = t_n + \frac{2(\delta_t^b)^{3/2}}{3\ \phi_o\ \dot{\varepsilon}_o} \left[\ln\left(\frac{1}{\delta_t^b}\right) + \frac{2}{3}\right] \left(\frac{\sigma_o}{\sigma_1}\right) + \frac{\alpha}{(n+1)\ \dot{\varepsilon}_o} \ln\left[\frac{1}{(n+1)\ \delta_t^b}\right] \left(\frac{\sigma_o}{\bar{\sigma}}\right)^n \tag{2.38}$$

The strain to rupture can be obtained by using equation (2.34), in which t_R is given by equation (2.38).

2.5.5 Coupled Surface Diffusion and Power-Law Creep

Similar to the coupled boundary diffusion and power-law creep mechanism, surface diffusion dominates from δ_i to δ_t^δ and power-law creep from δ_t^δ to δ_c (Figure 2.5(b)). Similar trends shown in Figures 2.8(a)

and (b) can be obtained for this coupled mechanism, but this time equations (2.22) and (2.26) are plotted. The point at which the dominant mechanism changes was found by equating these two equations. The result is:

$$\psi_o = \frac{(1-\delta_h)^4}{\alpha\, \delta_h^{\frac{1}{2}}} \left[\frac{1}{(1-\delta_h)^{n+1}} - 1\right] \left(\frac{\bar{\sigma}}{\sigma_o}\right)^n \left(\frac{\sigma_o}{\sigma_1}\right)^3 \tag{2.39}$$

and the critical area fraction at which the change in mechanism occurs is:

$$\delta_t^{\delta} \simeq \left[\frac{\alpha\, \psi_o}{(n+1)} \left(\frac{\sigma_o}{\bar{\sigma}}\right)^n \left(\frac{\sigma_1}{\sigma_o}\right)^3\right]^2 \tag{2.40}$$

The time to rupture was found by combining equations (2.25) and (2.30) with δ_t^{δ} inserted. The result is:

$$t_\delta = t_n + \frac{2\left[(\delta_t^{\delta})^{\frac{1}{2}} - \delta_i^{\frac{1}{2}}\right]}{\dot{\varepsilon}_o\, \psi_o} \left(\frac{\sigma_o}{\sigma_1}\right)^3 + \frac{\alpha}{(n+1)\,\dot{\varepsilon}_o} \ln\left[\frac{1}{(n+1)\,\delta_t^{\delta}}\right] \left(\frac{\sigma_o}{\bar{\sigma}}\right)^n \tag{2.41}$$

The rupture strain is due to power-law creep only, since the crack-like voids contribute almost nothing to the strain. The result is:

$$\varepsilon_R = t_R\, \dot{\varepsilon}_o \left(\frac{\bar{\sigma}}{\sigma_o}\right)^n \tag{2.42}$$

where t_R is given by equation (2.41).

2.5.6 Coupled Surface Diffusion and Boundary Diffusion

A different criterion to the other two coupled mechanisms was adopted for this coupled mechanism. It is based on using two limits of the driving force which can cause the damage to grow by either surface or boundary diffusion. When surface diffusion is very rapid, the driving force will cause the damage to grow by boundary diffusion (equation (2.16)). However, when surface diffusion is slow, the voids become crack-like and

therefore grow by surface diffusion only (Figure 2.5(c)). The damage rate is given by equation (2.22). The transition occurs when:

$$\frac{\sigma_1}{\sigma_{cap}} = 1.5 + \frac{9\ \Delta_o\ \ln\ (1/\delta_h)}{2\ \sqrt{2}\ (1 - \delta_h)} \tag{2.43}$$

where σ_{cap} is the capability stress at the crack tip, defined as:

$$\sigma_{cap} = \frac{2\ \gamma_s\ (1 - \delta_h)}{\rho_h} \tag{2.44}$$

and Δ_o is a new dimensionless material property:

$$\Delta_o = \frac{D_s\ \delta_s}{D_b\ \delta_b} \tag{2.45}$$

Voids cannot be considered to grow by alternative mechanisms in this type of coupled mechanism since both of them are diffusion mechanisms. However, regimes exist in which one or the other totally controls void growth. The equations given for damage rate and strain rate for these regimes are:

$$\frac{1}{\dot{\varepsilon}_o}\frac{d\delta_h}{dt} = \psi_o \frac{\gamma_s^{\,3}\ \delta_h^{\frac{1}{2}}}{\sigma_o^{\,3}\ \rho^{*3}} \tag{2.46}$$

$$\frac{1}{\dot{\varepsilon}_o}\frac{d\varepsilon}{dt} = \frac{4\ \psi_o\ \delta_h^{\frac{1}{2}}\ \gamma_s^{\,3}}{(1 - \delta_h)\ d\sigma_o^{\,3}\ \rho^{*2}} \tag{2.47}$$

where ρ^* is the tip radius, defined as:

$$\frac{\rho_h}{\rho^*} = \frac{(1 - \delta_h)^2}{\sqrt{2}\ \ln\ (1/\delta_h)\ \Delta_o}\left\{\left[1 + \frac{2\ \sqrt{2}\ \sigma_1\ \rho_h\ \ln\ (1/\delta_h)\ \Delta_o}{\gamma_s\ (1 - \delta_h)^3}\right]^{\frac{1}{2}} - 1\right\} \tag{2.48}$$

and ψ_o is given previously by equation (2.24).

The time to rupture can then be found by integrating equations

(2.46) and (2.47) numerically.

The strain to rupture will be due to boundary diffusion alone and is given by equation (2.21).

2.5.7 Comparisons Between Ashby's Void Growth Theory and the Kachanov/Robotnov Continuum Theory of Creep Damage

The theory of Kachanov and Robotnov was discussed previously in Chapter 1, Section 1.2.3. The general equations for damage rate and strain rate due to creep were given by equations (1.13) and (1.14). For the purpose of the present comparisons, the equations are re-written using the assumption $n = q$ and $m = r$ (Penny [1974]); therefore:

$$\dot{\omega} = \dot{\omega}_o \left(\frac{\sigma_1}{\sigma_o}\right)^m \left(\frac{1}{1-\omega}\right)^m \tag{2.49}$$

$$\dot{\varepsilon} = \dot{\varepsilon}_o \left(\frac{\sigma_1}{\sigma_o}\right)^n \left(\frac{1}{1-\omega}\right)^n \tag{2.50}$$

where $\dot{\omega}_o$ is a temperature-dependent rate constant, like $\dot{\varepsilon}_o$. Equations (2.49) and (2.50) can, in their present form, be compared with Ashby's void growth equations of power-law creep and diffusion.

The damage rate and strain rate equations for voids growing by power-law creep were given in Section 2.5.3 (equations (2.26) and (2.27)). If $m = n$, $\dot{\omega}_o = \dot{\varepsilon}_o$ and δ_h is large, then the term $-(1-\delta_h)$ in equation (2.26) can be neglected. Therefore, it becomes identical to equation (2.49). However, if δ_h is small, then the damage rate equations for the two theories become:

$$\dot{\omega} = \dot{\omega}_o \left(\frac{\sigma_1}{\sigma_o}\right)^m \tag{2.51}$$

and:

$$\frac{d\delta_h}{dt} = 0 \tag{2.52}$$

According to the continuum damage theory, the damage rate (equation (2.51)) is finite, even if there is no damage ($\omega = 0$), while Ashby's theory predicts zero damage rate (non-existent holes do not grow).

The time to rupture can also be compared by integrating the continuum damage rate (equation (2.49)) between the limits used in Ashby's power-law creep mechanism (equation (2.19)), assuming $m = n$ and $\dot{\omega} = \dot{\varepsilon}_o$. The result is:

$$t_R = t_n + \frac{(1 - \delta_i)}{(n+1)\ \dot{\varepsilon}_o} \left(\frac{\sigma_o}{\sigma_1}\right)^n \tag{2.53}$$

When δ_i is large, equation (2.51) will be identical to the previously integrated equation (2.30), because:

$$\frac{\alpha}{(n+1)\ \dot{\varepsilon}_o} \ln\left[\frac{1}{(n+1)\ \delta_i}\right] \left(\frac{\sigma_o}{\sigma_1}\right)^n = \frac{(1 - \delta_i)}{(n+1)\ \dot{\varepsilon}_o} \left(\frac{\sigma_o}{\sigma_1}\right)^n \simeq 0 \tag{2.54}$$

The rupture time will, therefore, be the nucleation time, t_n. However, when δ_i is small, Ashby's power-law creep equation (2.30) will predict much longer lives because the holes, when small, grow more slowly. Similar differences exist in rupture strains under the same conditions.

Under multi-axial loading conditions, the strain rate and the damage rate are accelerated in Ashby's power-law creep mechanism by two new terms which do not appear in the continuum damage theory. These are the hydrostatic tension which enters through the term α (equation (2.28)), and the grain size, d.

The boundary diffusion damage rate equation (2.16) can also be compared with the continuum damage equation (2.49), assuming $\delta_h \simeq 1$, which makes the term $\delta_h^{\frac{1}{2}} \ln(1/\delta_h) \simeq (1-\delta_h)$. Equation (2.16), with this assumption and $n = 1$ for diffusion, becomes:

$$\frac{d\delta_h}{dt} = \phi_o\ \dot{\varepsilon}_o \left(\frac{\sigma_1}{\sigma_o}\right) \left(\frac{1}{1 - \delta_h}\right) \tag{2.55}$$

If $\dot{\omega}_o = \dot{\varepsilon}_o \phi_o$, $m = 1$ and δ_h approaches 1, then equations (2.49) and (2.55) are identical. But when δ_h is much less than 1, the two equations differ significantly. Equation (2.55) predicts a damage rate which decreases as damage grows, as shown in Figure 2.8(b), while the continuum damage equation (2.49) predicts a steadily increasing damage rate.

Ashby's strain rate equation for boundary diffusion also becomes identical to the continuum damage equation (2.50) when δ_h is close to 1 and the holes are randomly distributed, $\ell = d$. This makes the term $\ln(1/\delta_h) \simeq (1-\delta_h)$; therefore, equation (2.17) becomes:

$$\frac{d\varepsilon}{dt} = 2 \phi_o \dot{\varepsilon}_o \left(\frac{\sigma_1}{\sigma_o}\right) \frac{1}{1-\delta_h} \tag{2.56}$$

As before, the two equations differ when δ_h is small.

The same conclusion holds for the surface diffusion void growth mechanism. When $\delta_h \simeq 1$, it predicts identical results to that of the continuum mechanics theory but significantly different behaviour when δ_h is small.

As a result of the comparisons between Ashby's void growth theory and the continuum mechanics theory, the following conclusions are made:

(a) Both theories are approximate.

(b) When δ_h or ω approach 1, both theories predict identical behaviour.

(c) When δ_h or ω are small, the results diverge significantly.

(d) The physical processes which can lead to fracture due to uni-axial or multi-axial loading conditions can be explained more consistently when using Ashby's theory.

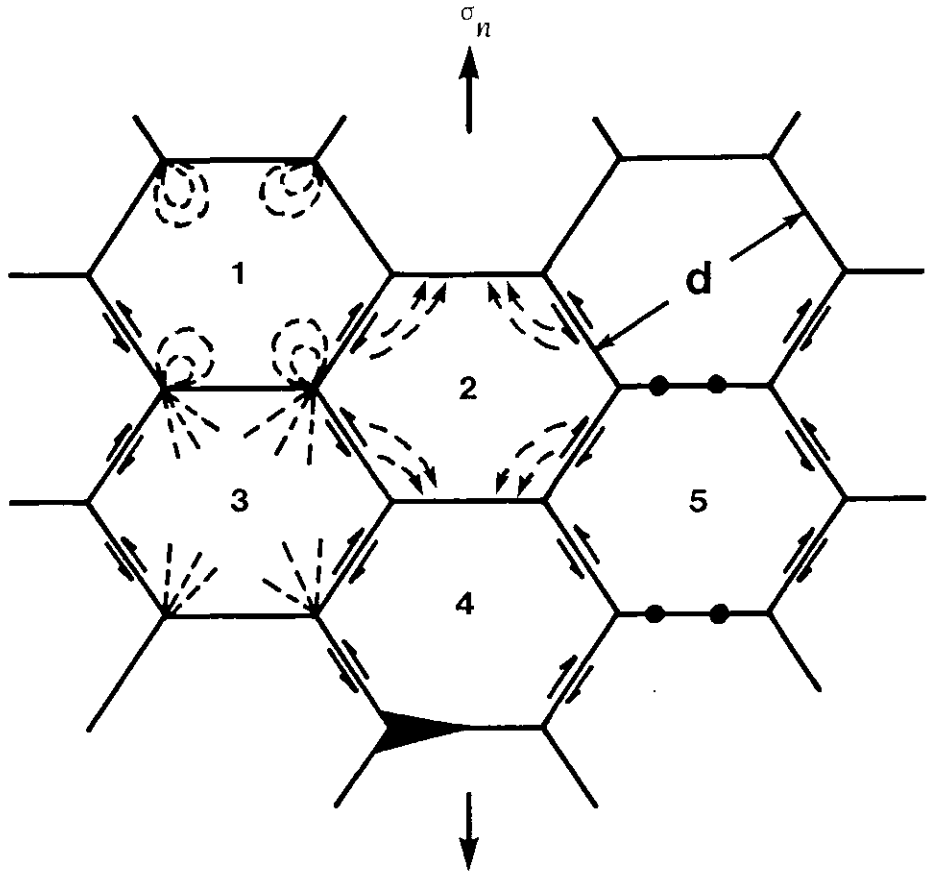

Figure 2.1: Grain boundary sliding

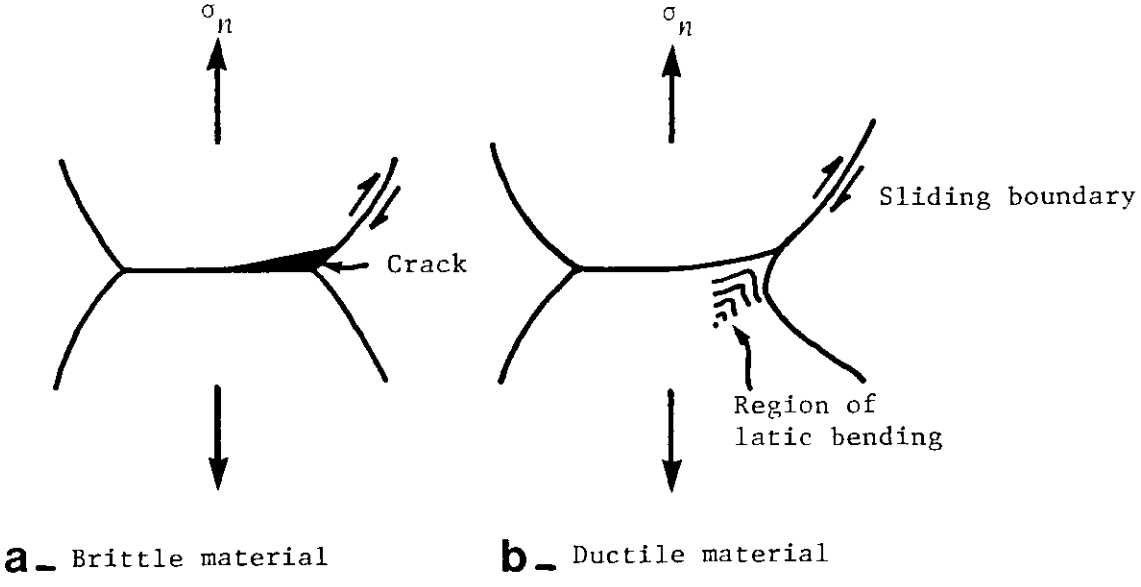

Figure 2.2: Brittle and ductile grain boundary sliding

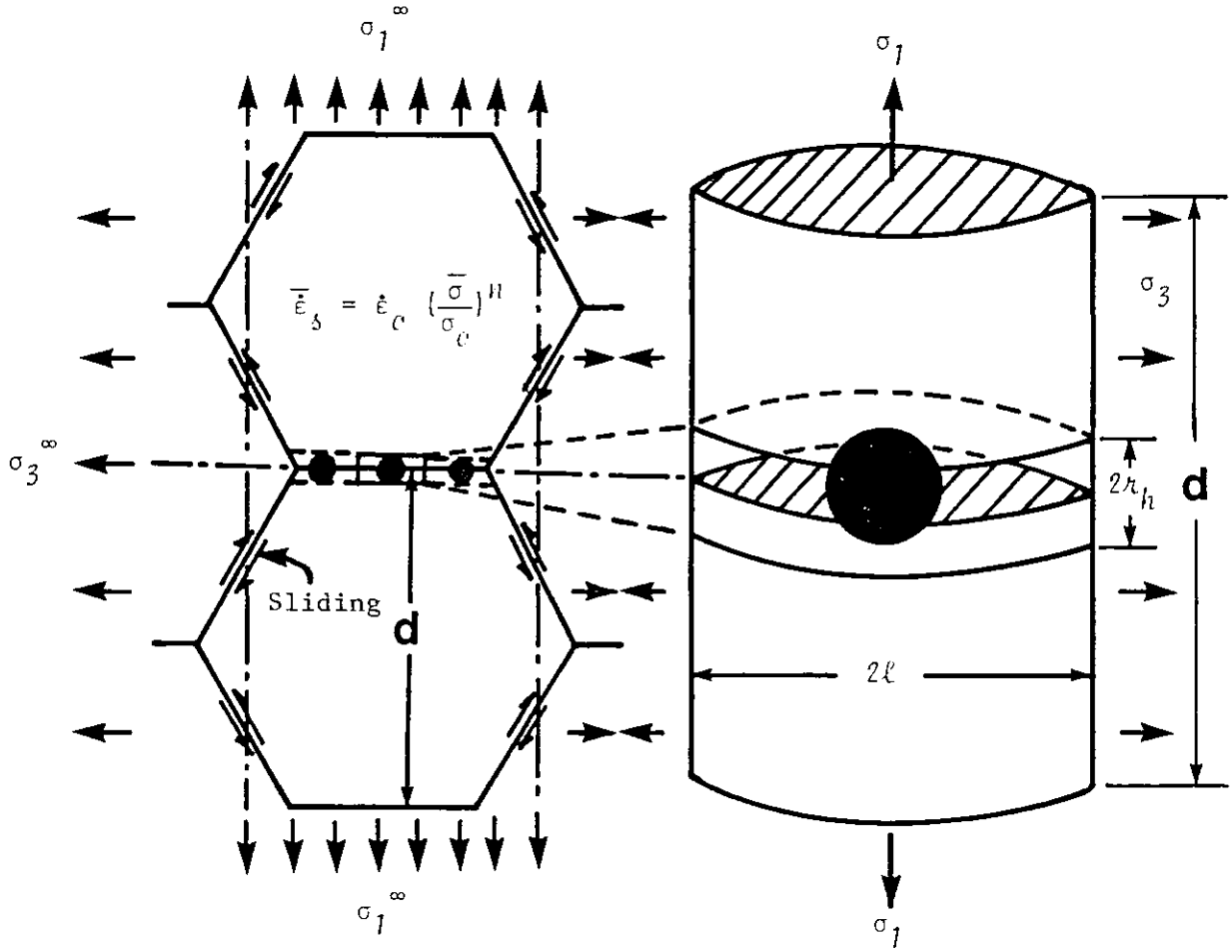

Figure 2.3: Voids growing on grain boundaries in a polycrystal subjected to local stresses σ_1, σ_3

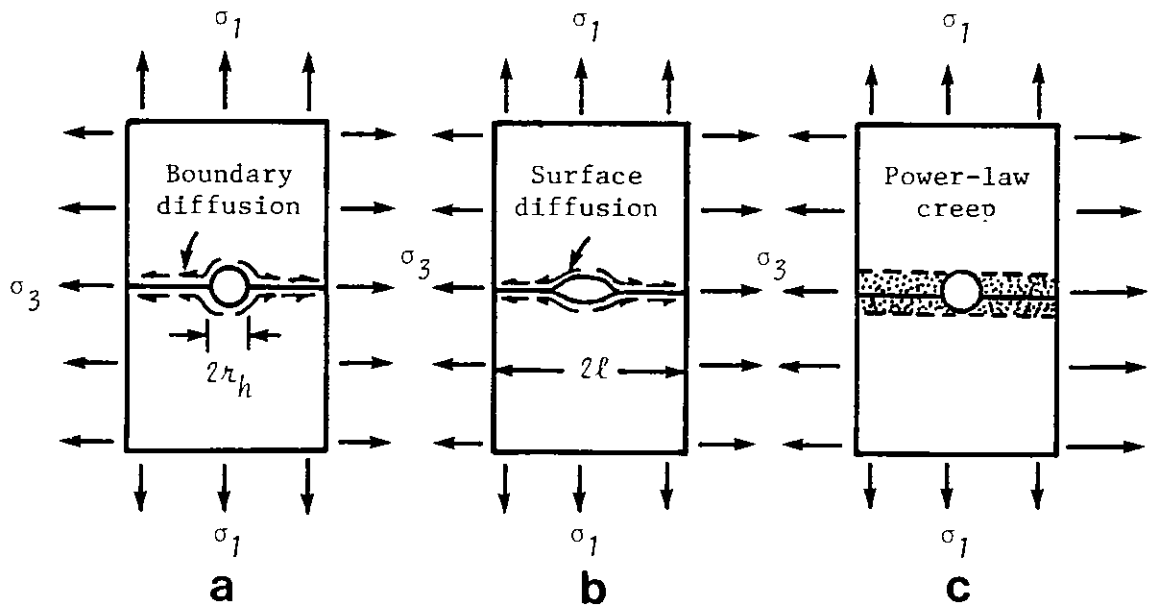

Figure 2.4: The three simple mechanisms which limit void growth

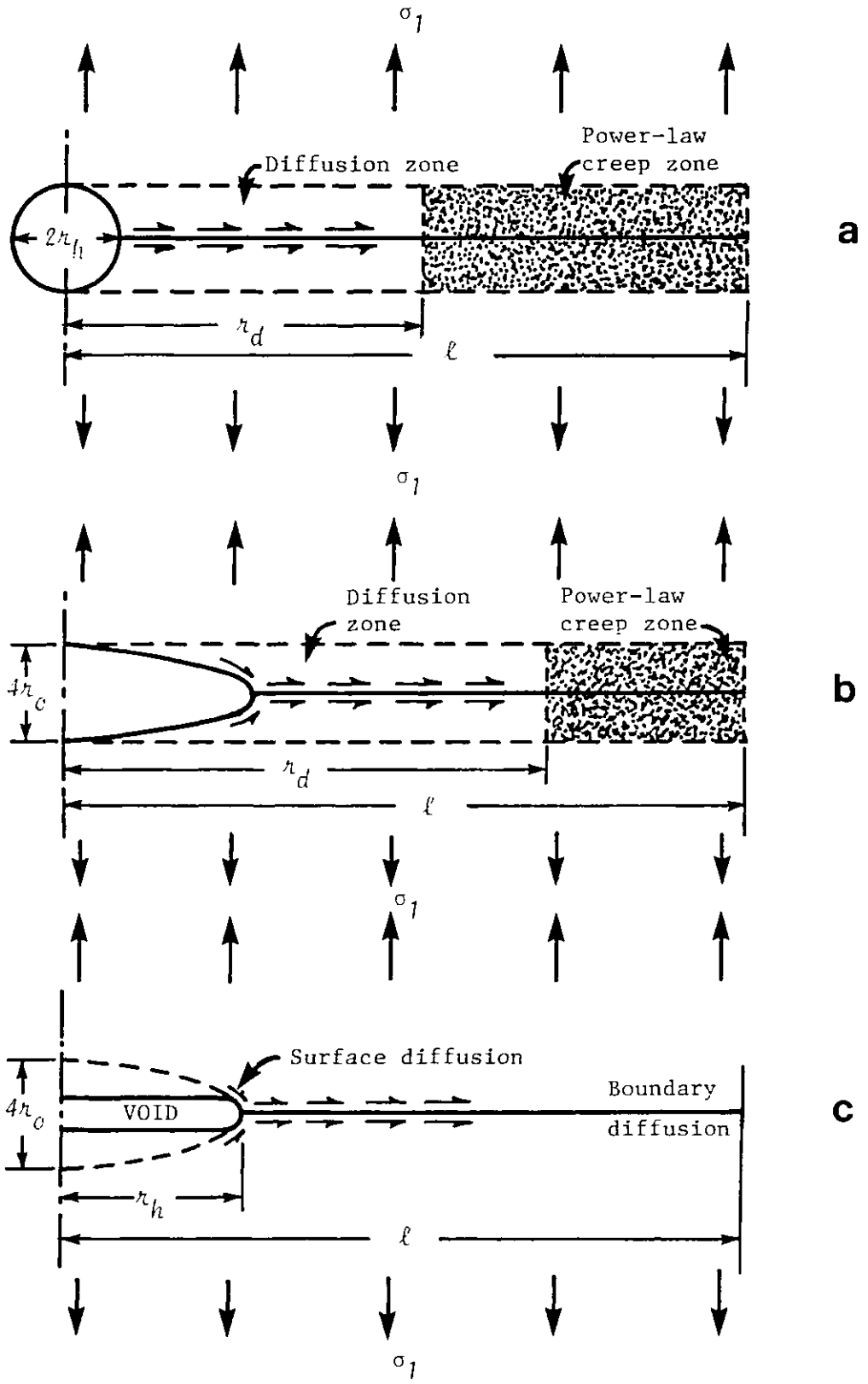

Figure 2.5: A void growing by: (a) coupled boundary diffusion and power-law creep; (b) coupled surface diffusion and power-law creep; (c) coupled surface diffusion and boundary diffusion

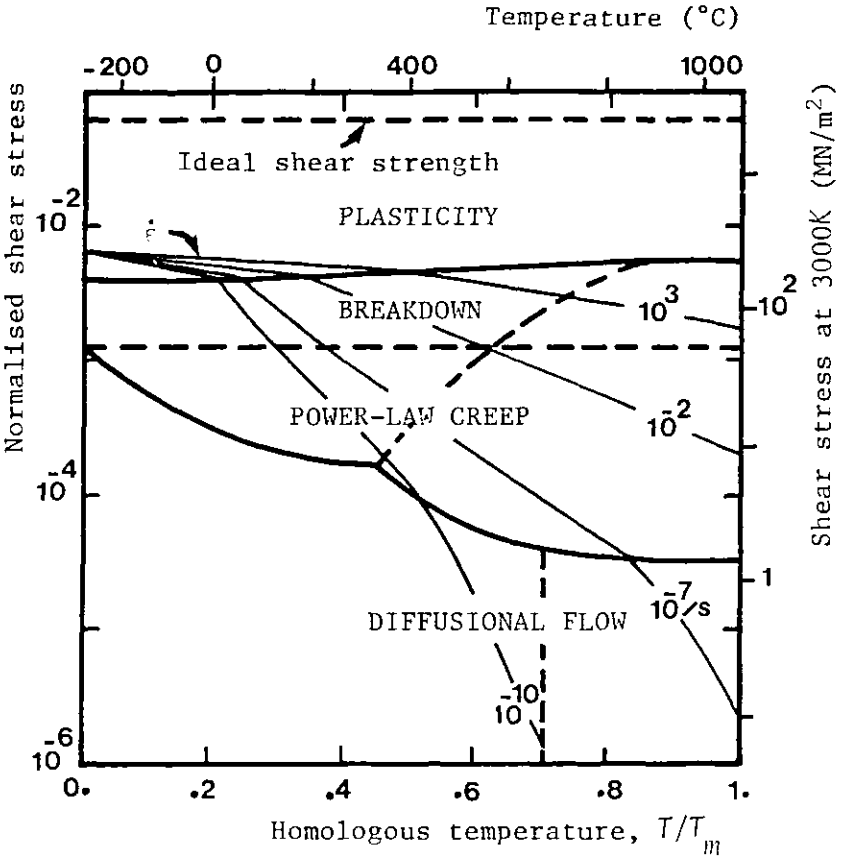

Deformation mechanism map for copper (Cocks and Ashby [1982])

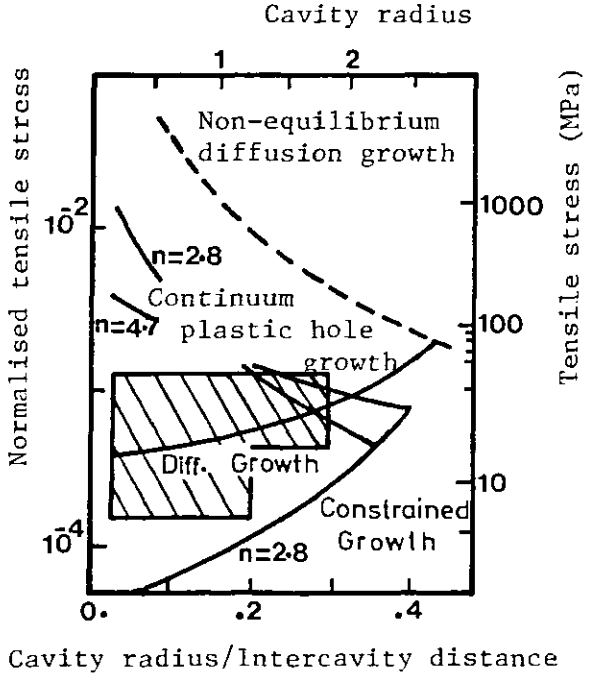

Cavity growth mechanism map for α-brass at 400°C (Svensson and Dunlop [1980])

Figure 2.6: Void growth mechanism maps

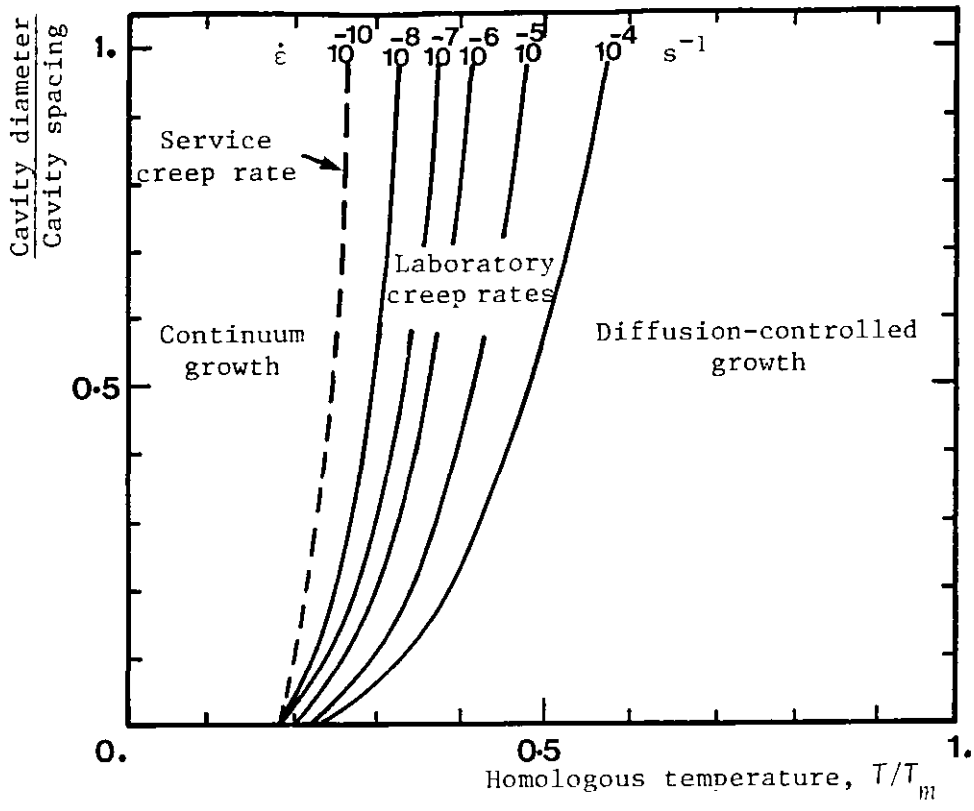

Figure 2.7: Showing the strain rate-dependent transition loci between continuum hole growth and diffusion-controlled growth

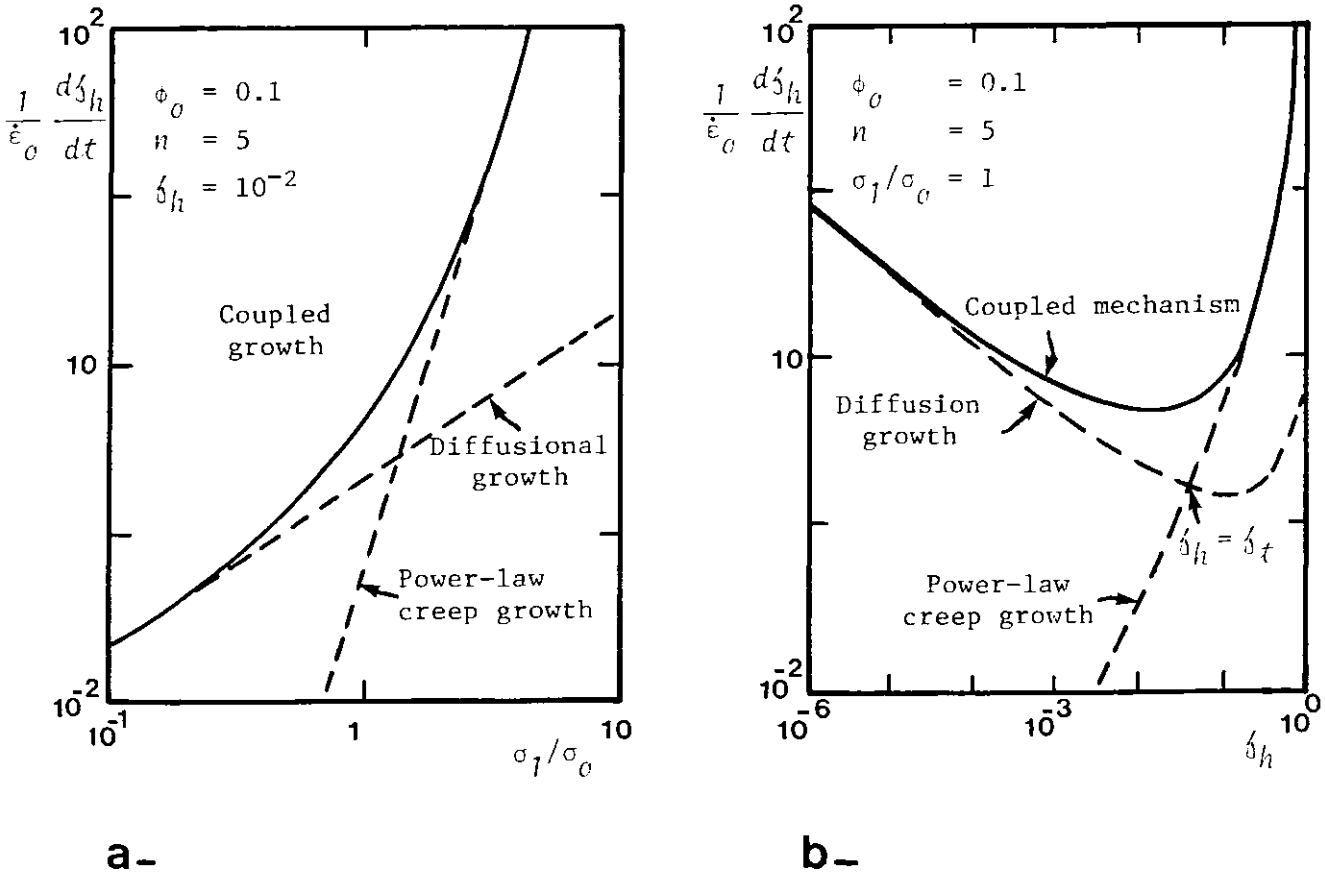

Figure 2.8: Damage rate as a function of: (a) stress; (b) damage; when voids grow by diffusion and power-law creep

CHAPTER 3

FINITE ELEMENT ANALYSES

3.1 INTRODUCTION

This chapter describes a numerical procedure, based on a finite element method, for calculating directly the steady-state stress distributions in axi-symmetric and two-dimensional components subjected to creep without the need to obtain solutions at intermediate time intervals. An iterative procedure is adopted, in which the elastic material properties are up-dated after each iteration until the final steady-state solution is achieved.

Two elastic finite element programs were developed to include this non-linear numerical method. One was used to solve axi-symmetric problems and the second to solve two-dimensional plane strain and plane stress problems. Two techniques for automatic mesh generation were used and tests for convergence and accuracy were carried out.

3.2 AXI-SYMMETRIC FINITE ELEMENT FORMULATION FOR SMALL STRAIN LINEAR ELASTICITY

A detailed elastic finite element analysis for axi-symmetric bodies is available in Fenner [1975], Zienkiewicz [1977] and Al-Faddagh, et al. [1982] (Appendix A). In this section, a short summary of the important linear elasticity equations are listed.

The relationship between stress and strain in terms of constitutive equations is:

$$[\sigma] = [\mathcal{D}]\,[\varepsilon] \tag{3.1}$$

where $[\sigma]$ and $[\varepsilon]$ are vectors of stresses and strains. $[\mathcal{D}]$ is the elastic property matrix, defined as:

$$[\mathcal{D}] = \frac{E^*}{1-\nu^{*2}} \begin{bmatrix} 1 & \nu^* & \nu^* & 0 \\ \nu^* & 1 & \nu^* & 0 \\ \nu^* & 1 & \nu^* & 0 \\ 0 & 0 & 0 & \frac{1}{2}(1-\nu^*) \end{bmatrix} \tag{3.2}$$

where E^* and ν^*, being the Young's modulus and Poisson's ratio, modified as for plane strain conditions:

$$E^* = \frac{E}{1-\nu^2} \quad ; \quad \nu^* = \frac{\nu}{1-\nu} \tag{3.3}$$

To assemble the overall stiffness matrix, $[K]$, for an axi-symmetric body, the condition for equilibrium must be satisfied, so that:

$$[K]\,[\delta] = [F] \tag{3.4}$$

where $[\delta]$ is the overall vector for displacement components, and $[F]$ is the overall vector for the externally applied forces.

3.3 NON-LINEAR FINITE ELEMENT ANALYSES

Many problems of practical consequence exist, in which linearity in material behaviour is not preserved. An example of this is the phenomena of creep and plastic deformation, which cause the effective elastic properties E and ν to vary with time or the local state of strain or stress. The constitutive relation that describes this phenomenon is:

$$\bar{\varepsilon} = C\,\bar{\sigma}^{n}\,t \tag{3.5}$$

One numerical approach of solving non-linear problems is to use equation (3.5) to obtain solutions at a series of time intervals, Δt. The advantage of this approach is that solutions are obtained not only at the final time required, but also at a number of intermediate times.

A second approach is to treat the elastic properties as variables, i.e. function of the local state of strain or stress. The solutions obtained by this method are the initial elastic and the final steady-state values.

3.3.1 Time Incremental Finite Element Analysis

It is a well-established fact that the main disadvantage of using this method is the ability to select an optimum time interval during the calculations.

Zienkiewicz [1977] suggested that choosing a small time increment can, in many cases, guarantee convergence. This, however, in situations where complicated solution domains are involved, requires excessive computing time to achieve fully converged solutions. On the other hand, if the time increment is made too large, the computed solutions will diverge from their true values.

Greenbaum and Rubinstein [1968] and Sutherland [1970], in

their finite element creep analysis of plane strain, plane stress and axi-symmetric bodies, reported that this numerical procedure becomes unstable when the maximum effective creep strain for a time interval exceeds the maximum effective strain. This condition limits the maximum time increment that can be used for any time interval. They suggested two equations for calculating time intervals. One of them is for the initial time increment:

$$\Delta t_o = \frac{\eta_o \, \bar{\sigma}^{(1-n)}}{10^{MT} \, C \, E} \tag{3.6}$$

where n, M and C are material constants, T is the temperature, and E is Young's modulus. The value of η_o falls within the following range:

$$0.04 \leqslant \eta_o \leqslant 0.1 \tag{3.7}$$

The second equation they suggested defines the current time interval:

$$\Delta t = \frac{(\Delta t_i) \, \eta}{(\Delta \bar{\sigma}/\bar{\sigma})_{max}} \tag{3.8}$$

where η falls within the following range:

$$0.03 \leqslant \eta \leqslant 0.1 \tag{3.9}$$

Experience or a trial-and-error procedure are needed in order to choose the specific value of η_o and η which depends upon the particular problem investigated.

Hayhurst, Dimmer and Chernuka [1975] used an incremental finite element method to investigate creep rupture behaviour of uni-axially loaded tension plates containing a central circular hole. The multi-axial

creep constitutive law used in the calculations was a Kachanov/Robotnov type of equation developed by Hayhurst [1973a,b], and Leckie and Hayhurst [1974]. They introduced in the finite element formulation a normalised time-scale, τ, defined such that:

$$\tau = \int_0^t K E \sigma_o^{n-1} \zeta(t) \, dt \tag{3.10}$$

where K is a material constant, E is Young's modulus, and σ_o is the outer boundary stress. Hayhurst, et al. [1977a,b] used the condition $\zeta(t) = t^m$ in a separate investigation of the behaviour of notched circular bars, in the absence of tertiary creep, to derive the following expression for the real time to steady-state, t_{ss}:

$$t_{ss} = \left[\frac{100 \, \sigma_o \, \tau_{ss}}{E}\right]^{1/(m+1)} t^* \tag{3.11}$$

where t^* is the time taken to achieve 1% creep strain in a uni-axial test conducted at the stress, σ_o. The steady-state solutions were subsequently used by Hayhurst, Leckie and Morrison [1978] in approximate analyses of the minimum sections of the same notches, which included creep damage or tertiary creep. The solutions produced used the following approximate strain rate field equation:

$$\frac{dU_i}{dt} = \left(\frac{dU_i^{ss}}{dt}\right) \zeta(t) \tag{3.12}$$

where U_i is a generalised displacement and U_i^{ss} is the steady-state value. The constitutive relations used in their calculations for describing damage in secondary and tertiary creep were:

$$\frac{\dot{\varepsilon}_{ij}}{\dot{\varepsilon}_o} = \frac{\psi^{-n} \, \phi^n \, \partial\phi}{\partial(\sigma_{ij}/\sigma_o)} \tag{3.13}$$

where $\dot{\varepsilon}_{ij}/\dot{\varepsilon}_o$ is the creep strain rate, n is a material constant, and the

dimensionless function ϕ is convex, homogeneous of degree one in (σ_{ij}/σ_o) and has the value of unity when σ_{ij} is the uni-axial stress, σ_o. The dimensionless variable ψ ($\omega = 1 - \psi$) represents the current damage of the material and takes the value zero at $t = 0$ and decreases to unity at $t = t_R$. When $t = 0$, equation (3.13) reduces to the steady-state relationship. As time progresses, ψ decreases and $\dot{\varepsilon}_{ij}/\dot{\varepsilon}_o$ increases to an infinite magnitude at $\psi = 0$. The rate of decrease of ψ depends upon the stress rupture criterion obeyed by the material. Three criteria were suggested, based on the experimental results of multi-axial stress creep rupture tests, collected by Hayhurst [1972]. These were the maximum principal tensile stress:

$$\dot{\psi} = - \left(\frac{\sigma_{max}}{\psi\ \sigma_o}\right)^n \tag{3.14}$$

where σ_{max} is the maximum principal tensile stress, and n is the stress index in rupture law. The second criterion was the maximum effective stress, so that:

$$\dot{\psi} = - \left(\frac{\bar{\sigma}_{max}}{\psi_o\ \bar{\sigma}_o}\right)^n \tag{3.15}$$

and, finally, for materials which obey mixed criteria, the rate of decrease of $\dot{\psi}$ is:

$$\dot{\psi} = - \left[\frac{A\ \sigma_{max}}{\psi\ \sigma_o} + \frac{(1 - A)\ \sigma_{max}}{\psi\ \sigma_o}\right]^n \tag{3.16}$$

where A is a material constant. The values of ψ after each time interval Δt were then determined from:

$$\psi_{t+\Delta t} = \psi_t + \dot{\psi}_t\ \Delta t \tag{3.17}$$

The time increment, Δt, was determined from:

$$\Delta t = -\frac{\psi_i}{20\,\dot{\psi}_i} \tag{3.18}$$

where i refers to the position where ψ is a maximum.

This method was generalised by Hayhurst, et al. [1977a,b] to solve axi-symmetric problems. Elastic and steady-state stress distributions in the throat of various notched bar geometries were calculated. They were faced with the same problem associated with using this method to solve complicated solution domains, i.e. excessive computing time due to the large number of time steps required to achieve fully converged solutions. Figure 3.1 shows the asymptotic approach of their solutions to steady-state for a semi-circular and BS V-notch geometries. It shows that complete stress redistribution in some complex geometries cannot be achieved.

In 1978, Hayhurst, et al., used the steady-state solutions obtained by Hayhurst, et al. [1977a,b] in a time incremental finite element calculation using the constitutive equation (3.13) for axi-symmetric bodies. When the rupture condition was satisfied for an element, i.e. $\psi \simeq 0$, the material was assumed to be no longer capable of transmitting or withstanding force. The elements in their stiffness matrix corresponding to the failed element were re-evaluated and a new matrix was formed. They were able to show how damage propagates in the throat of the notched geometries they investigated (Figure 3.2).

Hyde, Webster and Fessler [1980] used an axi-symmetric finite element method to calculate the elasto-plastic and creep strain distributions in a hemispherically ended cylindrical pressure vessel with constant wall thickness. The elasto-plastic solutions were obtained using an incremental load iterative procedure which is of no relevance to the present method. However, their creep solutions were obtained by using a

time incremental method applied after each load step. For the simple geometries they investigated, the number of time steps required to achieve steady-state were between 20 and 40. In their conclusions, they stated that, although the computing requirements for these simple geometries were modest, they could prove to be prohibitive for components with more complicated geometries. Similar conclusions were also drawn from an investigation on axi-symmetric shouldered tube components made by Dawson, et al. [1981].

3.3.2 Non-Linear Finite Element Analysis Using an Iterative Procedure

The non-linearity in this approach is introduced through making the overall stiffness matrix [K] in equation (3.4) variable. A new condition for equilibrium after each iteration has to be satisfied until steady-state is reached. This is made possible by making the elements representing the elastic properties in matrix [K] dependent on the local state of strain or stress; therefore, equation (3.4) is now written as follows:

$$[K(\delta)]\ [\delta] = [F] \tag{3.19}$$

When $\delta = \delta_0$, the elastic solution is obtained. Convergence to steady-state is achieved when the displacement components after the successive iterations differ by only a small amount:

$$\frac{\Sigma_i \{|\Delta u_i| + |\Delta v_i|\}}{\Sigma_i \{|u_i| + |v_i|\}} < \lambda \tag{3.20}$$

where Δu_i and Δv_i are the changes in the computed displacements between the successive iterations. The tolerance, λ, can take values of 10^{-2} to 10^{-8}, depending on the accuracy required. Figure 3.3 illustrates the

convergence and divergence possibilities in using this method.

Needleman and Shih [1978] used this method to solve plane strain and plane stress problems. In their analysis, the constitutive relation they had to satisfy was:

$$S_{ij} = \frac{\partial \phi}{\partial \varepsilon_{ij}} \tag{3.21}$$

where S_{ij} and ε_{ij} are the stress and strain deviators, and ϕ is a potential function which depends on the second invariant of strain, $\bar{\varepsilon}$, such that:

$$\phi(\varepsilon_{ij}) = \frac{C\, n}{n+1} \bar{\varepsilon}^{(n+1)/n} \tag{3.22}$$

where:

$$\bar{\varepsilon} = \frac{2}{3} \varepsilon_{ij} \cdot \varepsilon_{ij} \tag{3.23}$$

C and n are material constants. Substituting equation (3.22) into equation (3.21) gives:

$$S_{ij} = \frac{2}{3} C\, \bar{\varepsilon}^{(1-n)/n}\, \varepsilon_{ij} \tag{3.24}$$

Equation (3.24) is identical to the general non-linear equation (3.19). The variable matrix $[K(\delta)]$ is equivalent to $\frac{2}{3} C\, n\, \bar{\varepsilon}^{(1-n)/n}$, which has to be re-evaluated after each iteration. The stress deviator, S_{ij}, represents the applied force matrix $[F]$, and ε_{ij} the displacement matrix $[\delta]$.

The above method was modified by Kumar, et al. [1980] to solve axi-symmetric problems. They examined problems such as axially cracked cylinders under various applied loading, round bars with an internal circular crack subjected to remote uniform tension, and a notched round bar in tension. The last case study was compared with the time incremental steady-state solution of Hayhurst and Henderson [1977a]. They

observed some difference in the axial stress distribution between the two solutions, but similar trends. Their explanation for this discrepancy was that the time incremental steady-state solutions would have relaxed to their values if computation times were extended for a long enough time period.

3.3.3 The Present Non-Linear Finite Element Analysis

The present finite element analysis is based on an iterative procedure similar to that discussed in Section 3.3.2. The method of solution in the elastic region is based on using the displacement as the nodal point variables; therefore, the elastic modulus had to be expressed as a function of the local state of strain during the successive iterations needed to achieve steady-state. The Poisson's ratio, ν, responsible for incompressibility was initially made equal to the equivalent elastic value, say 0.3, and then modified to 0.49 during the non-linear calculation. The exact value of $\nu = 0.5$ cannot be used in solving axi-symmetric problems by the present method because it will make the overall stiffness matrix $[K]$ singular. The constitutive relation used in the present method was:

$$\bar{\varepsilon} = C\,\bar{\sigma}^{n}\,f(t) \tag{3.25}$$

which may be inverted to give:

$$\bar{\sigma} = \left(\frac{\bar{\varepsilon}}{C\,f(t)}\right)^{1/n} \tag{3.26}$$

An apparent or effective modulus, E', can now be defined, such that:

$$E' = \frac{\bar{\sigma}}{\bar{\varepsilon}} \tag{3.27}$$

Substituting in equation (3.26) gives:

$$E' = \frac{1}{\bar{\varepsilon}} \left(\frac{\bar{\varepsilon}}{C\ \delta(x)}\right)^{1/n} = E_o \left(\frac{\bar{\varepsilon}}{\bar{\varepsilon}_o}\right)^{(1/n)-1} \tag{3.28}$$

where E_o is the effective modulus at some convenient reference strain, ε_o. If $n = 1$, the modulus $E' = E_o$, whereas for $n > 1$, E' will be a function of the local state of strain. Before calculations can be made, it is necessary to define the appropriate equivalent stress $\bar{\sigma}$ and strain $\bar{\varepsilon}$. Either the Von Mises or the Tresca criteria can be used; this will be discussed in the next section. The general procedure for the present non-linear analysis is available in Appendix A.

3.4 AXI-SYMMETRIC NON-LINEAR CALCULATIONS USING VON MISES OR TRESCA CRITERIA

The Von Mises and Tresca criteria were used separately to calculate the steady-state stress distributions for various axi-symmetric problems. In this section, the necessary effective stress and strain equations for each criterion will be given.

(a) Von Mises Criterion

In a polar coordinate system, the effective stress equation is:

$$\bar{\sigma} = \left\{\frac{1}{2}\left[(\sigma_{zz} - \sigma_{rr})^2 + (\sigma_{rr} - \sigma_{\theta\theta})^2 + (\sigma_{\theta\theta} - \sigma_{zz})^2 + 6\sigma_{rz}^2\right]\right\}^{\frac{1}{2}} \qquad (3.29)$$

and the effective strain equation is:

$$\bar{\varepsilon} = \left\{\frac{2}{3}\left(\varepsilon_{zz}^2 + \varepsilon_{rr}^2 + \varepsilon_{\theta\theta}^2 + \frac{1}{2}\varepsilon_{rz}^2\right)\right\}^{\frac{1}{2}} \qquad (3.30)$$

where zz, rr and θθ refer to axial, radial and hoop directions, respectively.

(b) Tresca Criterion

According to Tresca (Section 1.3.2, equation (1.21)), the maximum and minimum principal stresses have to be identified in order to calculate the effective stress. The finite element method employed in this work is based on the coordinate system zz, rr, θθ, which is not the principal one. To transform it to the principal direction, the following cubic equation has to be solved (Ford [1963]):

$$S^3 - S^2 (\sigma_{xx} + \sigma_{yy} + \sigma_{zz}) -$$

$$S (\tau_{xy}^2 + \tau_{yz}^2 + \tau_{zx}^2 - \sigma_{xx}\sigma_{yy} - \sigma_{yy}\sigma_{zz} - \sigma_{zz}\sigma_{xx}) -$$

$$(\sigma_{xx}\sigma_{yy}\sigma_{zz} + 2\tau_{xy}\tau_{yz}\tau_{zx} - \sigma_{xx}\tau_{yz}^2 - \sigma_{yy}\tau_{zx}^2 - \sigma_{zz}\tau_{xy}^2) = 0 \qquad (3.31)$$

This cubic equation in a real physical situation has three real roots which are the principal stresses, σ_1, σ_2, σ_3, of the particular stress system.

In the case of plane stress:

$$\sigma_{zz} = \tau_{zx} = \tau_{yz} = 0 \qquad (3.32)$$

Therefore, the cubic equation is reduced to:

$$S^2 - S (\sigma_{xx} + \sigma_{yy}) + (\sigma_{xx}\sigma_{yy} - \tau_{xy}^2) = 0 \qquad (3.33)$$

and: $$\sigma_1, \sigma_2 = \frac{1}{2} \{(\sigma_{xx} + \sigma_{yy}) \mp \sqrt{(\sigma_{xx} - \sigma_{yy})^2 + 4\tau_{xy}^2}\} \qquad (3.34)$$

In the case of plane strain:

$$\tau_{zx} = \tau_{yz} = 0 \qquad \text{but} \qquad \sigma_{zz} \neq 0 \qquad (3.35)$$

Therefore, the cubic equation (3.31) remains cubic and the roots have to be found by a very complicated trial-and-error method.

Axi-symmetric problems are solved in this finite element method by considering a two-dimensional solution domain lying in a radial plane through the axis of symmetry of the body considered. The hoop component

of the stress is always normal to the two-dimensional domain. Therefore, it is justifiable to calculate the three principal stresses using the following equations:

$$\sigma_1 , \sigma_2 = \frac{1}{2} \{(\sigma_{rr} + \sigma_{zz}) \mp \sqrt{(\sigma_{rr} - \sigma_{zz})^2 + 4\sigma_{rz}^2}\} \tag{3.36}$$

and:

$$\sigma_3 = \sigma_{\theta\theta} \tag{3.37}$$

The maximum and minimum principal stresses can now be identified and the Tresca effective stress can be calculated.

Similarly, the three principal strains in a polar coordinate system are:

$$\varepsilon_1 , \varepsilon_2 = \frac{1}{2} \{(\varepsilon_{rr} + \varepsilon_{zz}) \mp \sqrt{(\varepsilon_{rr} - \varepsilon_{zz})^2 + \varepsilon_{rz}^2}\} \tag{3.38}$$

and:

$$\varepsilon_3 = \varepsilon_{\theta\theta}$$

The Tresca effective strain can, therefore, be calculated:

$$\bar{\varepsilon} = \frac{2}{3} (\varepsilon_{max} - \varepsilon_{min}) \tag{3.39}$$

3.5 TWO-DIMENSIONAL FINITE ELEMENT ANALYSIS

In this section, the formulation of a finite element analysis for two-dimensional plane strain or plane stress problems is described. The necessary equations are formulated in cartesian coordinates (x,y,z), shown previously in Figure 1.4(a). A typical triangular finite element lying in a two-dimensional solution domain is shown in Figure 3.4(a). The global coordinates for the overall solution domain are X and Y, whereas x and y are local to the particular element. Figure 3.4(b) shows the displacements of the typical element which are in the plane of, rather than normal to, the solution domain.

The same axi-symmetric finite element formulation for small strain linear elasticity, discussed in Section 3.2, applies for the two-dimensional problems. The difference is that the element strain components are now expressed in terms of nodal point displacements, as follows:

$$[\varepsilon] = [\varepsilon_{xx} \quad \varepsilon_{yy} \quad \varepsilon_{xy}]^T = \frac{1}{2\Delta_m} [B] [\delta]_m \tag{3.40}$$

where:
$$[\delta]_m = [u_i \quad w_i \quad u_j \quad w_j \quad u_k \quad w_k]^T \tag{3.41}$$

and:
$$[B] = \begin{bmatrix} b_i & 0 & b_j & 0 & b_k & 0 \\ 0 & a_i & 0 & a_j & 0 & a_k \\ a_i & b_i & a_j & b_j & a_k & b_k \end{bmatrix} \tag{3.42}$$

where $[B]$ is the dimension matrix, and Δ_m is the element area.

The relationship between the element stresses and strains also differ since the hoop stress component is excluded from the constitutive equations, therefore:

$$[\sigma] = [\sigma_{xx} \quad \sigma_{yy} \quad \sigma_{xy}]^T = [D] [\varepsilon] \tag{3.43}$$

where $[\mathcal{D}]$ is the elastic property matrix, defined as:

$$[\mathcal{D}] = \frac{E^*}{1-\nu^{*2}} \begin{bmatrix} 1 & \nu^* & 0 \\ \nu^* & 1 & 0 \\ 0 & 0 & \frac{1}{2}(1-\nu^*) \end{bmatrix} \tag{3.44}$$

where E^* and ν^* are the Young's modulus and Poisson's ratio, equal for plane stress to:

$$E^* = E \quad \text{and} \quad \nu^* = \nu \tag{3.45}$$

and for plane strain to:

$$E^* = \frac{E}{1-\nu^2} \quad \text{and} \quad \nu^* = \frac{\nu}{1-\nu} \tag{3.46}$$

Similar to the axi-symmetric analysis, plane strain problems for incompressible material, where $\nu = \frac{1}{2}$, cannot be solved because matrix $[\mathcal{D}]$ will become singular. However, it is possible to obtain solutions when ν is nearly equal to $\frac{1}{2}$ (Al-Faddagh, et al. [1982]).

The same non-linear analysis discussed in Section 3.3.3 applies for two-dimensional problems. The only difference is the formulation of the effective stress and the effective strain equations.

For plane strain and plane stress, the Von Mises effective stress and strain are:

$$\bar{\sigma} = \left[\frac{1}{2}\left(\sigma_{xx}^2 - \sigma_{xx}\,\sigma_{yy} + \sigma_{yy}^2 + 3\tau_{xy}\right)\right]^{\frac{1}{2}} \tag{3.47}$$

$$\bar{\varepsilon} = \left[\frac{2}{3}\left(\varepsilon_{xx}^2 + \varepsilon_{yy}^2 + \frac{1}{2}\varepsilon_{xy}^2\right)\right]^{\frac{1}{2}} \tag{3.48}$$

However, the correct values of E^* and ν^* (equations (3.45) and (3.46)) have to be chosen according to the type of problem. For plane strain incompressible problems, the value of ν is also chosen to be approximately equal to $\frac{1}{2}$.

As previously discussed (Section 3.4), the Tresca criterion can only be used for plane stress, otherwise the cubic equation (3.31) remains cubic for plane strain.

The Tresca effective stress and strain for plane stress is calculated as follows:

$$\bar{\sigma} = \frac{1}{2}\left[(\sigma_{xx} - \sigma_{yy})^2 + 4\tau_{xy}^2\right]^{\frac{1}{2}} \tag{3.49}$$

$$\bar{\varepsilon} = \frac{2}{3}\left[(\varepsilon_{xx} - \varepsilon_{yy})^2 + \varepsilon_{xy}^2\right]^{\frac{1}{2}} \tag{3.50}$$

3.6 MESH GENERATION

Solution of the overall linear equations, which is equivalent to inverting the stiffness matrix [K] in equation (3.4), yields the nodal point displacements and hence stresses. An important consequence of using constant strain triangular (CST) finite elements is that the method of solution can be either a direct elimination type technique or an iterative technique, such as Gauss-Seidel (Fenner [1975]). The latter can be particularly useful when dealing with non-linear problems.

In this section, the techniques used for generating meshes of triangular elements to suit the solution domain of the non-linear problems considered will be discussed.

3.6.1 Mesh Data in Numerical Form

The main requirement of a finite element mesh is to fit the shape of the boundary of the solution domain as closely as possible. Factors such as element size, shape, distribution, and the numbering of both elements and nodal points also need to be considered.

One way of providing the mesh data required by a finite element program is to enter them on data cards. A considerable amount of labour is involved in preparing these data. For any finite element solution domain, the total number of elements and nodal points has to be defined, as well as the X and Y coordinates of each triangular element. The data must, therefore, be carefully checked since mistakes are likely to be made.

A better alternative would be to have a program to generate the mesh data from a minimal amount of input data. In the present finite element analysis, two automatic mesh generation techniques were used; these will be discussed in the coming sections.

The data generated using automatic mesh generation programs

are saved individually in separate data files. These files are then checked for suitability of element distribution and correct X and Y coordinates using the graphics facilities provided by the computer system. If suitable hard copies or microfilms for each individual data file are produced, the required axi-symmetric or two-dimensional non-linear solutions are then obtained by calling any of the mistake-free mesh data files by the main finite element program. The flow chart of this procedure is shown in Figure 3.5.

3.6.2 Automatic Mesh Generation for Stress Concentration Problems

The listing of this program and the data required to generate meshes for solving stress concentration problems is available in Fenner [1975]. This program was used in the present two-dimensional finite element program only to solve non-linear plane strain and plane stress problems such as thick-walled cylinder subjected to internal pressure and a hole in a plate subjected to uniform tension. The procedure followed to generate the required meshes is shown in Figures 3.6(a) to (d). Each individual diagram in this figure is explained as follows:

(a) A square mesh of mainly isosceles triangular elements is generated using a subroutine listed in Fenner [1975]. The only input data required is the number of rows and columns.

(b) The coordinates of the basic square mesh are modified to obtain the required boundary shape and element distribution. Horizontal rows are modified to form an arc using the following relation:

$$X_i = r \sin\theta \quad ; \quad Y_i = r \cos\theta \tag{3.51}$$

Since elements are to be concentrated near the edge of the hole and the degree of this concentration is to be varied, a scale factor, S, is introduced to define the radial width of successive rows of elements as follows:

$$S = \frac{\ell_n}{\ell_{n-1}} \tag{3.52}$$

After this stage, the mesh data could be used as input in the non-linear solution of a thick-walled cylinder subjected to internal pressure.

(c) The points adjacent to the ends of the outermost arc are moved either vertically or horizontally to the edge of the domain and extra nodal points are added on the top boundary to complete the required shape of the solution domain.

(d) This shape is the end result of the automatic mesh generation procedure and could be used in solving non-linear stress concentration problems.

3.6.3 Automatic Mesh Generation for Complicated Boundary Domains

A technique reported by Segerlind [1976] for automatic mesh generation is discussed in this section. It was used effectively to fit complicated solution domains from a small number of geometric parameters in the present non-linear finite element calculations.

The essence of this technique is to divide the solution domain into several quadrilateral regions, define the coordinates of the mid and end points of each region, indicate how the separate regions are linked together, and, finally, state how many rows and columns are required in each region. Figure 3.7 shows two examples of finite element meshes generated by this technique.

3.7 TESTS FOR THE AXI-SYMMETRIC FINITE ELEMENT METHOD

The general calculation procedure followed to achieve steady-state in axi-symmetric bodies and the tests for accuracy carried out on this method are summarised in Appendix A. In this section, more information on these tests is presented.

3.7.1 Thick-Walled Cylinder Subjected to Internal Pressure

This case study was chosen because the exact linear elastic and non-linear creep solutions are available in the literature (Bailey [1951]). Figure 3.8 shows the finite element mesh used for this example. The case of $R_1 = 2R_2$ was considered, where R_1 and R_2 are the internal and external radii of a thick-walled cylinder subjected to an internal pressure, P. Figures 3.9 and 3.10(a) and (b) show the finite element effective, hoop and radial stress distributions calculated for n = 1, 2, 3, 9 and 100 using the Von Mises criterion. The exact hoop and radial stresses given by Bailey [1951] are included in Figures 3.10(a) and (b).

In all cases, the computed stresses for Poisson's ratio equal to 0.49 agreed with the exact solutions to within 0.3%, as shown in Table 3.1.

This very satisfactory level of agreement was also reported by Needleman and Shih in 1978, who investigated the same problem but for complete incompressible materials. Their finite element hoop and radial stresses, normalised with respect to the effective stress for n = 1, 3 and 100, and the present solutions, are shown in Figures 3.11(a) and (b).

3.7.2 Comparisons with Bridgman and Other Finite Element Calculations

The present finite element method was used to calculate the steady-state stress distributions across the throat of circumferentially notched round tensile bars using the Von Mises criterion. The notch

dimensions were chosen to enable comparisons to be made with previous finite element calculations made by Hayhurst, et al. [1977a,b], and Kumar, et al. [1980]. Bridgman's approximate plasticity solutions were also used in the comparisons. The meshes required in the analysis were generated using the method discussed in Section 3.6.3. The diagrams showing the various ways of calculating steady-state stress distributions for the different notched geometries are available in Appendix A.

3.7.3 Creep Stress Analysis Using Von Mises or Tresca Criteria

Stress analysis can prove that the steady-state hoop and radial stress distributions in a thick-walled cylinder subjected to internal pressure, P, are the same when using either Von Mises or Tresca definitions of the effective strain and stress in the derivation. Figure 3.12 shows a schematic diagram representing this problem with an inner and outer radii of R_1 and R_2. The boundary conditions for the radial stress, σ_r, are:

$$r = R_1 \ , \ \sigma_r = -P \quad ; \quad r = R_2 \ , \ \sigma_r = 0 \tag{3.53}$$

For secondary creep, the strains in the z and θ directions are:

$$\varepsilon_z = C\,\bar{\sigma}^{(n-1)}\left[\sigma_z - \tfrac{1}{2}(\sigma_\theta + \sigma_r)\right] \tag{3.54}$$

$$\varepsilon_r = C\,\bar{\sigma}^{(n-1)}\left[\sigma_\theta - \tfrac{1}{2}(\sigma_r + \sigma_z)\right] \tag{3.55}$$

The condition for equilibrium is:

$$\sigma_\theta - \sigma_r = r\,\frac{d\sigma_r}{dr} \tag{3.56}$$

and compatibility is:

$$\varepsilon_\theta - \varepsilon_r = -r\frac{d\varepsilon_\theta}{dr} \tag{3.57}$$

For plane sections to remain plane, $d\varepsilon_z/dr = 0$, and therefore equation (3.54) led to:

$$\frac{d\sigma_z}{dr} - \frac{1}{2}\left(\frac{d\sigma_\theta}{dr} + \frac{d\sigma_r}{dr}\right) = -\frac{(n-1)}{\bar{\sigma}}\left[\sigma_z - \frac{1}{2}(\sigma_\theta + \sigma_r)\right]\frac{d\bar{\sigma}}{dr} \tag{3.58}$$

Assuming built-in ends, i.e. $\varepsilon_z = 0$, gives:

$$\sigma_z = \frac{1}{2}(\sigma_\theta + \sigma_r) \tag{3.59}$$

Therefore:
$$\frac{d\sigma_z}{dr} = \frac{1}{2}\frac{d\sigma_\theta}{dr} + \frac{1}{2}\frac{d\sigma_r}{dr} \tag{3.60}$$

Substituting equations (3.60), (3.57), (3.55) and (3.54) in equation (3.58) gives:

$$\frac{3}{2}(\sigma_\theta - \sigma_r) = -\frac{3}{4}r\left[\left(\frac{d\sigma_\theta}{dr} - \frac{d\sigma_r}{dr}\right) + \frac{(n-1)}{\bar{\sigma}}(\sigma_\theta - \sigma_r)\frac{d\bar{\sigma}}{dr}\right] \tag{3.61}$$

Substituting in equation (3.56) gives:

$$\frac{d\sigma_\theta}{dr} + \frac{d\sigma_r}{dr} + \frac{(n-1)}{\bar{\sigma}}(\sigma_\theta - \sigma_r)\frac{d\bar{\sigma}}{dr} = 0 \tag{3.62}$$

Equation (3.62) cannot be integrated until $\bar{\sigma}$ is defined. Using Tresca's definition:

$$\bar{\sigma} = \sigma_\theta - \sigma_r \tag{3.63}$$

therefore:
$$\frac{d\bar{\sigma}}{dr} = \frac{d\sigma_\theta}{dr} - \frac{d\sigma}{dr}$$

Equation (3.62) becomes:

$$\frac{d\sigma_\theta}{dr} + \frac{d\sigma_r}{dr} + (n-1)\left(\frac{d\sigma_\theta}{dr} - \frac{d\sigma_r}{dr}\right) = 0 \tag{3.64}$$

The Von Mises definition of $\bar{\sigma}$ is:

$$\bar{\sigma} = \left[\frac{1}{2}(\sigma_\theta - \sigma_r)^2 + (\sigma_\theta - \sigma_z)^2 + (\sigma_z - \sigma_\theta)^2\right]^{\frac{1}{2}} \tag{3.65}$$

Substituting equation (3.59) in equation (3.65) gives:

$$\bar{\sigma} = \frac{\sqrt{3}}{2}(\sigma_\theta - \sigma_r) \tag{3.66}$$

If equation (3.66) is substituted in equation (3.62), the result will be a similar equation derived using Tresca's criterion (equation (3.64)). This indicates that the stress distributions are the same.

This fact was confirmed when a similar mesh geometry to that shown in Figure 3.8 was used in the finite element program to calculate the hoop, radial and effective stress distributions using Tresca's criterion for n = 1, 3 and 100. Identical results were obtained to those shown previously in Figures 3.9 and 3.10.

3.8 TESTS FOR THE TWO-DIMENSIONAL FINITE ELEMENT METHOD

The numerical procedure used in this method to achieve steady-state is similar to that used in the axi-symmetric analysis. In this section, the case studies chosen to test the accuracy of this method are presented.

3.8.1 Comparison with an Exact Solution

The exact elastic and non-linear solutions presented previously in Figures 3.9 and 3.10 for a thick-walled cylinder subjected to an internal pressure were used in this comparison. Plane stress and plane strain solutions for n = 1, 2, 3, 9 and 100 were calculated for a quarter-segment of a thick-walled tube shown in Figure 3.13. The finite element mesh was generated using the method described previously in Section 3.6.2. The uniform internal pressure was represented by two components, P_x and P_y, which act on the nodes describing the inner surface of the cylinder. P_x vary from zero at $\phi = \pi/2$ to one at $\phi = 0$, and P_y from one at $\phi = \pi/2$ to zero at $\phi = 0$. The square root of these pressure components has to always equal one; this represents the value of the applied internal pressure:

$$P = \sqrt{P_x + P_y} = 1 \tag{3.67}$$

The hoop and radial stress distributions calculated using this method for both plane strain and plane stress situations were similar to those presented in Figures 3.9 and 3.10. Some tabulated results for n = 1, 3 and 100 at $\phi = 0$ are listed in Table 3.2. The computed stresses agreed with the exact solutions to within 0.9%, which is higher than the 0.3% obtained in the axi-symmetric calculations. This is because the real ϕ in the centroid of the elements in the bottom row is not exactly equal to zero. To correct this, the small angle between $\phi = 0$ axis and the centroid of each element has to be considered. This, however, is not

necessary for the level of accuracy achieved which is still very satisfactory.

3.8.2 Hole in an Infinite Plate

The case of a hole in an infinite plate subjected to a uniform tensile stress was considered. The two-dimensional plane stress incompressible solutions for n = 1, 3 and 20 were compared with those calculated by Needleman and Shih [1978]. The mesh used in the present calculations is shown in Figure 3.14. It was generated using the technique described in Section 3.4.2 for stress concentration problems. The elastic and the non-linear normalised axial stress distributions, calculated by both method agree perfectly, as shown in Figure 3.15.

3.9 CONCLUSIONS

The conclusions for this chapter are:

1. Two finite element programs have been developed to calculate the steady-state stress distributions in axi-symmetric and two-dimensional bodies. The listing of these programs is available in Appendix B and Appendix C.

2. The iterative procedure used in calculating the steady-state stress distribution directly by means of an effective modulus, E', is consistent with exact, approximate non-work hardening plasticity solutions, and other numerical procedures.

3. The efficient techniques used in generating meshes from a small number of geometrical parameters makes it possible to use these programs to calculate the steady-state stress distributions for complicated solution domains.

4. These programs can be used to calculate steady-state stress distributions using either the Von Mises or Tresca criteria.

5. This method of calculation is not restricted to the assumption of secondary creep. Provided the variables of stress and time are separable in the creep law, solutions for primary, secondary and tertiary creep can be obtained.

TABLE 3.1

Selective Comparisons Between Exact and Computed Solutions for a Thick-Walled Cylinder Subjected to Internal Pressure Using the Mesh Shown in Figure 3.8

Radius, r/R_i	n = 1					
	Hoop Stress, $\sigma_{\theta\theta}/P$			Radial Stress, σ_{rr}/P		
	Exact	Computed	% Error	Exact	Computed	% Error
0.515	1.5914	1.592	0.03	-0.9249	-0.9255	0.065
0.75	0.9259	0.9259	0	-0.2592	-0.2589	0.115
0.985	0.6767	0.6766	0.014	-0.01	-0.01	0
r/R_i	n = 3					
0.515	0.8189	0.821	0.256	-0.9481	-0.9489	0.084
0.75	0.9588	0.9588	0	-0.3599	-0.3609	0.277
0.985	1.129	1.126	0.265	-0.0167	-0.01677	0.179
r/R_i	n = 100					
0.515	0.4941	0.4953	0.242	-0.9578	-0.9585	0.073
0.75	1.0276	1.0276	0	-0.4138	-0.4144	0.145
0.985	1.412	1.409	0.212	-0.02128	-0.0213	0.094

TABLE 3.2

Selective Comparisons Between Exact and Computed Plane Strain and Plane Stress Solutions for a Thick-Walled Cylinder Subjected to Internal Pressure Using the Mesh Shown in Figure 3.13

Radius, r/R_1	n = 1					
	Hoop Stress, $\sigma_{\theta\theta}/P$			Radial Stress, σ_{rr}/P		
	Computed	Exact	% Error	Computed	Exact	% Error
1.063	1.5425	1.5425	0	-0.864	-0.8632	0.1
1.511	0.9327	0.9345	0.193	-0.2556	-0.2553	0.117
1.892	0.7187	0.719	0.043	-0.0395	-0.03968	0.4
r/R_1	n = 3					
1.063	0.8603	0.8534	0.808	-0.9033	-0.909	0.63
1.511	1.0304	1.0377	0.703	-0.3529	-0.3558	0.815
1.892	1.126	1.1348	0.775	-0.0643	-0.0648	0.77
r/R_1	n = 100					
1.063	0.55	0.5458	0.77	-0.9366	-0.9291	0.807
1.511	1.0479	1.0532	0.503	-0.415	-0.4114	0.875
1.892	1.364	1.375	0.806	-0.0836	-0.083	0.723

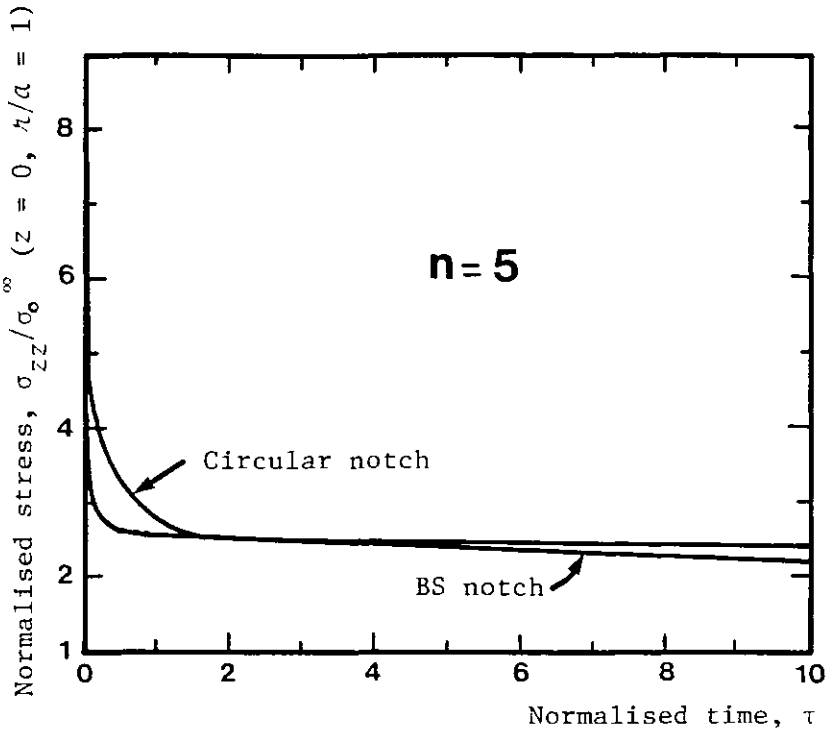

Figure 3.1: Variation of maximum stress with time for circular and BS notches (n = 5)

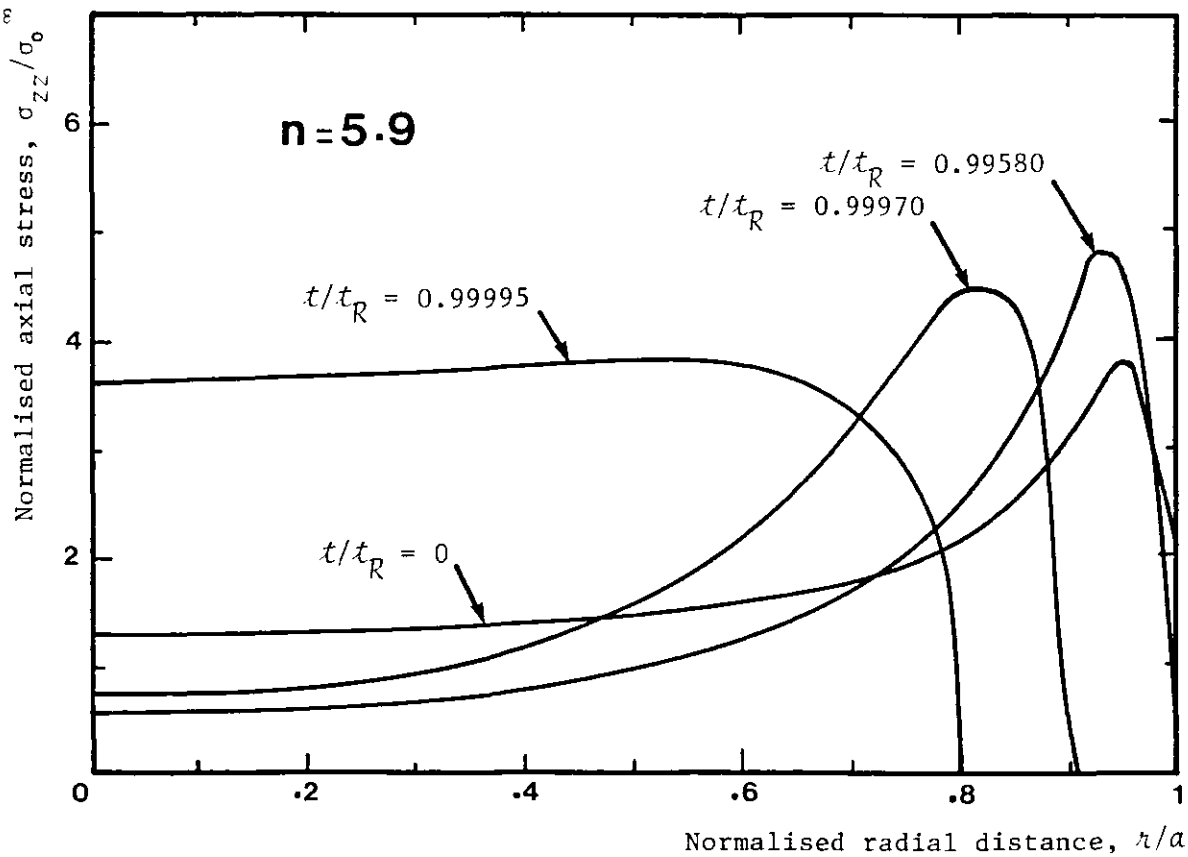

Figure 3.2: Spatial variation of the normalised axial stress with time for a material which obeys a maximum octahedral shear stress rupture criterion

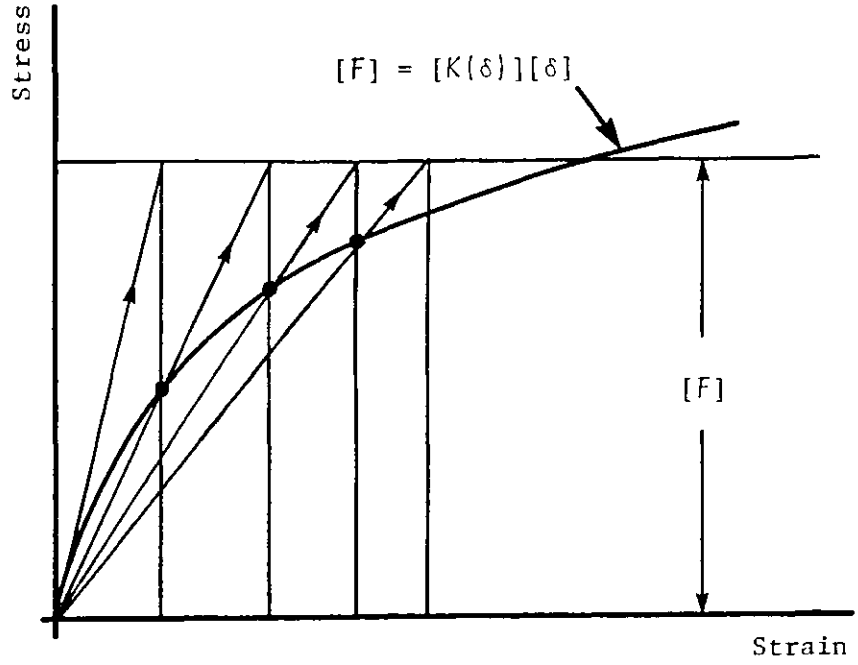

a _ Convergent

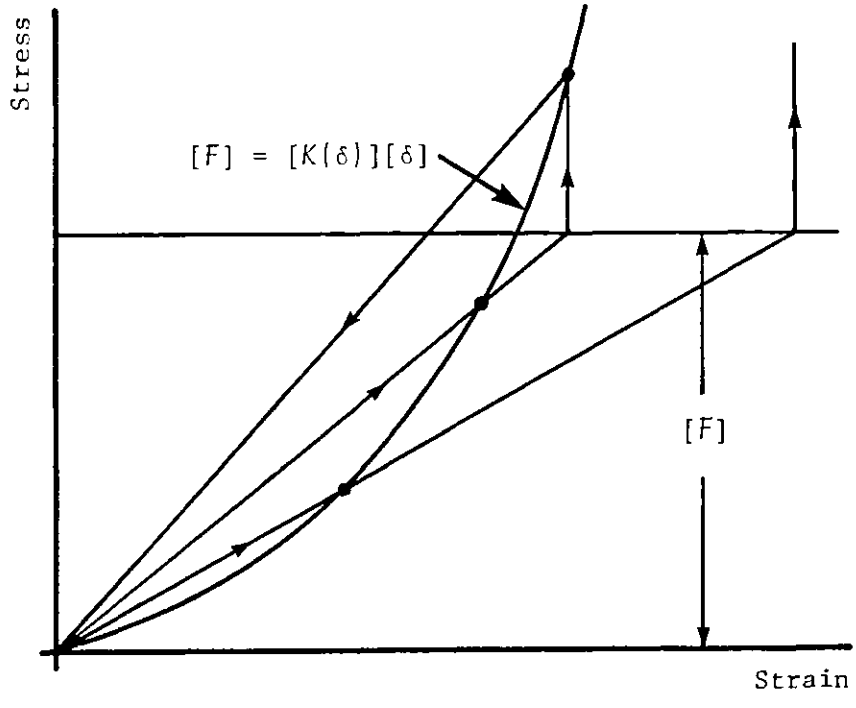

b _ Divergent

Figure 3.3: Direct iteration

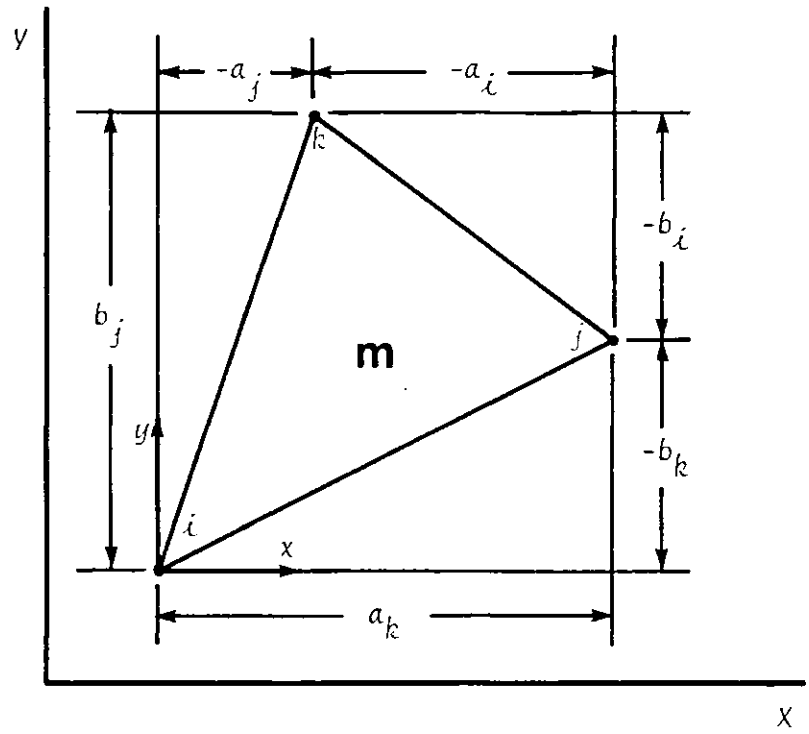

a_Dimensions of the typical element

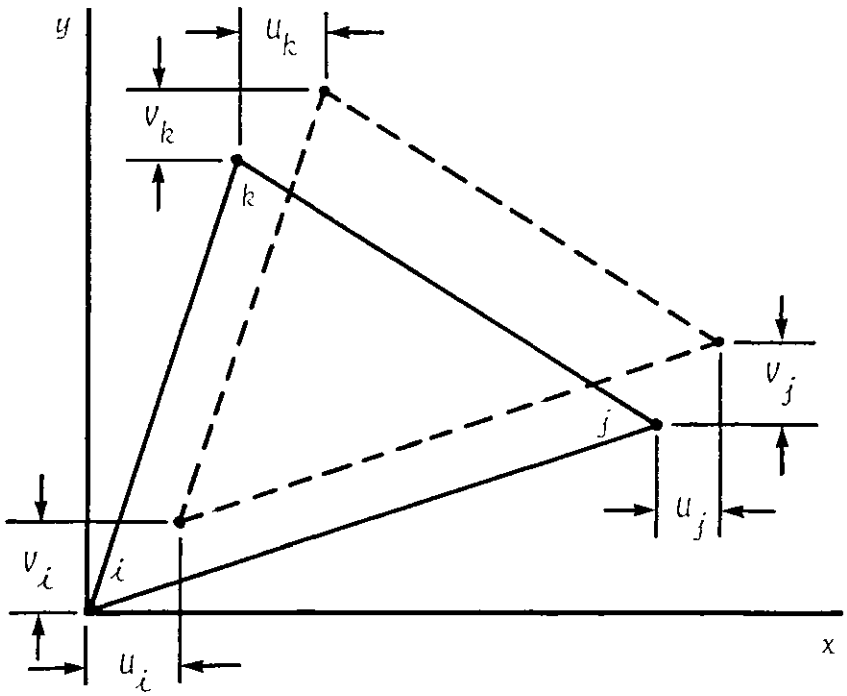

b_ Displacement of the typical element

Figure 3.4: Triangular finite element in a two-dimensional solution domain

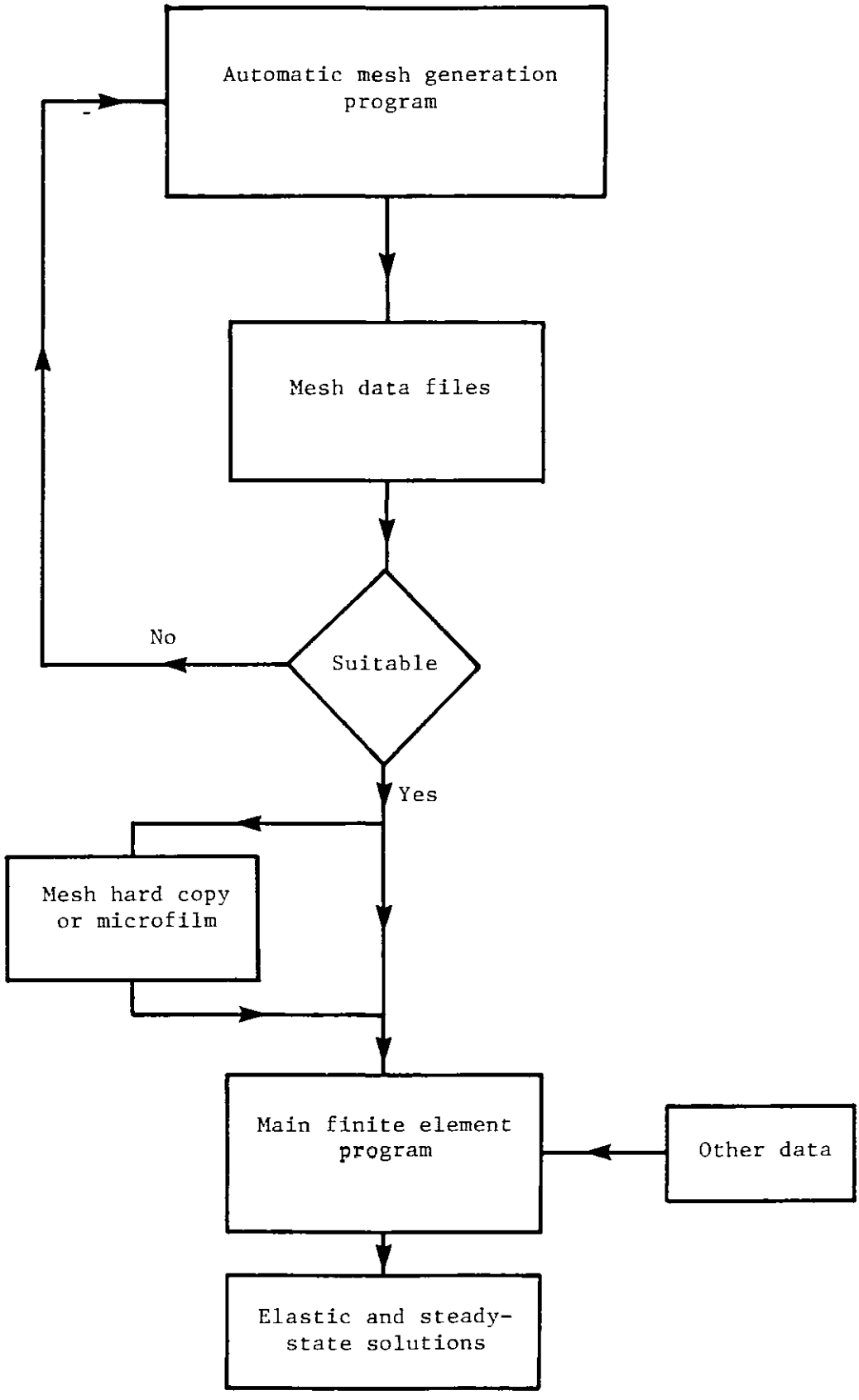

Figure 3.5: Mesh data input flow chart

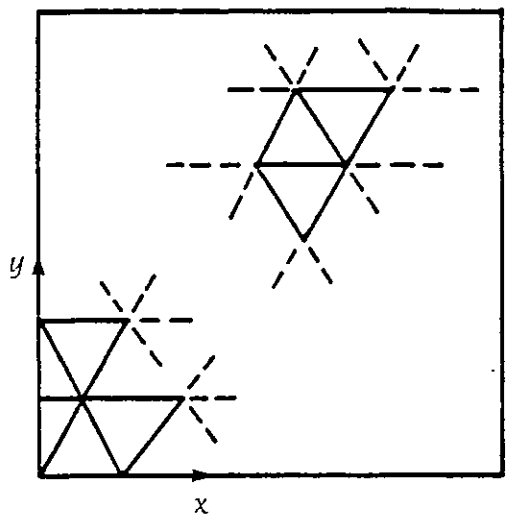

a_

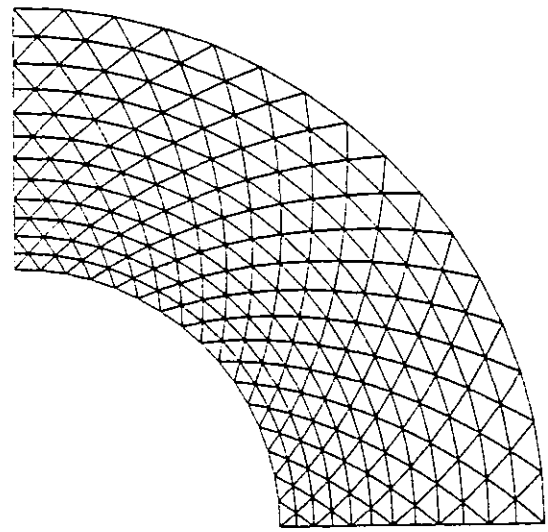

b_

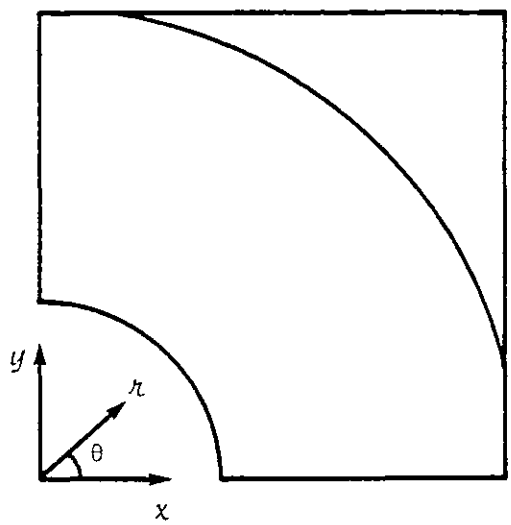

c_

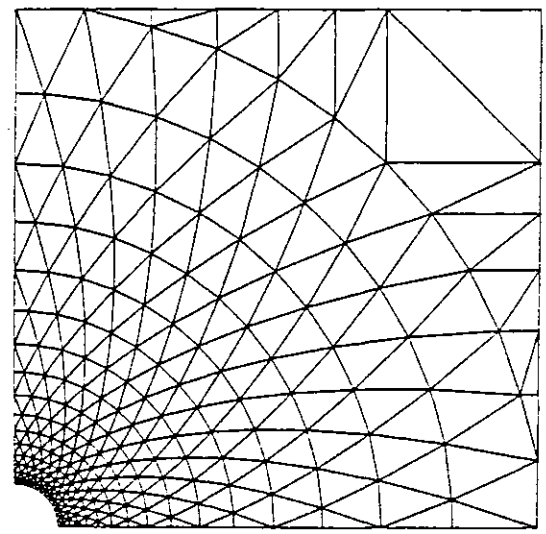

d_

Figure 3.6: Automatic mesh generation for stress concentration problems

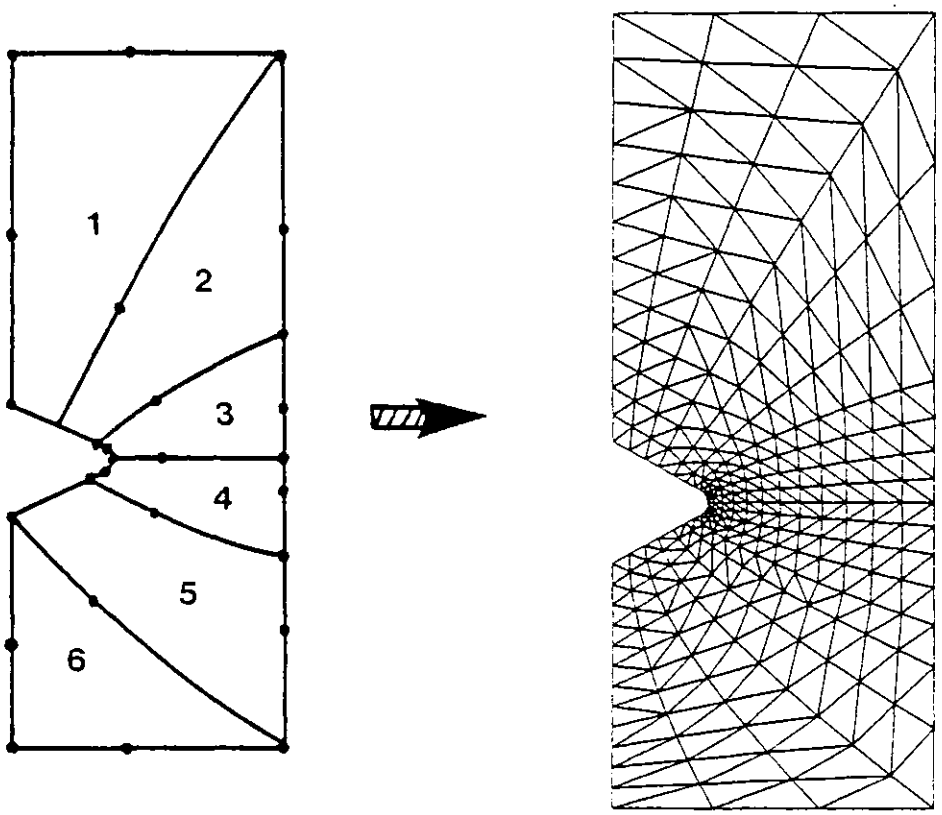

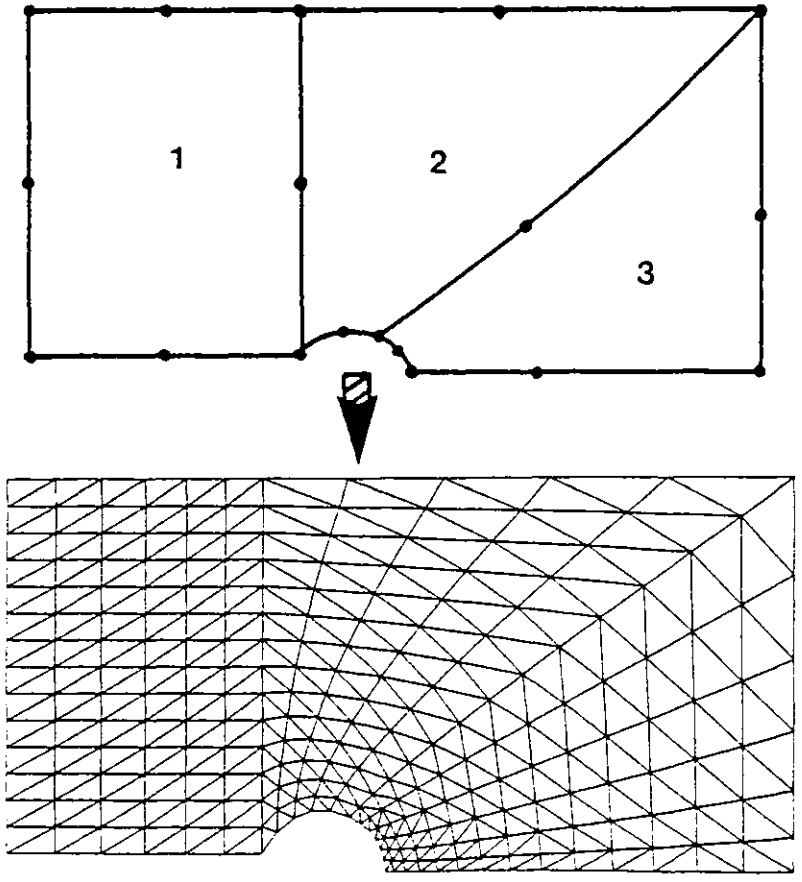

Figure 3.7: Examples of two finite element meshes generated using the method described in Section 3.6.3

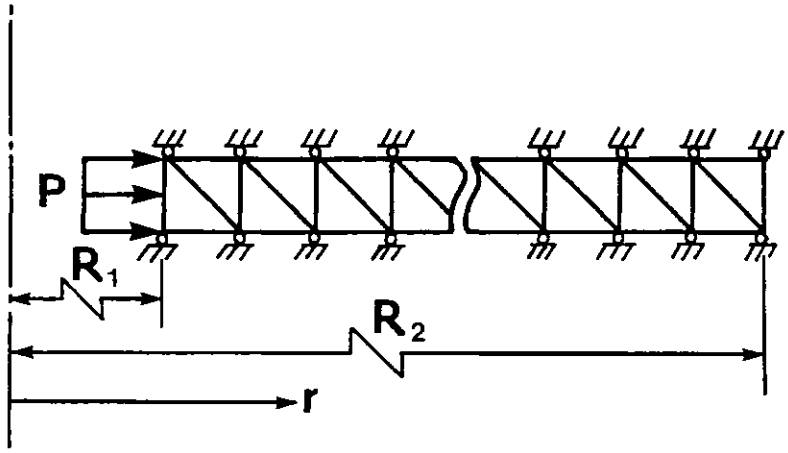

Figure 3.8: Simple finite element mesh for thick-walled cylinder problem: $R_2 = 2R_1$

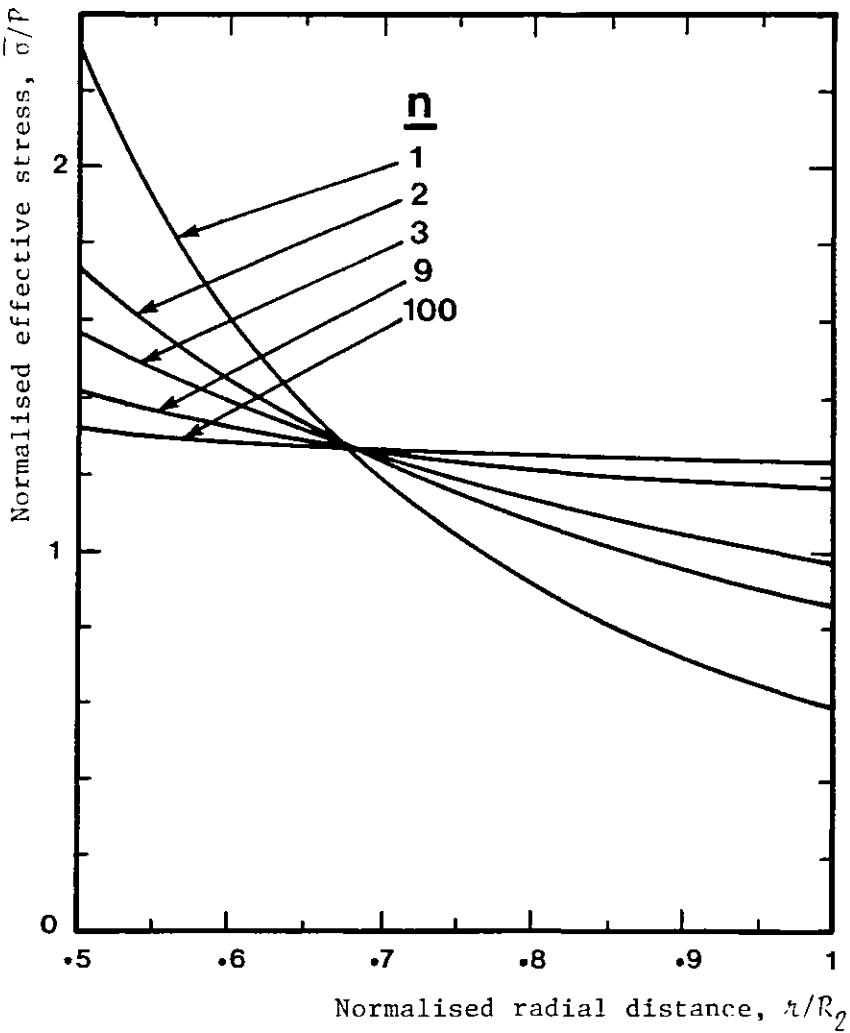

Figure 3.9: Elastic and steady-state effective stress distributions in a thick-walled cylinder subjected to internal pressure

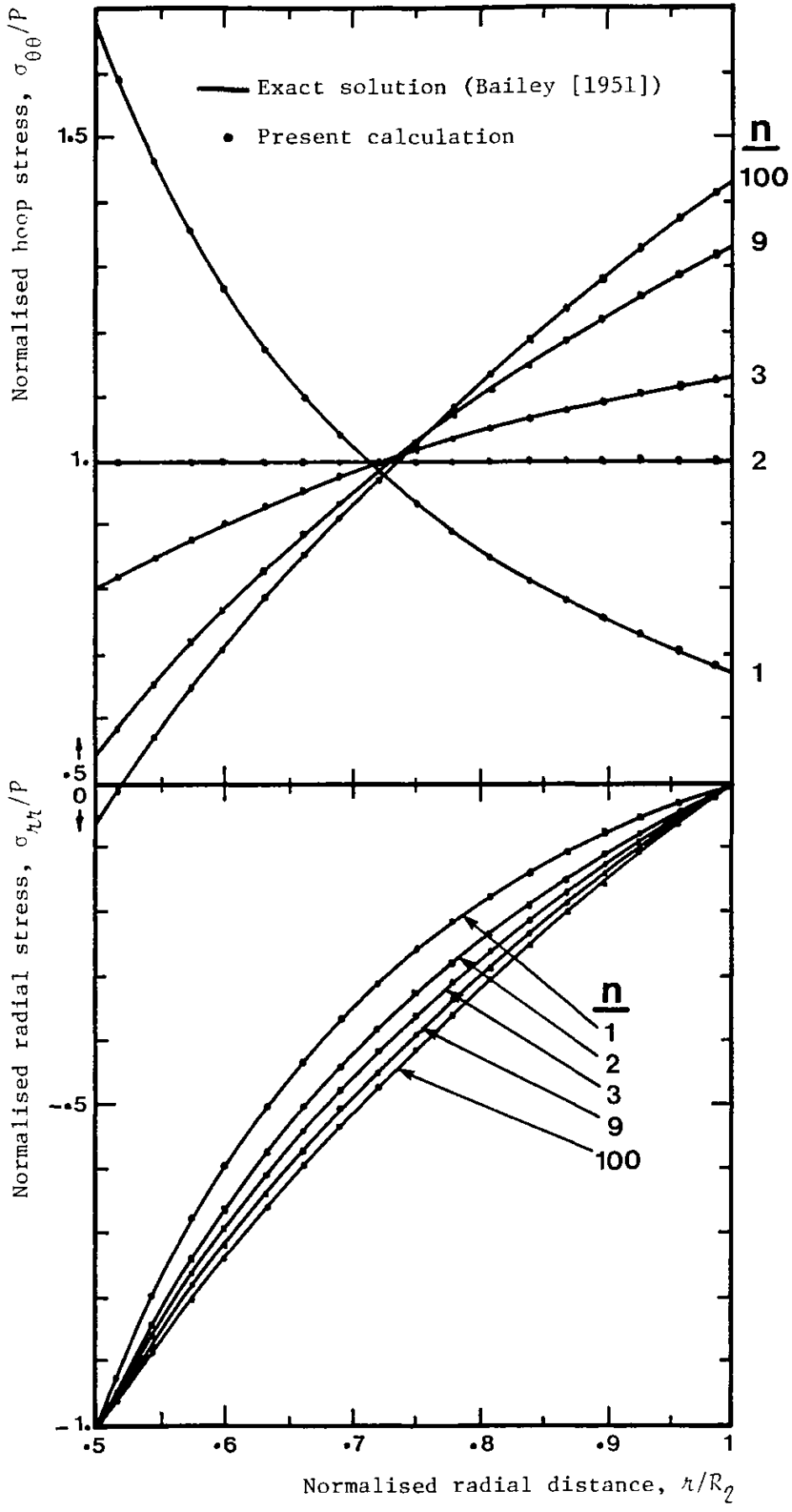

Figure 3.10: Exact and finite element hoop and radial stress distributions for a thick-walled cylinder subjected to internal pressure

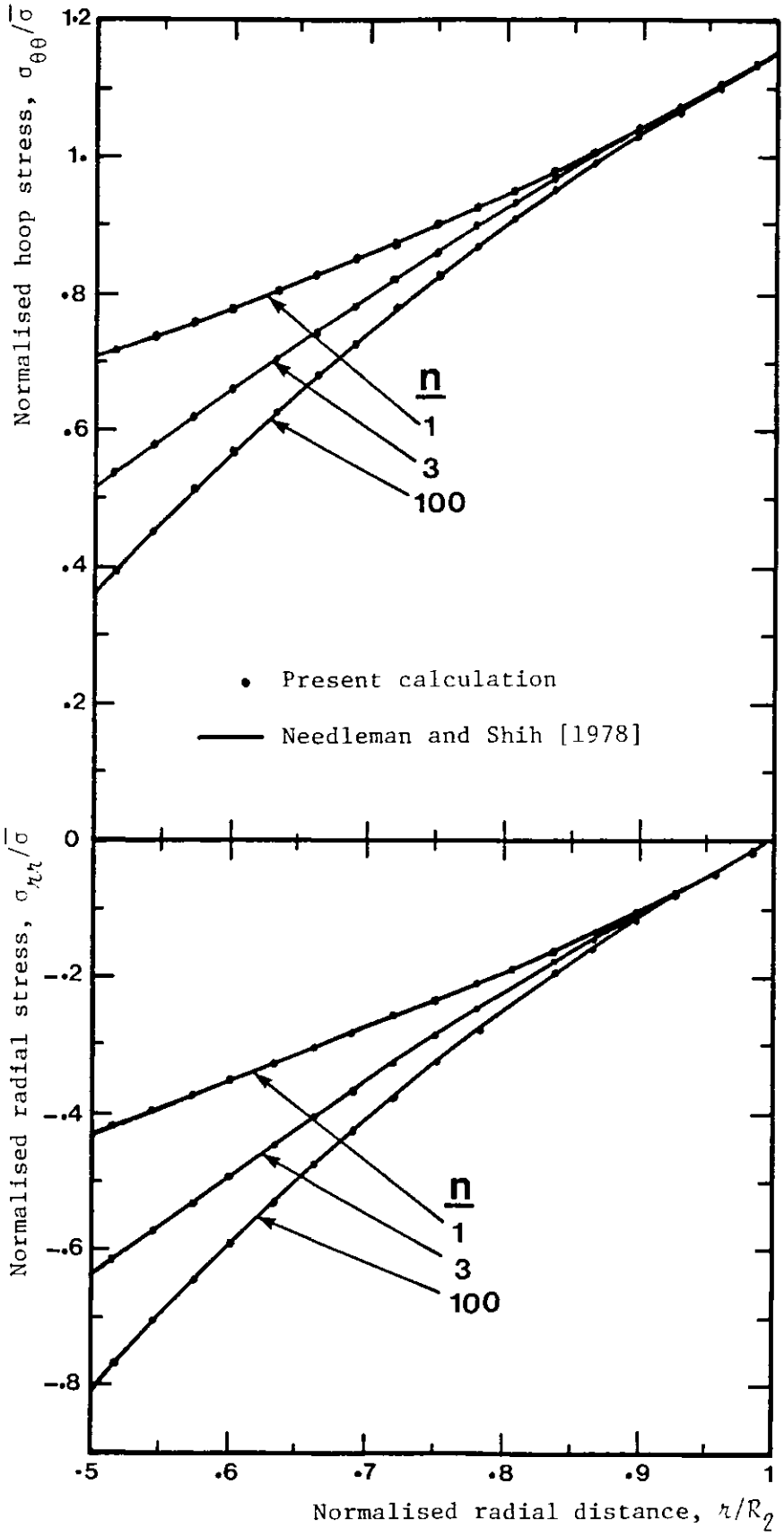

Figure 3.11: Finite element solutions for a thick-walled cylinder subjected to an internal pressure

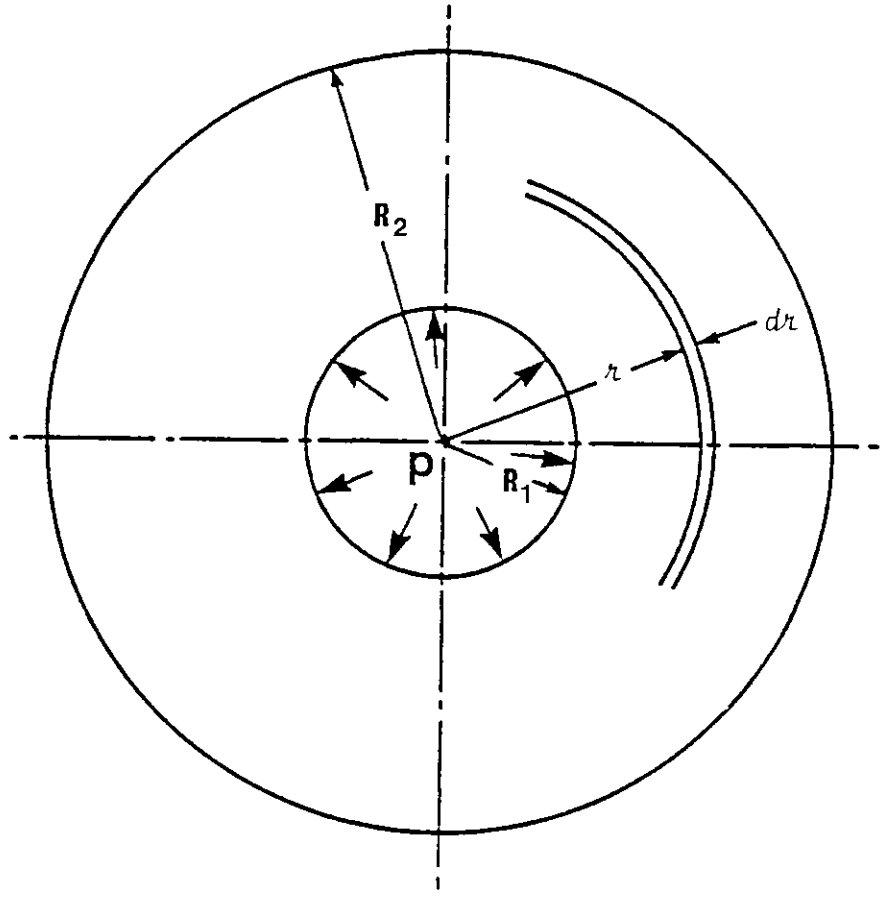

Figure 3.12: Schematic diagram of a thick-walled cylinder subjected to internal pressure, P

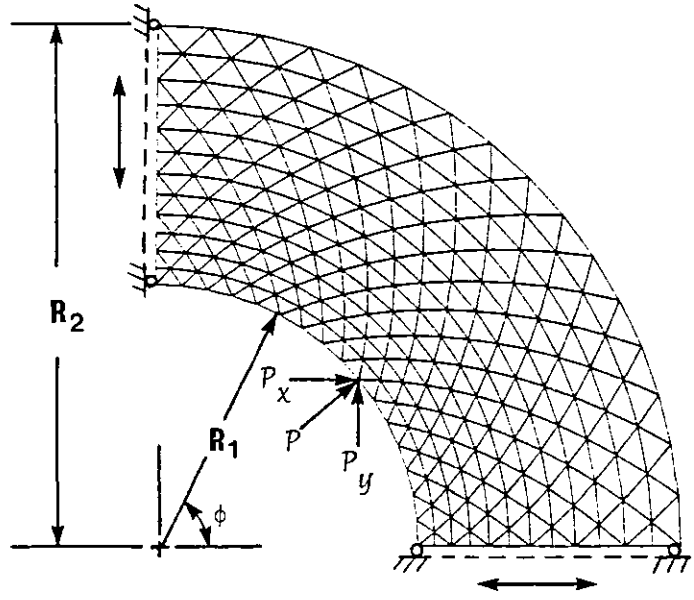

Figure 3.13: Finite element mesh of a quarter segment of a thick-walled cylinder; $R_2/R_1 = 2$

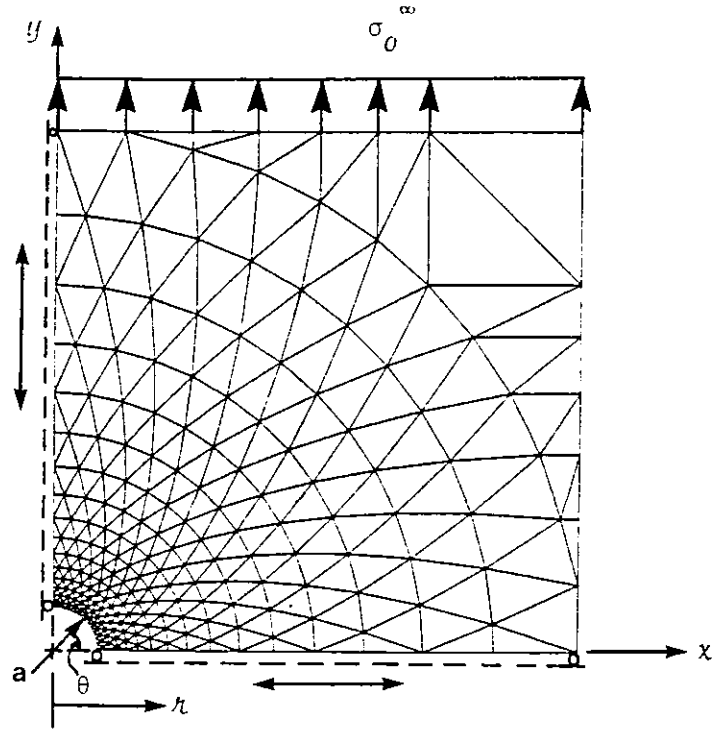

Figure 3.14: Finite element mesh for a quarter segment of a hole in an infinite plate

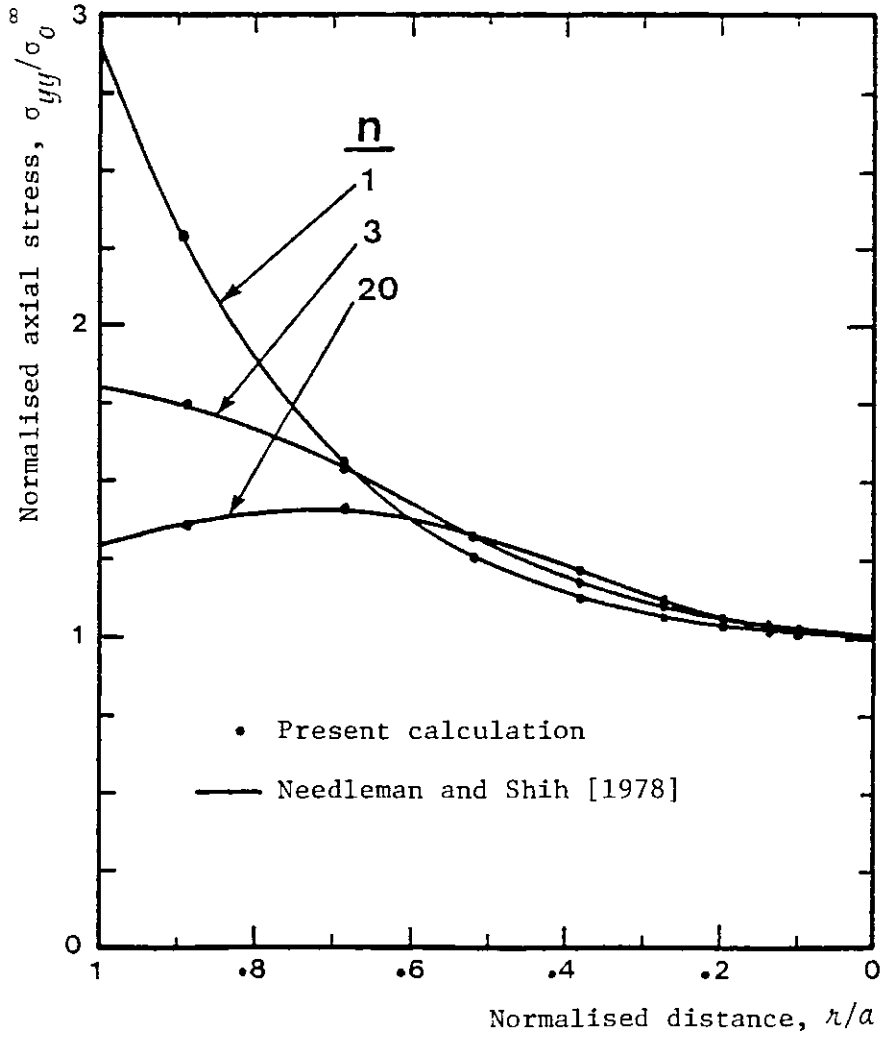

Figure 3.15: Axial stress distributions along θ = 3.75 for a hole in an infinite plate

CHAPTER 4

FINITE ELEMENT CASE STUDIES FOR COMPLEX GEOMETRIES

4.1 INTRODUCTION

This chapter describes in detail the elastic and steady-state finite element calculations, using the axi-symmetric and the two-dimensional programs developed in Chapter 3. The axi-symmetric problems considered were mainly a selection of various notch bar geometries under remote uniform tension. The elastic and steady-state stress distributions in the notched region for different values of creep index, n, are investigated. A special case was also considered, that is of blunt and sharp double notches under the same loading conditions.

The two-dimensional case studies considered were three compact tension specimens containing different circular hole sizes in the crack plane. The stress concentration factors and the stress distributions for each geometry were estimated for different values of n.

4.2 BRIDGMAN'S ANALYSIS

An approximate method of estimating both the stress and strain distributions when fully plastic conditions are reached in the minimum section of a necked tensile specimen was first suggested by Bridgman [1952]. Finite element analysis by Hayhurst, et al. [1977a,b] and Al-Faddagh, et al. [1982], for materials undergoing creep deformation, showed that Bridgman's distributions are applicable for notched bar geometries with the following reservations:

(a) The variation in the axial component of the stress across the throat must be small, i.e. applicable only for blunt notches (low tri-axiality).

(b) The creep stress index, n, must be higher than 9.

The assumptions made by Bridgman to derive the final distribution equations were:

i) The Von Mises condition has to be satisfied.

ii) The plastic deformation in the necked region dominates the total behaviour of the tensile specimen.

iii) The radial and hoop stresses in the necked region are equal.

Figure 4.1 shows a schematic diagram of the Bridgman stress and strain distributions in the throat of a circular notched bar. The normalised stress distribution equations, with respect to the nominal stress, σ_{nom}, are:

$$\frac{\sigma_{zz}}{\sigma_{nom}} = \left[1 + \ln\left(\frac{a^2 + 2aR - r^2}{2aR}\right)\right] \qquad (4.1)$$

$$\frac{\sigma_{rr}}{\sigma_{nom}} = \frac{\sigma_{\theta\theta}}{\sigma_{nom}} = \ln \left(\frac{a^2 + 2aR - r^2}{2aR}\right) \tag{4.2}$$

The effective stress distribution equation using Von Mises is:

$$\frac{\bar{\sigma}}{\sigma_{nom}} = 1 \tag{4.3}$$

The effective plastic strain distribution equation is:

$$\bar{\varepsilon}_p = 2 \ln \left(\frac{a_o}{a}\right) \tag{4.4}$$

where a_o and a are the initial and current throat radii.

The Bridgman analysis also shows that the effective stress for different notched geometries is a function only of geometry and σ_{nom} such that:

$$\frac{\bar{\sigma}}{\sigma_{nom}} = \left[\left(1 + \frac{2R}{a}\right) \ln \left(1 + \frac{a}{2R}\right)\right]^{-1} \tag{4.5}$$

4.3 NUMERICAL ESTIMATES FOR NOTCHED BARS

Finite element methods have been used successfully to calculate steady-state stress distributions in the throat of various notched bar geometries (Hayhurst, et al. [1977a,b], Kumar, et al. [1980], and Al-Faddagh, et al. [1982]). In this section, the axi-symmetric program developed in Chapter 3 was used in a systematic method of calculation, where the notch dimensions and the stress index, n, were varied to vary, accordingly, the tri-axial state of stress and the steady-state stress distribution in the notched region. The automatic mesh generation technique discussed in Section 3.6.3 was used to generate the meshes required for the calculations.

4.3.1 Geometries Considered

Figure 4.2 shows the dimensions and the boundary conditions of a finite element mesh representing a typical notched bar solution domain. In the present calculations, the ratio b/a was kept constant and the notch radius, R, was varied, therefore changing the ratio a/R. When $a/R = 0$, the case represents a uni-axial round bar with a diameter equal to b. As a/R or notch sharpness increases, the tri-axiality in the notched region increases accordingly. Three groups of notched geometries were investigated, each having a different b/a ratio. They consist of a total number of 23 notches which are listed in Table 4.1.

The reason behind choosing these particular b/a ratios was that experimental uni-axial and notched rupture data are available on each one of them. These are summarised as follows:

(a) For $b/a = 1.67$, uni-axial and notched rupture data are available in the literature on the brittle ½%Cr ½%Mo ¼%V steel due to the investigation conducted by Ng, Webster and Dyson

[1980]. The range of notched geometries they investigated was between a/R = 0 and a/R = 18.

(b) For b/a = 1.46, uni-axial and notched rupture data were made available due to the experimental investigation conducted by the present author (Chapter 6) on the ductile 2¼%Cr 1%Mo steel. The range of geometries investigated was between a/R = 0 and a/R = 44.7.

(c) For b/a = 1.33, uni-axial and notched rupture data are available in the literature on a wide range of high temperature alloys with different grain size, hardness, ductility, and heat treatment. These data were collected by Davis and Manjoine [1953] for a range of notched geometries having a/R = 0 to a/R = 50.

4.3.2 Calculations

The boundary conditions applied in the calculation procedure for all the notched geometries investigated are similar to those presented in Figure 4.2. A uniform axial stress, σ_0^{∞}, was applied at the specimen remote boundaries. The specimen axis was constrained to move only in a vertical direction, while the notch throat was prevented from moving vertically. The finite element mesh distribution for all geometries was carefully designed, so that it was finest where the stress gradient and the geometrical changes were greatest. A tolerance, λ, of 10^{-5} (equation (3.20)) with 476 elements representing the total solution domain, in which the notch throat was divided into a row of 28 elements, was found to give satisfactory accuracy during the whole calculation exercise.

The finite element results for all the notched geometries representing the three b/a ratios cannot be included in this chapter due

to the large space they would occupy. However, samples of these results showing broadly the changes in trends due to the increase in tri-axiality are summarised in Figures 4.3 to 4.20. Only the stress distributions across the minimum diameter of the throat region are presented, since this section is the most critically loaded, and may, therefore, be expected to determine the deformation and fracture characteristics of such samples.

Both Von Mises and Tresca effective strain and stress definitions were used in the calculations. A value of $\nu = 0.49$ was adopted to avoid making the $[D]$ matrix becoming singular (equation (3.2)).

4.3.3 Discussion

The way in which the sample results were presented for each b/a ratio investigated was as follows:

(a) Three finite element meshes were first presented for each b/a ratio. These were a blunt, sharp, and a geometry with a/R lying between these two extremes (Figures 4.3, 4.9 and 4.15).

(b) The normalised elastic and steady-state effective stress, $\bar{\sigma}/\sigma_0^{\infty}$, across the throat of a blunt and a sharp notched geometry using the Von Mises criterion are presented in Figures 4.4, 4.5, 4.10, 4.11, 4.16 and 4.17. For $b/a = 1.67$, the distributions were for two notched geometries with $a/R = 0.75$ and 20. The calculations were made for $n = 1$, 3, 5, 9 and 16, as shown in Figures 4.4 and 4.5. For $b/a = 1.46$, the distributions were for $a/R = 1$ and 32.5, with values of $n = 1$, 3, 5 and 9 (Figures 4.10 and 4.11). Finally, for $b/a = 1.33$, the distributions were for $a/R = 3$ and 30, and values of $n = 1$, 3, 7 and 12 (Figures 4.16 and 4.17). For all these geometries, $\bar{\sigma}$ is always maximum at the notch root

for all values of n. The magnitude of the maximum effective stress, $\bar{\sigma}_{max}$, decreases with the increase in n, and the whole stress distribution nearly levels out when $n > 9$. For these and other notch geometries when $n > 1$, there is a tendency for the effective stress distribution to cross at almost the same value of r/a, implying an approximate point of constant stress, often called a skeletal point (Penny and Marriott [1971]). The position of the skeletal point varies between $r/a = 0.6$ and 0.95, as shown in Table 4.2 for the three b/a ratios. For blunt notches, it tends to be nearer to $r/a = 0.6$, and for sharp notches nearer to $r/a = 0.95$. Similar trends were observed when Tresca's criterion was used in the calculations. The distributions for all values of n were parallel to those when the Von Mises criterion was applied. Examples of this are shown in Figures 4.10 and 4.11. The maximum difference between the values of the effective stress at the skeletal point for the sharp notches is always less than 15%. For blunt notches, the difference is nearly negligible (uni-axial). This is consistent with the plasticity flow rules which show that, for a material with a uni-axial yield stress, Y, the difference between the normalised stress, σ/Y, and shear stress, τ/Y, in pure tension is zero when either the Von Mises or Tresca criterion is used. However, the difference is about 15.5% (corresponding to the difference between 0.5 and 0.577) in pure torsion (Johnson and Mellor [1975]).

The presence of a skeletal point may enable the stress there to be used as a reference stress to characterise the overall deformation behaviour of the notched bars, provided sufficient time exists for a steady-state creep stress

distribution to be achieved.

(c) The steady-state stress distributions across the throat of two notched geometries for each b/a ratio when the Von Mises criterion was adopted are presented in Figures 4.6, 4.7, 4.12, 4.13, 4.18 and 4.19. In these figures, the normalised, effective, $\bar{\sigma}/\sigma_o^{\infty}$, axial, $\sigma_{zz}/\sigma_o^{\infty}$, hoop, $\sigma_{\theta\theta}/\sigma_o^{\infty}$, radial, $\sigma_{rr}/\sigma_o^{\infty}$, and the hydrostatic, $\sigma_m/\sigma_o^{\infty}$, stresses are plotted for different notched geometries and values of n. The line marked with * in these figures refers to the skeletal point position taken from the graphs of the corresponding effective stress distributions. As discussed in part (b), the effective stress distribution is always maximum at the notch root for all values of n. However, for the axial, hoop, radial and hydrostatic stresses, the maximum values move from the notch centre-line, $r = 0$, for blunt notches, towards the notch root, $r = a$, as the notch sharpness increases. Similar trends were previously observed by Hayhurst, et al. [1977a,b], Kumar, et al. [1980], and Al-Faddagh, et al. [1982].

(d) Finally, Figures 4.8, 4.14 and 4.20 show how the state of stress parameters at the skeletal point vary with the increase in tri-axiality for the three b/a ratios investigated. The values of the axial, effective and hydrostatic stresses at the skeletal points for each notched geometry of a particular b/a ratio are normalised with respect to the nominal stress across the notch throat, σ_{nom}. A fourth ratio of $\sigma_m/\bar{\sigma}$ is also shown. The trends these states of stress followed are the same for the three b/a ratios. The effective and axial stresses are normalised as $\sigma_{nom}/\bar{\sigma}$ and σ_{nom}/σ_1, to show notch strengthening and weakening for materials in which internal damage

accumulation rates are dominated either by the effective or the axial stress (Hayhurst [1972], Leckie and Hayhurst [1974], and Dyson and McLean [1977]). A tendency for the effective stress to decrease when either the Von Mises or Tresca criterion is adopted, and both the axial and hydrostatic stresses to increase, is observed when the tri-axiality increases (a/R). The ratio $\sigma_m/\bar{\sigma}$ has been used in plasticity and power-law creep failure mechanisms to describe the geometrical tri-axial state of stress (Hancock and Mackenzie [1976], Needleman and Rice [1980], and Cocks and Ashby [1980b]). $\sigma_m/\bar{\sigma}$ is plotted in these figures to be used in the coming chapters in modelling notched bar behaviour. At $a/R = 0$ (uni-axial), $\sigma_m/\bar{\sigma} = 1/3$, and this ratio increases with a/R.

4.4 CASE STUDY: THE INFLUENCE OF DOUBLE NOTCHES IN ROUND BARS ON THE STEADY-STATE STRESS DISTRIBUTIONS

Circumferentially notched bar specimens, loaded axially, are frequently used in laboratories to study the effect of tri-axial stressing on creep deformation and life time. For physical metallurgists concerned with understanding the mechanics of high temperature fracture micro-mechanisms, these geometries are of considerable interest. The distribution of grain boundary creep damage is usually analysed away from and near to the fractured surfaces of the notched bars. However, if the notched region is to be analysed before fracture, interrupted tests have to be performed, which means two specimens for each notched geometry have to be manufactured. More material and testing times are therefore needed.

Loveday and Dyson [1979] suggested that if two accurately manufactured, circumferential notches are machined in on the specimen, then creep deformation in the two notched regions should be identical up to about $0.8t_R$. The weaker notch then will dominate until fracture. They used this technique to measure the diametral displacement occurring at one notch throat using a special type of extensometer designed by Furse and Loveday [1981]. They calculated the current hoop strain using the measurements, as follows:

$$\varepsilon_{\theta\theta} = \frac{a_o - a}{a_o} \tag{4.6}$$

where a_o and a are the initial and current notch radii, respectively. The experimental steady-state time and hoop strain rate, $t_{\delta\delta}$ and $\dot{\varepsilon}_{\theta\theta}$, were estimated and compared with the theoretical predictions based on Hayhurst, et al. [1977b] steady-state finite element calculations. The same notched data were later used by Dyson and Loveday [1980] to study creep fracture under tri-axial tensile stressing. They used Bridgman's effective stress

equation (4.5) to calculate the term $[(1 + 2R/a) \ln (1 + a/2R)]^{-1}$, required to convert the net section stress in the notch, to become equivalent to the uni-axial stress.

The interesting observation made in reading the literature on double notches is that the finite element calculations and the Bridgman analysis used predicts the deformation and fracture behaviour of a single notch. There is no information in the literature to justify using single notch analysis in a comparison with double notched experimental data.

In this section, the axi-symmetric program developed in Chapter 3 was used to calculate the elastic and steady-state stress distributions in a single and double notched bar geometries. The geometries considered and the comparisons made are presented in the coming sections.

4.4.1 Geometries Considered

Four double notched round bar geometries were considered; these were:

(a) British Standard V-notch; $a/R = 18.18$, $b/a = 1.41$

(b) Semi-circular notch; $a/R = 1.5$, $b/a = 1.67$

(c) Blunt notch; $a/R = 1.67$, $b/a = 1.46$

(d) Sharp notch; $a/R = 13$, $b/a = 1.46$

The BS and semi-circular notches (a) and (b) were considered because they have been widely used in many analyses to show the difference in creep behaviour between a sharp and a Bridgman-type notch (Hayhurst, et al. [1977a,1978], Kumar, et al. [1980], and Al-Faddagh, et al. [1982]).

The two other notched geometries (c) and (d) have a similar b/a ratio to those experimentally creep tested notched geometries investigated by the present author (Chapter 6). Again, two extreme

geometries were considered, a blunt and a sharp notch.

The finite element meshes were generated using the program discussed previously in Section 3.6.3. Because of symmetry, only a quarter of the solution domain is considered, as shown in Figures 4.21(a) and (b). The difference in the boundary conditions applied during the calculations for a BS double and a single V-notched geometry is shown in Figures 4.21(b) and (c). Figures 4.21(d) to (f) show the other geometries considered, for which the same boundary conditions apply.

4.4.2 Calculations and Discussion of the Results

Calculations have been made for values of n = 1 and 9 for all the geometries investigated. The same value of σ_0^{∞} was applied for the single and the double notched geometries. The stresses in the minimum section of the double notched geometries were averaged for the two rows of elements in that region, the results of which are shown in Figures 4.22 to 4.25 compared with the single notch distributions. It is evident that the elastic stress distributions were identical for both geometries. For n = 9, the distributions differ slightly for the two blunt notches; however, the margins are always less then 1% (Figures 4.23 and 4.25). In the case of the two sharp notches, the error margins near the notch root where the stresses peak are always less than 2% (Figures 4.22 and 4.24). These errors are acceptable for two reasons: first, only 24 elements were used across the throat of the double notched geometries compared with 28 elements for the single notch; this obviously reduces the accuracy. If 28 elements are used in the double notch solution domain, the array lengths will exceed the 500 limit set in the program. The second reason is to do with the double notch geometry and the way the boundary conditions are applied.

4.5 NUMERICAL ESTIMATES FOR COMPACT TENSION SPECIMENS

In the field of fracture mechanics, it is a well-established laboratory technique to use compact tension specimens to collect crack growth data on materials operating under creep conditions.

Morzeria [1979] carried out creep cracking tests on a low alloy steel at 565°C using compact tension specimens with notches of various sharpnesses. The reason behind introducing these notches was to examine the dependence of the initiation and propagation rate of a creep crack on the root radius. His conclusions were that the initial cracking rate decreases with increase in hole size.

Webster and Nikbin [1981] used the boundary integral equation method (BIE) to estimate the effective elastic stress concentration factor (SCF) at the edge of the hole for three of Morzeria's compact tension geometries. Their results showed that the elastic SCF is highly sensitive to notch sharpness. For materials where the crack initiation time is smaller than the redistribution time (mainly brittle materials) due to creep, they showed that the initial crack growth rate is highly sensitive to the elastic SCF. However, for ductile materials, the redistribution time is expected to be much shorter than crack initiation time; therefore, the steady-state SCF at the edge of the hole has to be used in the calculations. For this reason, the two-dimensional finite element program developed in Chapter 3 was used to calculate the steady-state stress distributions for the geometries Webster and Nikbin investigated.

4.5.1 Compact Tension Geometries

The main dimension of a compact tension specimen is shown in Figure 4.26. Three geometries were considered in the finite element analysis with ratios of d/w = 0.2, 0.133 and 0.066. The dimension w was kept constant and the notch sharpness was increased by decreasing d.

Because of symmetry, only half of the geometry was considered as a solution domain. The finite element mesh generation program discussed in Section 3.6.3 was used to generate the required meshes, shown for the three geometries in Figure 4.27. Experimentation with progressively finer grid sizes has shown that satisfactory accuracy is achieved with approximately 480 elements and the crack line divided into a row of 28 elements. The stress was applied on four elements representing a segment of a circle similar in profile to the loading pins in the real specimen. This was found to be adequate to produce the required solutions.

4.5.2 Estimates of the Nominal Stress, σ_{nom}

The definition of the stress concentration factor is:

$$SCF = \frac{local\ stress}{\sigma_{nom}} \tag{4.7}$$

The nominal stress for the compact tension specimen consists of the tensile stress on the net section, σ_t, added to the bending stress, σ_b, as shown in Figure 4.26(b). The equation for each one of them is:

$$\sigma_t = \frac{F}{B\ (w - a)} \tag{4.8}$$

and:

$$\sigma_b = \frac{3F\ (w + a)}{B\ (w - a)^2} \tag{4.9}$$

where F is the applied force, and B is the specimen thickness. Both w and a are shown in Figure 4.26. The nominal stress, σ_{nom}, is therefore:

$$\sigma_{nom} = \sigma_t + \sigma_b = \frac{F\ (4w + 2a)}{B\ (w - a)^2} \tag{4.10}$$

The SCF can then be calculated using equation (4.7).

4.5.3 Calculations and Discussion of the Results

Elastic and steady-state calculations were made for each of the three compact tension geometries for values of n = 1, 3 and 9. The normalised axial stress distributions, σ_{yy}/σ_{nom}, in the crack line region for each geometry are summarised in Figures 4.28 to 4.30. Finally, the SCF at the edge of the hole for each geometry and n are presented in Figure 4.31.

The calculations were performed, assuming plane stress conditions and incompressible material behaviour, i.e. $\nu = 0.5$. The Von Mises criterion was adopted and a tolerance, $\lambda = 10^{-5}$, for all the calculations. Several elastic computer runs were performed for each geometry to find the optimum over-relaxation factor used in the Gauss-Seidel iterative method adopted in the program to solve the linear simultaneous equations (Fenner [1975]). The values were found to vary between 1.94 and 1.98, depending on the geometry.

The normalised axial stress distributions shown in Figures 4.28 to 4.30 for n = 1 have similar trends for all three geometries. The maximum is always near the hole edge; however, it increases in value with the increase in hole sharpness. For values of $n > 1$, the stress redistributes and the maximum tends to move away from the hole edge. The trends observed are similar for all geometries. Initially, at time zero on first loading, and in the absence of plastic deformation, the stress distribution is elastic. As creep takes place, regions of high stress shed load onto the lower stress regions because of the high sensitivity to stress of creep deformation. The extent of the stress redistribution that takes place in order to achieve steady-state conditions increases with increase in the value of n.

The elastic and steady-state SCF are presented in Figure 4.31 for the three compact tension geometries. The elastic SCF is compared

with Webster and Nikbin's [1981] BIE predictions which shows identical trends and values to the present calculations. For values of $n > 1$, the SCF becomes less sensitive to the notch sharpness, therefore making crack initiation much more difficult.

4.6 CONCLUSIONS

Calculations have been made for a range of circumferential notch geometries and values of n to determine the steady-state stress distributions across the notch throat region using an axi-symmetric finite element program developed and tested in Chapter 3.

A skeletal point at which the effective stress remained constant, independent of n, was observed for each notch dimension investigated. The value of the effective stress at the skeletal point can be used as a reference stress to characterise the overall deformation behaviour of the notched bars, excluding situations where a dominating crack can cause a premature failure and when steady-state is not achieved.

The variation of the effective, axial and hydrostatic stresses at the skeletal point as notch sharpness increases were plotted for three b/a ratios. Similar trends were observed which could be used in continuum mechanics and microstructural models to explain notch strengthening and weakening.

Finite element calculations have been performed to investigate the influence of having two notches in a round bar on the stress distributions. The results showed satisfactory agreement with the single notch finite element predictions. These findings make it justifiable to use either single or double notch solutions in further theoretical studies on creep behaviour of notched bars.

Three compact tension specimens with different notch sharpnesses were investigated using the two-dimensional finite element program developed in Chapter 3. Elastic and steady-state axial stress distributions and stress concentration factors were estimated. The results showed that for ductile materials, crack initiation is not sensitive to notch sharpness.

TABLE 4.1

The Finite Element Notched Geometries Investigated

b/a	a/R									
1.67	0.75	1.5	2	4	6.66	10	15	20	-	-
1.46	0.5	1	1.67	2.6	5	8.125	11.818	13	16.25	32.5
1.33	1	3	6	13.125	30	-	-	-	-	-

TABLE 4.2

Effective Stress Values at the Skeletal Point When the Von Mises Criterion is Adopted

b/a = 1.67			b/a = 1.46			b/a = 1.33		
a/R	r/a*	$\sigma_{nom}/\bar{\sigma}$*	a/R	r/a*	$\sigma_{nom}/\bar{\sigma}$*	a/R	r/a*	$\sigma_{nom}/\bar{\sigma}$*
0.75	0.68	1.2	0.5	0.645	1.19	1	0.6	1.195
1.5	0.675	1.35	1	0.65	1.242	3	0.765	1.384
2	0.685	1.435	1.67	0.73	1.352	6	0.833	1.468
4	0.765	1.56	2.6	0.755	1.443	13.125	0.87	1.508
6.66	0.818	1.665	5	0.81	1.553	30	0.91	1.539
10	0.85	1.737	8.125	0.84	1.606			
15	0.87	1.788	11.818	0.86	1.608			
20	0.895	1.79	13	0.873	1.618			
			16.25	0.895	1.621			
			32.5	0.93	1.624			

* Position of the skeletal point

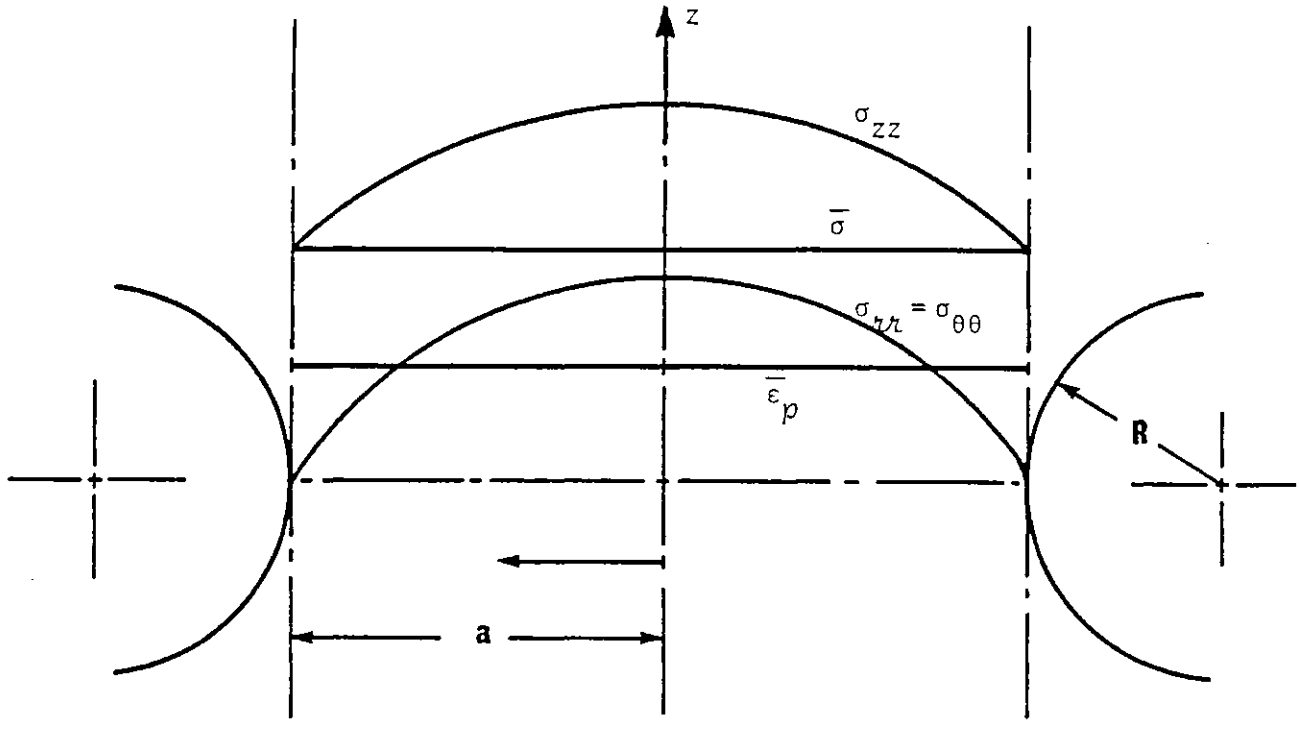

Figure 4.1: Bridgman stress and strain distributions

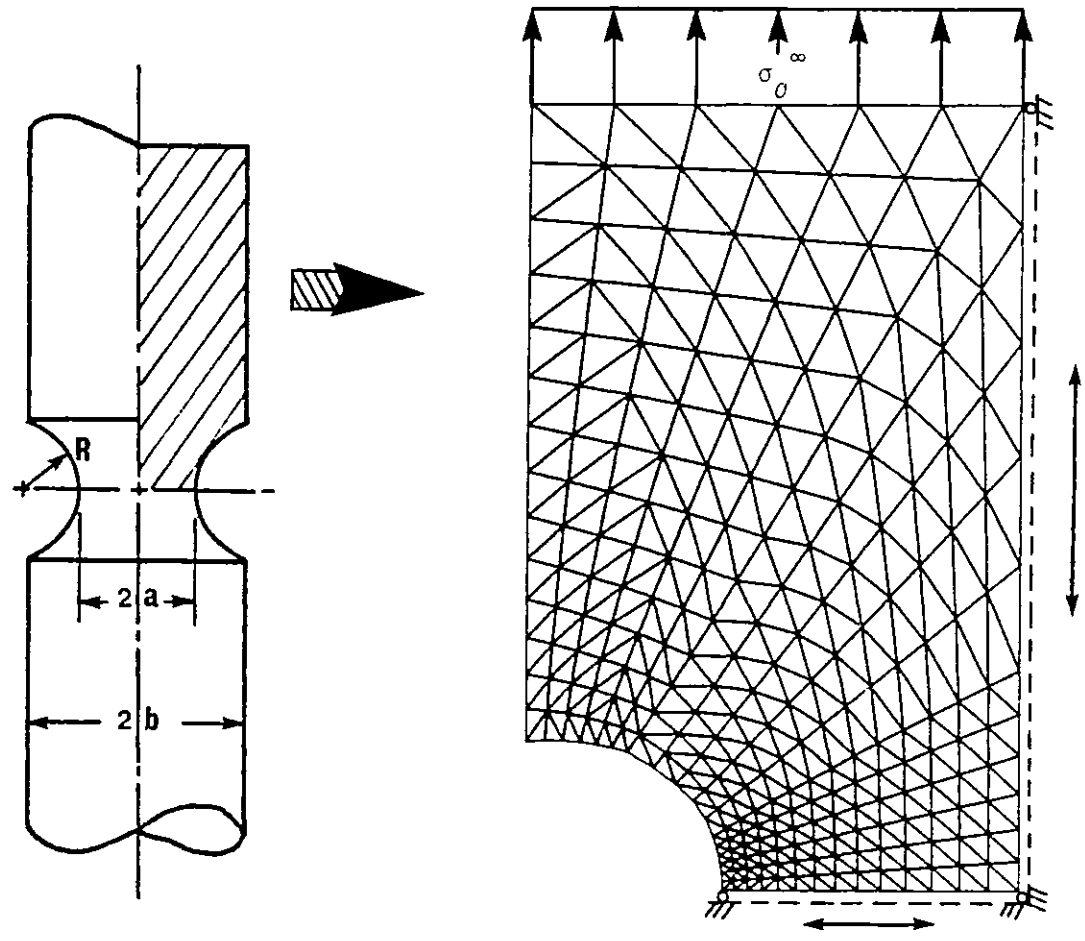

Figure 4.2: A typical notched bar solution domain

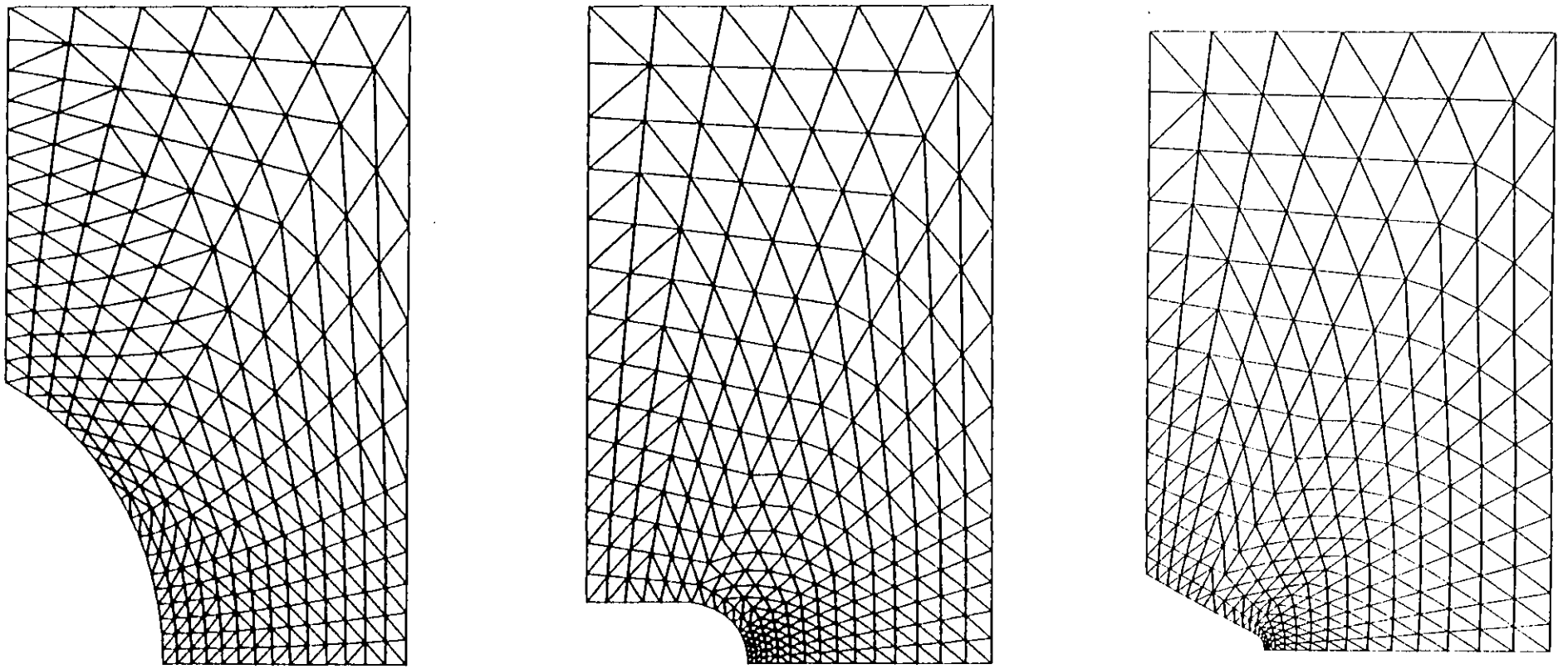

a $a/R = 0.75$ **b** $a/R = 4$ **c** $a/R = 20$

Figure 4.3: A selection of finite element meshes for the notch geometries with $b/a = 1.67$

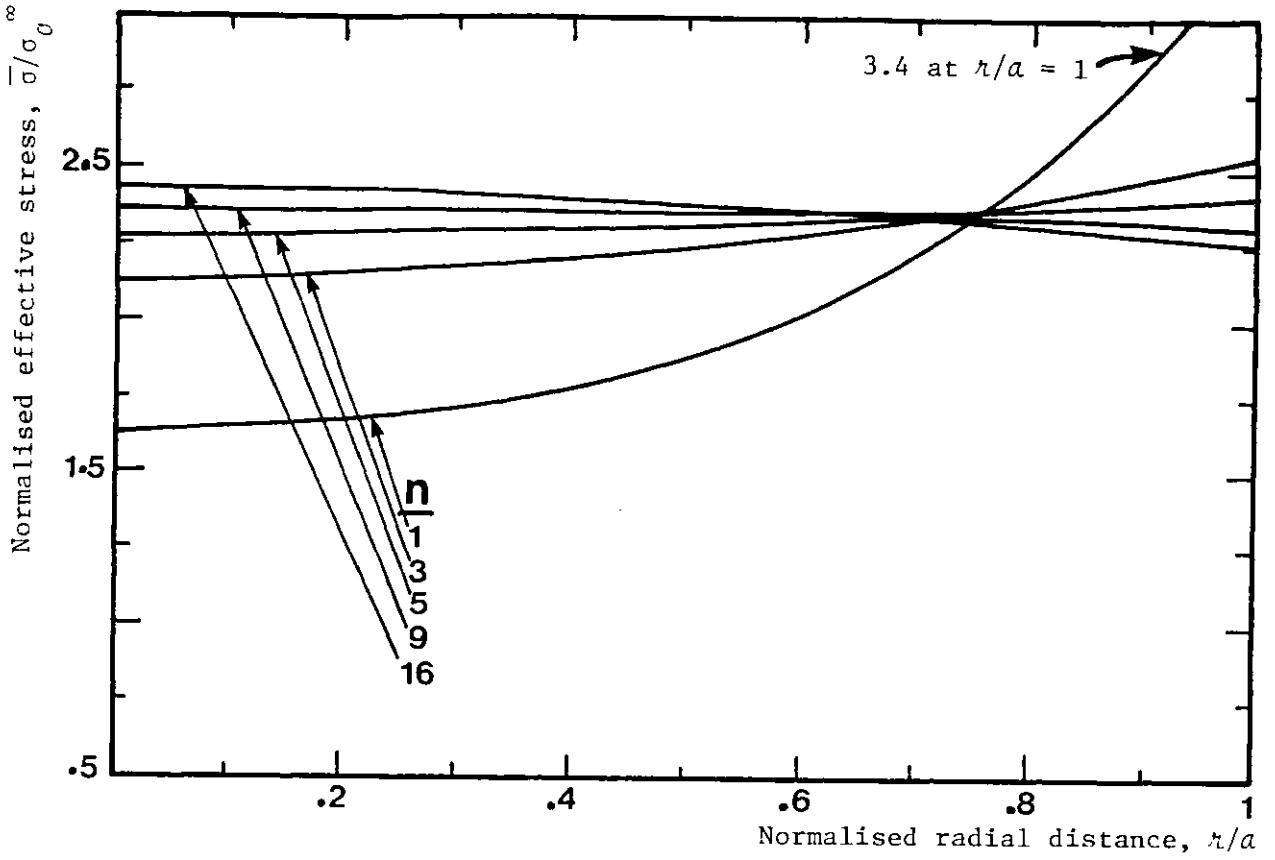

Figure 4.4: Effective stress distribution at steady-state across the throat of a notch with b/a = 1.67 and a/R = 0.75

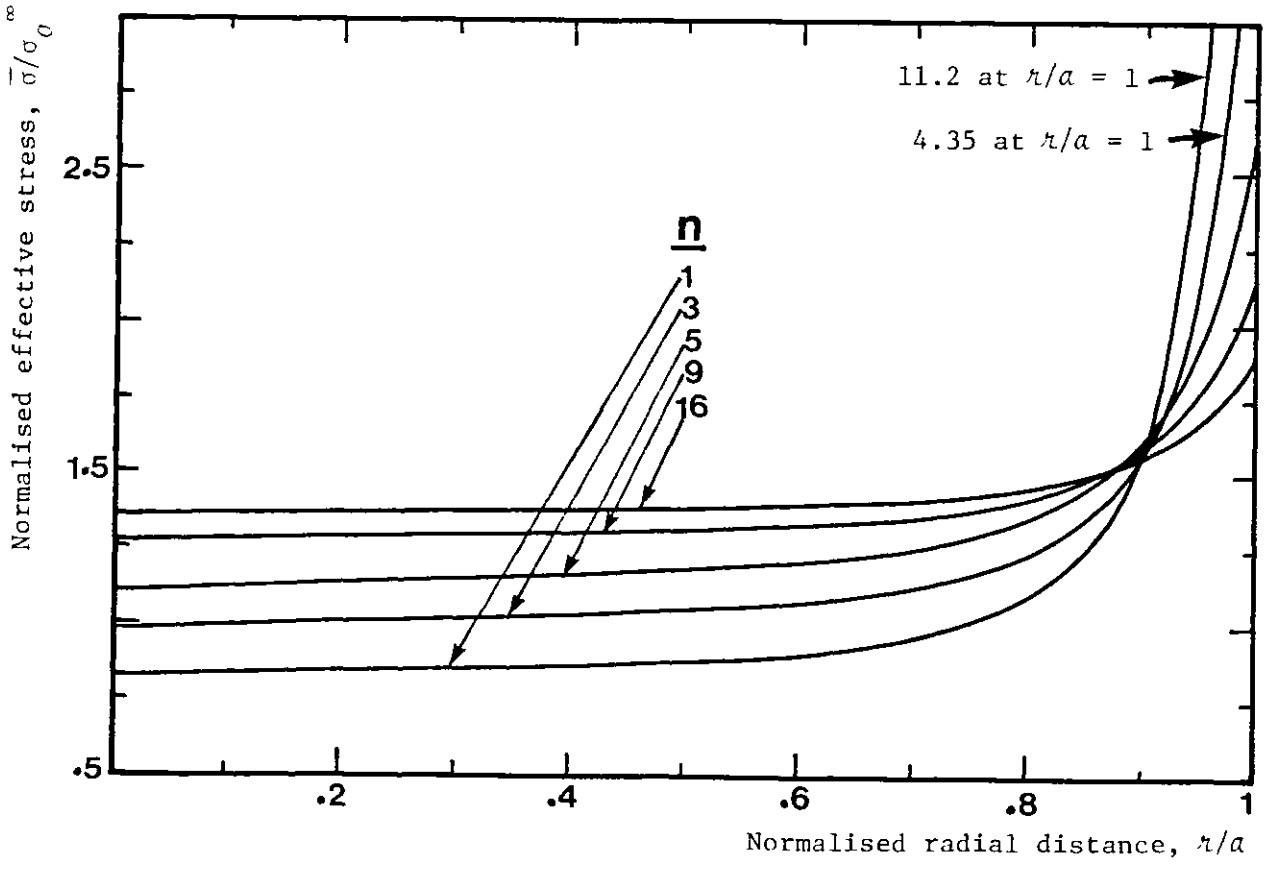

Figure 4.5: Effective stress distribution at steady-state across the throat of a notch with b/a = 1.67 and a/R = 20

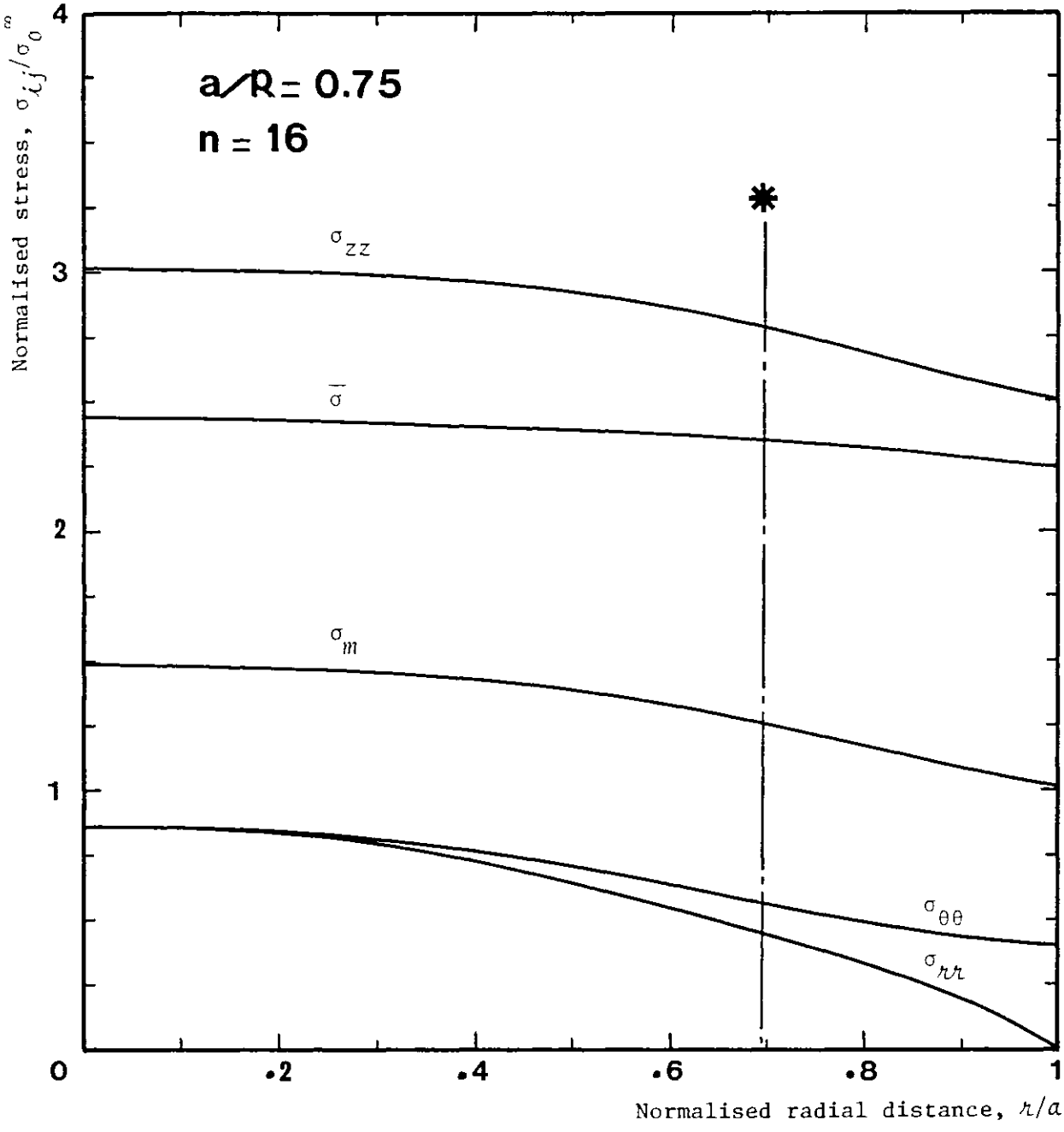

Figure 4.6: Stress distribution at steady-state across the throat of a notch with b/a = 1.67, a/R = 0.75 and for n = 16

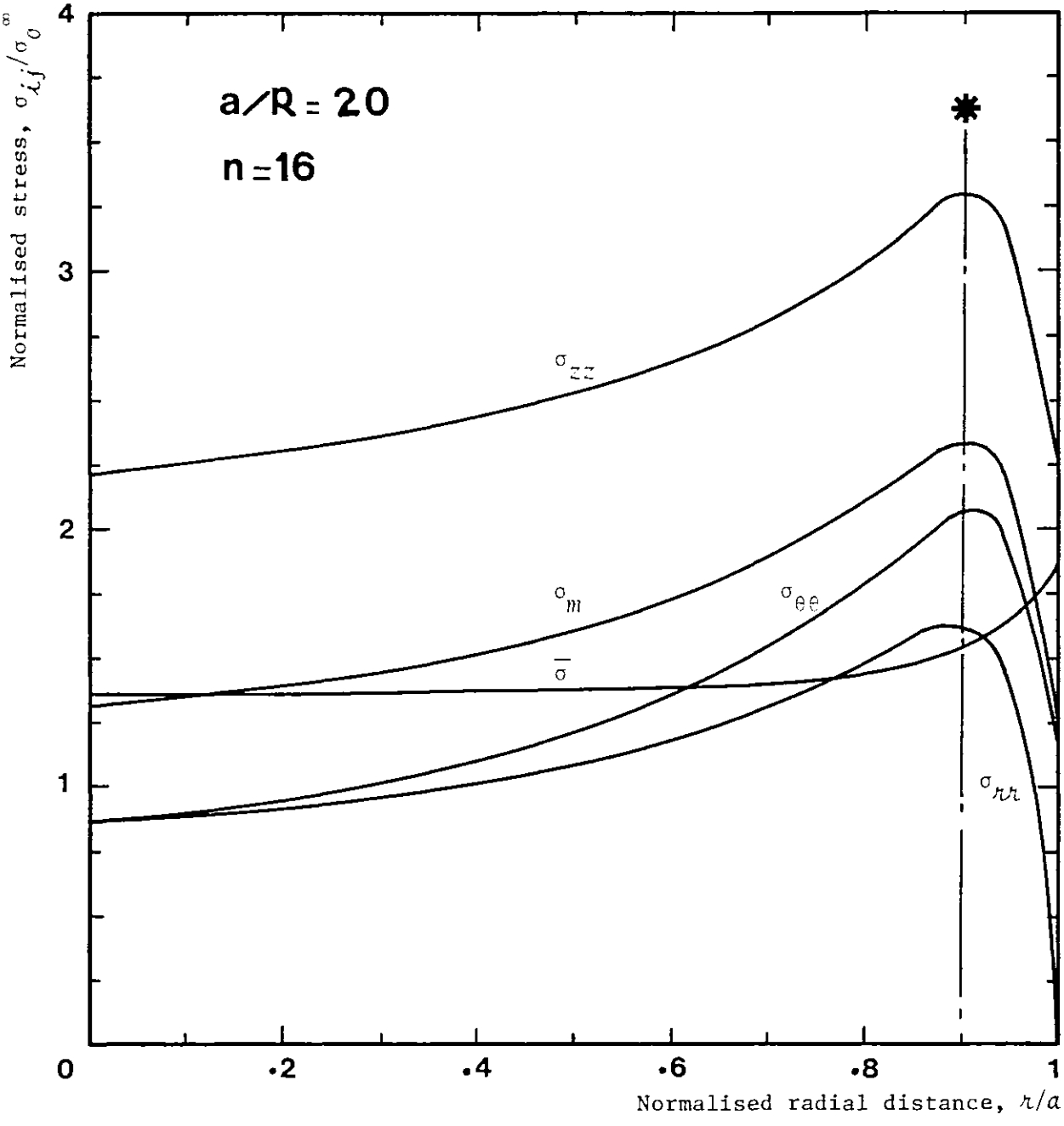

Figure 4.7: Stress distribution at steady-state across the throat of a notch with b/a = 1.67, a/R = 20 and for n = 16

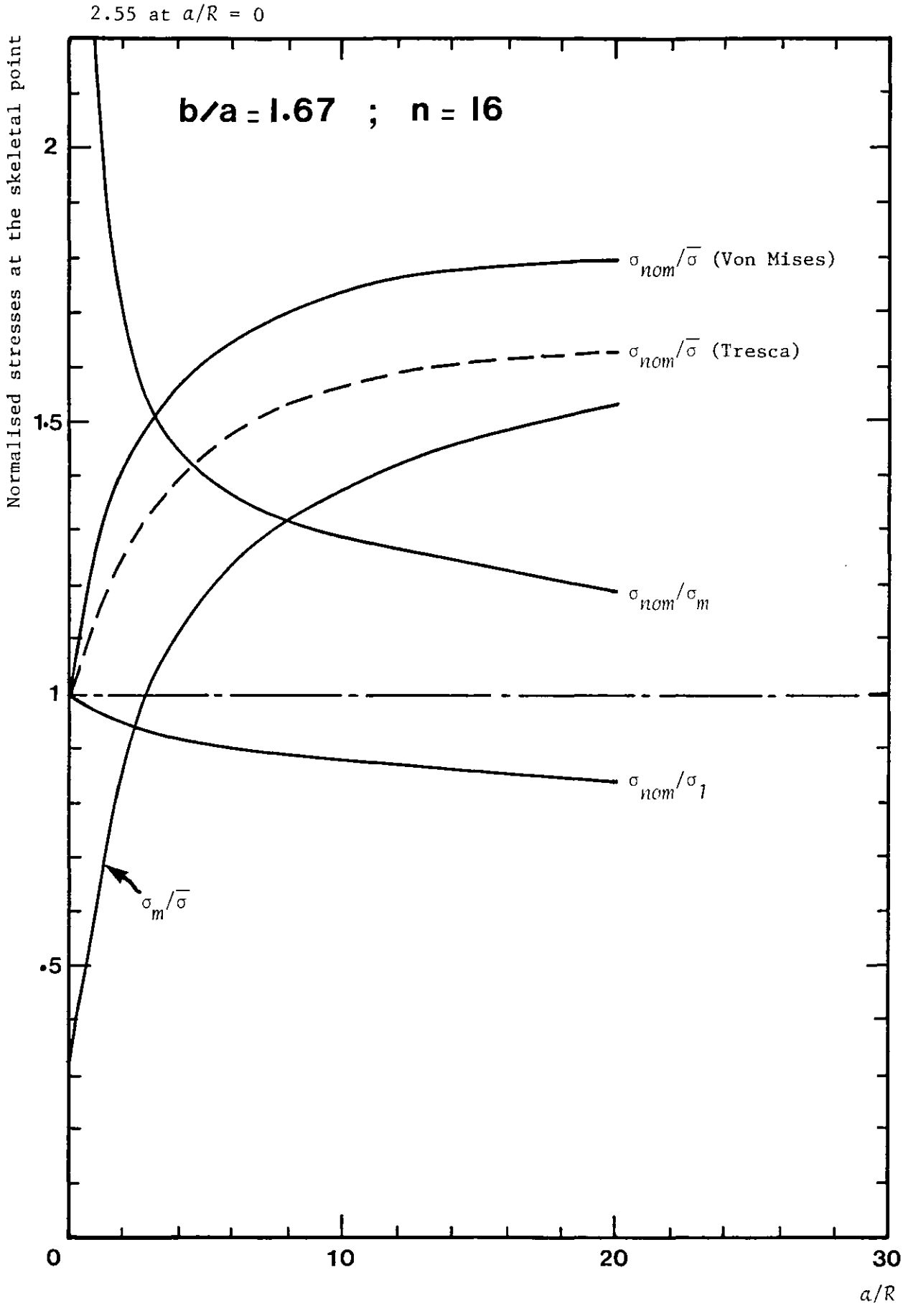

Figure 4.8: Dependence of the state of stress parameters at the skeletal point on notch sharpness for the notched geometries with b/a = 1.67 and for n = 16

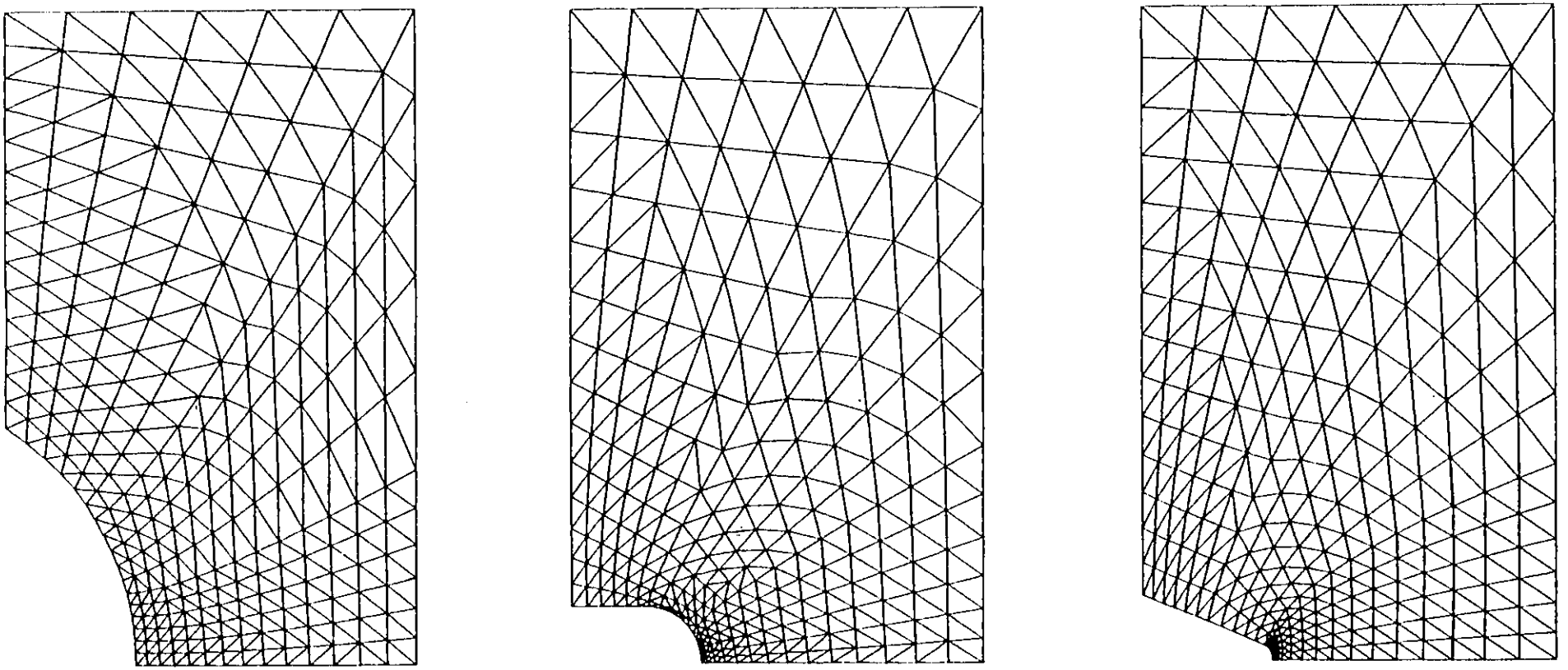

a_ $a/R = 1$ **b**_ $a/R = 5$ **c**_ $a/R = 32.5$

Figure 4.9: A selection of finite element meshes for the notch geometries with $b/a = 1.46$

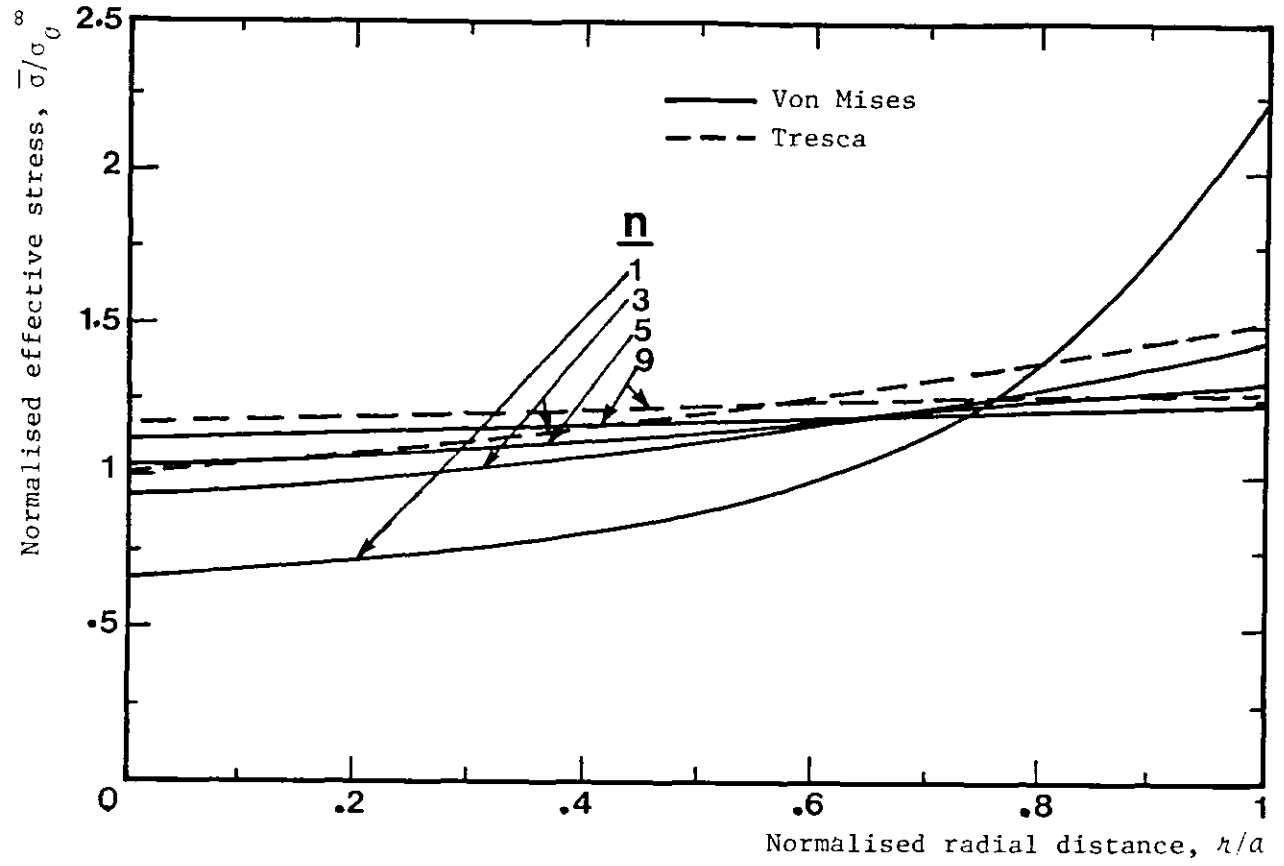

Figure 4.10: Effective stress distribution at steady-state across the throat of a notch with b/a = 1.46 and a/R = 1

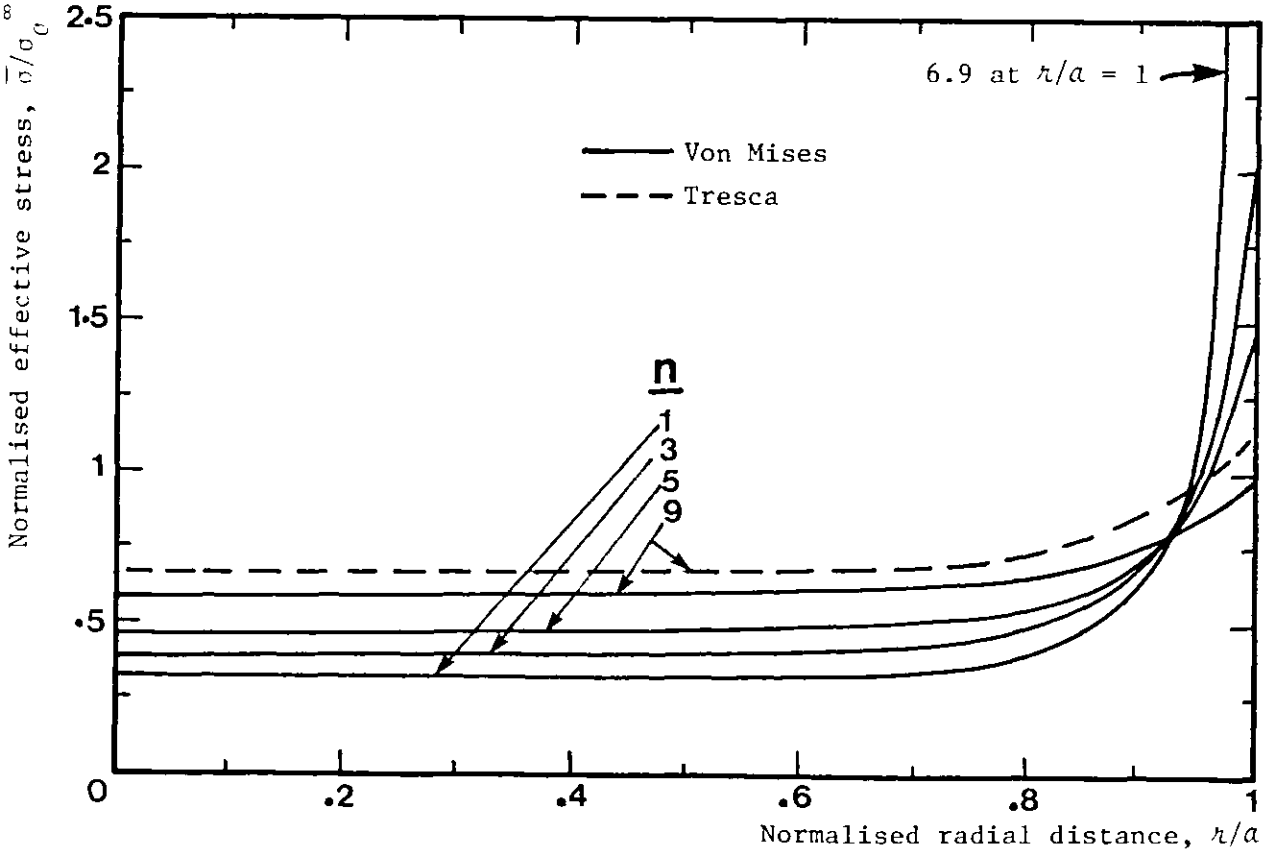

Figure 4.11: Effective stress distribution at steady-state across the throat of a notch with b/a = 1.46 and a/R = 32.5

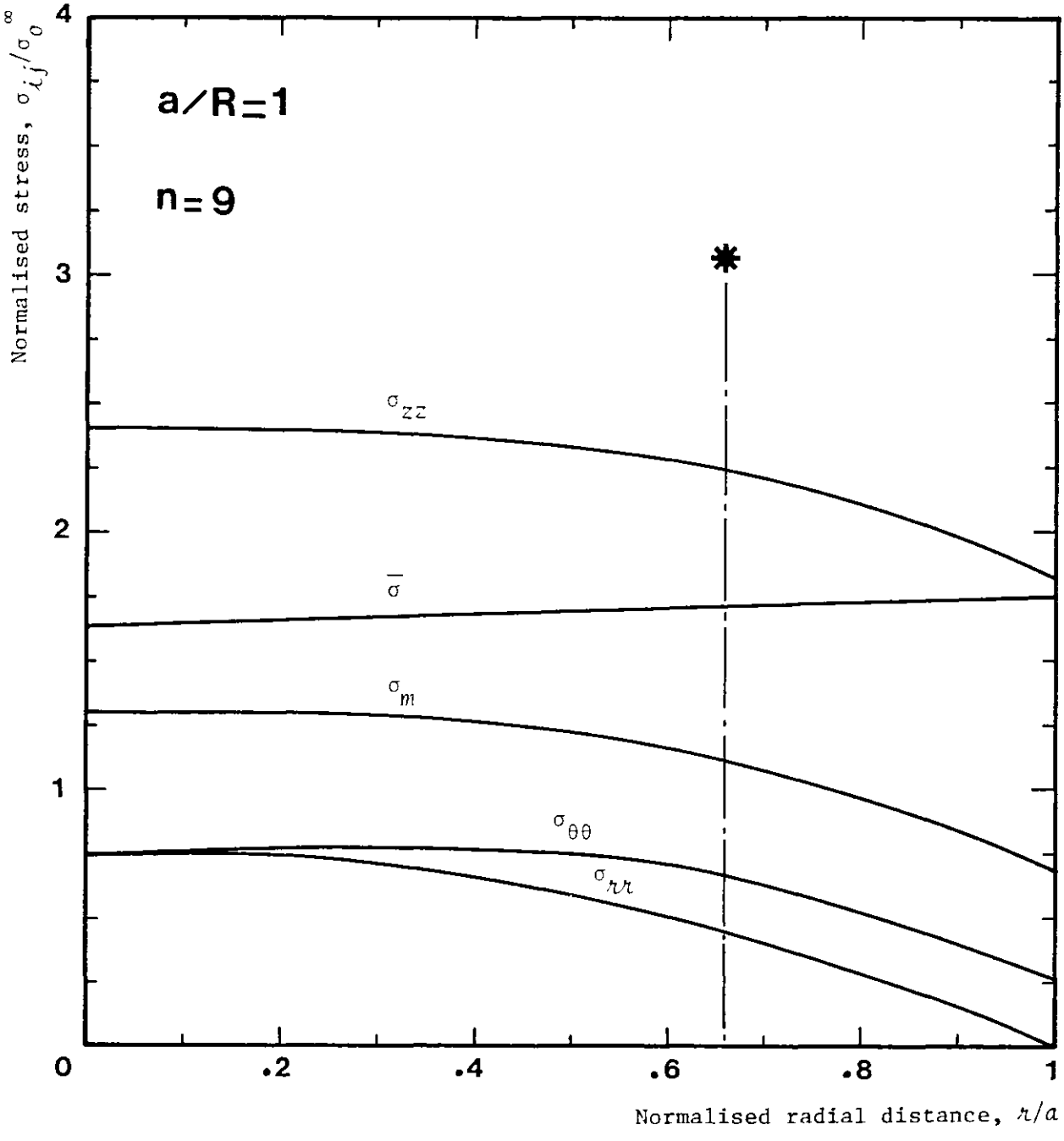

Figure 4.12: Stress distribution at steady state across the throat of a notch with b/a = 1.46, a/R = 1 and for n = 9

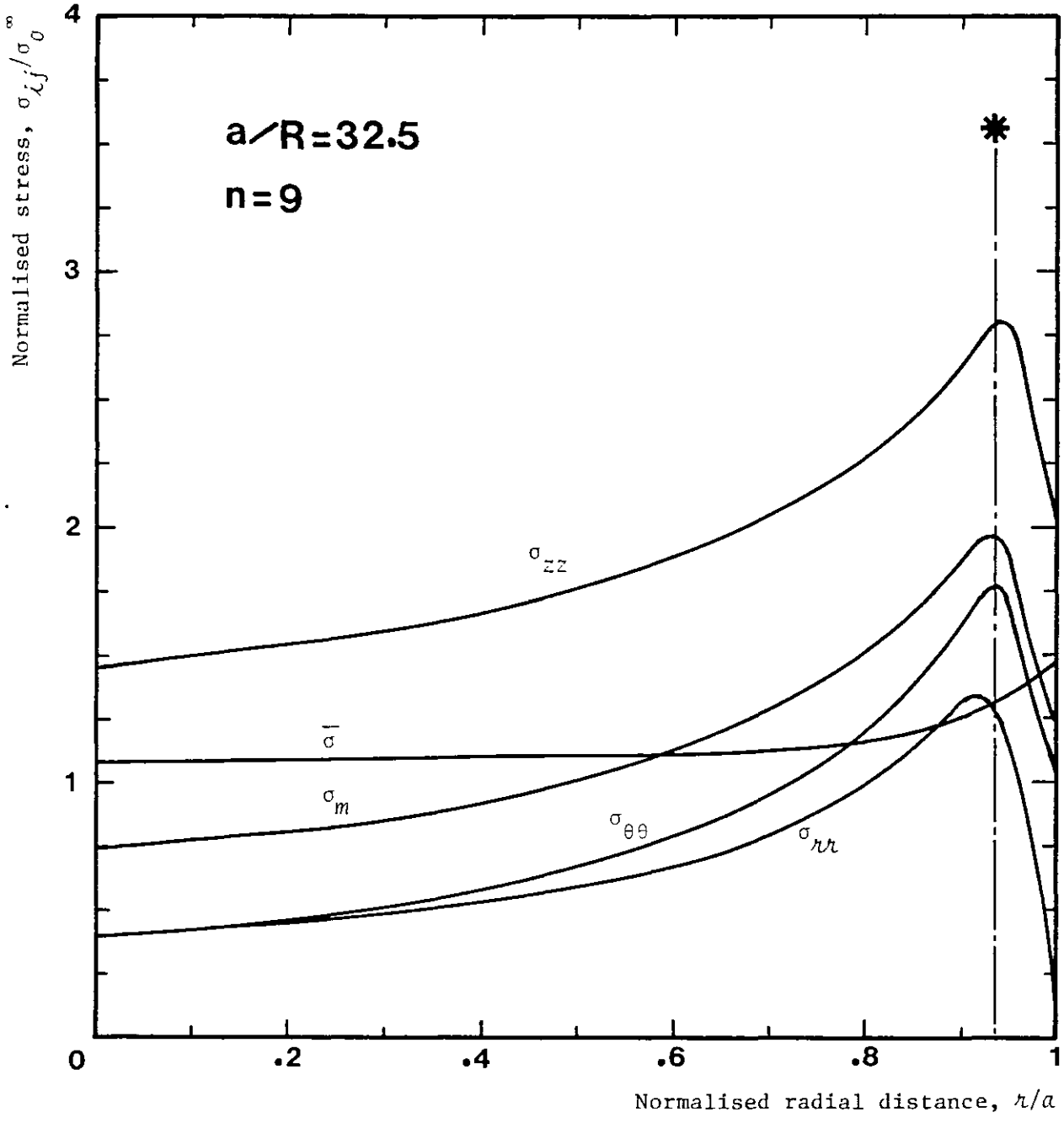

Figure 4.13: Stress distribution at steady-state across the throat of a notch with b/a = 1.46, a/R = 32.5 and for n = 9

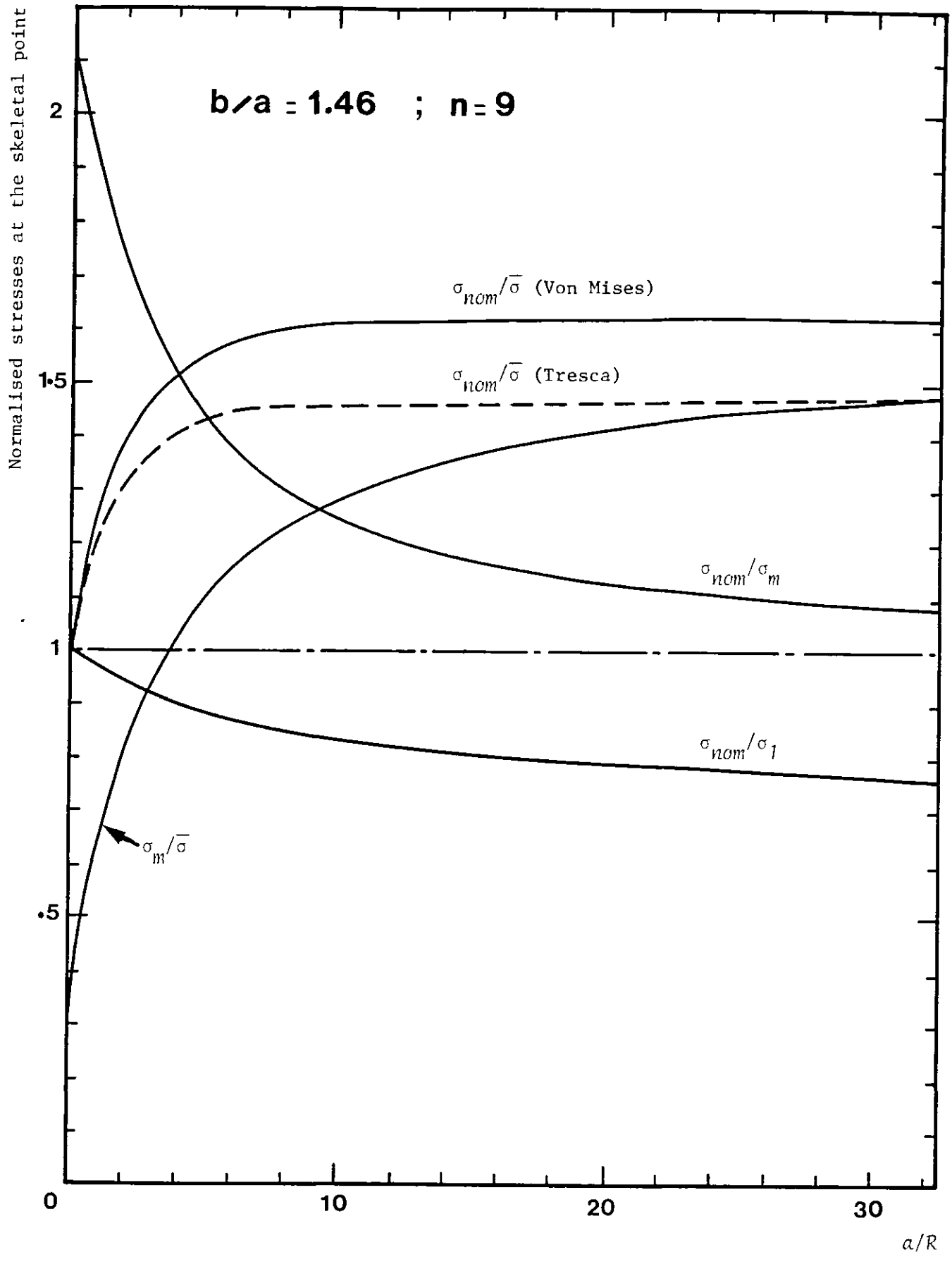

Figure 4.14: Dependence of the state of stress parameters at the skeletal point on notch sharpness for the notched geometries with b/a = 1.46 and for n = 9

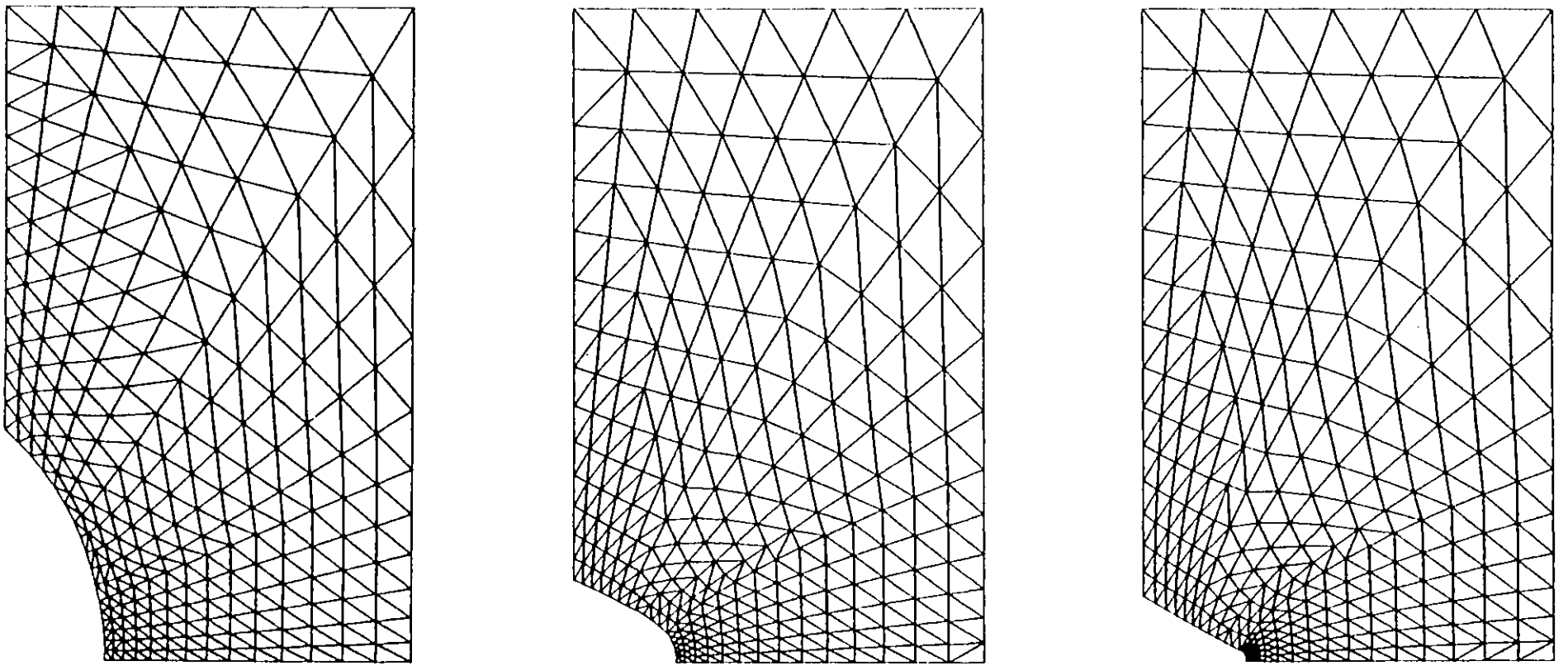

a_ a/R = 1 **b**_ a/R = 13.125 **c**_ a/R = 30

Figure 4.15: A selection of finite element meshes for the notch geometries with b/a = 1.33

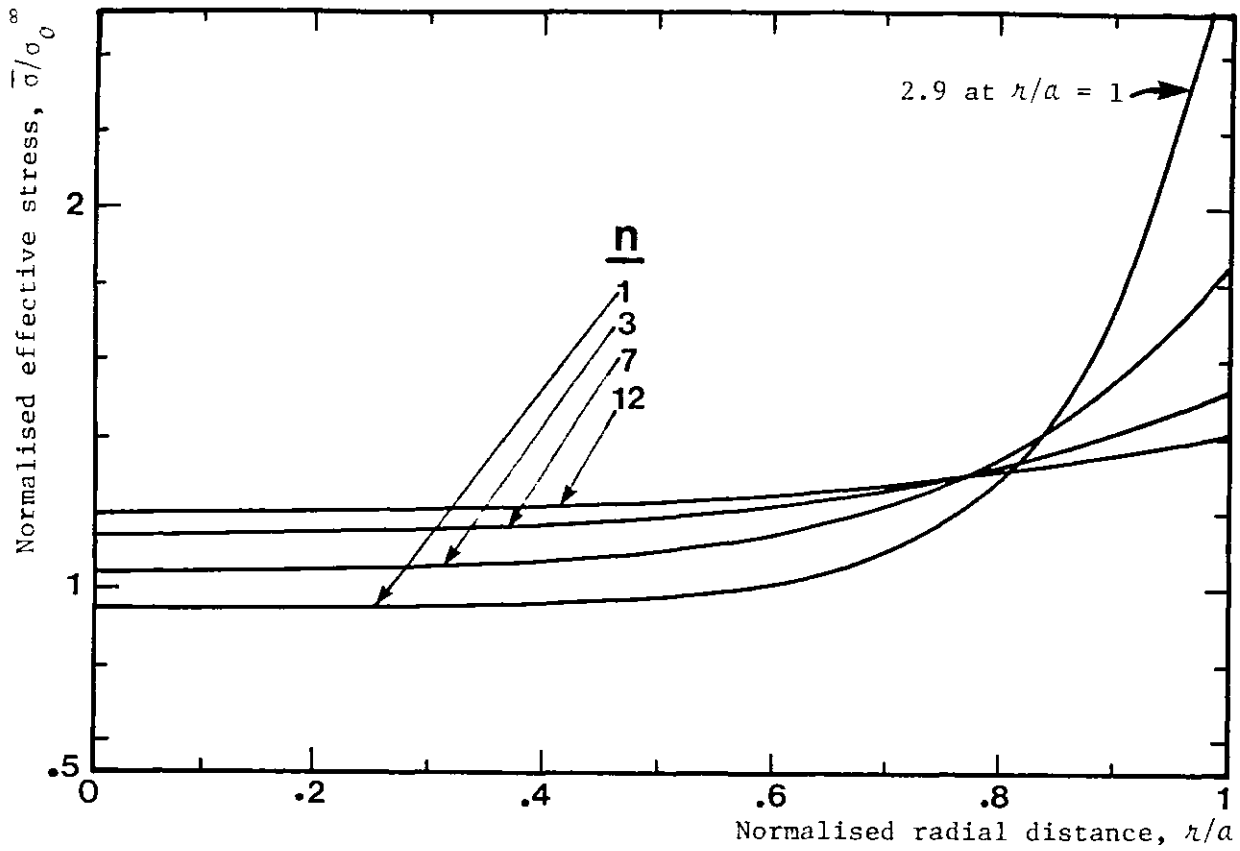

Figure 4.16: Effective stress distribution at steady-state across the throat of a notch with b/a = 1.33 and a/R = 3

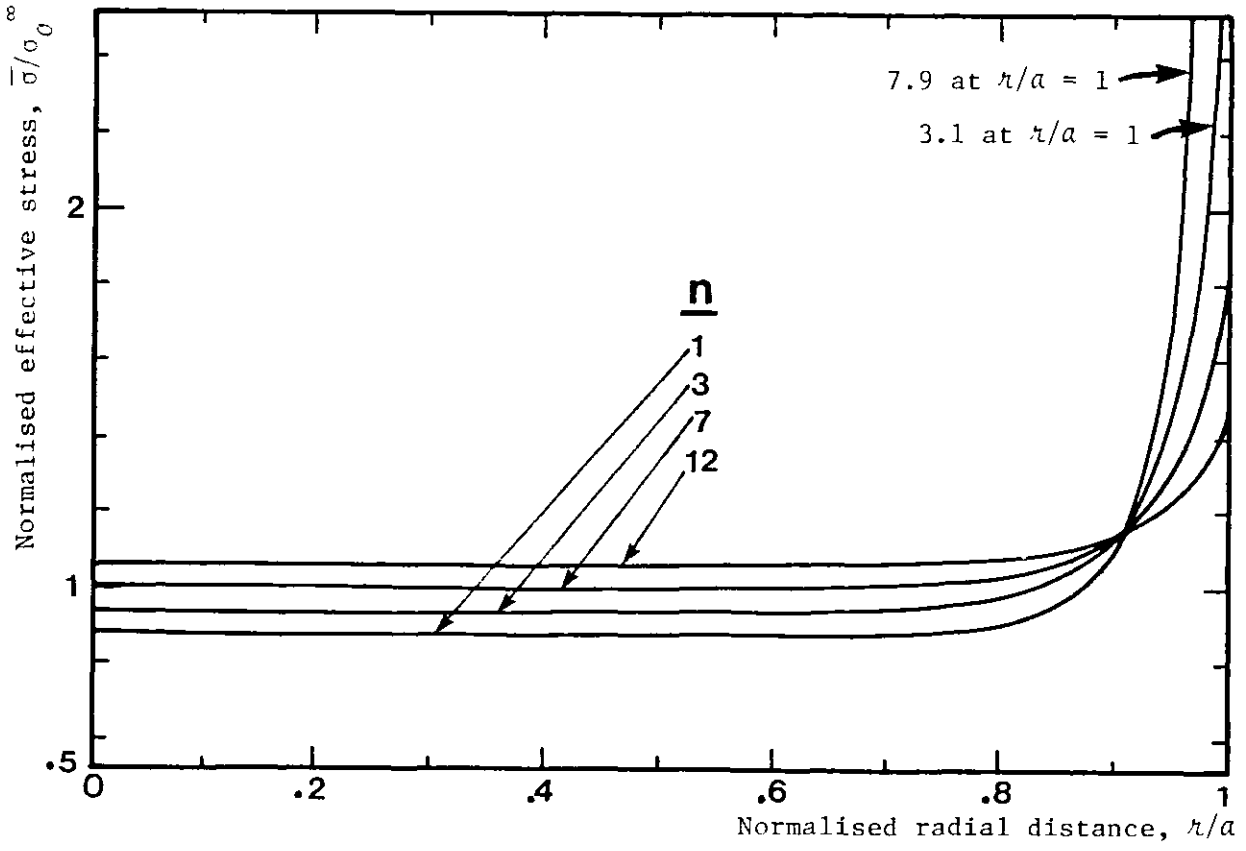

Figure 4.17: Effective stress distribution at steady-state across the throat of a notch with b/a = 1.33 and a/R = 30

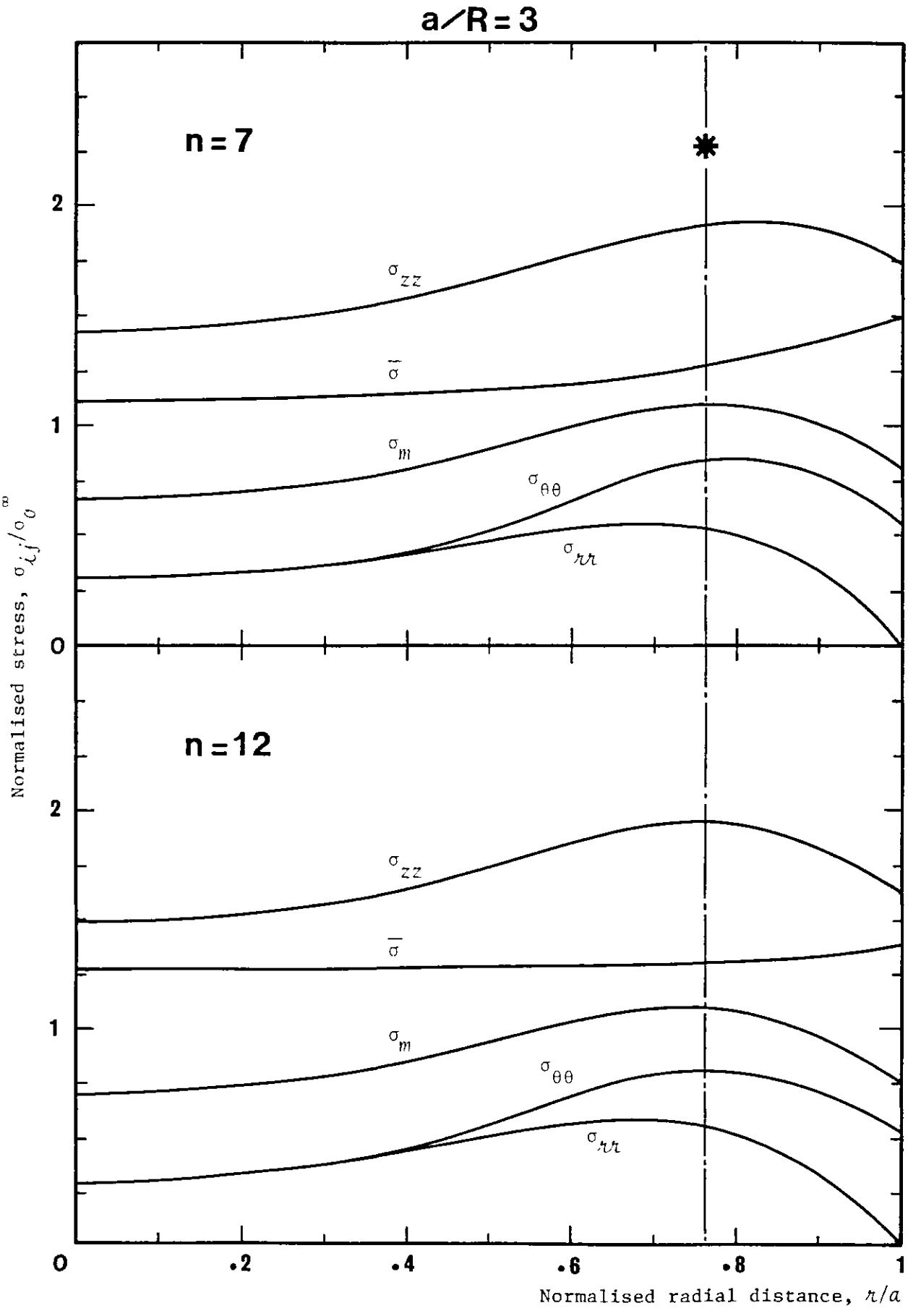

Figure 4.18: Stress distribution at steady-state across the throat of a notch with b/a = 1.33, a/R = 3 and for n = 7 and 12

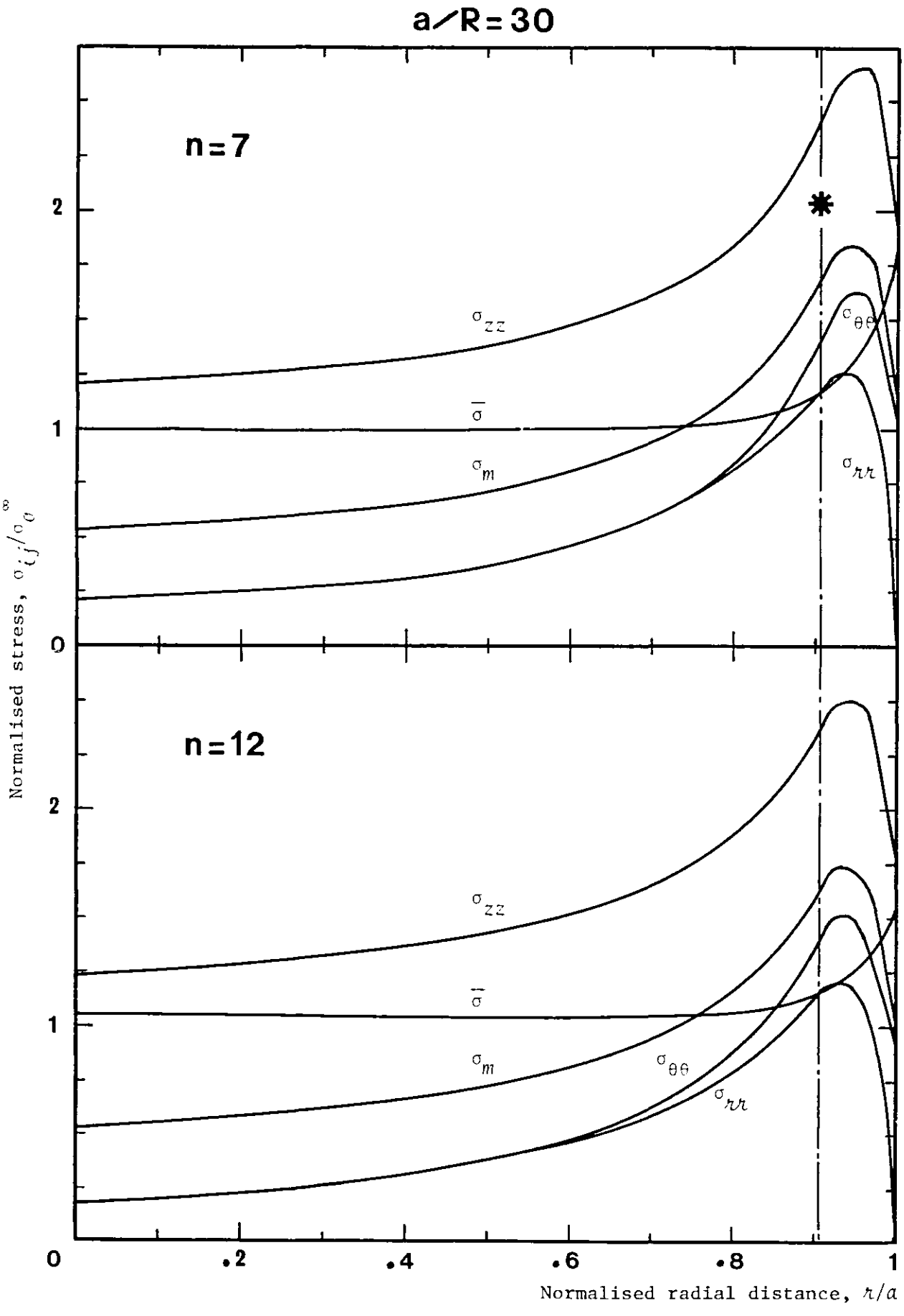

Figure 4.19: Stress distribution at steady-state across the throat of a notch with b/a = 1.33, a/R = 30 and for n = 7 and 12

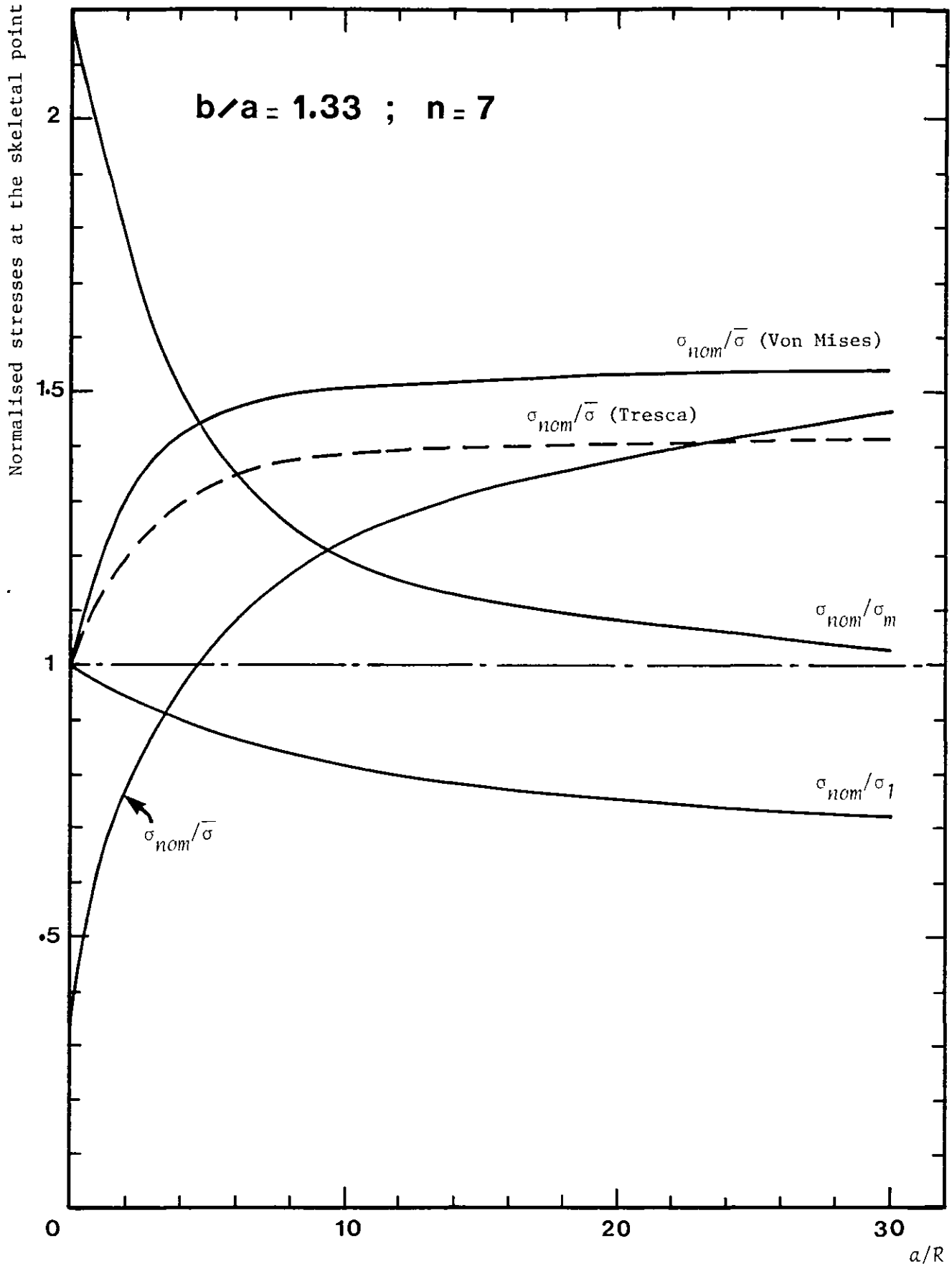

Figure 4.20: Dependence of the state of stress parameters at the skeletal point on notch sharpness for the notched geometries with b/a = 1.33 and for n = 7

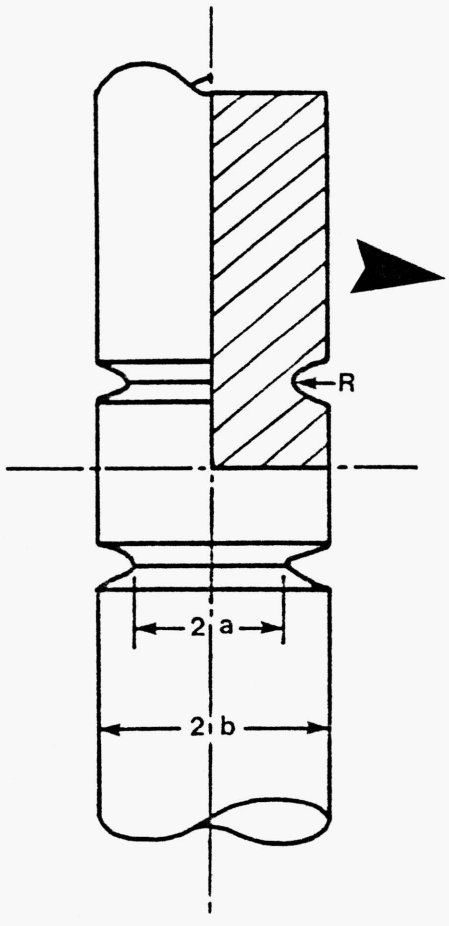

(a) A specimen with two notches

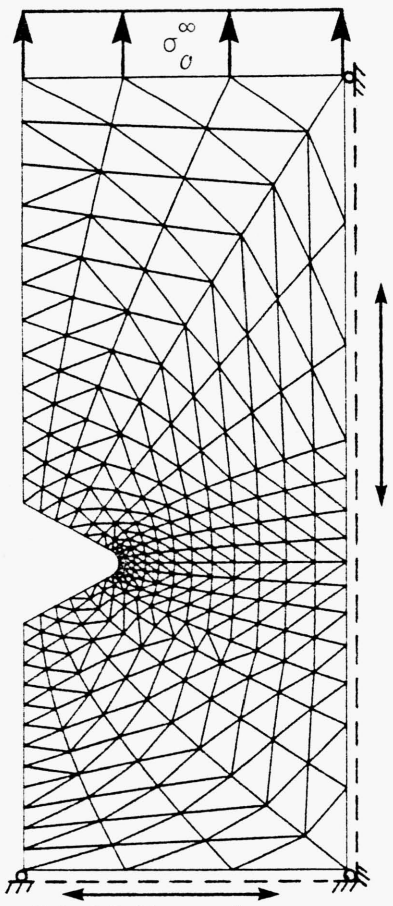

(b) BS V-notch

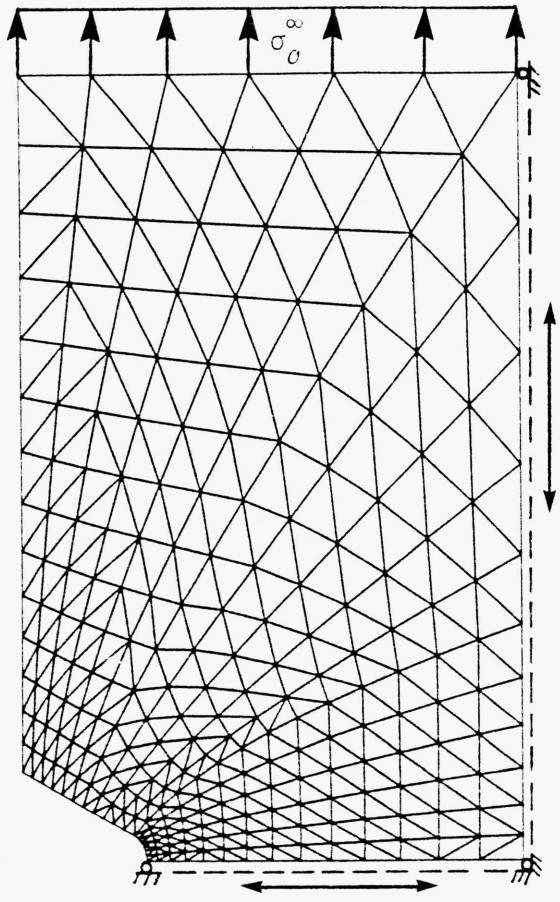

(c) Single BS V-notch, a/R = 18.18, b/a = 1.41

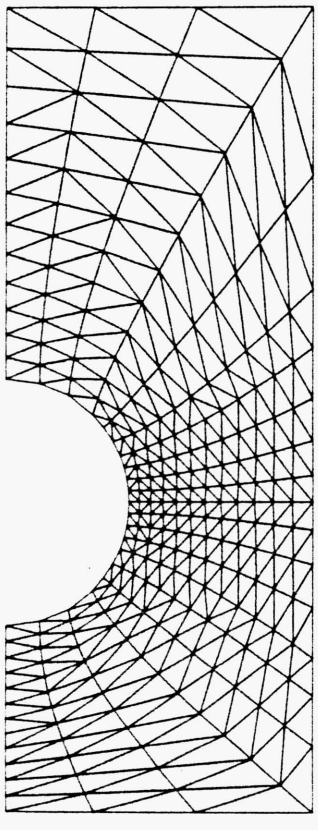

(d) Semi-circular notch, a/R = 1.5, b/a = 1.67

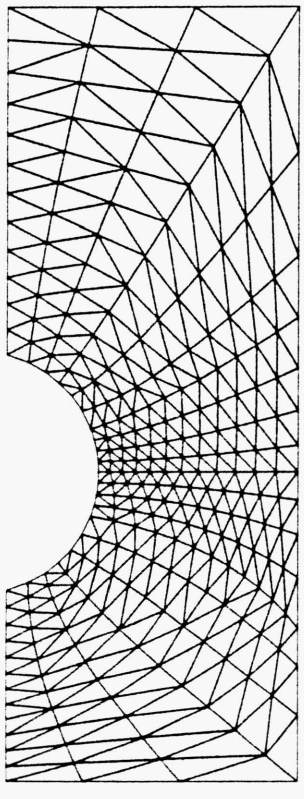

(e) A notch with a/R = 1.67, b/a = 1.46

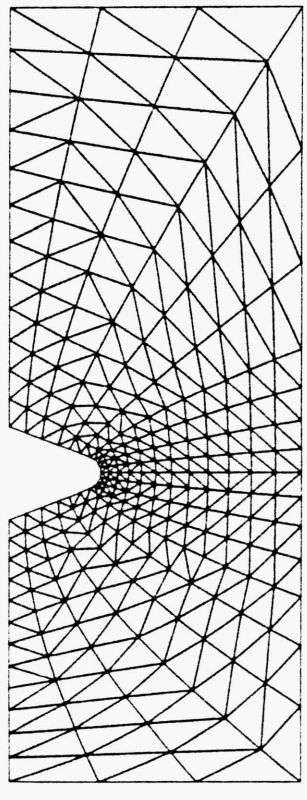

(f) A notch with a/R = 3, b/a = 1.46

Figure 4.21: Finite element meshes and their boundary conditions for round bars with two notches machined into their gauge length

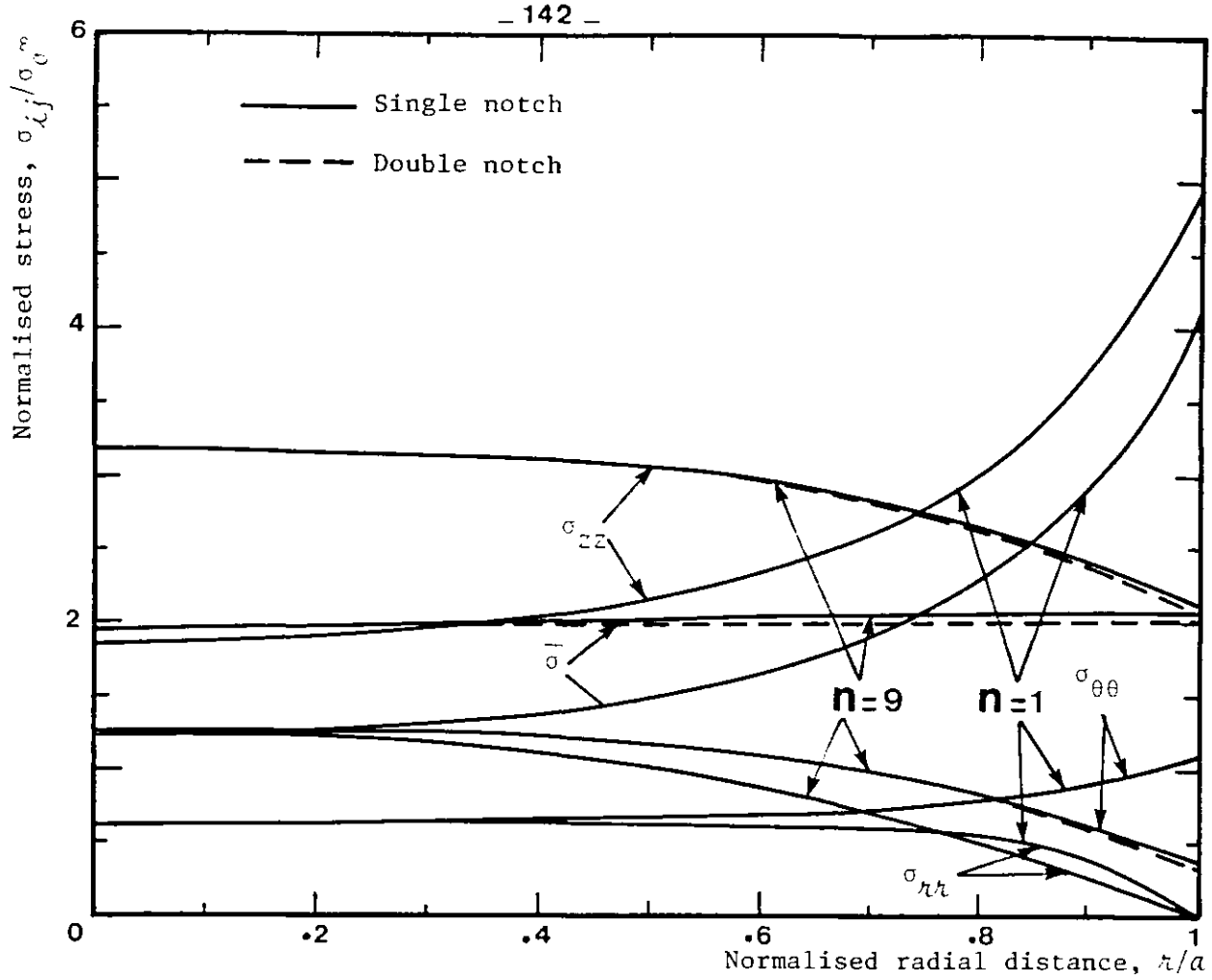

Figure 4.22: Stress distribution at steady-state across the throat of a single and double semi-circular notch with b/a = 1.67, a/R = 1.5 and for n = 1 and 9

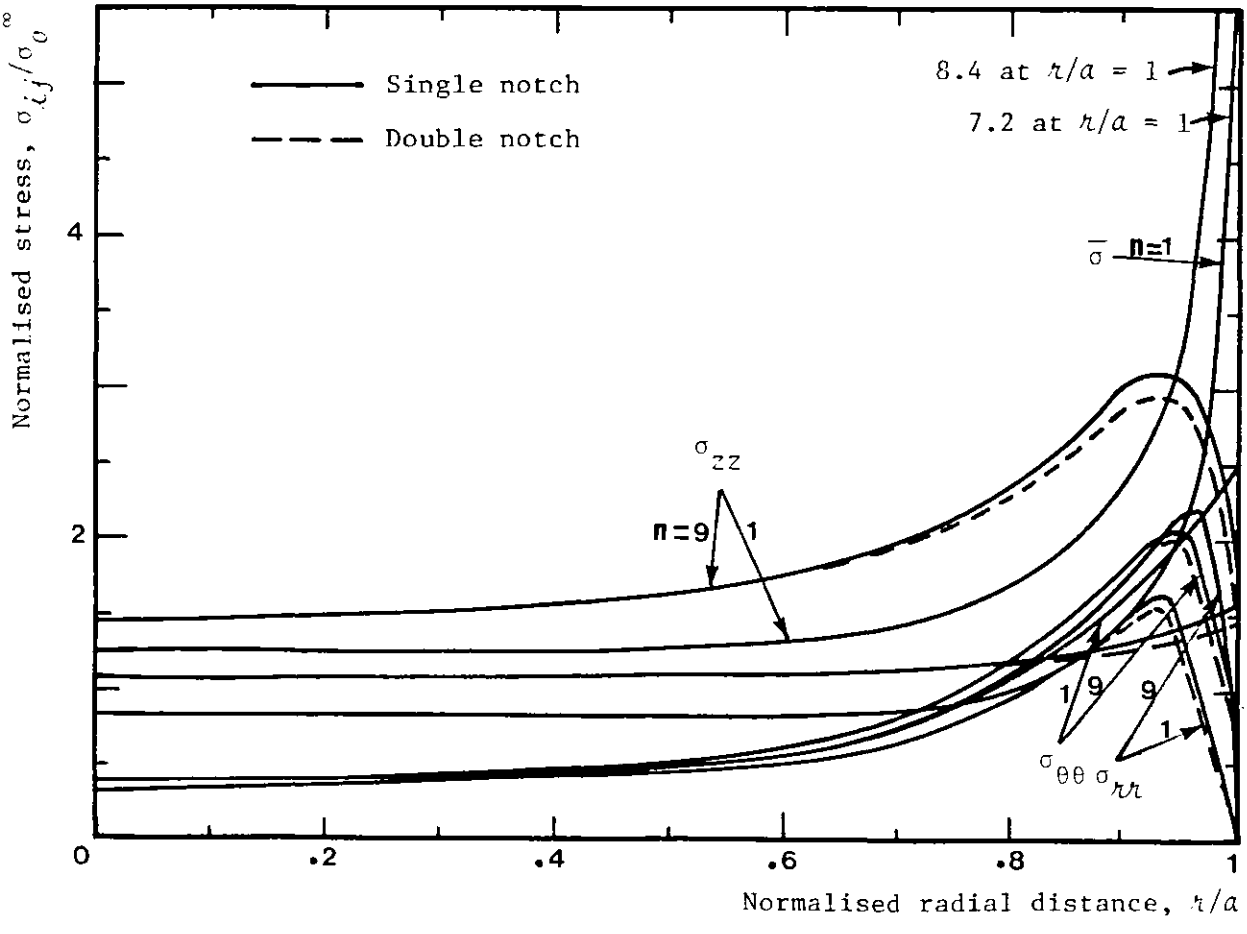

Figure 4.23: Stress distribution at steady-state across the throat of a single and double BS V-notch with b/a = 1.41, a/R = 18.18 and for n = 1 and 9

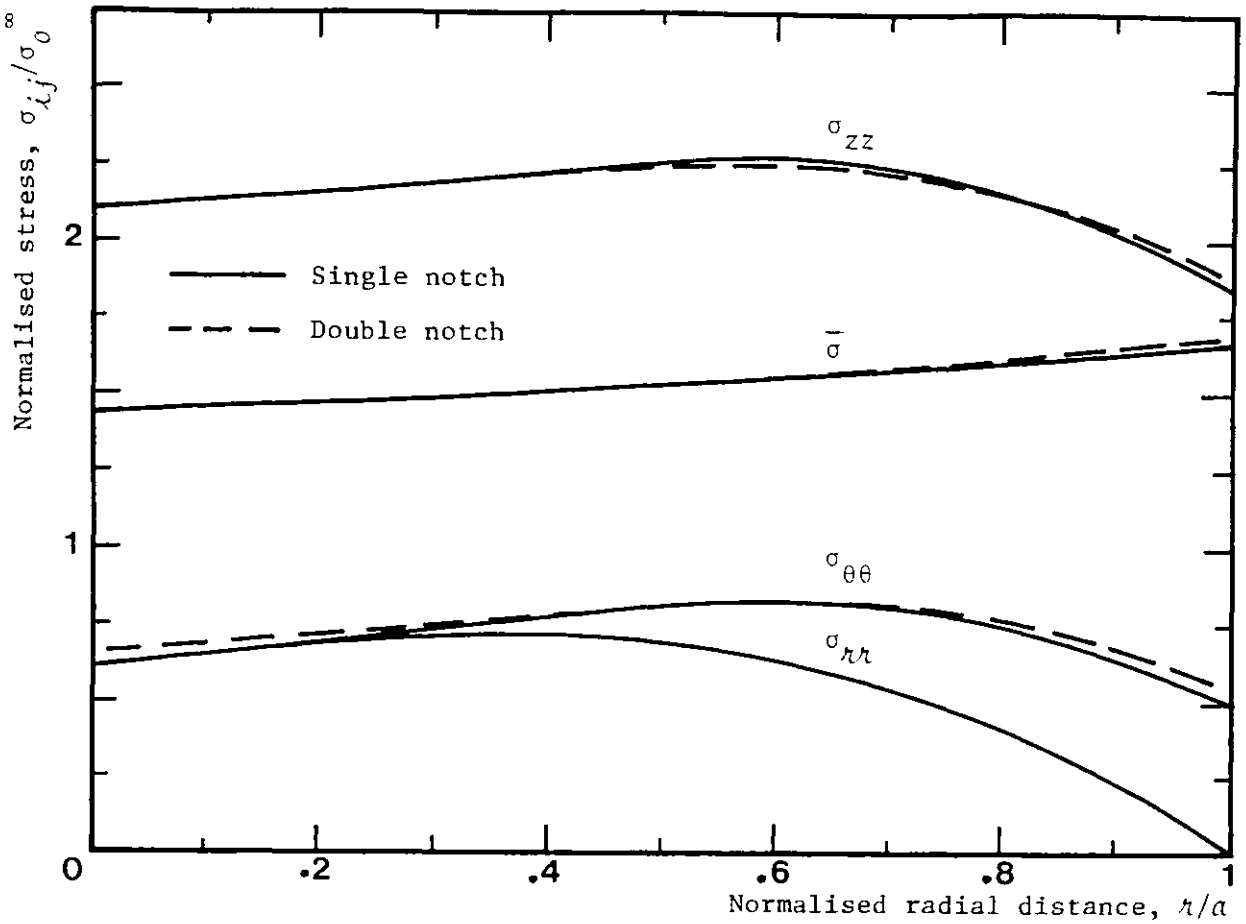

Figure 4.24: Stress distributions at steady-state across the throat of a single and double notched bar specimen with b/a = 1.46, a/R = 1.67 and for n = 9

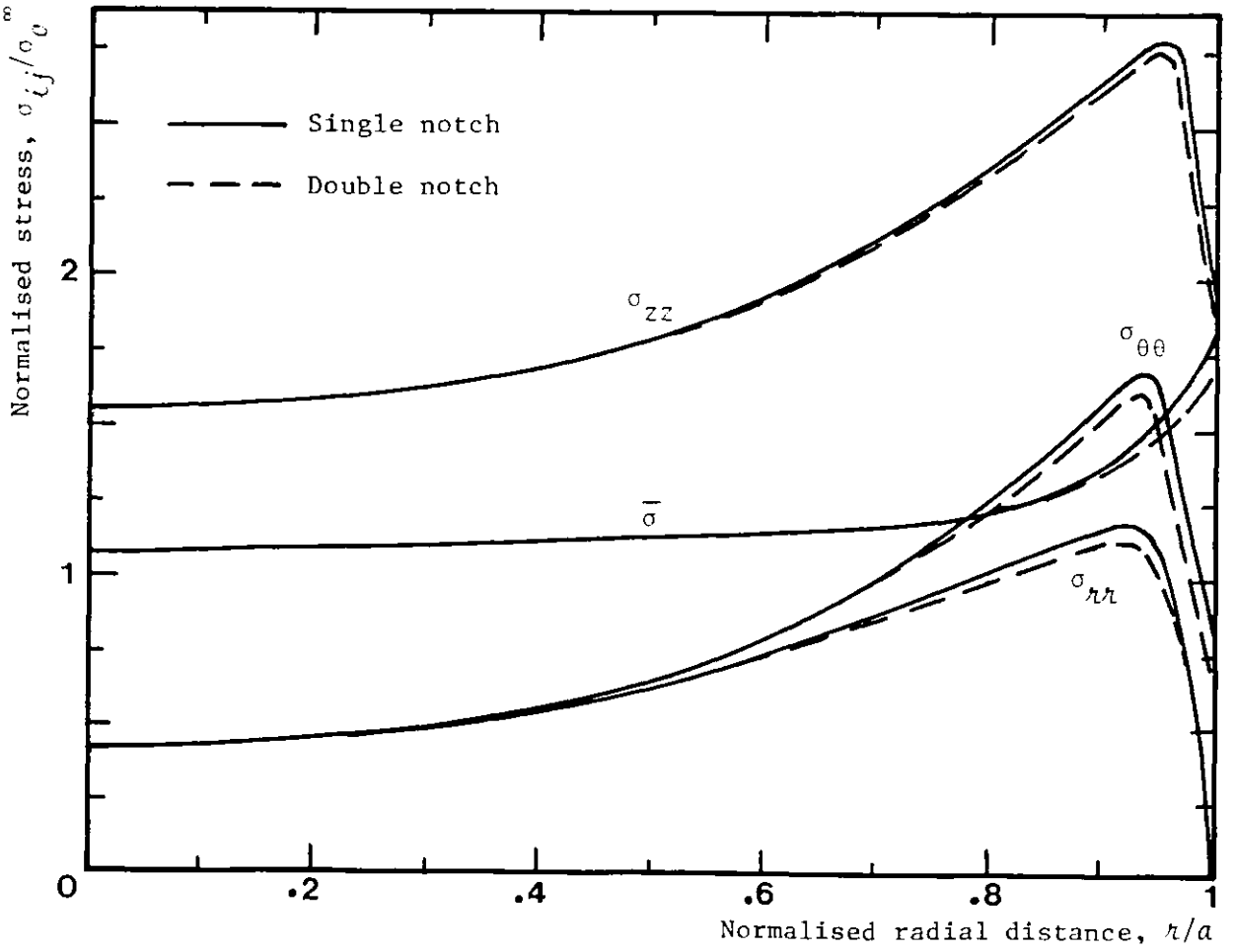

Figure 4.25: Stress distributions at steady-state across the throat of a single and double notched bar specimen with b/a = 1.46, a/R = 13 and for n = 9

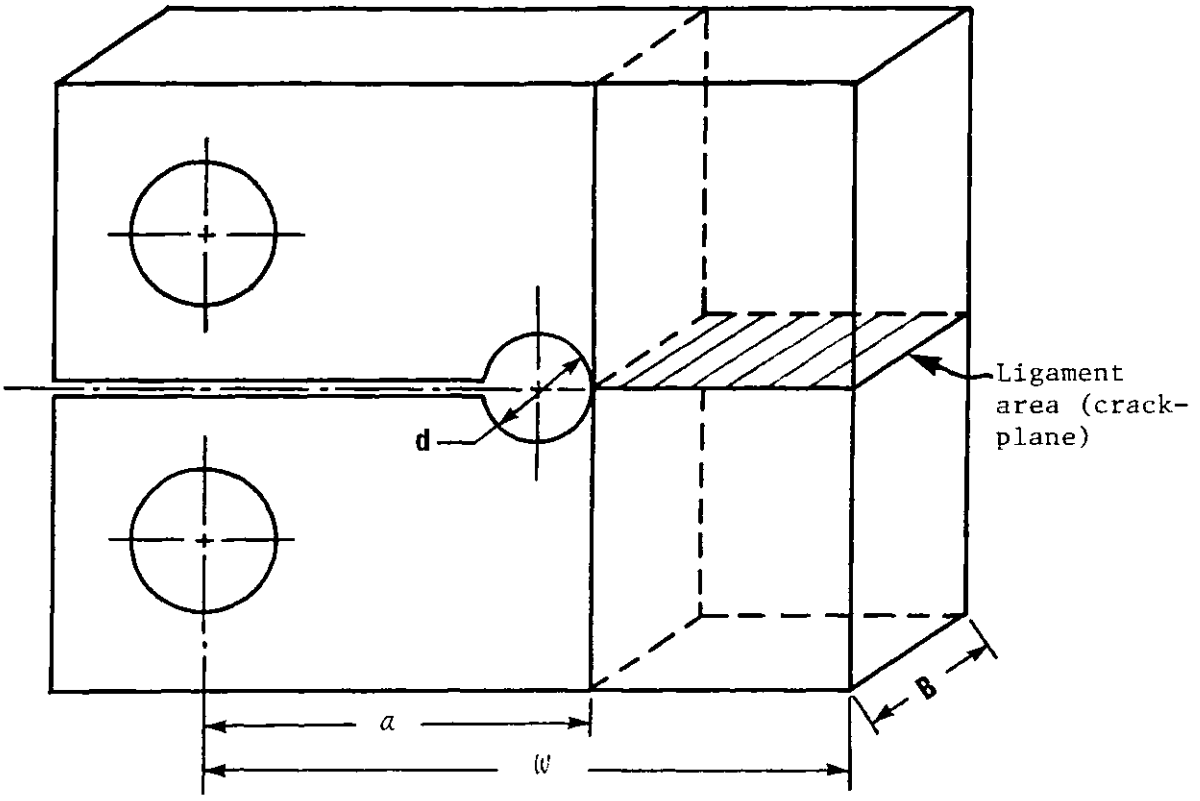

a_ Three-dimensional view of a compact tension specimen

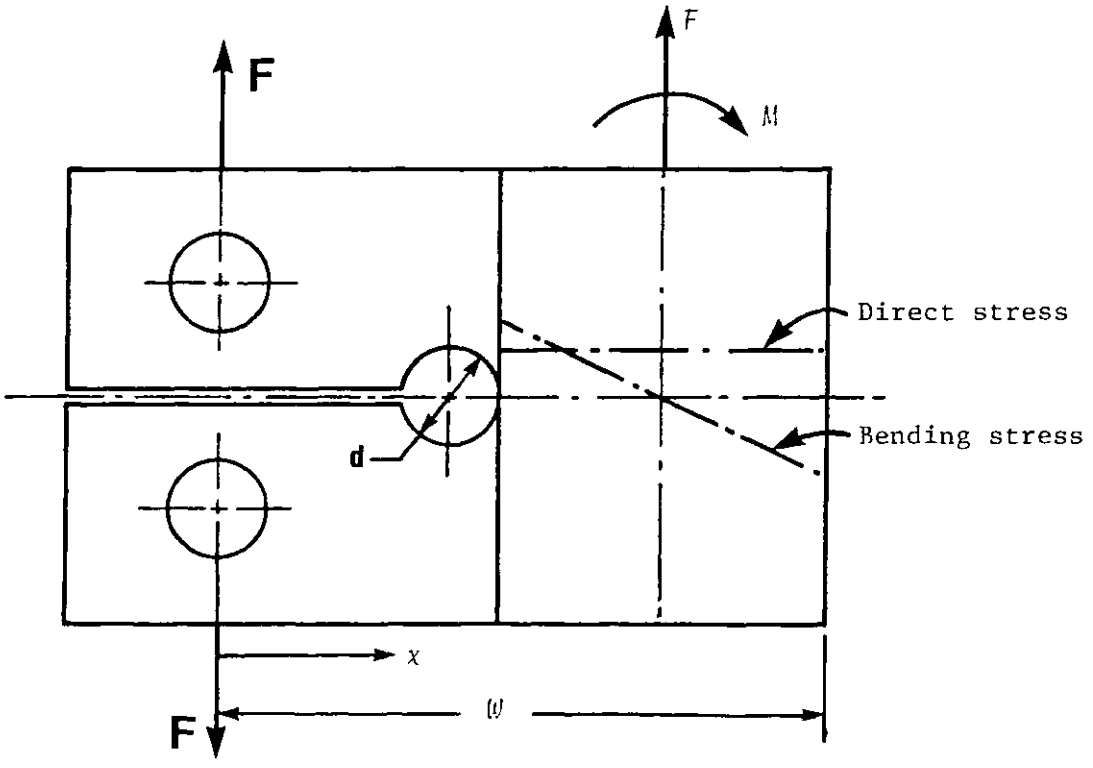

b_ Direct and bending stress distribution in ligament section of a compact tension specimen

Figure 4.26: Compact tension specimen

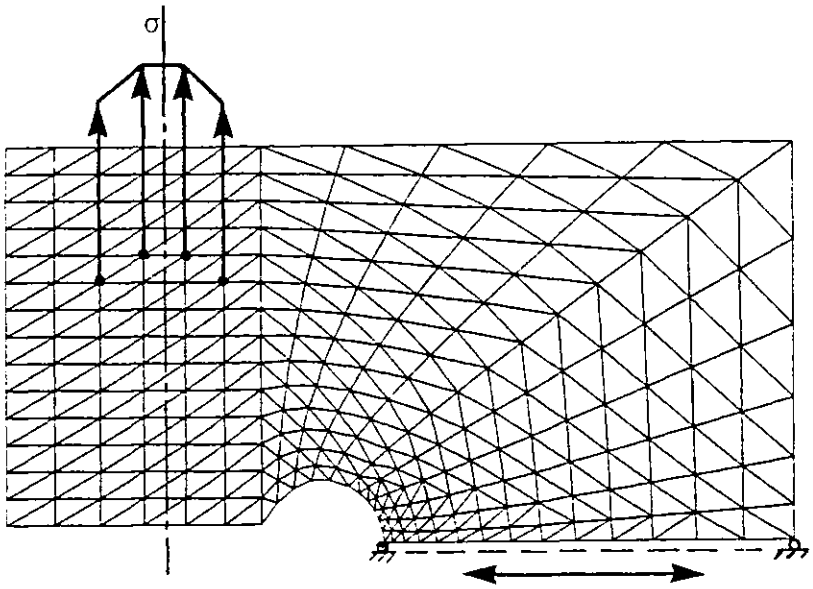

(a) $a/W = 0.2$

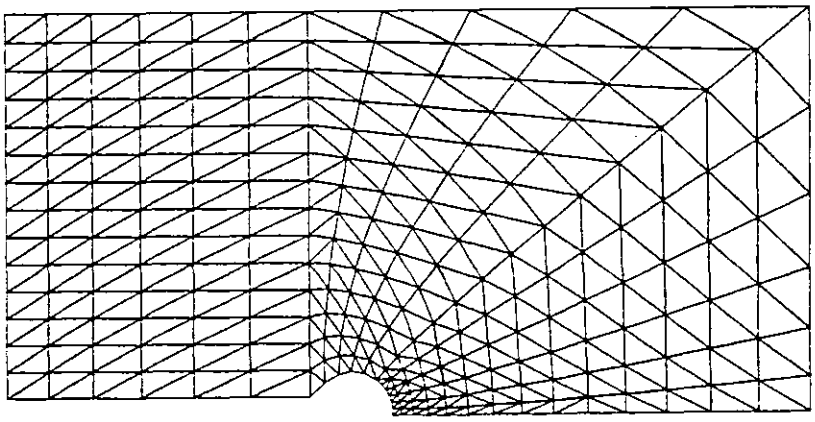

(b) $a/W = 0.133$

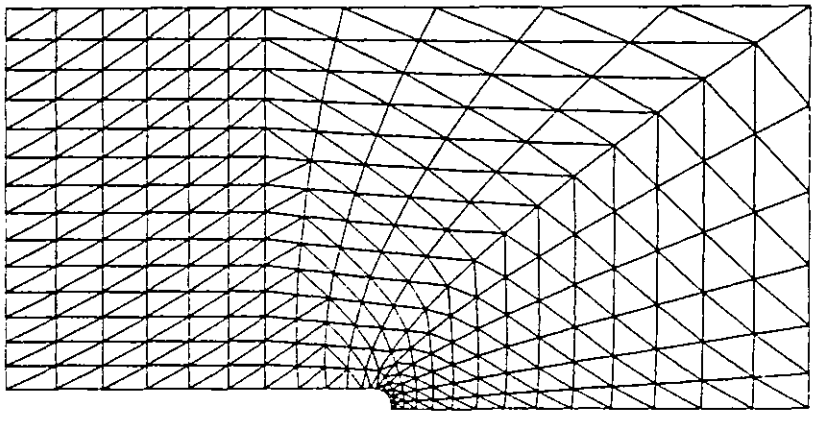

(c) $a/W = 0.066$

Figure 4.27: Finite element meshes and their boundary conditions for compact tension specimens

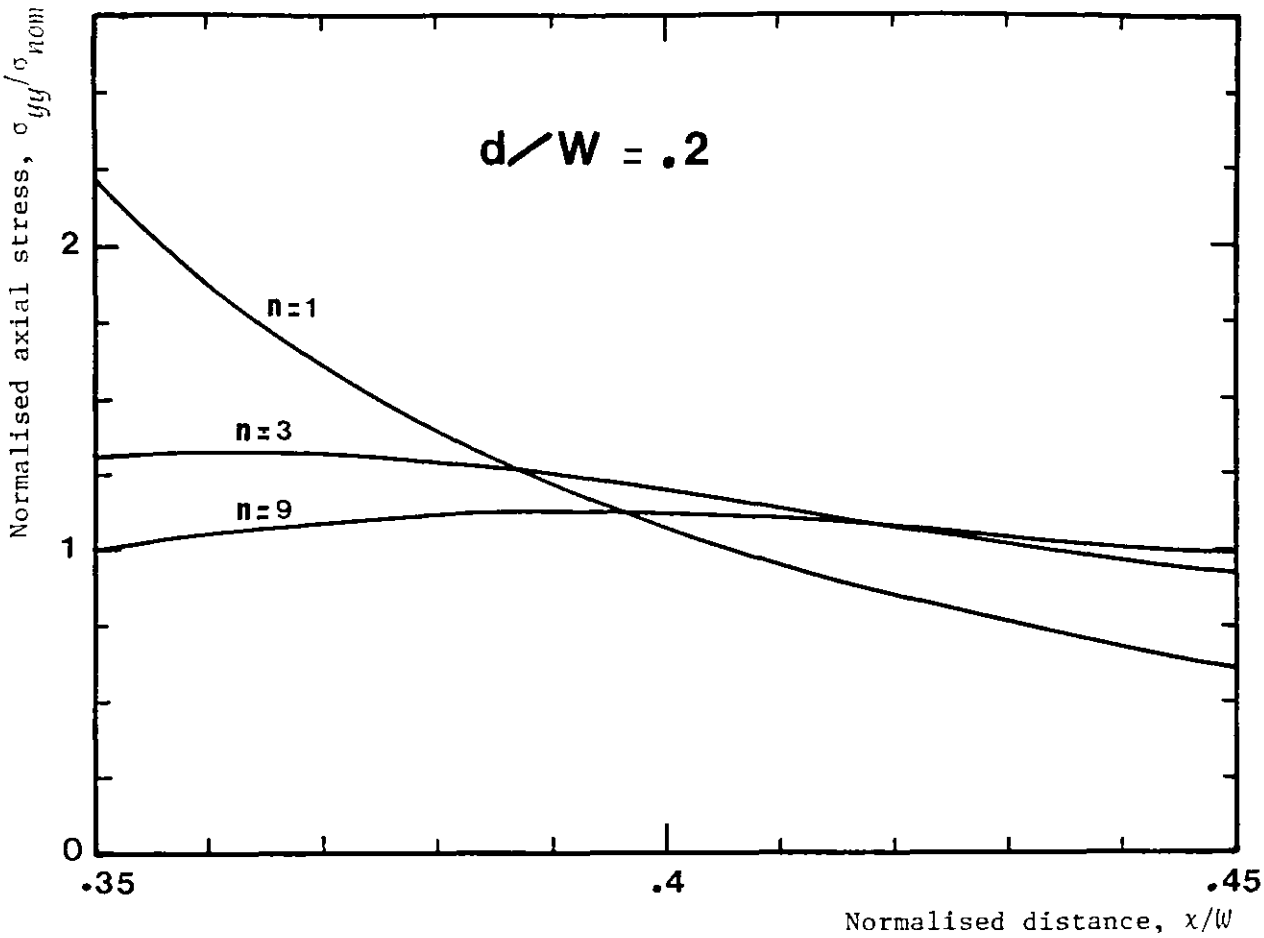

Figure 4.28: Axial stress distribution at steady-state across the crack plane for a compact tension specimen with $d/W = 0.2$

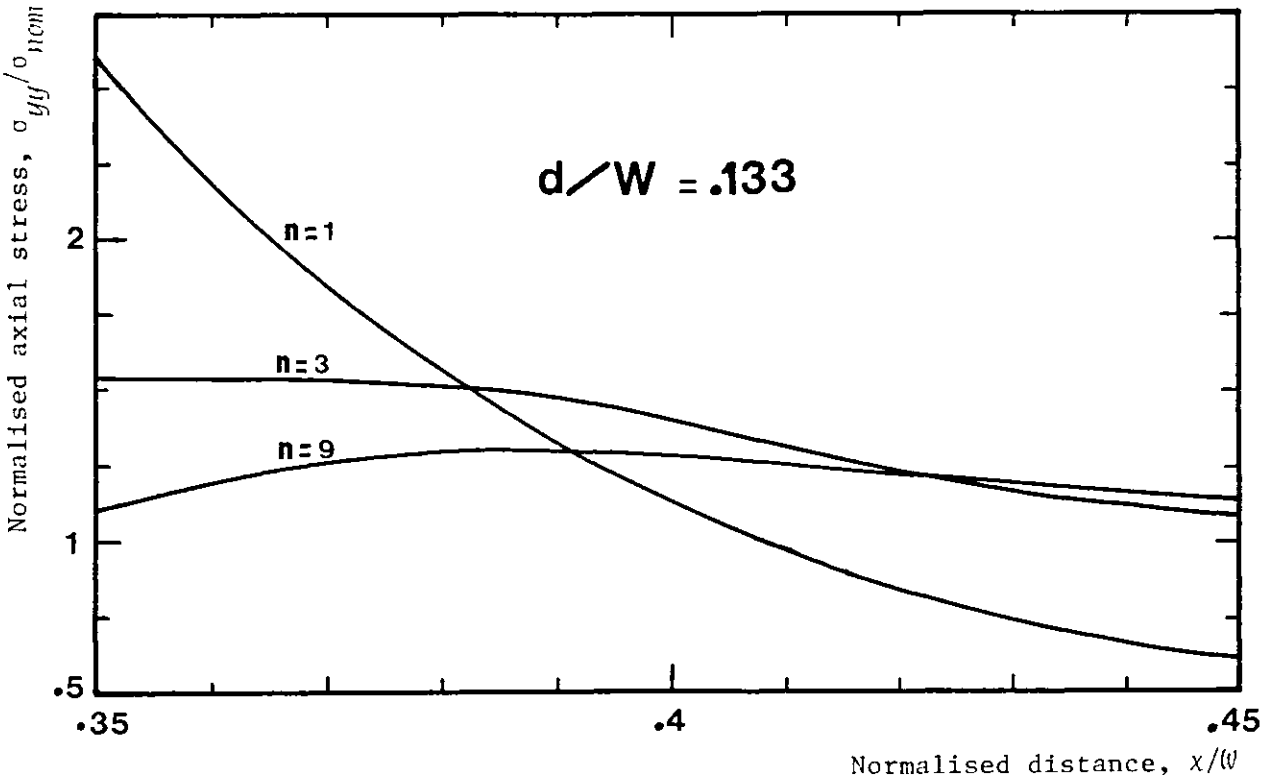

Figure 4.29: Axial stress distribution at steady-state across the crack plane for a compact tension specimen with $d/W = 0.133$

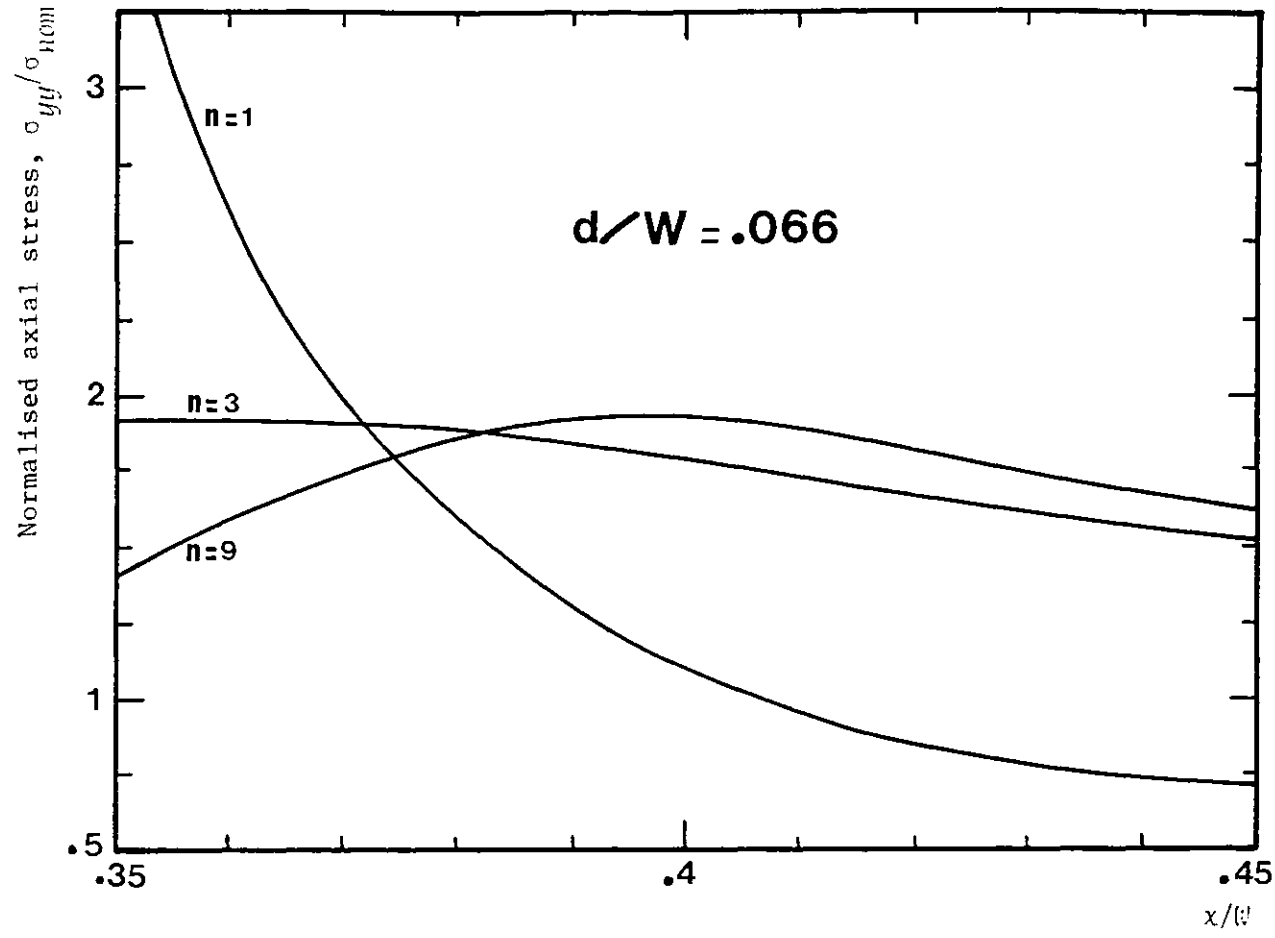

Figure 4.30: Axial stress distribution at steady-state across the crack plane for a compact tension specimen with d/W = 0.066

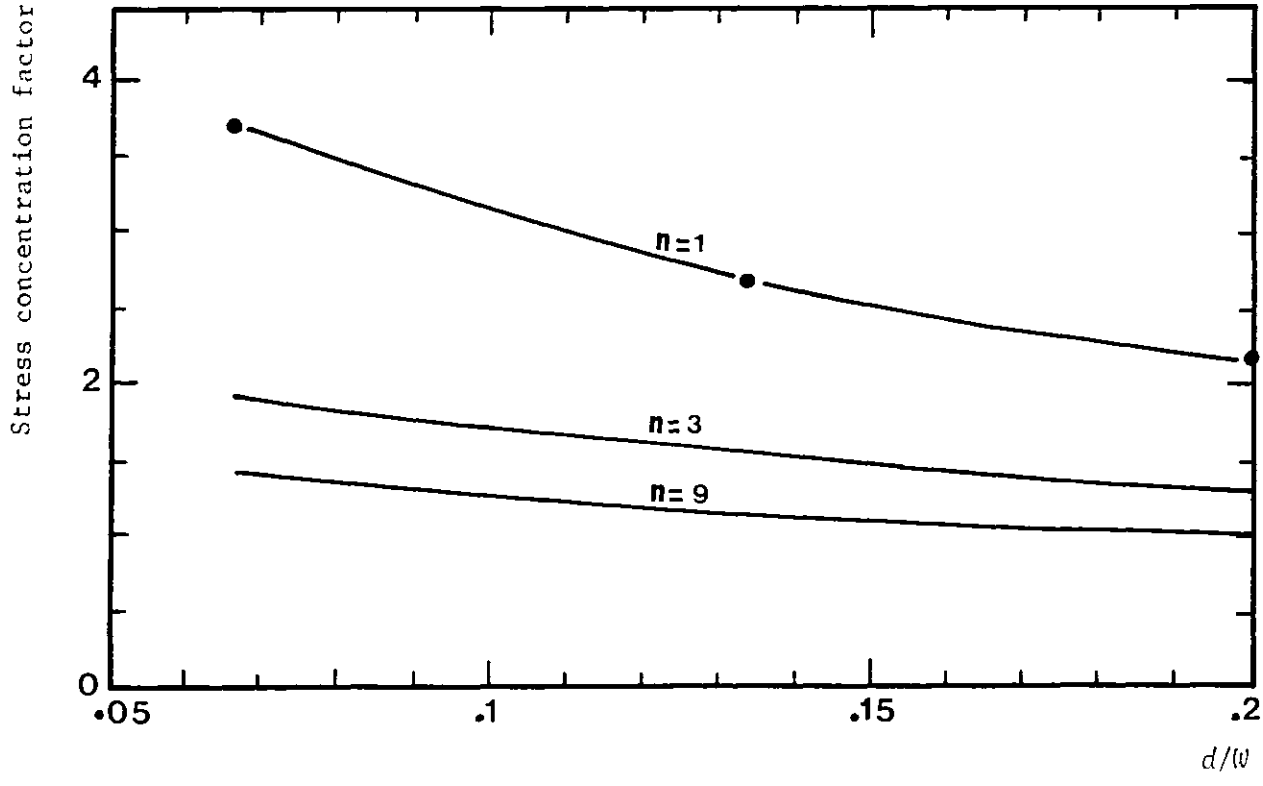

Figure 4.31: Stress concentration factor of compact tension specimen with different notch sharpness

CHAPTER 5

CONTINUUM MECHANICS AND MICROSTRUCTURAL PREDICTIONS OF NOTCH BAR BEHAVIOUR

5.1 INTRODUCTION

Continuum mechanics and microstructural laws describing the behaviour of components undergoing creep deformation which terminates in fracture were presented in Chapters 1 and 2. These laws can be used effectively to provide useful design information for an unlimited number of materials under different loading conditions.

In this chapter, the finite element predictions of state of stress parameters in the throat of the notched bar geometries investigated in Chapter 4 are used in continuum mechanics and microstructural approaches to predict the lives of these geometries. The analysis is based on the assumption that the stresses at the skeletal point determine the overall behaviour of these notched bars, provided that steady-state is achieved relatively early in life. An approximate method for calculating steady-state time scales in structures is also presented, based on the assumption that the maximum stress determines the overall structure behaviour.

5.2 AN APPROXIMATE METHOD FOR ESTIMATING THE GREATEST STRESS IN STRUCTURES SUBJECTED TO CREEP

Calladine [1963-1967] used an approximate method for interpolating for the greatest stress in structures between the limits $n = 1$ and $n \to \infty$, which corresponds to linear elastic and perfectly plastic materials, respectively. He investigated a wide range of problems such as beams, shells, plates, rotating discs, etc. The maximum effective stress for any value of n was normalised with respect to its corresponding elastic value. This new term was called the "relative stress concentration factor":

$$F = \frac{\bar{\sigma}_{max,n=n}}{\bar{\sigma}_{max,n=1}} \tag{5.1}$$

A series of graphs showing the variation of F with $m = 1/n$ were presented. These can be used to provide rapid design estimates of $\bar{\sigma}_{max}$ for any value of n, therefore pointing out the areas where local failure is possible.

5.2.1 Application to Notch Bar Geometries

The finite element effective stress distributions for the notched geometries investigated in Chapter 4 can now be used to produce a series of figures similar to those presented by Calladine. The effective stress is always a maximum at the notch root; therefore:

$$F = \frac{\bar{\sigma}_{max,n=n}}{k\,\sigma_0^{\infty}} \tag{5.2}$$

where k is the elastic effective stress concentration factor. For each b/a ratio, a graph of F against $1/n$ is plotted as shown in Figures 5.1 to 5.3. The figures indicate that $\bar{\sigma}_{max}$ decreases with increase in n in an approximately linear fashion for a fixed notch geometry. The decrease is greatest for the sharpest notches. Comparison is also made in Figures 5.1

to 5.3 with the Bridgman prediction of the effective stress across a notch throat for a rigid plastic material having $n = \infty$. The Bridgman analysis gives a constant effective stress since it is only dependent on the applied stress, σ_o^{∞}, and the notch geometry dimensions. Equation (4.5) can now be written as:

$$\bar{\sigma} = \bar{\sigma}_{max} = \frac{(b/a)^2 \, \sigma_o^{\infty}}{\{(1 + 2R/a) \ln (1 + a/2R)\}} \tag{5.3}$$

The values of $\bar{F}$ determined from this equation are shown on the vertical axes of Figures 5.1 to 5.3. The Bridgman equation predicts higher values than those from the computer calculations. This is due to the fact that the Bridgman analysis results in lower values of σ_{rr} and $\sigma_{\theta\theta}$ than the computer estimates, and hence a greater effective stress.

Conservative estimates of $\bar{F}$, using Bridgman's prediction for $n = \infty$ as a reference point, are possible. The dotted lines in Figures 5.1 to 5.3 are drawn by combining equations (5.2) and (5.3), thus giving the following linear relation between $\bar{F}$ and n:

$$\bar{F} = \frac{1}{n} + \frac{(1 + 1/n) \, (b/a)^2}{k \, (1 + 2R/a) \ln (1 + a/2R)} \tag{5.4}$$

Equation (5.4) gives good agreement with computer estimates for sharp notches, but increasingly conservative predictions for progressively blunter notches.

5.2.2 Approximate Time Scales for Stress Redistribution Due to Creep

A simple approximate formula has been proposed by Calladine [1969] to estimate the time taken for the stress to relax from its initial elastic to a final steady-state. The time scale is expressed in terms of the time taken for creep strain to become equal to a certain multiple of

the elastic strain in a constant stress creep test. The assumption used in the analysis was that the overall behaviour of a structure under creep conditions is dominated by the redistribution of the peak stress.

For materials in which the creep strain rate is proportional to the nth power of stress (equation (3.5)), Calladine showed that:

$$\delta(t) = \frac{1}{C\, n\, E\, \bar{\sigma}_{ss}^{(n-1)}} \ln \left(\frac{\sigma_o - \bar{\sigma}}{\bar{\sigma} - \bar{\sigma}_{ss}}\right) \qquad (5.5)$$

where E is Young's modulus, and $\bar{\sigma}_{ss}$ is the effective stress at steady-state. Using the assumption that $\bar{\sigma}_{max}$ dominates the overall behaviour and the time taken for stress relaxation to be 90% complete, equation (5.5) becomes:

$$\delta(t_{ss}) = \frac{2.3}{C\, n\, E\, \bar{\sigma}_{max}^{(n-1)}} \qquad (5.6)$$

For n typically in the range 5 to 10, it can be shown from equation (5.6) that the time to steady-state, t_{ss}, is approached when the maximum equivalent creep strain, $\bar{\varepsilon}_{max}$, is between, respectively, about $\frac{1}{2}$ and $\frac{1}{4}$ of the corresponding maximum elastic strain.

The iterative finite element method used in Chapter 4 to calculate the steady-state stress distributions for the various notch bar geometries cannot predict the time taken to achieve steady-state. However, Calladine's approximate equation (5.6) and the values of F in Figures 5.1 to 5.3 can be used as a useful design tool to predict notch behaviour, provided that stress redistribution is achieved rapidly. This will be discussed in more detail in Chapter 6.

5.3 CONTINUUM MECHANICS APPROACH TO PREDICT NOTCH STRENGTHENING AND WEAKENING

In this section, the steady-state finite element predictions of the state of stress parameters summarised in Chapter 4 (Figures 4.8, 4.14 and 4.20) for the various notch geometries investigated are used to predict notch strengthening and weakening (illustrated and discussed in Section 1.4.1) from a continuum mechanics approach.

Following the laws of plasticity under multi-axial stresses, it has generally been found that when shear processes predominate, the deformation rate under creep conditions is dictated by the effective stress, $\bar{\sigma}$, otherwise known as the second invariant stress. Those materials whose rupture lives are functions of $\bar{\sigma}$ only exhibit little or no cracking, except in regions adjacent to the fracture. It has also been found that the rupture lives of some materials are functions of the maximum principal tensile stress, σ_1, only. They exhibit spatially homogeneous grain boundary cracking which gradually accumulates during tertiary creep (Johnson, et al. [1962], Hayhurst [1972], and Cane [1980]).

Two continuum mechanics models can now be proposed to predict notch strengthening and weakening, based on the assumption that creep rupture under multi-axial conditions is either controlled by deformation which is dependent on $\bar{\sigma}$ only, or by crack propagation dictated by σ_1.

5.3.1 Calculations

Starting from the secondary creep equation:

$$\dot{\bar{\varepsilon}}_s = \dot{\varepsilon}_o \left(\frac{\bar{\sigma}}{\sigma_o}\right)^n \tag{5.7}$$

the rupture time for a uni-axial specimen subjected to a constant stress, σ_o, is:

$$t_{un} = \frac{\varepsilon_R}{\dot{\varepsilon}_o} \tag{5.8}$$

where $\dot{\varepsilon}_o$ is the minimum creep rate which corresponds to the applied stress, σ_o.

For a notched specimen, the rupture time is:

$$t_{no} = \frac{\varepsilon_R}{\dot{\varepsilon}_o} \left(\frac{\sigma_o}{\bar{\sigma}}\right)^n \tag{5.9}$$

here, σ_o is equivalent to the nominal stress across the notch throat, σ_{nom}.

The time-strength ratio, given previously by equation (1.29) for a constant ductility model, i.e. similar failure strains for uniaxial and notched specimens, is therefore:

$$\frac{t_{no}}{t_{un}} = \left(\frac{\sigma_{nom}}{\bar{\sigma}}\right)^n \tag{5.10}$$

Equation (5.10) is valid for materials whose rupture lives are controlled by $\bar{\sigma}$. However, for materials where the principal stress, σ_1, controls failure, the above equation becomes:

$$\frac{t_{no}}{t_{un}} = \left(\frac{\sigma_{nom}}{\sigma_1}\right)^n \tag{5.11}$$

Similarly, when the stress-strength ratio is used in a constant ductility model, the result for a $\bar{\sigma}$ material is:

$$\frac{\sigma_n}{\sigma_{un}} = \frac{\sigma_{nom}}{\bar{\sigma}} \tag{5.12}$$

and for a σ_1 material:

$$\frac{\sigma_n}{\sigma_{un}} = \frac{\sigma_{nom}}{\sigma_1} \tag{5.13}$$

Calculations were made to evaluate the strength ratios, using equations (5.10) to (5.13), and the Bridgman estimates (equation (4.5)) of $\bar{\sigma}$. The values of $\sigma_{nom}/\bar{\sigma}$ and σ_{nom}/σ_1 were taken at the skeletal point from the finite element predictions given in Chapter 4, when the Von Mises criterion was adopted. The results are presented in Figures 5.4 to 5.6 in terms of time and stress-strength ratios, plotted against notch sharpness, a/R.

5.3.2 Discussion

The time-strength ratio for materials in which $\bar{\sigma}$ controls the deformation and rupture during creep are presented in Figure 5.4 for the notched geometries with b/a = 1.46. Equation (5.10) was used to calculate the constant ductility lines shown for n = 1, 3, 5, 7 and 9. It is shown in Figure 5.4 that the time-strength ratio for $\bar{\sigma}$ materials always predict notch strengthening which increases as n increases. The trends these predictions follow are similar. They all start from t_{no}/t_{un} = 1 and increase asymptotically with notch sharpness, a/R. Also shown in Figure 5.4 are the Bridgman predictions for notch strengthening using equation (4.5). They are consistent with the continuum mechanics predictions for blunt notches but overestimate the time-strength ratio as the notch sharpness increases. It must be noted that for each notch geometry, the term $\sigma_{nom}/\bar{\sigma}$ used in equation (5.10) is constant and independent of n since it represents the value of the effective stress at the skeletal point. For b/a = 1.46, the values were given previously in Figure 4.14.

Similarly, for materials where σ_1 is responsible for failure, the time-strength ratio for b/a = 1.46 is plotted for different values of n and notch sharpness, a/R, in Figure 5.5. The results always predict notch weakening. The values of σ_{nom}/σ_1 used in the calculations were read at the effective stress skeletal point. Although a skeletal point

for the steady-state axial stress distribution was not reported in the conclusions of Chapter 4, a zone, where the axial stress is nearly independent of n, exists at the position of the effective stress skeletal point. These values of σ_{nom}/σ_1 with some adjustments can therefore be used as a reference axial stress. The notch weakening predictions shown in Figure 5.5 for all values of n follow the same trends. They all start from $t_{no}/t_{un} = 1$ and decrease asymptotically with the increase in notch sharpness.

Finally, Figure 5.6 shows the stress-strength ratios for $\bar{\sigma}$ and σ_1 materials and for the three b/a notch ratios investigated in Chapter 4. Equations (5.12) and (5.13), which are independent of n, were used in the calculations. Two master curves were estimated for each b/a ratio; one predicts notch strengthening for $\bar{\sigma}$ materials, and the second notch weakening for σ_1 materials. An upper notch strengthening for each b/a ratio is also shown in Figure 5.6. It is due to gross section creep caused by the notch constraint and represented by $(b/a)^2$. The maximum value of a/R for which full constraint can be maintained was estimated to be 1.5 for $b/a = 1.33$, 1.55 for $b/a = 1.46$ and 1.85 for $b/a = 1.67$ (Neimark [1968]).

5.4 MICROSTRUCTURAL APPROACH TO PREDICT NOTCH STRENGTHENING AND WEAKENING

Ashby's theory of creep rupture by void growth is used in this section to predict both notch strengthening and weakening. A detailed analysis of this theory was previously given in Chapter 2 (Section 2.5). The required information concerning the state of stress parameters, which appear in most of Ashby's equations, are taken from the detailed finite element calculations performed and presented in Chapter 4. In particular, the information available on the notch geometries with b/a = 1.46 were used in the analysis. The calculation procedure should also be applicable for the notch geometries with the other b/a ratios. Two assumptions were made during these calculations:

(a) Nucleation time, t_n, is negligible.

(b) Steady-state is achieved relatively early in life, otherwise the finite element predictions of the state of stress parameters cannot be used in the calculations.

5.4.1 Diffusion Models

For boundary diffusion, the approximate expression for rupture time was given by equation (2.19). Assuming t_n = 0 leads to:

$$t_R \simeq \frac{0.17}{\phi_o \dot{\varepsilon}_o} \left(\frac{\sigma_o}{\sigma_1}\right) \tag{5.14}$$

ϕ_o is a material property defined by equation (2.18). Therefore, it should be constant for uni-axial and multi-axial states of stress. For uni-axial tension, $\sigma_o = \sigma_1$, which leads to a time-strength ratio derived from equation (5.14) for boundary diffusion:

$$\frac{t_{no}}{t_{un}} = \frac{\sigma_{nom}}{\sigma_1} \tag{5.15}$$

The above equation is similar to the continuum mechanics equation (5.11) for $n = 1$. It predicts notch weakening as shown in Figure 5.5 for the notch geometries with $b/a = 1.46$.

For surface diffusion, the rupture time equation (2.25), when $t_n = 0$, becomes:

$$t_R \simeq \frac{1 - 2\delta_i}{\dot{\varepsilon}_o \psi_o} \left(\frac{\sigma_o}{\sigma_1}\right)^3 \tag{5.16}$$

Similarly, a time-strength ratio can be derived from equation (5.16) for surface diffusion:

$$\frac{t_{no}}{t_{un}} = \left(\frac{\sigma_{nom}}{\sigma_1}\right)^3 \tag{5.17}$$

Equation (5.17) also predicts notch weakening, as shown in Figure 5.5 for the notch geometries with $b/a = 1.46$ and when $n = 3$.

The effect of varying ϕ_o and ψ_o in equations (5.14) and (5.16) on rupture time, expressed as $t_R \dot{\varepsilon}_o$, for uni-axial and notch bar specimens with $b/a = 1.46$ are shown in Figure 5.7 when $n = 9$. For boundary diffusion, $t_R \dot{\varepsilon}_o$ is plotted against a/R, which corresponds to the finite element predictions of σ_{nom}/σ_1 for a particular notched geometry for a range of ϕ_o values of 0.1 to 5×10^{-4}, as shown in Figure 5.7. The lines are parallel and always predict notch weakening. However, rupture times increase when ϕ_o decreases. For surface diffusion, one valid assumption that can be made is that $\delta_i < 0.01$, therefore making $t_R \dot{\varepsilon}_o$ in equation (5.16) dependent on ψ_o and $(\sigma_o/\sigma_1)^3$ only, so that:

$$t_R \dot{\varepsilon}_o \simeq \frac{1}{\psi_o} \left(\frac{\sigma_o}{\sigma_1}\right)^3 \tag{5.18}$$

Similar notch weakening trends are observed to those of boundary diffusion when ψ_o is varied in equation (5.18), as those shown in Figure 5.7.

When the stress is used to model notch strengthening ratios for both boundary and surface diffusion, equations (5.14) and (5.16) simply become equivalent to the continuum mechanics equation (5.13) which predicts notch weakening as shown previously in Figure 5.6.

5.4.2 Power-Law Creep Models

A new parameter, α, defined by equation (2.30), appeared in Ashby's equations of damage rate and strain rate when voids grow by power-law creep alone. It is dependent on state of stress through the ratio $\sigma_m/\bar{\sigma}$ (where σ_m is the hydrostatic stress component). Graphs of α as the tri-axiality is increased (a/R) are plotted in Figure 5.8 for different values of n and for notch geometries with $b/a = 1.46$. The ratio $\sigma_m/\bar{\sigma}$ is taken at the effective skeletal stress point, since it is nearly constant and independent of n at that position for all the notch geometries investigated. The graphs of α shown in Figure 5.8 decrease sharply from the initial uni-axial value α_o. They become less sensitive to n for values of $n > 7$.

The rupture strain equation (2.34) for a uni-axial state of stress, and when $t_n = 0$, reduces to:

$$\varepsilon_R = t_R \dot{\varepsilon}_o + 0.2 \frac{\ell}{d} \tag{5.19}$$

$\dot{\varepsilon}_o$ is the secondary creep rate; therefore, according to equation (5.19), the strain-time curve for a constant stress test is represented by a long line with a slope $\dot{\varepsilon}_o$ and a small upturn in the end, respresenting the tertiary stage and dictated by the value $0.2\ell/d$. For constant load tests, the matter is different since the current stress has to be updated using

equation (2.31). Figure 5.9 shows a schematic diagram of strain-time behaviour of a uni-axial specimen failing by power-law creep under constant load and constant stress conditions.

The rupture time equation (2.31) for constant load, when $\delta_i \ll 1$, reduces to equation (2.33). Substituting $\dot{\varepsilon}_\delta$ by ε_R/t_R in equation (2.33), the following linear relation is derived:

$$\frac{t_R}{t_R^L} = n\,\varepsilon_R \tag{5.20}$$

where t_R^L and t_R are rupture times at constant load and constant stress, respectively. The lines calculated for different values of n are shown in Figure 5.10. They indicate that for large values of n and high ductilities, the difference increases between the rupture times of specimens tested under constant load and constant stress.

An expression for the time-strength ratio can be derived from the general rupture time equation (2.30) for constant stress. For uni-axial tension and assuming $t_n = 0$, it reduces to:

$$t_R = \frac{\alpha_o}{(n+1)\,\dot{\varepsilon}_o} \ln\left[\frac{1}{(n+1)\,\delta_i}\right] \tag{5.21}$$

and for a multi-axial state of stress, it remains the same, excluding t_n. If δ_i is assumed to remain constant under both uni-axial and multi-axial conditions, then an expression for time-strength ratios could be derived from equations (5.21) and (2.30), as follows:

$$\frac{t_{no}}{t_{un}} = \left(\frac{\alpha}{\alpha_o}\right)\left(\frac{\sigma_{nom}}{\bar{\sigma}}\right)^n \tag{5.22}$$

α_o refers to the uni-axial value. Equation (5.22) is plotted in Figure 5.11 for different values of n and for notch geometries with $b/a = 1.46$.

Both notch strengthening and weakening are predicted by this model. For values of $n < 5$, equation (5.22) predicts notch weakening, but when $n \geq 5$ it predicts the notch strengthening ratio which drops in value beyond a critical a/R. For these particular notch geometries and n values, the drop in strength started at $a/R = 2$ to 7.

If δ_i is assumed to vary as the tri-axiality is increased, then rupture time, $\dot{\varepsilon}_o t_R$, in equation (2.30) becomes dependent on n, notch sharpness a/R, and δ_i. Therefore, a series of curves, having different δ_i values, can be plotted for each value of n. These are shown in Figure 5.12 for $n = 3$ and 9 and δ_i values of 10^{-2} to 10^{-10}. For $n = 3$, the model predicts notch weakening for all δ_i values, but for $n = 9$ it predicts notch strengthening time ratio which drops after a certain amount of constraint, approximately constant for these geometries and equal to $a/R = 8$.

The drop in ductility due to the increase in tri-axiality can be shown when the rupture strain equation (2.34) is used in the following analysis. Assuming $0.2\ell/d$ to be negligible and substituting equation (2.30) (t_R) into equation (2.34) results:

$$\varepsilon_R = \frac{\alpha}{(n+1)} \ln \left[\frac{1}{(n+1)\,\delta_i}\right] \tag{5.23}$$

The above equation is plotted in Figure 5.13 for a range of $\delta_i = 10^{-2}$ to 10^{-10} and for $n = 9$. The a/R is related to ε_R through the parameter α. All the curves follow the same trend, i.e. ε_R decreases asymptotically from an initial uni-axial value as a/R increases. The difference between the maximum and the minimum ε_R is always an order of magnitude. To make the notch bar ductility ε_R remain constant and always equal to the uni-axial ε_R, δ_i has to change by about eight orders of magnitude, as illustrated in Figure 5.13 by the horizontal constant ductility line for

the case of ε_R = 30%.

The rupture strain equation (2.34) can also be used to show the influence of ductility on rupture time expressed as $\dot{\varepsilon}_o\, t_R$. Assuming $0.2\ell/d$ to be negligible, equation (2.34) reduces to:

$$\dot{\varepsilon}_o\, t_R = \varepsilon_R \left(\frac{\sigma_{nom}}{\bar{\sigma}}\right)^n \tag{5.24}$$

Assuming that ductility is constant at failure for uni-axial and notch bar specimens, a series of curves can be drawn using equation (5.24), as shown in Figure 5.14. The trends are similar for all curves; they all predict notch strengthening. Rupture times increase with the increase in ductility.

Finally, three types of stress strength ratios are shown in Figure 5.15. The mathematical expressions were derived from the rupture time equation (2.30), with the assumption that t_n = 0. For uni-axial tension, equation (2.30) reduces to equation (5.21). If δ_i is assumed to remain constant under uni-axial and multi-axial states of stress, then a relation for stress strength ratio can be derived from equations (2.30) and (5.21) as follows:

$$\frac{t_{no}}{t_{un}} = \left(\frac{\alpha}{\alpha_o}\right)^{1/n} \frac{\sigma_o}{\bar{\sigma}} \tag{5.25}$$

Using the definition of the notch rupture strength (equation (1.31)), when $t_{no} = t_{un} = 1$, the result is:

$$S_\Delta = \left(\frac{\alpha}{\alpha_o}\right)^{1/n} \frac{\sigma_{nom}}{\bar{\sigma}} \tag{5.26}$$

here, the ratio $\sigma_{nom}/\bar{\sigma}$ is taken at the skeletal point.

The rupture time equation (2.30) can be written in terms of

the rupture strain, such that:

$$t_R = \frac{\varepsilon_R}{\dot{\varepsilon}_o} \left(\frac{\sigma_o}{\bar{\sigma}}\right)^n \tag{5.27}$$

The assumption made in equation (5.27) is $0.2\ell/d$ is negligible. Assuming constant rupture strain for uni-axial and multi-axial specimens gives an expression for stress strength ratio identical to that reached by the continuum mechanics approach, i.e.

$$S_\Delta = \frac{\sigma_{nom}}{\bar{\sigma}} \tag{5.28}$$

Cocks [1980] derived an expression for stress strength ratio, based also on equation (2.30) and for $t_n = 0$. He used a constraint parameter, N, which defines the stress state on the minimum section of a notched bar as follows:

$$N = \frac{\sigma_n}{\bar{\sigma}} \tag{5.29}$$

where σ_n and $\bar{\sigma}$ are the slip line field predictions of the average axial stress and the equivalent stress in the minimum section of a notched bar. Cocks' final expression was:

$$S_\Delta = N \left\{\frac{\sinh\left[\frac{2}{3}\left(\frac{n-1/2}{n+1/2}\right)\right]}{\sinh\left[2\left(\frac{n-1/2}{n+1/2}\right)\left(N-\frac{2}{3}\right)\right]}\right\}^{\frac{1}{n}} \tag{5.30}$$

Equations (5.26), (5.28) and (5.30) are plotted in Figure 5.15. Equation (5.28) gave similar predictions to the continuum mechanics approach when ε_R is constant. Equation (5.26) predicts notch strengthening for $n \geq 5$ which drops in value around about $a/R = 8$ for these particular notched bar geometries. For values of $n < 5$, notch weakening is predicted, excluding the case when $n = 4$ for which both notch strengthening and

weakening are observed. Cocks equation (5.30), based on values of $N = \sigma_{nom}/\bar{\sigma}$ at the skeletal point, always predicts upper bounds to the strength ratio calculated by equation (5.27), and similar in trends to the continuum mechanics prediction for $n > 3$.

5.5 GENERAL DISCUSSION

The assumption used to derive the continuum mechanics equations (5.10) to (5.13), defining the time and stress strength ratio, was that the final ductility remains constant, even when the ratio $\sigma_m/\bar{\sigma}$ increases due to the increase in constraint. This assumption is physically invalid, since it has been observed and reported in the literature that ductility drops with the increase in tri-axiality (Dyson and Loveday [1980], Hancock, et al. [1976], Mackenzie, et al. [1977]). The equations mentioned, therefore, will always predict upper strengthening bounds when $\bar{\sigma}$ is adopted, or lower weakening bounds if expressed in terms of σ_1. It is expected that real material data will depart from the theoretical bound after a certain amount of constraint.

The diffusion models proposed by equations (5.15) and (5.17) are totally dependent on the ratio σ_{nom}/σ_1 which is equal to unity for uni-axial tension and always less than one for notched bar specimens, as the steady-state finite element stress distributions show (Hayhurst, et al. [1977a,b], Al-Faddagh, et al. [1982]). It is therefore expected that diffusion models predict notch weakening.

Two main assumptions were used to derive the notch rupture strength ratios when voids grow by power-law creep. These were f_i varies with the increase in tri-axiality or remains constant. The assumption that f_i is variable means that small and large voids nucleate initially in which large voids start to grow under the influence of the applied stress, therefore dictating the deformation and rupture response. As the hydrostatic component begins to increase and the effective stress decreases due to the increase in tri-axiality, smaller voids are activated and, in turn, start to influence the deformation and rupture behaviour. The area fraction of holes was given previously by equation (2.11) as:

$$f_h = \frac{r_h^2}{\ell^2} \tag{5.31}$$

Therefore, it is expected that δ_h may vary by an order of magnitude if the difference in void size is between 2 and 4. However, if the difference is 10, then δ_h varies by two orders of magnitude, which is the difference between the neighbouring curves plotted in Figure 5.12. The attraction of using the assumption 'δ_i is constant' is that the state of stress is well represented in the time-strength ratio through the parameters α/α_o and $\sigma_{nom}/\bar{\sigma}$, as well as the material creep index, n. Therefore, both notch strengthening and weakening can be predicted by the proposed model.

Uni-axial or notched bar specimens are expected to fail by diffusion if the following condition is satisfied:

$$t_{R,d}\ (by\ diffusion) \ < \ t_{R,PL}\ (by\ power\text{-}law\ creep) \tag{5.32}$$

Using the rupture time equations (2.20) and (2.30) for boundary diffusion and power-law creep, the following expression is derived:

$$\frac{t_{R,PL}}{t_{R,d}} = \frac{\phi_o\ \varepsilon_R}{0.17} \left(\frac{\sigma_o}{\bar{\sigma}}\right)^n \left(\frac{\sigma_1}{\sigma_o}\right) \tag{5.33}$$

where the suffixes PL and d refer to power-law and boundary diffusion, respectively. If the ratio given by equation (5.33) is greater than one, then failure is diffusion controlled, but if it is less than one, then failure will be power-law creep controlled. For uni-axial tension, equation (5.33) reduces to:

$$\frac{t_{R,PL}}{t_{R,d}} = \frac{\phi_o\ \varepsilon_R}{0.17} \tag{5.34}$$

The above equation indicates that $\phi_o\ \varepsilon_R$ has to be greater than 0.17 in order to make a uni-axial specimen to fail by diffusion. This is very unlikely since ε_R for most materials varies between 0.5 and 0.01, and ϕ_o is usually less than 1. However, for high degrees of tri-axiality, the

ratio $(\sigma_o/\bar{\sigma})^n$ and (σ_1/σ_o) become significant and always greater than 1, so that failure by diffusion becomes possible.

If rupture time due to power-law creep and, say, boundary diffusion are assumed to be equal, then the following equation can be derived:

$$\frac{C_1}{\sigma_1} = \frac{\varepsilon_R}{\dot{\varepsilon}_o} \left(\frac{\sigma_o}{\bar{\sigma}}\right)^n \tag{5.35}$$

where:

$$C_1 = \frac{0.17\ k\ T\ \ell^3}{2\ D_b\ \delta_b\ \Omega} \tag{5.36}$$

The finite element predictions at the skeletal point gives:

$$\sigma_1 = C_2\ \sigma_{nom} \tag{5.37}$$

Substituting equation (5.37) into equation (5.2) and using the stress strength ratio definition given by equation (1.31) gives:

$$S_s = \frac{C_1}{C_2} \frac{\dot{\varepsilon}_s}{\varepsilon_R} \frac{1}{\sigma_{un}} \tag{5.38}$$

where $\dot{\varepsilon}_s$ is the secondary creep rate. Equation (5.38) indicates that weakening is likely to occur at low strain rates and large ratios, σ_1/σ_{nom}.

5.6 CONCLUSIONS

An approximate method has been presented for estimating time-scales for stress redistribution due to creep. The method is based on the assumption that the maximum stress in structures determines the overall behaviour. It is applicable to notch bar geometries. Therefore, it can be used to provide useful design predictions of notch behaviour.

Continuum mechanics and void growth analyses have been used to provide some theoretical models to predict notch strengthening and weakening in round bars subjected to creep. The influence of state of stress parameters, ductility, and area fraction of holes were analysed and discussed.

It was found that continuum mechanics models predict upper notch strengthening bounds for $\bar{\sigma}$ materials and lower notch weakening bounds for σ_1 materials, when the assumption that ductility remains constant for uni-axial and multi-axial states of stress is used.

The diffusion models proposed always predict notch weakening and are totally dependent on the ratio σ_{nom}/σ_1 raised to the power 1 or 3.

Several power-law creep models have been proposed for estimating rupture times and notch strength ratios. These models were derived using either rupture time or rupture strain equations with the assumptions that area fraction of holes, f_i, varies with the increase in tri-axiality or remains constant. Another assumption was also used, that is ductility remains constant when notch constraint is increased. It was shown, however, that for this assumption to remain valid, f_i has to decrease from an initial uni-axial value by about eight orders of magnitude when a/R increases to about 32. Both notch strengthening and weakening were observed when the proposed power-law creep models were adopted.

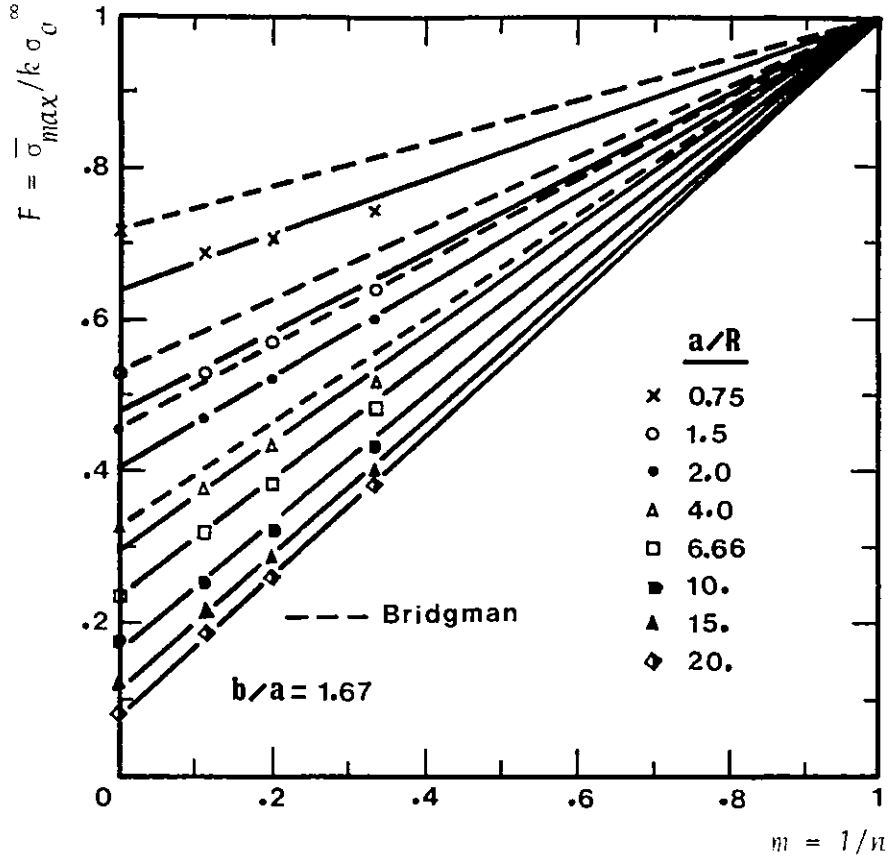

Figure 5.1: Relative maximum stress concentration factor, F, as a function of $1/n$ for notched geometries with b/a = 1.67

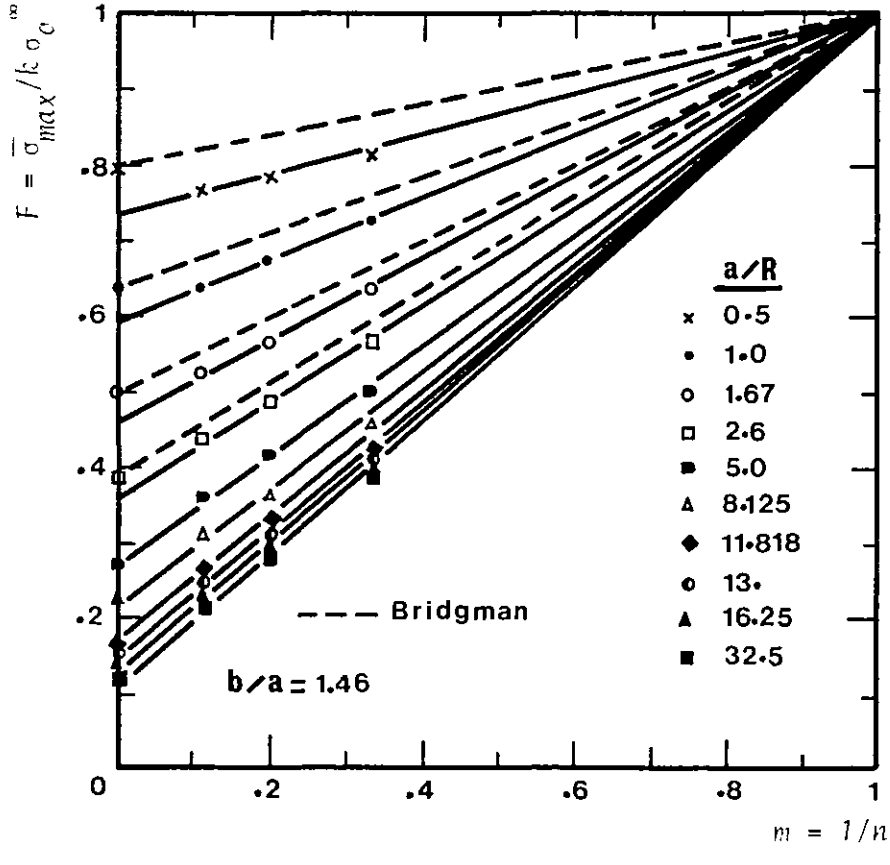

Figure 5.2: Relative maximum stress concentration factor, F, as a function of $1/n$ for notched geometries with b/a = 1.46

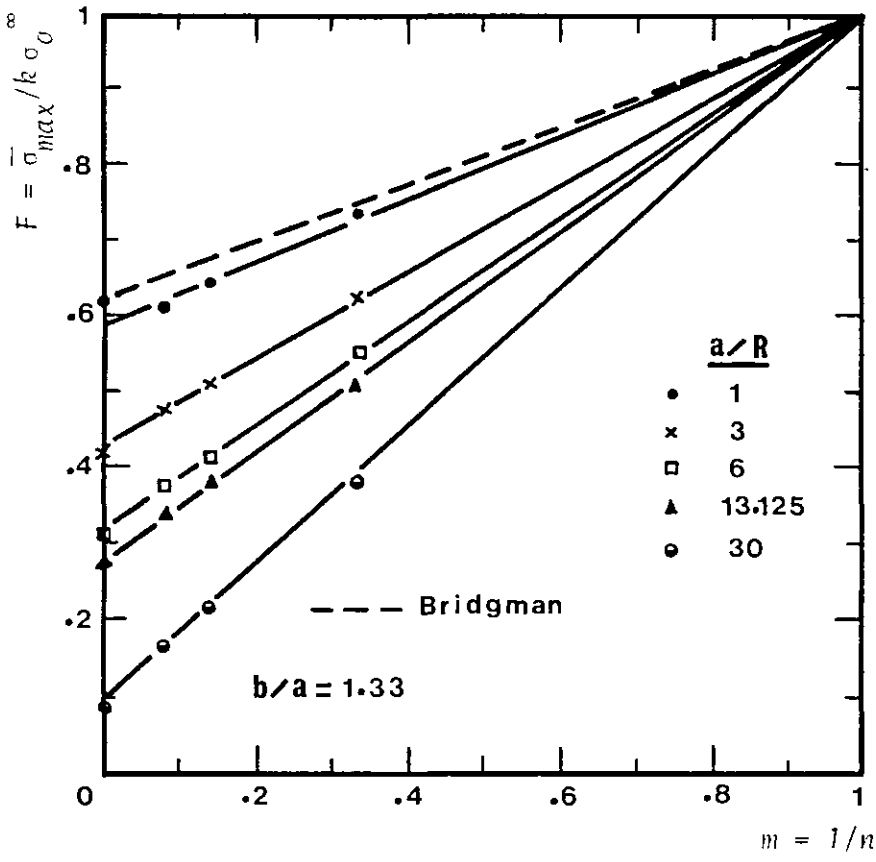

Figure 5.3: Relative maximum stress concentration factor, F, as a function of $1/n$ for notched geometries with b/a = 1.33

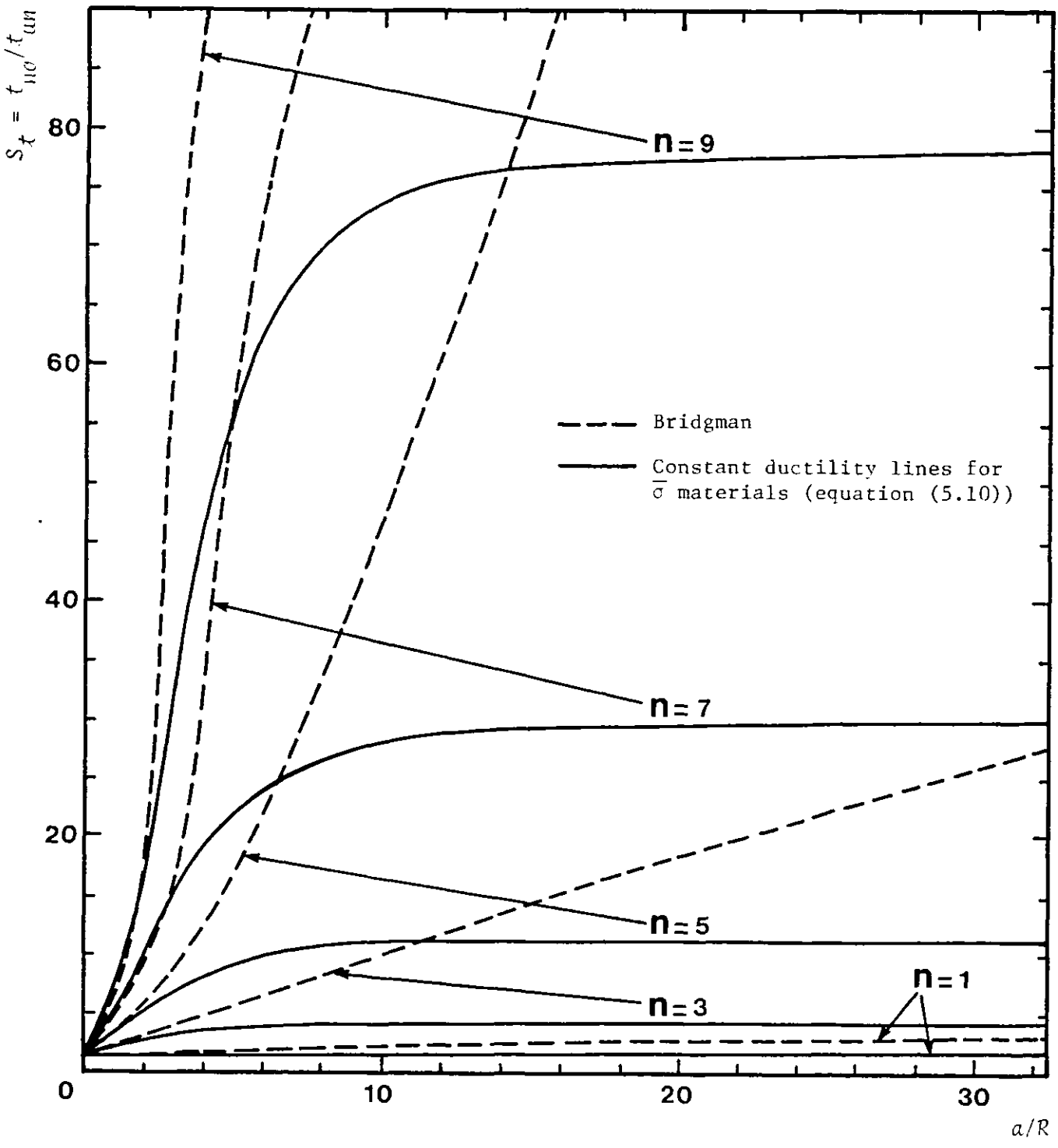

Figure 5.4: Continuum mechanics notched to unnotched life ratio predictions for a range of notched bar geometries with b/a = 1.46, using equation (5.10)

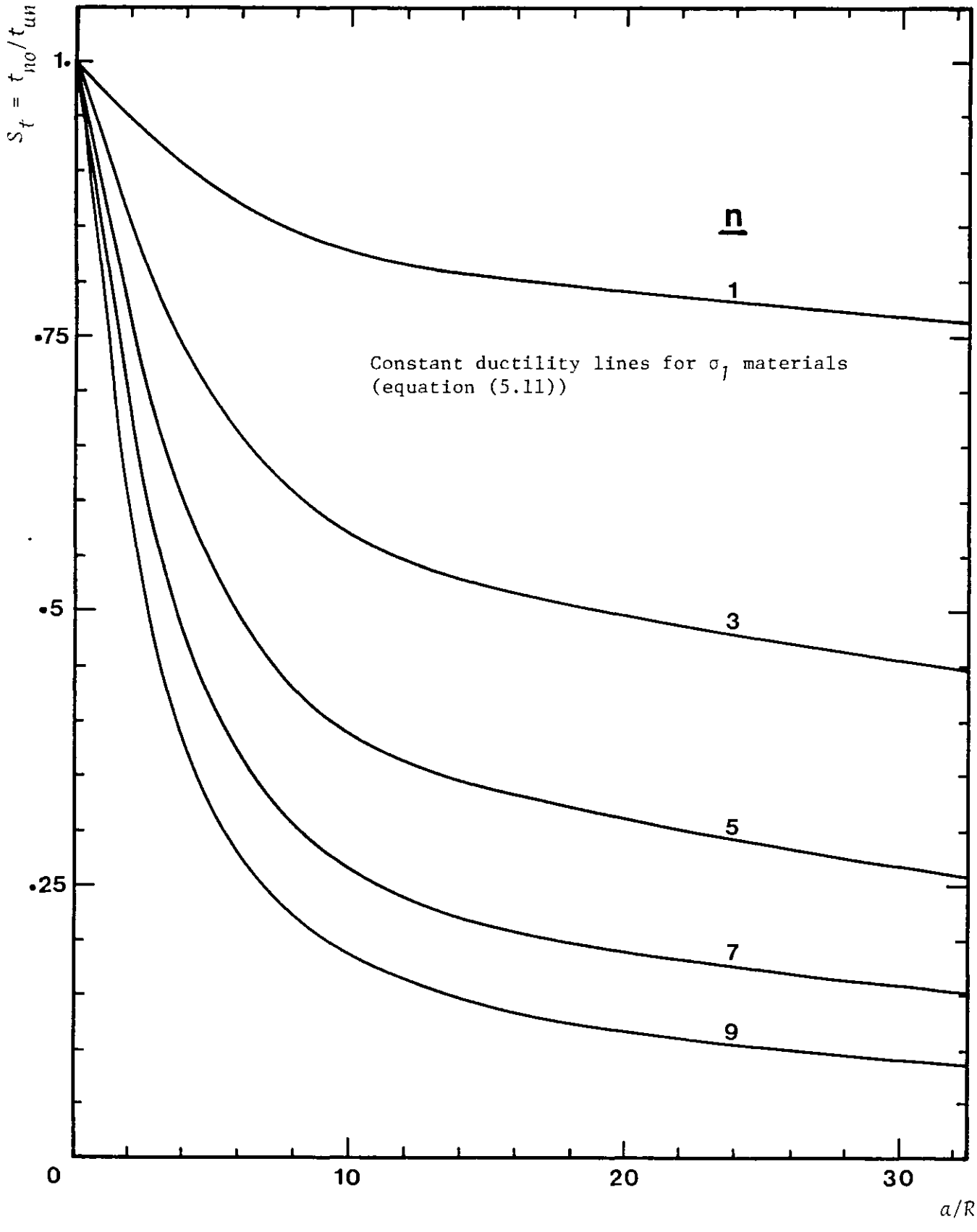

Figure 5.5: Continuum mechanics notched to unnotched life ratio predictions for a range of notched bar geometries with b/a = 1.46, using equation (5.11)

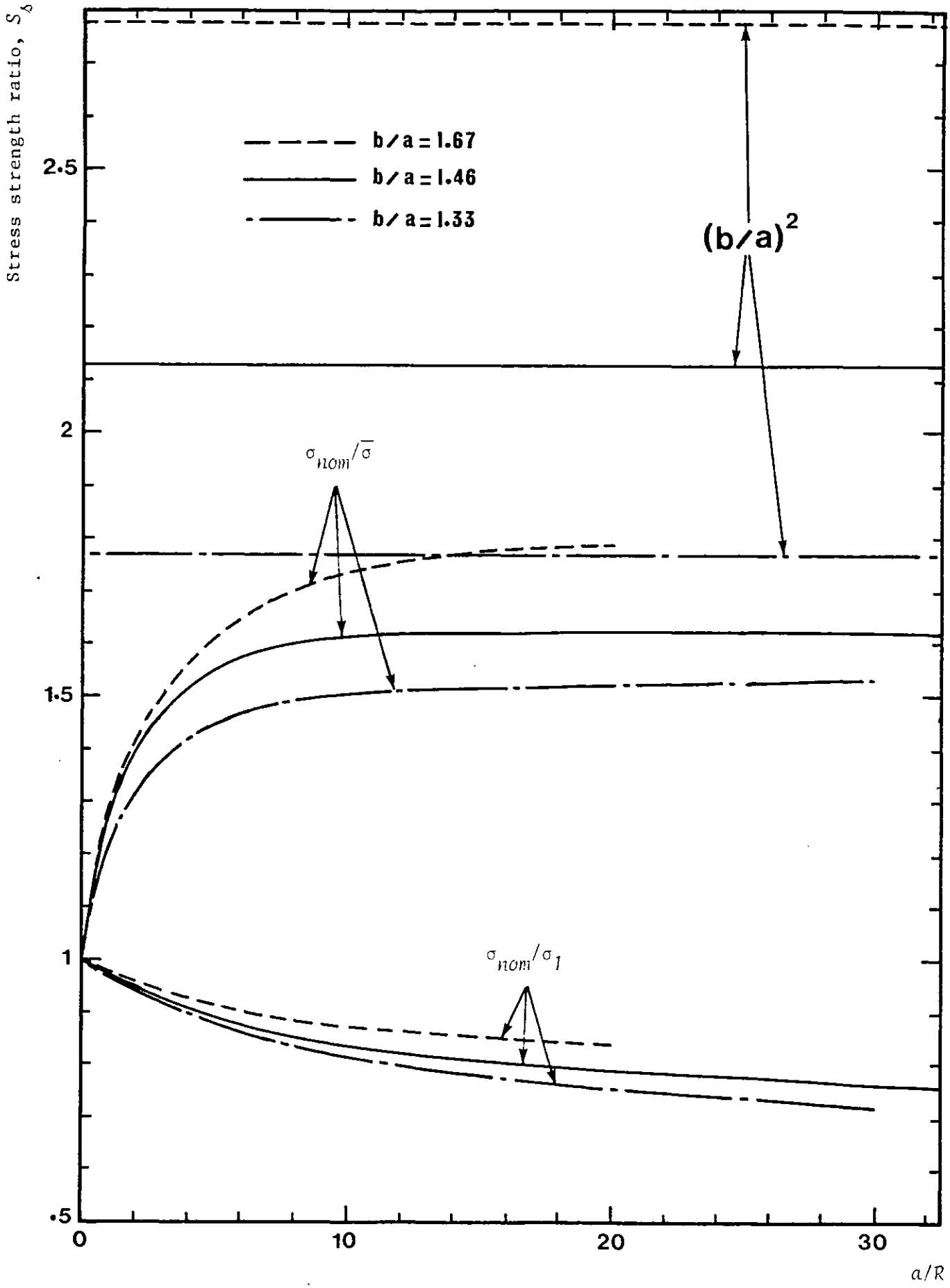

Figure 5.6: Continuum mechanics notched to unnotched rupture strength ratio predictions for a range of notched bar geometries.

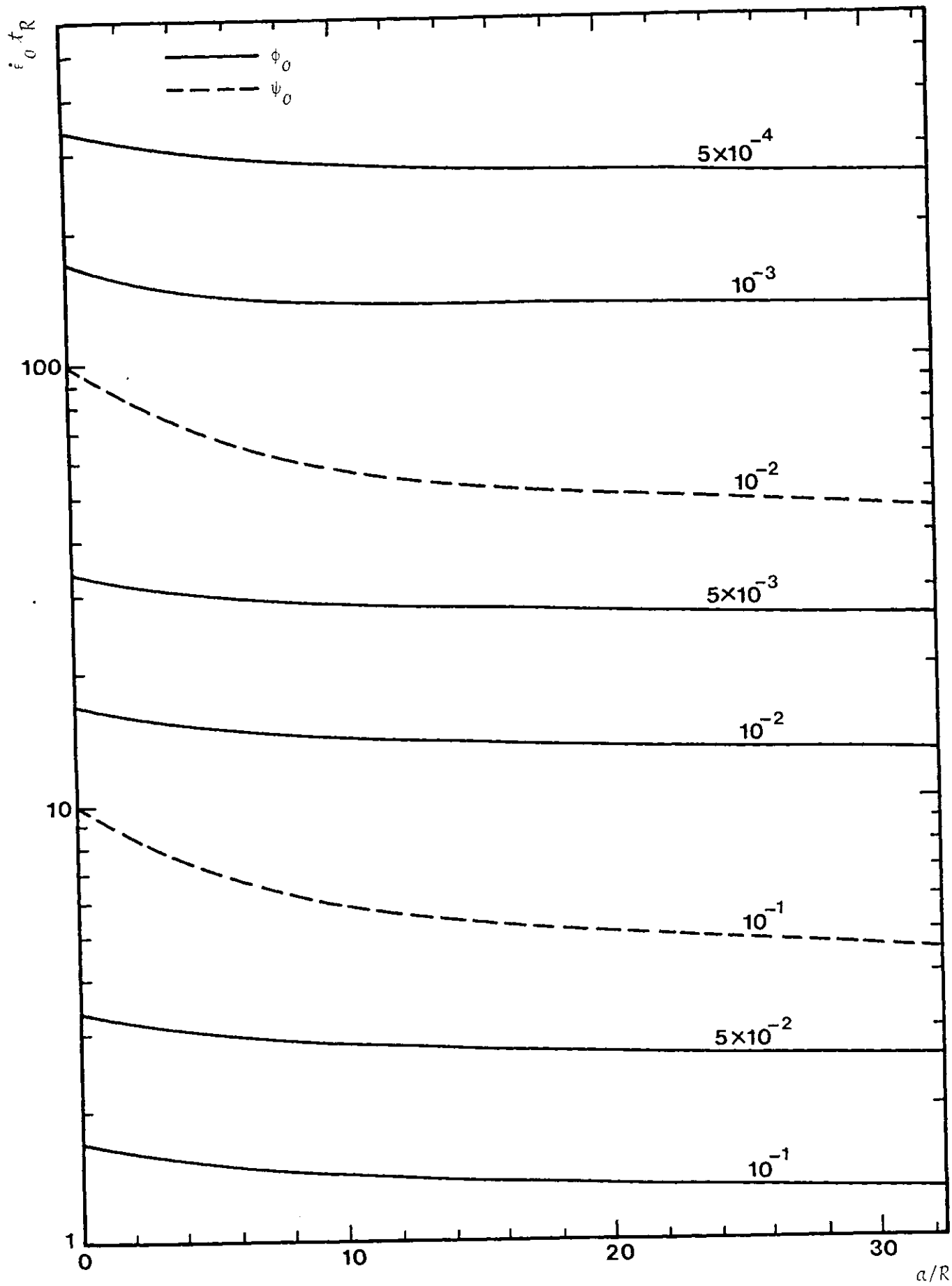

Figure 5.7: Dependence of rupture times on the dimensionless diffusion material quantities, ϕ_o and ψ_o, for a range of notched geometries with b/a = 1.46

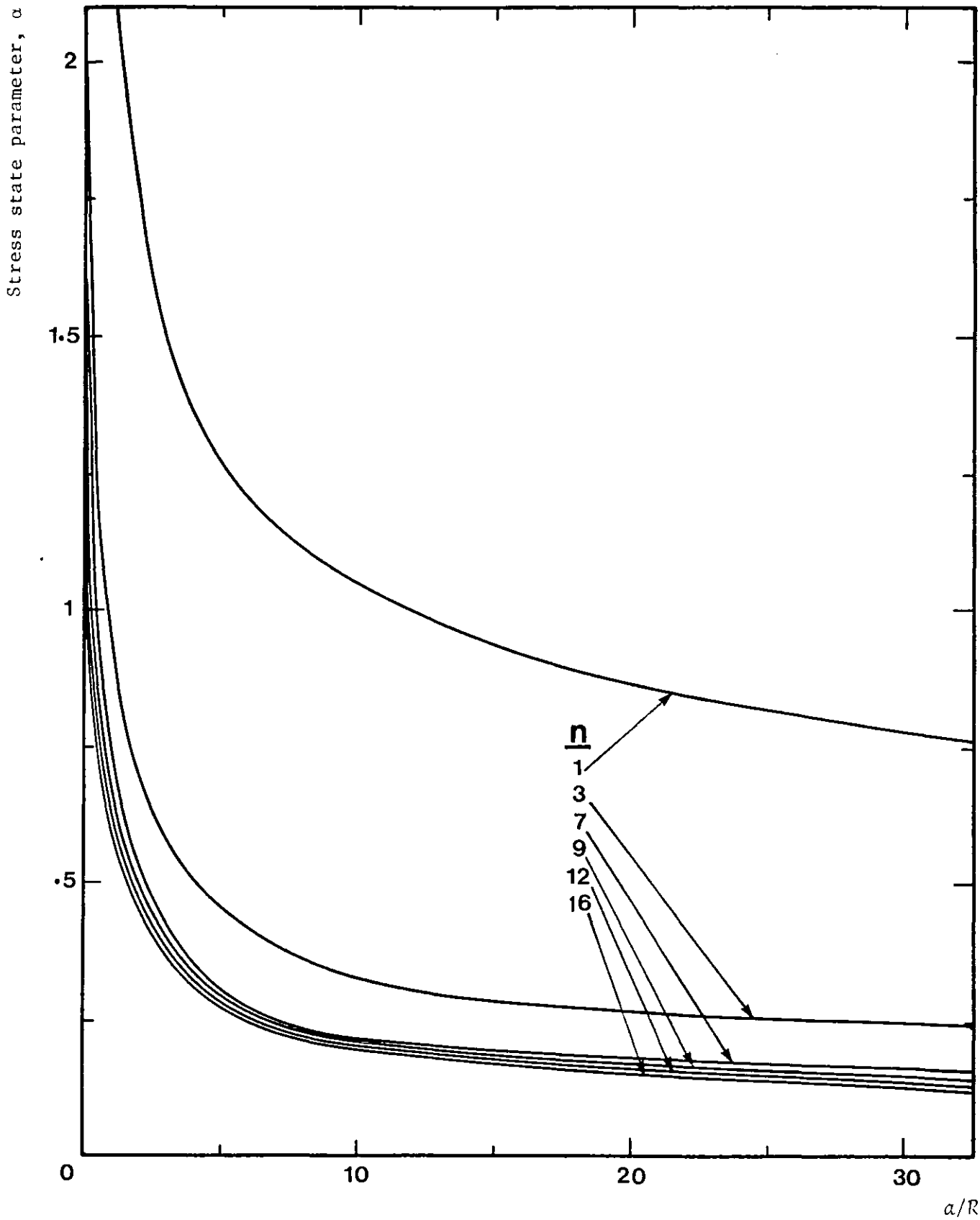

Figure 5.8: Dependence of the stress state parameter, α, on notch sharpness, a/R, for a range of notched bar geometries with b/a = 1.46

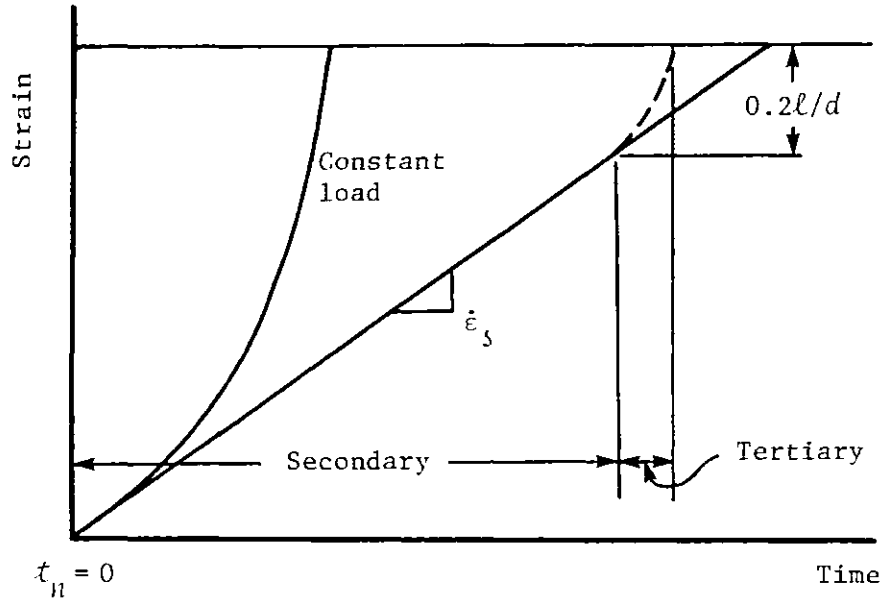

Figure 5.9: Schematic diagram showing the uni-axial strain-time expected behaviour of a specimen failing by power-law creep

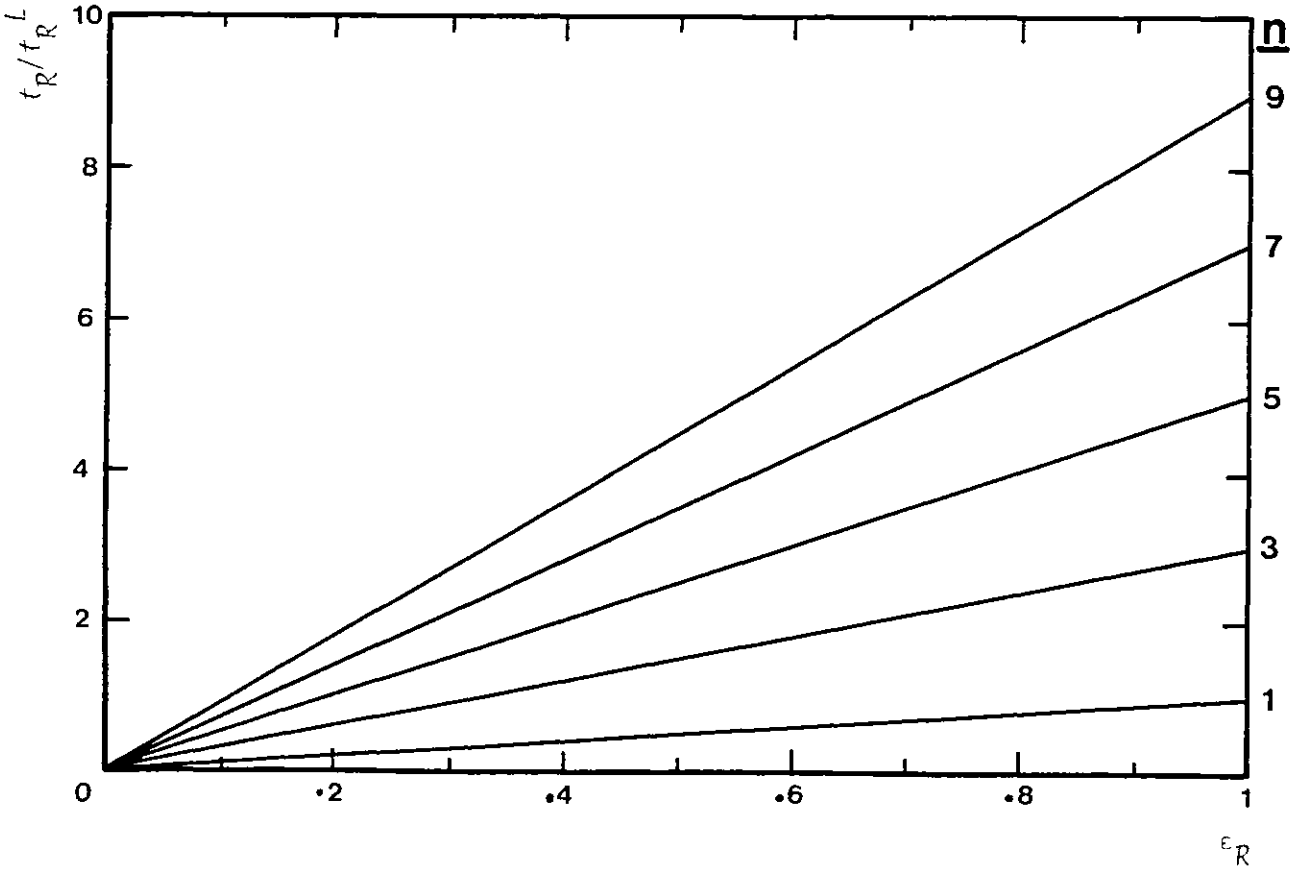

Figure 5.10: Dependence of rupture time ratios of uni-axial specimens tested under constant stress or constant load on ductility and n

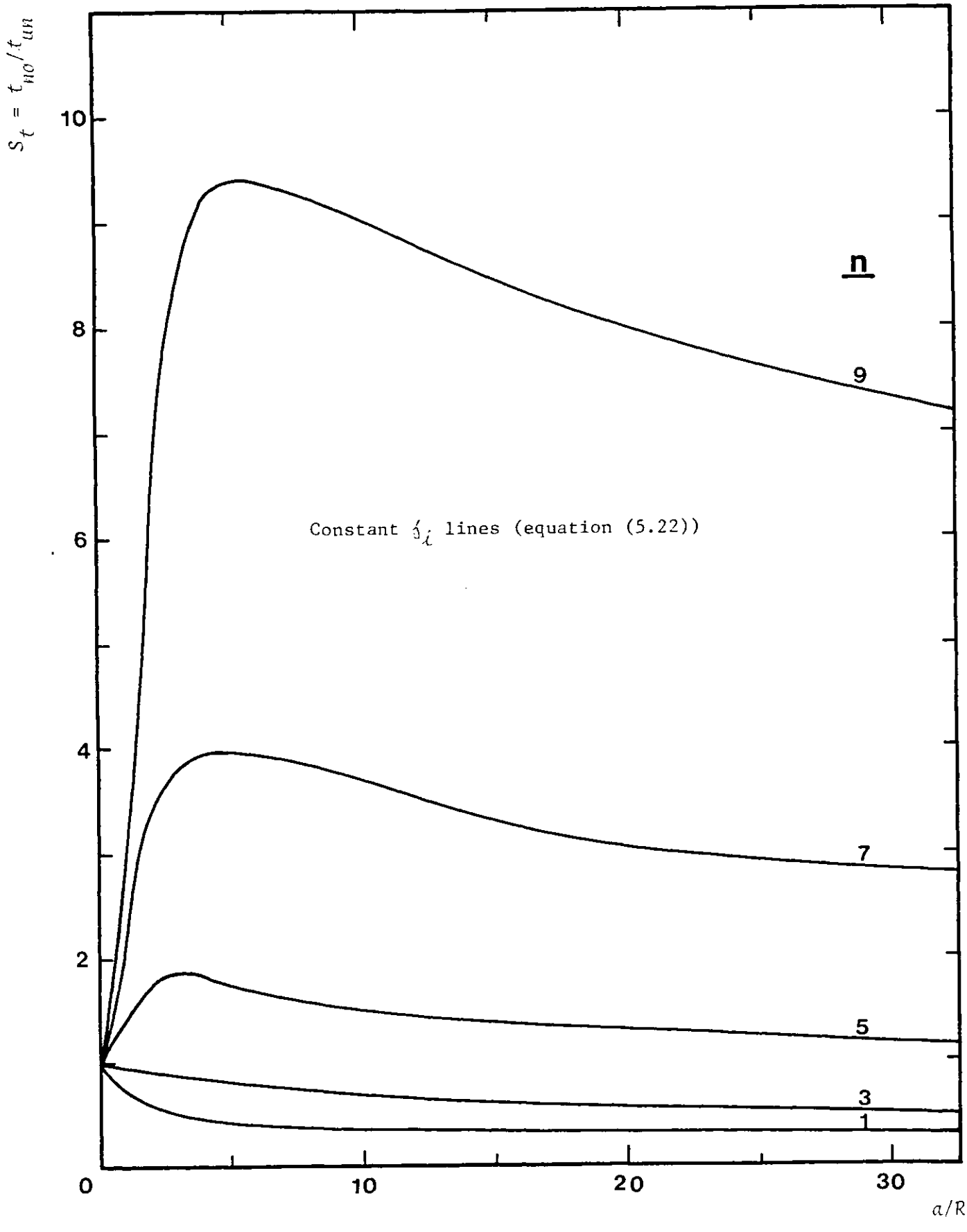

Figure 5.11: Microstructural predictions of the notched to unnotched life ratios for a range of notched bar geometries with b/a = 1.46 and when δ_i is assumed constant (equation (5.22))

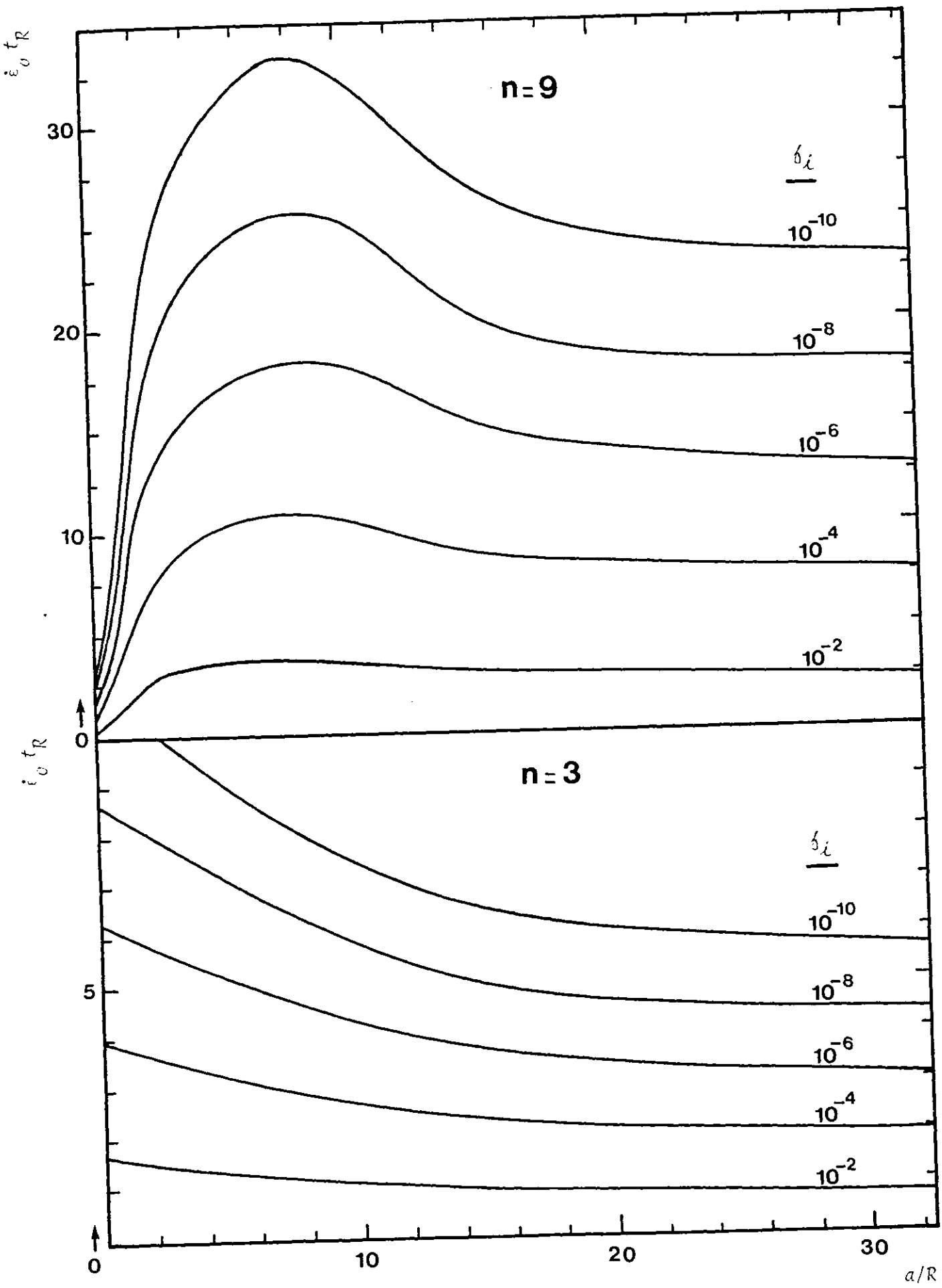

Figure 5.12: Dependence of rupture times on δ_i for a range of notched bar geometries with b/a = 1.46 and when n = 9 and 3

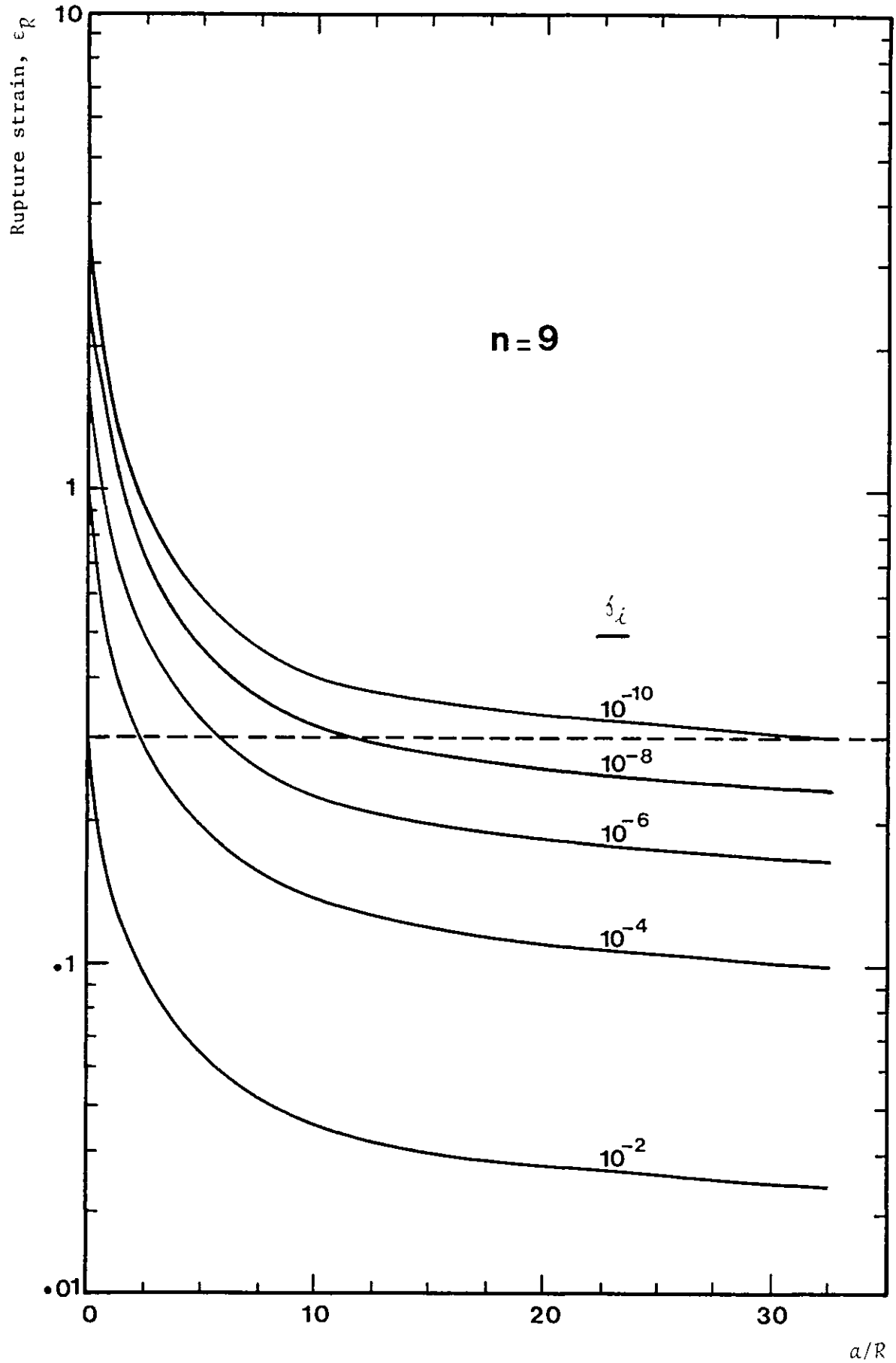

Figure 5.13: Dependence of rupture strains on δ_i for a range of notched bar geometries with b/a = 1.46 and when n = 9

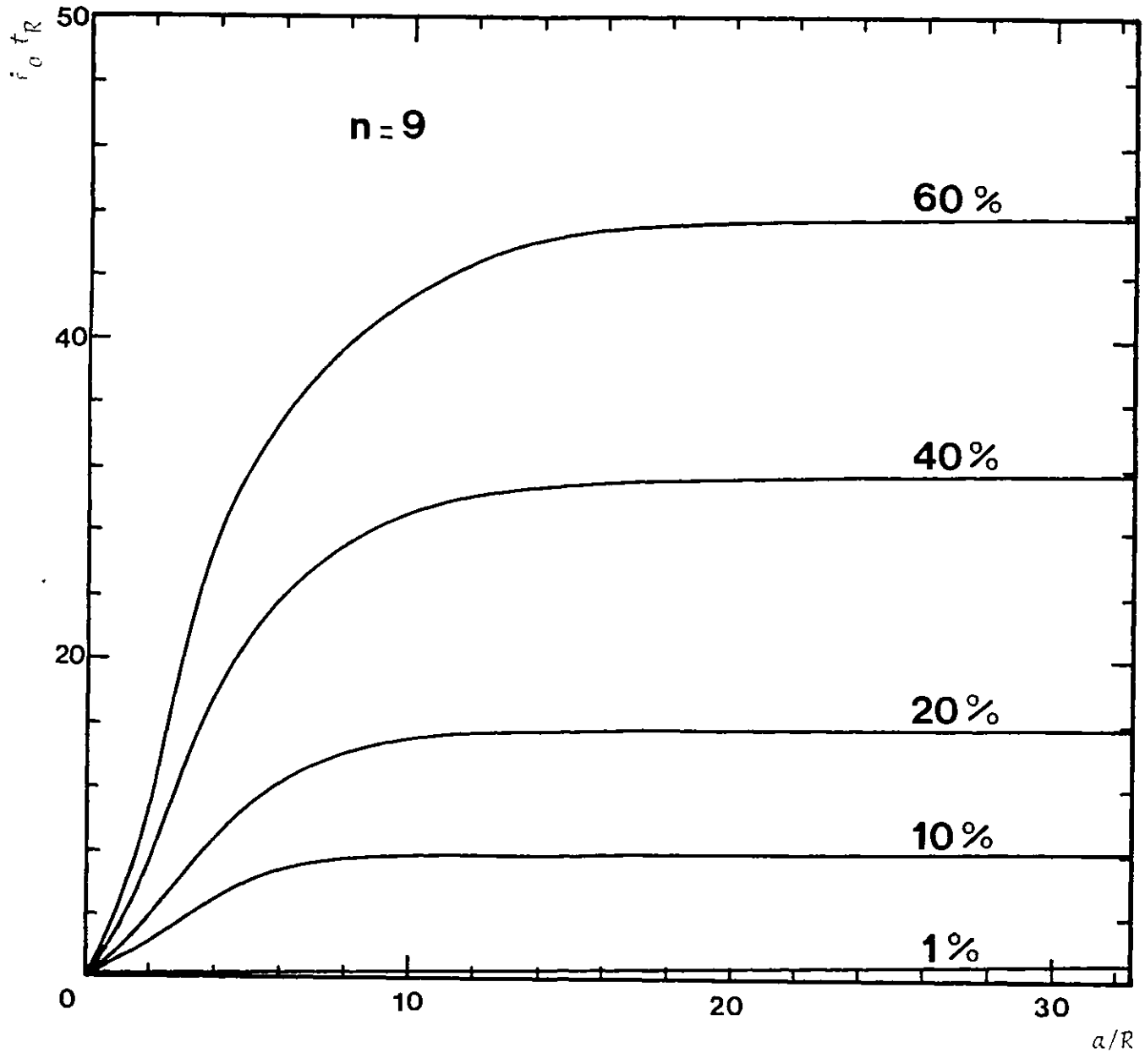

Figure 5.14: Dependence of rupture times on ductility for a range of notched bar geometries with b/a = 1.46 and when n = 9

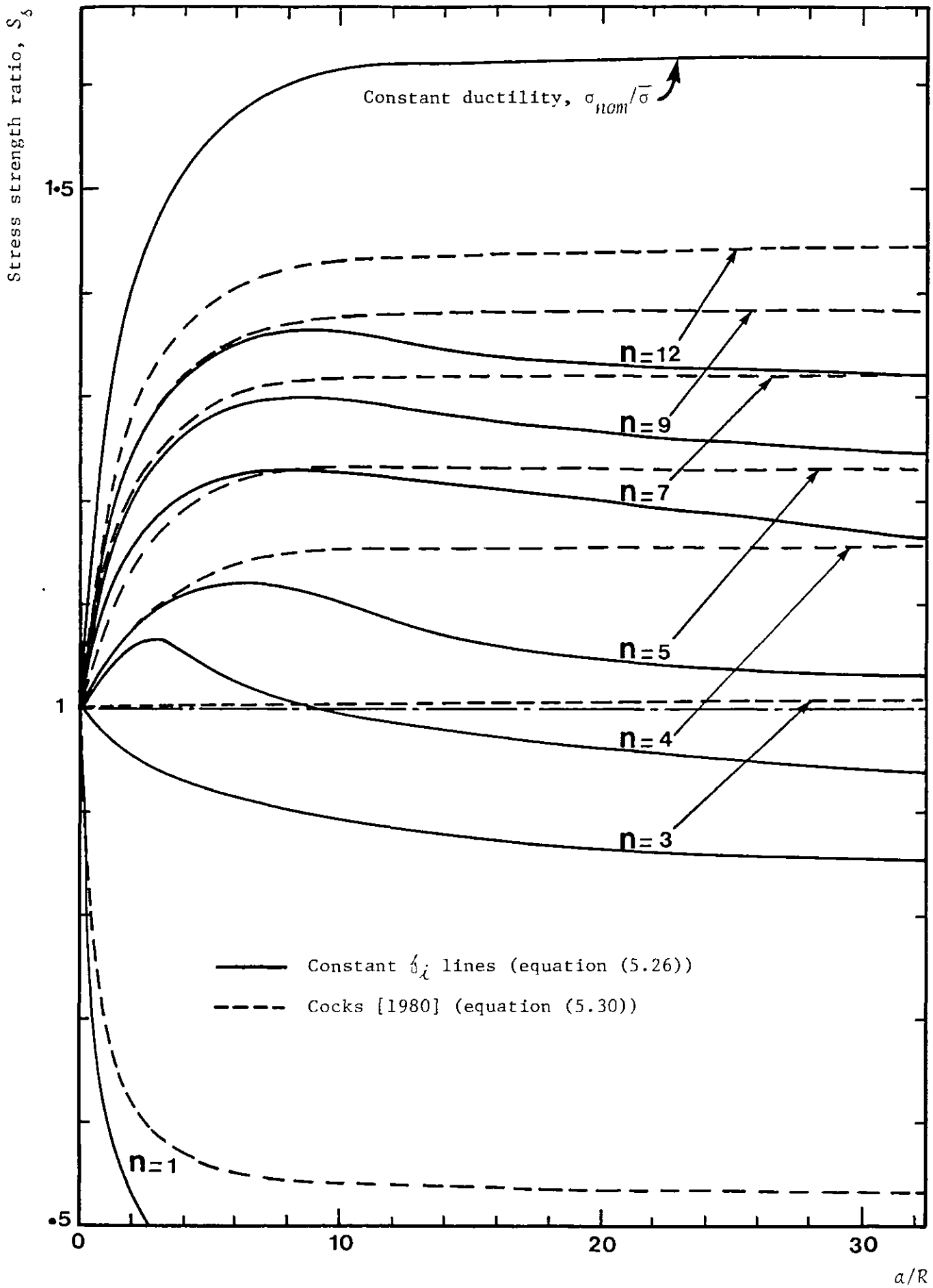

Figure 5.15: Notched to unnotched stress strength ratios for a range of notched bar geometries with b/a = 1.46 using equations (5.26), (5.28) and (5.30)

CHAPTER 6

EXPERIMENTAL INVESTIGATIONS

6.1 INTRODUCTION

This chapter describes in detail the experimental investigations carried out on the 2¼%Cr 1%Mo steel used in the electric power generation industries. Basic creep data were obtained at 538°C on uni-axial and notched bar specimens which had the same throat diameter as the plain tensile bars. The results were analysed and compared with those obtained by Ng, Webster and Dyson [1980] on two casts, named as 4F and 10G, of the brittle ½%Cr ½%Mo ¼%V steel.

6.2 MATERIALS AND SPECIMEN GEOMETRIES

6.2.1 Creep Resistant Steels

As power-law creep is largely a matter of movement of dislocations, any form of obstacle used for blocking dislocations will reduce creep. Many of the obstacles used to give room temperature strength do not remain effective at high temperatures. For example, in heat-treated plain carbon steels, martensite breaks down on tempering, the carbide becomes less dispersed, and the material becomes softer. At higher temperatures, the carbide dissolves in the austenite, therefore producing a poor creep resistant structure.

In low alloy steels containing strong carbide-forming elements, such as chromium, tungsten, vanadium and molybdenum, the carbides remain in a finely dispersed condition to much higher temperatures, therefore giving satisfactory creep resistant properties up to about 550°C and possibly higher temperatures for some high alloy steels.

6.2.2 Materials and Their Heat-Treatments

Both the 2¼%Cr 1%Mo and ½%Cr ½%Mo ¼%V steels are used predominantly in the power generation industry, in pressure vessels, steam chests and numerous items of turbine components and associated pipeworks, all operating in the creep range. The compositions of both materials are given in Table 6.1.

The heat-treatments carried out on each material prior to creep tests were as follows: for the 2¼CM steel, the material was first annealed for 15 hours at 960°C, then furnace-cooled, normalised for 12 hours at 960°C, then fan-assisted cooled, tempered for 12 hours at 700°C, then furnace-cooled, and finally stress relieved for 36 hours at 690°C, then furnace-cooled. The result of this heat-treatment was a fine grain mixed bainite and ferrite structure with grain size of 8 to 33 μm.

For the ½CMV steel, the heat-treatments carried out on the two casts, creep tested by Ng, et al. [1980] at 565°C, were as follows: a 25 mm thick slice was removed from the side of a cast block and subsequently austenitised for half an hour at 1250°C, quenched in oil, tempered for 24 hours at 680°C, and finally air-cooled. It resulted in a tempered martensitic structure with a prior austenite grain size of 200 to 300 μm. A representative microstructure of each material is shown in Figure 6.1.

6.2.3 Specimens

Two types of specimen were used in the high temperature creep tests carried out on the 2¼CM steel. These were uni-axial plain bar and round notched bar specimens. Both types of specimen were machined from a cast block approximately 300 mm square and 100 mm thick. The main dimensions of the plain bar specimens were 38 mm gauge length and 6.5 mm diameter, as shown in Figure 6.2(a).

All notched bar specimens had a shank diameter $2b$ = 9.5 mm and a notch throat diameter $2a$ = 6.5 mm, giving a constant b/a ratio of 1.46. The only geometrical variable was the notch root radius, R. This was decreased from R = 6.5 mm for a blunt notch to R = 0.0727 mm for a sharp notch. The main dimensions of a typical notched bar specimen are shown in Figure 6.2(b). Some specimens had two notches separated by a centre-to-centre distance of 10 mm, as shown in Figure 6.2(c). Some of these were used after the test in simple optical metallography. The circumferential notches of different geometries were machined accurately into the gauge length using specially contoured cutting tools, excluding the case for the very sharp notch with a/R = 44.7, where the notch was machined by spark errosion. Dimensional details of all the specimens made can be found in Table 6.2. Samples of notched bar specimens before

and after creep testing are shown in Figure 6.3, for specimens having single and double notches machined into their gauge lengths.

6.3 EQUIPMENT

Two types of creep machine were used to obtain the data on the 2¼CM steel. One type is the standard constant load creep machine in which some uni-axial and all notched bar specimens were creep tested at 538°C. The second type was a modified creep machine (Figure 6.4), in which constant stress conditions are approximated by removing weights from the loading rod to compensate for the reduction in cross-sectional area with extension. Several uni-axial creep tests were carried out, using the constant stress creep machine.

6.3.1 Standard Creep Machine

Three dead-load creep machines were used during the course of the experiments, each having a lever ratio of 10:1 and a specially designed cylindrical furnace which provides the high temperature environment around the tested specimen. Each machine had two Nimonic 90 pull rods with a loading capacity of 10,000 lbs. Two shackles, also made from Nimonic 90, were connected to the pull rods, in which the plain bar specimens were clamped in position by a horizontal pin through each shackle. Specially designed clamps with internal M12 metric threads were connected to the shackles when the notched bar specimens with threaded ends were tested. These clamps were also made of Nimonic 90.

The three-zone electrical furnace was able to slide on a vertical guide rod. It was usually kept in its upmost position during the mounting of the specimens and other attachments (Figure 6.4(b)) and was then slid into position surrounding the specimen. The temperature was automatically controlled by a three-zone temperature controller, utilising resistance thermometers implanted in the furnace wall. The temperature controller produced a region of uniform temperature in its central zone.

During creep tests, temperatures were monitored using three

Chromel-Alumel thermocouples (type MA) equally spaced along the gauge length and firmly attached by heat resistant cords.

The test piece length extension was measured by a single LVDT (linear variable differential transformer), clamped centrally between aluminium plates attached to the end of Nimonic 75 extensometer legs. The LVDT had a maximum sensitivity of 10 mV output for each 0.2 mm travel of the armature and a total displacement range of ±51 mm. Strain measurements for all the creep tests were made on a Rikadenki chart recorder with a full scale setting of 10 mV to give a resolution of 0.38 mm.

A portable loading device was used to control the initial loading rate. It consisted of two screw-type jacks linked together and driven by a variable speed dc motor. This loading arrangement was used in all tests to prevent shock loading of the specimen.

Prior to creep testing, each specimen was partially loaded to check alignment and ensure that the extensometer system was working properly.

6.3.2 Constant Stress Creep Machine

A standard creep machine was modified and used by Cox [1981] to investigate the uni-axial creep properties of a nickel base alloy at high temperatures and constant stress conditions. The modifications involve adding two separate mechanisms to the standard creep machine. One mechanism consisted of a lever-mounted jockey compensating arrangement, shown in Figure 6.4(a). A screw rod is driven by a dc motor coupled to a commutator transmitter driven by a Honeywell recorder pen drive motor which was recording the creep strain. This gave a linear movement of the jockey, and hence a reduction in specimen load, directly proportional to the axial creep strain. Thus, a continual load compensation was made

while the specimen was deforming uniformly. The linear relation between the axial creep strain and load compensation is only valid before the onset of necking.

The second modification consisted of adding an automatic lever-levelling system, shown in Figure 6.4(b), to overcome the problem arising when high ductilities (approximately 30%) cause a change in lever level, therefore altering the effective lever ratio (nominally 10:1). This mechanism used a $\frac{1}{4}$ hp dc motor, activated by a micro-switch mounted close to the rear of the lever arm on the top platform, which drove the worm and pinion arrangement to relevel the lever arm. There was no shock loading from the motor and the lever arm was kept horizontal to within $\pm 2°$.

6.4 EXPERIMENTAL PROCEDURE

Before setting up the specimen in any of the creep machines described in the previous section, preliminary measurements of the specimen dimensions were made to an accuracy of 0.005 mm using a ×50 magnification projection shadowgraph to ensure that the dimensions were within an acceptable tolerance.

The universal joints and associated linkages prior to creep testing were checked for proper fitting and freedom of movement. The parts in the high temperature zone were coated with an anti-seizure compound (Copaslip) to prevent welding of mating parts during the test. Next, the loading lever was balanced using a counterweight on the front of the lever to ensure that the load exerted on the specimen is a true function of the weights placed at the back of the lever (10:1).

The specimen was then installed and the three thermocouples tied to the gauge length using heat resistant cords. The extensometry and transducer mechanisms were then attached and the transducer circuit set to give the requisite value of strain for 10 mV output. A load-extension test was then carried out using a Bryans X-Y recorder where an instant assessment could be made of the alignment of the specimen.

The furnace was then lowered so that the specimen was in the centre in both the axial and longitudinal directions. The ends were lightly packed to a depth of no more than 2 cm with Kaowool ceramic fibre, and the load-extension test was repeated to ensure that the extensometry was still moving freely.

The furnace was switched on with a deadweight stress in the specimen of 1.8 MPa to keep the universal joints and extensometry aligned. A 24 hour soak was allowed to fully stabilise the specimen, grips and extensometry temperature.

The required load was applied using a motorised jack which lowers the

weights onto the rear loading pan gradually. For the duration of the test, the output from the LVDT transducer and the thermocouples were continually recorded.

On failure of the test specimen, the falling action of the lever arm activates a micro-switch which switches off power to the furnace and hour meter. When the furnace had cooled, the specimen was extracted and labelled for future microstructural investigations.

The test procedure was similar when the constant stress machine was used. The only difference was that both the mounted jockey compensation mechanism and the automatic lever levelling system had to be adjusted and switched on before loading.

6.5 RESULTS

Creep tests were carried out on the 2¼CM steel at 538°C ±1°C. The test temperature is of practical relevance and corresponds to approximately $0.5T_m$. In this section, the results of these tests and those carried out on the ½%Cr ½%Mo ¼%V steel by Ng, et al. [1980] are presented.

6.5.1 Uni-Axial Constant Load Creep Tests

Creep tests on plain bar specimens were carried out using three standard creep machines described in Section 6.3.1. The loads were chosen to give stresses on the initial cross-sectional area of the specimen in the range of 200 to 125 MPa which gave rupture lives between approximately 10 and 900 hours. The results of these tests are summarised in Table 6.3 and the strain-time curves are shown in Figures 6.5 and 6.6.

The creep curves for all the specimens exhibited short primary and secondary regions, but a relatively long and very pronounced tertiary region. A slight increase in both the creep ductility, from about 40% to 48%, and the reduction in area, from about 83% to 90%, is observed as the applied stress decreases. This can only be explained in terms of (a) decreasing cavity spacing with increasing stress, and/or (b) true tertiary being caused by mechanical instability which is n-dependent.

6.5.2 Uni-Axial Constant Stress Creep Tests

Constant stress creep tests were carried out on plain bar specimens using the modified creep machine described in Section 6.3.2. The applied stress in each test was kept constant by reducing the load as the creep strain accumulates, using the constant stress compensation mechanism. The assumption used to calibrate the jockey movement with the specimen axial strain was that all the creep deformation is plastic strain and a constant volume condition exists.

Stresses in the range of 220 to 125 MPa were applied which gave rupture lives between approximately 20 and 4000 hours. The results of these tests are summarised in Table 6.4 and the strain-time curves are shown in Figures 6.7 and 6.8. Small primary and tertiary regions, and a very pronounced secondary region, are observed in all the creep curves. A slight increase in creep ductility from about 40% to 48% as the applied stress decreases is again observed. However, the reduction in area remained nearly constant at about 88.5% for all stresses.

6.5.3 Notched Bar Creep Tests

Notched specimens, having the same throat diameter as the plain specimens, were machined to give a constant b/a ratio and a/R between 0.5 and 44.7, as shown previously in Table 6.2. These specimens were creep tested in the ordinary dead-load creep machines described in Section 6.3.1. The loads were selected to give constant nominal stress levels across the notch throat, σ_{nom}, of 200 and 175 MPa. Axial elongations were measured continuously along the gauge length of all the samples and were converted to nominal strains by dividing by the initial notch height, ℓ_o. The strains due to the reduction in area were also calculated using the shadowgraph measurements of the initial and rupture throat diameters, $2a_o$ and $2a$. The results of these tests are listed in Table 6.5 for σ_{nom} = 200 and 175 MPa. It is observed that the nominal strains due to the axial elongation have no significant pattern; however, the strains due to the reduction in area dropped from a uni-axial constant stress value of about 89% to about 67% as the notch sharpness increased.

The lives of the notched bars, t_R, have been plotted in Figure 6.9 for all a/R values and the two nominal stresses. For blunt notches, the lives increase progressively for both stress levels as notch sharpness (a/R) increases. For sharp notches, there is a tendency for

the lives to decrease and then remain approximately constant with further increase in a/R. The rupture times when $a/R = 0$ (uni-axial) were taken from the plain bar constant stress results given in Table 6.4, with the applied stress equal to 200 and 175 MPa, respectively.

6.5.4 Cumulative Damage Notched Bar Creep Tests

Four creep tests were conducted on notched bars, in which the nominal stress was changed from 200 to 175 MPa and vice versa to examine Robinson's linear cumulative damage rule discussed in Chapter 1, Section 1.2.1, and defined by the following equation:

$$D = \sum \frac{t_i}{t_{R_i}} \tag{6.1}$$

where $D = 1$ at rupture. Two of the specimens tested had blunt notches with $a/R = 1.67$; the other two had sharp notches with $a/R = 13$. The results of these tests are listed in Table 6.6. The sum $\{(t_1/t_{R_1}) + (t_2/t_{R_2})\}$ is shown to be equal to approximately 1, which suggests that Robinson's life fraction rule is valid for this material within the small stress range investigated.

6.5.5 Experimental Data on the ½%Cr ½%Mo ¼%V Steel

Ng, Webster and Dyson [1980] carried out some creep tests on two blocks, labelled as 4F and 10G, of the ½CMV steel used for high temperature applications in steam power generation equipment. They creep tested in tension a number of plain bar and notched bar specimens at a temperature of 565°C. The loads for the plain bar specimens were chosen to give stresses in the range 220 to 400 MPa and rupture lives between about 5 and 430 hours, as shown in Table 6.7. The loads on the notched specimens were selected to give a nominal stress of 300 MPa across the

notch throat. The notched bar data for blocks 4F and 10G are listed in Table 6.8.

6.5.6 Optical Metallography

After fracture, some notched specimens of the 2¼CM and ½CMV steels were slit longitudinally to within 0.1 mm of the gauge length centre-line, polished and etched for examination by optical microscopy. They were:

(a) A double notched specimen with a/R = 1.67 of the 2¼CM steel. The photographs shown in Figure 6.10 are of the notch which has not failed after the creep test.

(b) A double notched specimen with a/R = 13 of the 2¼CM steel. The photographs shown in Figure 6.11 are of the complete section of the specimen, showing the two notches.

(c) A notched specimen with a/R = 0.297 (10GA7) of the ½CMV steel, as shown in Figure 6.12.

(d) A notched specimen with a/R = 1.961 (10GA1) of the ½CMV steel, as shown in Figure 6.13.

6.6 DATA ANALYSIS AND DISCUSSION

6.6.1 Uni-Axial Data

The uni-axial constant load and constant stress creep curves for the 2¼CM steel exhibit primary, secondary and tertiary regions. However, the overall behaviour of this material under constant load is dominated by a long tertiary region, while under constant stress, it is dominated by a long secondary region, as shown in Figures 6.5 to 6.8.

The common way of presenting uni-axial creep data is to plot log/log graphs of the minimum creep rate against time and stress against time. The best fits for each set of data for the 2¼CM and ½CMV steels are shown in Figures 6.14 to 6.17. The secondary creep material coefficients for each material were evaluated from the log $\dot{\varepsilon}_s$ - log t_R graphs (Figures 6.14 and 6.16) and were found to have the following values:

(a) For the 2¼CM steel:

$$\dot{\varepsilon}_s = C\,\sigma^n$$

where:

$$C = 2.5156 \times 10^{-25}\ 1/[\text{MPa}]^n\text{h} \qquad (6.2)$$

and: $n = 9.77$

(b) For the ½CMV steel:

$$\dot{\varepsilon}_s = C\,\sigma^n$$

where:

$$C = 2.2 \times 10^{-46} \ 1/[\text{MPa}]^{n_h} \tag{6.3}$$

and: $n = 16.66$

In the logarithmic stress-time graph for the 2¼CM steel (Figure 6.15), the experimental constant load and constant stress rupture times are presented and compared with some theoretical predictions. The theoretical rupture times under constant stress were calculated using Norton's equation for secondary creep rate (equation (1.3)) with the assumption that the nominal stress remains constant throughout the test. The result is:

$$t_R = \frac{\varepsilon_R}{\dot{\varepsilon}_s} \tag{6.4}$$

The above equation represents an upper bound for rupture times under constant stress, as shown in Figure 6.15. Under constant load, Hoff's equation (1.11), derived in Chapter 1, Section 1.2.2, was used to calculate the rupture times. The analysis is based on the assumption that the initial cross-sectional area, A_0, of the test piece will shrink to zero under a constant applied load, P, without any change in volume. The result is:

$$t_R^L = \frac{1}{n \dot{\varepsilon}_s} \tag{6.5}$$

The above equation is only valid for ductile materials failing by necking and not by internal damage. It represents an upper theoretical bound, as shown in Figure 6.15. The ratio between the predicted rupture times under constant stress and load can simply be found by dividing equation (6.4) by equation (6.5). The result is:

$$\frac{t_R}{t_R^L} = n\,\varepsilon_R \qquad (6.6)$$

A similar linear expression to equation (6.6) was previously reached in Chapter 5, Section 5.4.2 (equation (5.20)), from Ashby's equations for rupture times under constant stress and constant load for materials failing by power-law creep alone. The assumption used was that the initial area fraction of voids, f_i, is very small ($f_i \ll 1$), and therefore negligible.

The experimental and theoretical predictions of the rupture times under constant stress and constant load and their ratios are summarised in Table 6.9. It is observed that the theoretical predictions always over-estimate the experimental rupture times; however, the ratios t_R/t_R^L are approximately constant.

6.6.2 Notched Bar Data

The notch rupture lives versus notch sharpness (a/R) for the 2¼CM steel specimens were previously presented in Figure 6.9. The results for the two nominal stresses of 200 and 175 MPa indicate that, no matter how severe the notch sharpness is, this material will not exhibit notch weakening. The condition is that the geometrical ratio b/a remains constant for all specimens and equal to 1.46. This can be observed clearly when the data are presented in terms of time strength ratio t_{no}/t_{un}, as shown in Figure 6.18. The time strength ratio for σ_{nom} = 200 MPa increases from a uni-axial value of 1 to a maximum value of about 45, as a/R increases from zero to about 6. With further increase in notch sharpness, the strength ratio drops to about 40 and remains constant for all values of $a/R > 10$. However, when the nominal stress is 175 MPa, it is observed from the few data points shown in Figure 6.18 that the strength for the sharp notch with a/R = 13 has dropped to about 22,

indicating that for the 2¼CM steel the data are strain rate sensitive. The uni-axial rupture time, t_{un}, used to normalise the data in Figure 6.18, is equivalent to either 46 or 170 hours. These times correspond to an applied constant stress of either 200 or 175 MPa, respectively.

The data published by Ng, Webster and Dyson [1980] on the ½CMV steel showed an overall behaviour different from that of the 2¼CM steel. Block 10G exhibits only notch strengthening, while block 4F always showed notch weakening when the time strength ratio, t_{no}/t_{un}, is plotted against notch sharpness, a/R, as shown in Figure 6.19. The uni-axial rupture time used to normalise the notch data is equivalent to 41 hours at σ_{nom} = 300 MPa, as shown previously in Figure 6.17. The maximum notch strengthening for the 10G block is about 6 which corresponds to a notch sharpness of about 1.5. No data are available for values of $a/R > 2$ and $a/R < 17$, therefore it is assumed that the strength will drop in the way shown in Figure 6.19 to about 1.02 when $a/R = 17$. Block 4F exhibited hardly any notch strengthening and the lowest time strength ratio for the sharpest notch is about 0.5. The uni-axial rupture time used to normalise the data is also 41 hours.

6.6.3 Metallurgical Observations

The fracture characteristics of the 2¼CM and ½CMV steels were investigated using simple optical metallography. The results of these investigations were reported in Section 6.5.6, Figures 6.10 to 6.13. A fibrous type of failure is observed in the fractured surfaces of the 2¼CM steel, while the ½CMV steel shows a clear intergranular type of failure.

In the case of the 2¼CM steel, grains in the vicinity of the fractured surfaces deformed considerably before failure. No damage in terms of voids or microcracks can be observed away from the fractured

surface of the sharp notch investigated (Figure 6.11). The longitudinal section of the second unfractured blunt and sharp notches, shown in Figures 6.10 and 6.11, shows no evidence of voiding or severe deformation relatively early in life for these geometries. Machining inaccuracy or initial internal damage could be blamed for this, since it was expected that both notches were to deform simultaneously until about 0.5 to 0.8 of the total rupture time and then one notch will dominate the overall behaviour until failure.

The fractured surfaces of the blunt and sharp notches of the ½CMV steel, shown in Figures 6.12 and 6.13, show a distinct intergranular type of failure which coincides with the low ductility reported during the creep tests (less than 1%) (Tables 6.7 and 6.8).

Some attempts were made to use transmission electron microscopy for higher magnifications which can lead to quantitative measurements of voids and their approximate initial sizes in both materials. The lack of superior polishing equipment and the expertise required for these types of magnifications terminated these attempts.

6.7 CONCLUSIONS

Creep tests at 538°C have been carried out on plain and notched bar specimens pulled in tension. The material tested was the 2¼%Cr 1%Mo steel. Some plain bar specimens were creep tested under constant stress conditions using a modified dead-load creep machine. Other creep data on the brittle ½%Cr ½%Mo ¼%V steel, available in the literature, were also given for the purpose of comparison.

Simple analysis on the uni-axial data revealed that the secondary creep coefficients are as follows:

(a) $n = 9.77$ and $C = 2.5156 \times 10^{-25}$ $1/[\text{MPa}]^n\text{h}$ for the 2¼%Cr 1%Mo steel.

(b) $n = 16.66$ and $C = 2.2 \times 10^{-46}$ $1/[\text{MPa}]^n\text{h}$ for the ½%Cr ½%Mo ¼%V steel.

Theoretical estimates of uni-axial rupture times under constant load and constant stress conditions were given for the 2¼CM steel. They always predicted higher rupture times than the experimental values, and are therefore considered as upper bounds.

The notched bar data on the 2¼CM steel showed that no matter how severe the notch sharpness is, this material will always notch strengthen. The results have been discussed and compared with the notch data on the ½CMV steel which exhibits both notch strengthening and weakening.

Cumulative damage creep tests have been carried out on some notched bar specimens made of 2¼CM steel, between two nominal stress levels of 200 and 175 MPa and vice versa. The rupture times were analysed using Robinson's life fraction rule which was found to be valid for this material when the stresses fluctuate between the above two nominal stresses.

TABLE 6.1

Chemical Compositions of Materials

(a) 2¼%Cr 1%Mo steel

% Weight												
C	Si	Mn	S	P	Ni	Cr	Mo	Al	Zr	Ti	Cu	Sn
0.12	0.34	0.59	0.005	0.015	0.19	2.4	1.0	0.02	0.01	0.034	0.07	0.01

(b) ½%Cr ½%Mo ¼%V steel

	% Weight																	
Cast	C	Mn	Mo	V	Cu	Sn	Al	Ce	Ti	Zr	Cr	S	P	Si	Ni	Nb	Co	As	Sb
4F	0.11	0.36	0.42	0.22	0.07	0.005	0.019	0.002	0.005	0.001	0.37	0.012	0.012	0.29	0.05	0.005	0.01	0.011	0.0015
10G	0.08	0.37	0.69	0.33	0.06	0.005	0.005	0.025	0.005	0.002	0.42	0.013	0.012	0.48	0.05	0.008	0.012	0.011	0.0025

TABLE 6.2

Dimensions of the Circumferentially Notched Bar Specimens

a/R	$2a$ (mm)	$2R$ (mm)	$2b$ (mm)	ℓ_o (mm)	G (mm)
0.5	6.55	13.1	9.57	8.206	25.41
1.0	6.517	6.517	9.52	5.705	25.4
1.0	6.515	6.515	9.52	5.705	25.395
1.67	6.49	3.892	9.485	3.77	25.4
1.67	6.5	3.892	9.5	3.77	25.415
1.67*	6.5	3.892	9.5	3.77	25.41
2.6	6.482	2.49	9.473	2.49	25.398
4.0625*	6.475	1.594	9.46	1.6	25.395
5.0	6.5024	1.3	9.503	1.334	25.41
6.5	6.48	0.995	9.47	1.0	25.411
9.285*	6.481	0.696	9.47	2.45	25.4
13.0*	6.55	0.504	9.572	2.54	25.398
13.0*	6.495	0.5	9.492	2.53	25.398
13.0	6.497	0.5	9.495	2.53	25.398
21.66*	6.52	0.301	9.52	2.57	25.41
44.7*	6.48	0.145	9.47	0.145	25.4

* The specimen has two notches

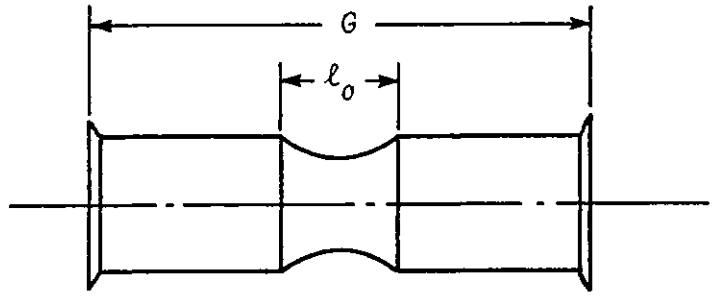

TABLE 6.3

Uni-Axial Constant Load Creep Test Results at 538°C for the 2¼%Cr 1%Mo Steel

Number	d_o (mm)	ℓ_o (mm)	Stress (MPa)	d (mm)	ℓ (mm)	t_R (h)	$\%\varepsilon_R = \frac{\ell - \ell_o}{\ell_o}$	$\%\varepsilon_R = \frac{d_o^2 - d^2}{d_o^2}$	$\dot{\varepsilon}_s$ (1/h)
18	6.502	37.85	200	2.54	54.35	8.5	43.6	84.7	8.05×10^{-3}
11	6.515	37.84	198	2.635	53.55	9.93	41.5	83.6	9.1×10^{-3}
14	6.55	37.88	185	2.524	55.6	33.25	47.7	85.1	2.59×10^{-3}
10	6.525	37.57	168	2.35	55.14	52.92	46.6	87.0	1.8×10^{-3}
13	6.515	37.86	152	2.27	55.9	186.2	47.65	87.7	5.09×10^{-4}
15	6.55	37.81	141	2.11	55.82	425.26	47.63	89.7	1.77×10^{-4}
12	6.55	37.87	125	1.994	56.0	875.0	47.87	90.7	1.03×10^{-4}

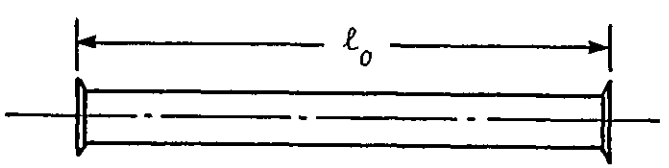

TABLE 6.4

Uni-Axial Constant Stress Creep Test Results at 538°C for the 2¼%Cr 1%Mo Steel

Number	d_o (mm)	ℓ_o (mm)	Stress (MPa)	Jockey Load (N)	d (mm)	ℓ (mm)	t_R (h)	$\%\varepsilon_R = \frac{\ell - \ell_o}{\ell_o}$	$\%\varepsilon_R = \frac{d_o^2 - d^2}{d_o^2}$	$\dot{\varepsilon}_s$ (1/h)
9	6.5024	38.1	220	5.67	2.26	53.15	22.4	39.5	87.9	1.367×10^{-2}
8	6.5024	37.95	200	5.255	2.221	53.47	46.9	40.9	88.3	7.07×10^{-3}
2	6.527	37.9	175	4.77	2.153	55.5	148.7	46.3	89.1	2.15×10^{-3}
4	6.517	37.81	160	4.15	2.155	55.63	414.3	47.15	89.0	7.16×10^{-4}
7	6.517	37.88	125	3.25	2.15	55.91	4233.0	47.6	89.1	9.6×10^{-5}

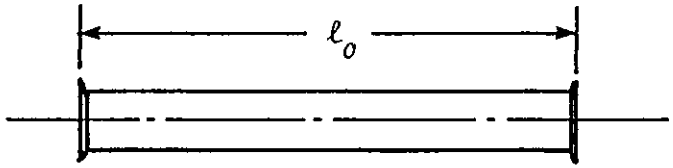

TABLE 6.5

Notched Bar Creep Test Results at 538°C for the 2¼%Cr 1%Mo Steel

a/R	t_R (h)	ℓ_o (mm)	ℓ (mm)	$2a_o$ (mm)	$2a$ (mm)	$\%\epsilon_R = \frac{\ell - \ell_o}{\ell_o}$	$\%\epsilon_R = \frac{a_o^2 - a^2}{a_o^2}$
σ_{nom} = 200 MPa							
1.0	639.4	5.705	8.357	6.517	2.87	46.5	80.6
1.67	779.8	3.77	5.487	6.49	2.96	45.56	79.33
1.67*	850.8	3.77	5.442	6.5	2.944	44.36	79.48
2.6	1064.5	2.49	4.504	6.482	3.01	80.88	78.4
4.0625*	1533.2	1.6	2.979	6.475	3.057	86.19	77.7
5.0*	1860.5	1.334	2.745	6.5024	3.08	105.8	77.56
6.5	2262.0	1.0	1.86	6.48	3.12	86.0	76.81
9.285*	1779.0	2.45	4.0915	6.481	3.34	67.0	73.4
13.0	1885.2	2.53	4.296	6.495	3.395	69.8	72.67
13.0*	1738.1	2.54	4.32	6.55	3.43	70.1	72.57
21.66*	1872.1	2.57	3.998	6.52	3.403	55.58	72.7
44.7*	1960.4	0.145	0.3175	6.48	3.68	118.9	67.75
σ_{nom} = 175 MPa							
0.5	595.12	8.206	10.75	6.55	2.781	31.0	81.97
1.0	1146.5	5.705	8.152	6.515	2.83	42.9	81.13
1.67	1788.4	3.77	5.447	6.5	2.906	44.5	80.0
13.0*	3799.4	2.53	4.74	6.495	3.485	87.33	71.2

* The specimen had two notches

TABLE 6.6

Cumulative Damage Notched Bar Creep Tests at

538°C for the 2¼%Cr 1%Mo Steel

a/R	σ_{nom_1} (MPa)	σ_{nom_2} (MPa)	t_{R_1} (h)	t_{R_2} (h)	t_1	t_2	D
1.67	200	175	840	1800	420	939	1.021
1.67	175	200	1800	840	900	434	1.016
13.0	200	175	1800	3800	900	1892	0.998
13.0	175	200	3800	1900	1900	940.5	0.995

TABLE 6.7

Uni-Axial Constant Load Creep Test Results at 565°C for the ½%Cr ½%Mo ¼%V Steel

Block 4F					Block 10G				
Number	Stress (MPa)	t_R (h)	$\%\varepsilon_R = \frac{\ell - \ell_o}{\ell_o}$	$\dot{\varepsilon}_s$ (1/h)	Number	Stress (MPa)	t_R (h)	$\%\varepsilon_R = \frac{\ell - \ell_o}{\ell_o}$	$\dot{\varepsilon}_s$ (1/h)
4F8	375	4.31	4.2	5.17×10^{-1}	10G4	350	6.1	2.79	2.34×10^{-1}
4F7	350	13.06	1.18	3.71×10^{-2}	10G2	300	47.0	1.29	9.67×10^{-3}
4F1	300	39.2	0.3	2.85×10^{-3}	10G6	275	135.0	0.417	1.09×10^{-3}
4F5	275	87.46	0.312	1.23×10^{-3}	10G3	250	187.5	0.39	8.42×10^{-4}
4F3	246	131.0	0.17	5.83×10^{-4}	10G5	240	325.9	0.234	2.5×10^{-4}
4F4	226	428.9	0.245	2.18×10^{-4}	10G1	229	300.0	0.24	3.13×10^{-4}

TABLE 6.8

Notched Bar Creep Test Results at 565°C for the ½%Cr ½%Mo ¼%V Steel

σ_{nom} = 300 MPa, uni-axial t_R = 41 hours, and b/a = 1.67							
Block 4F				Block 10G			
Number	a/R	t_R (h)	$\%\varepsilon_R$*	Number	a/R	t_R (h)	$\%\varepsilon_R$*
4F1J	0.29	43.0	0.084	10GA5	0.0	63.4	0.625
4F1K	0.72	30.1	0.0925	10GA7	0.297	215.7	0.17
4F1C	1.0	24.85	0.052	10GA3	0.974	240.45	0.09
4F1B	1.49	24.0	0.032	10GA2	1.541	239.9	0.02
4F1E	2.0	13.2	0.05	10GA1	1.961	185.5	0.074
4F1F	18.0	23.2	0.15	10GA8	17.0	49.4	0.056

* Measured over the specimen gauge length

TABLE 6.9

Experimental and Theoretical Predictions of Rupture Times for the 2¼CM Steel

(Material constant, n = 9.77)

Stress (MPa)	$\dot{\varepsilon}_\delta$ (1/h)	$\%\varepsilon_R^* = \frac{\ell - \ell_o}{\ell_o}$	Experimental			Theoretical		
			t_R^* (h)	t_R^L (h)	t_R/t_R^L	$t_R^\dagger$ (h)	$t_R^{L\S}$ (h)	$t_R/t_R^{L\P}$
220	1.367×10^{-2}	39.5	22.4	-	-	28.9	-	-
200	7.07×10^{-3}	40.9	46.9	9.5	4.93	57.85	14.5	4.0
175	2.15×10^{-3}	46.3	148.7	36.0	4.13	215.3	47.6	4.52
160	7.16×10^{-4}	47.15	414.3	95.0	4.36	658.5	142.9	4.6
125	9.6×10^{-5}	47.6	4233.0	875.0	4.83	4958.0	1066.2	4.65

* Constant stress data

† Equation (6.4): $t_R = \varepsilon_R/\dot{\varepsilon}_\delta$

§ Equation (6.5): $t_R^L = 1/(n\,\dot{\varepsilon}_\delta)$

¶ Equation (6.6): $t_R/t_R^L = n\,\varepsilon_R$

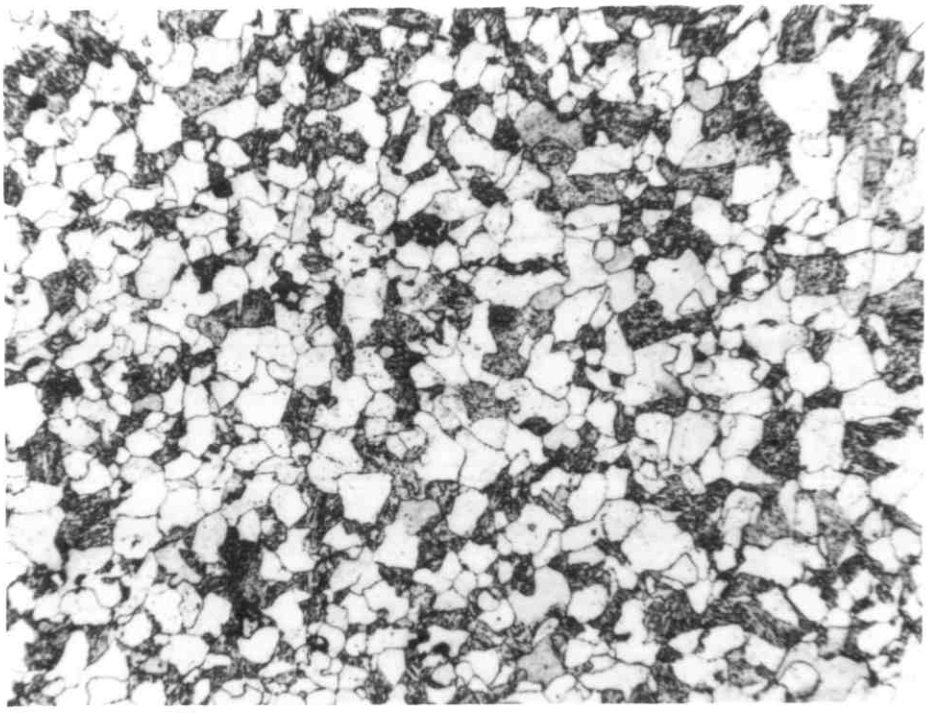

a. $2\frac{1}{4}$%Cr 1%Mo X109

b. $\frac{1}{2}$%Cr $\frac{1}{2}$%Mo $\frac{1}{4}$%V X109

Figure 6.1:Microstructure of ;(a)2¼%Cr 1%Mo steel ;(b)½%Cr ½%Mo ¼%V steel

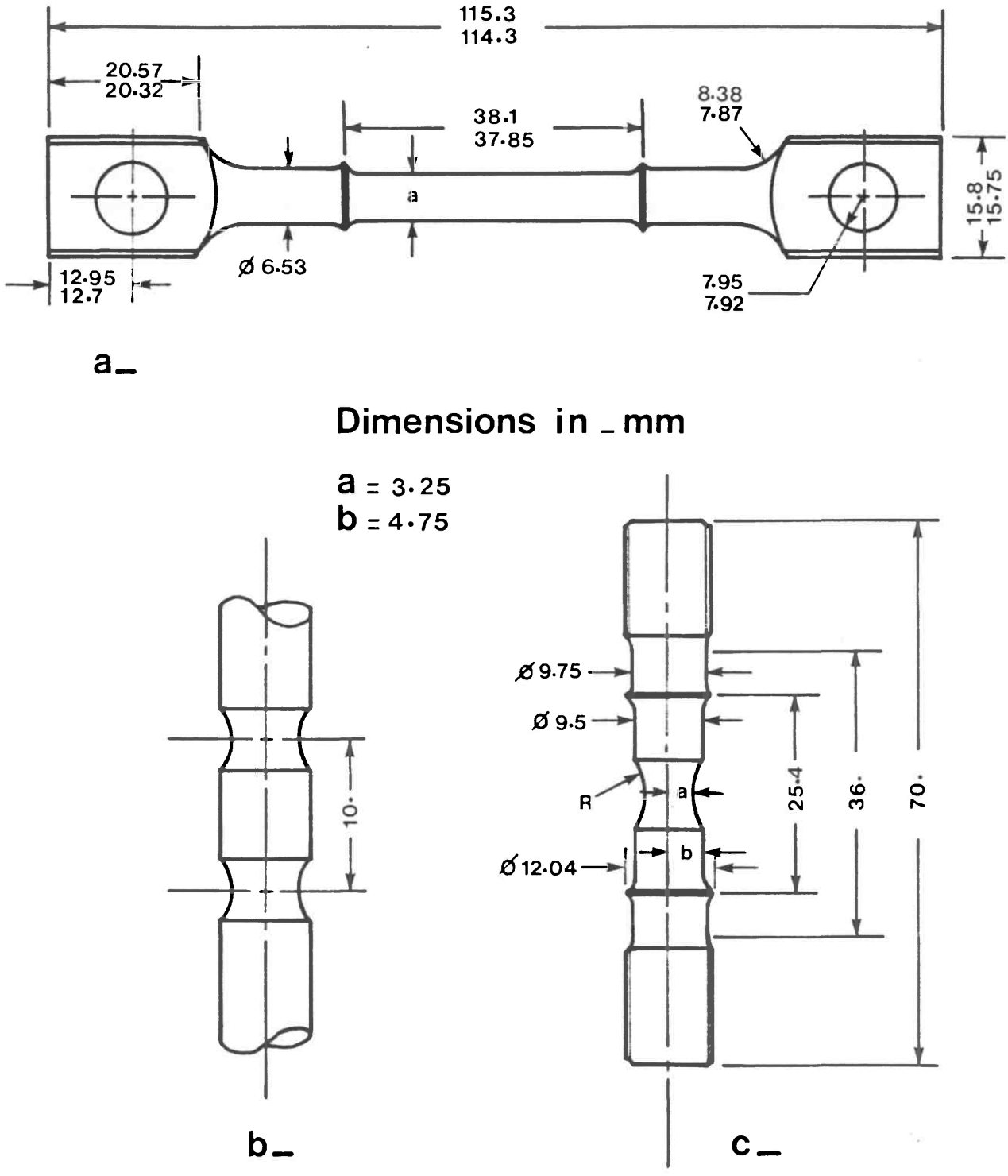

Figure 6.2: Dimensions of the plain tensile and circumferentially notched bar specimens

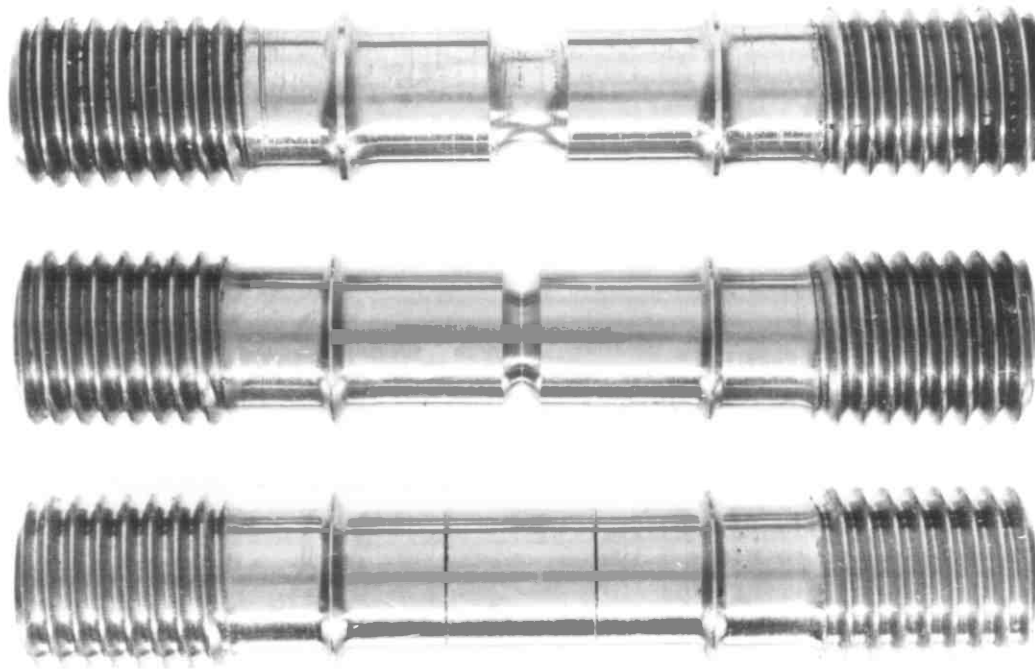

a- From top to bottom a/R = 1 , 13 , 44.7

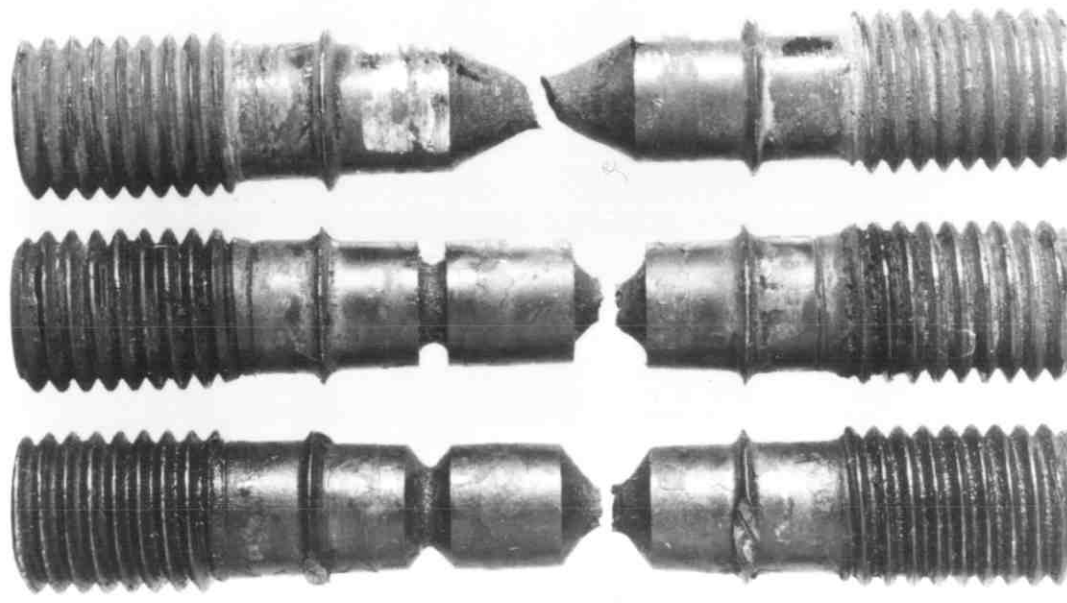

b- From top to bottom a/R = 0.5 , 5 , 21.66

Figure 6.3: A selection of notched bar specimen ;(a)Untested ;(b)Tested .

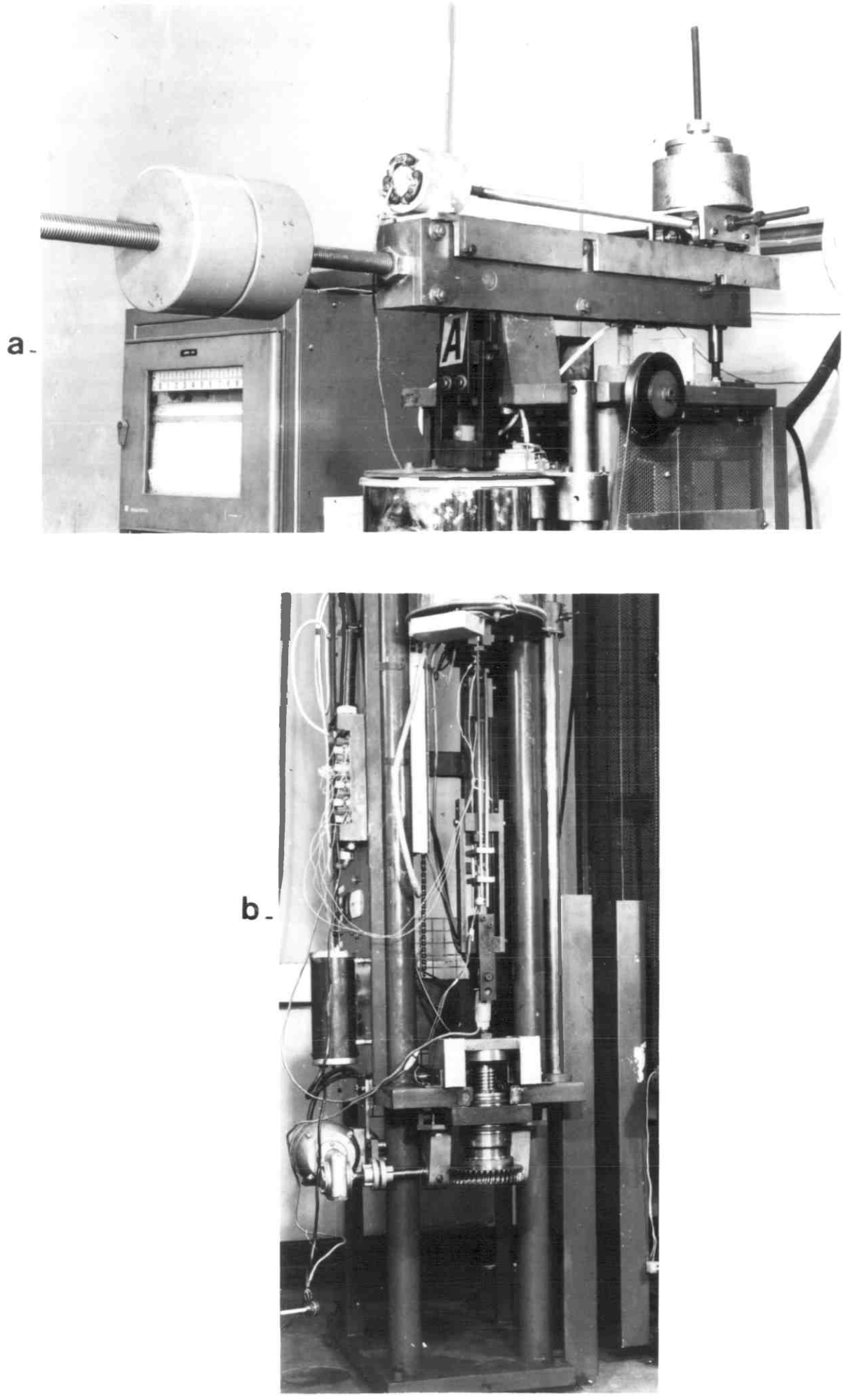

Figure 6.4. General view of constant stress creep machine .

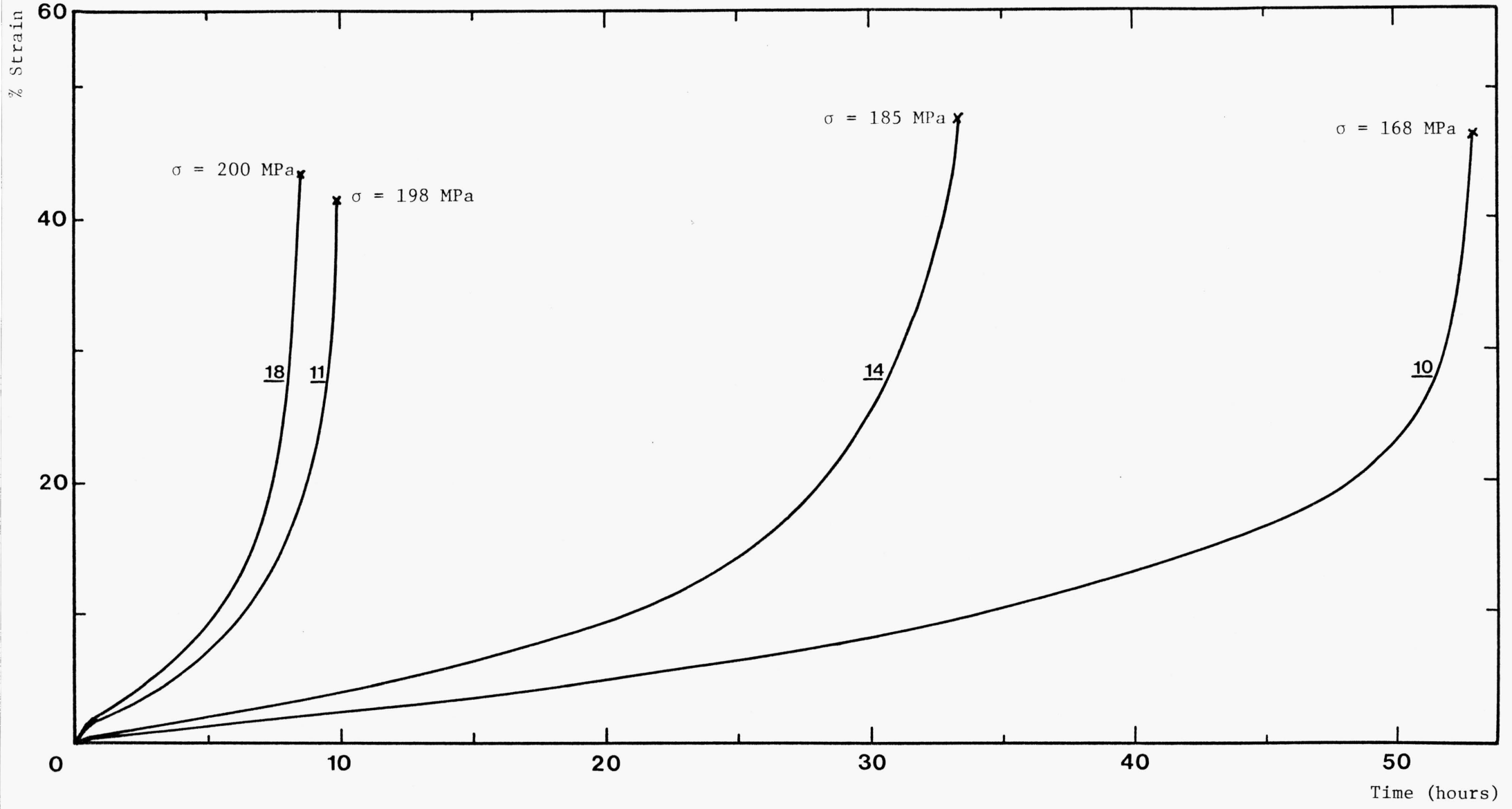

Figure 6.5: Uni-axial constant load strain-time creep curves at 538°C for some $2\frac{1}{4}$%Cr 1%Mo steel specimens

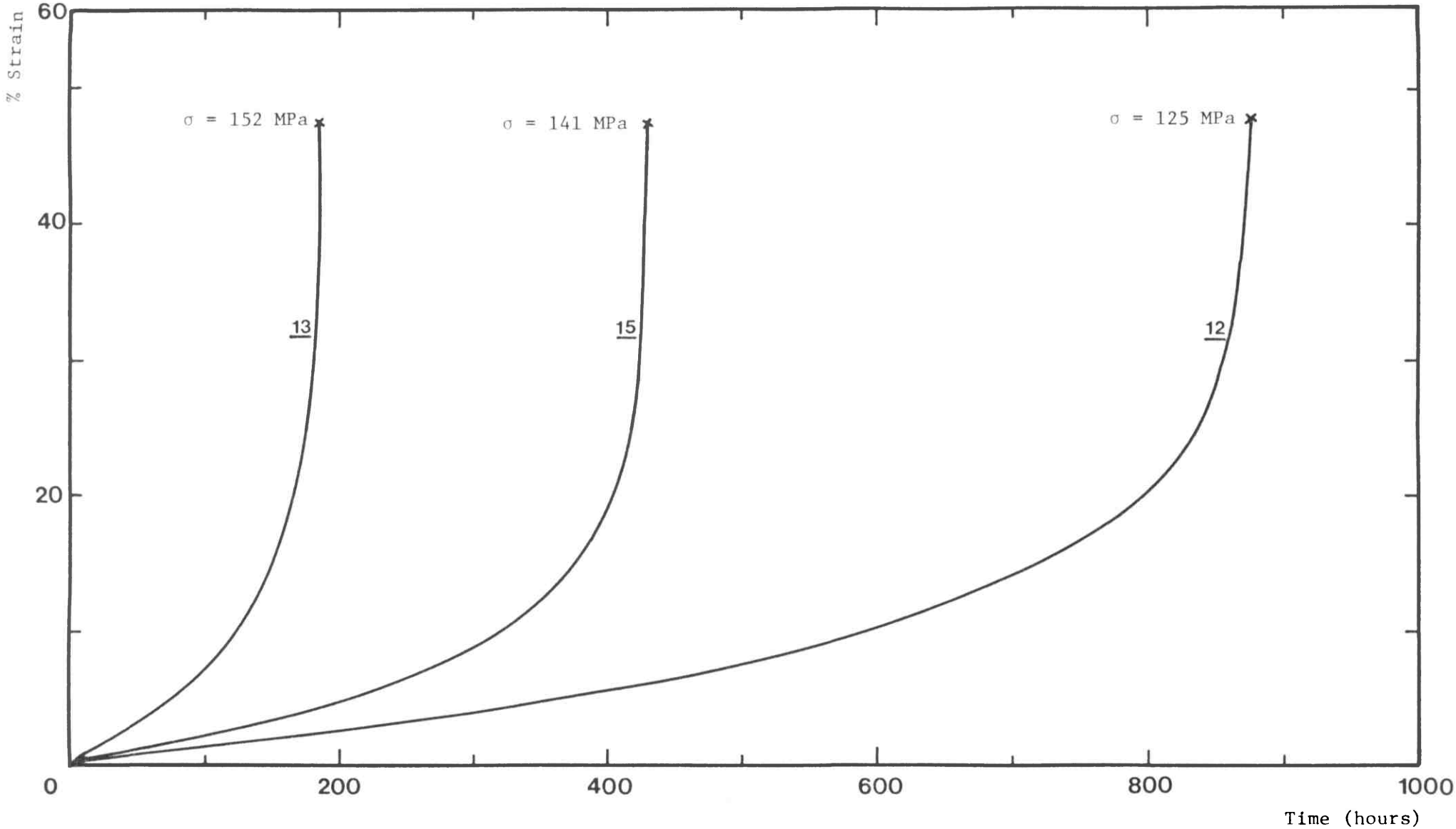

Figure 6.6: Uni-axial constant load strain-time creep curves at 538°C for some 2¼%Cr 1%Mo steel specimens

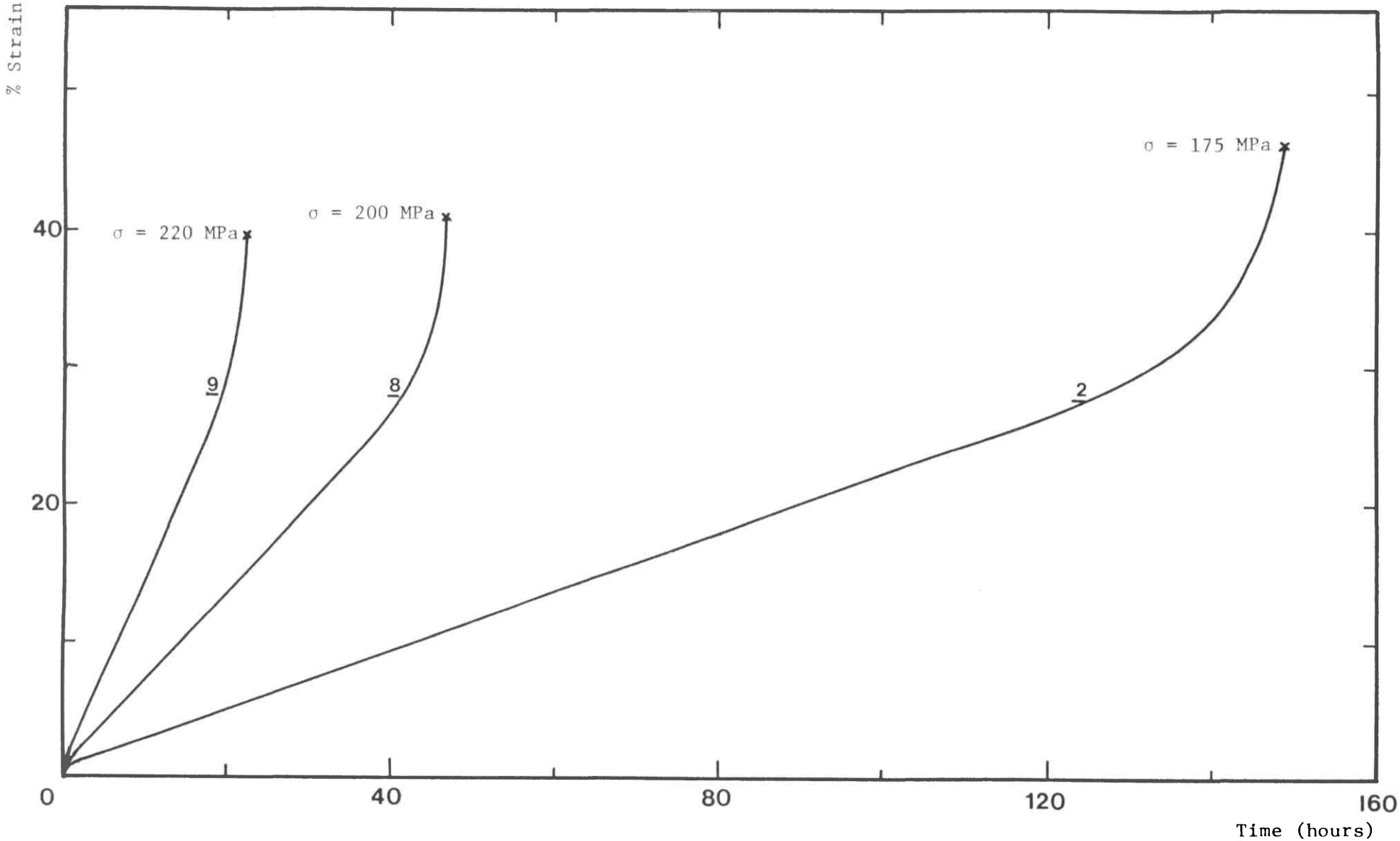

Figure 6.7: Uni-axial constant stress strain-time creep curves at 538°C for some 2¼%Cr 1%Mo steel specimens

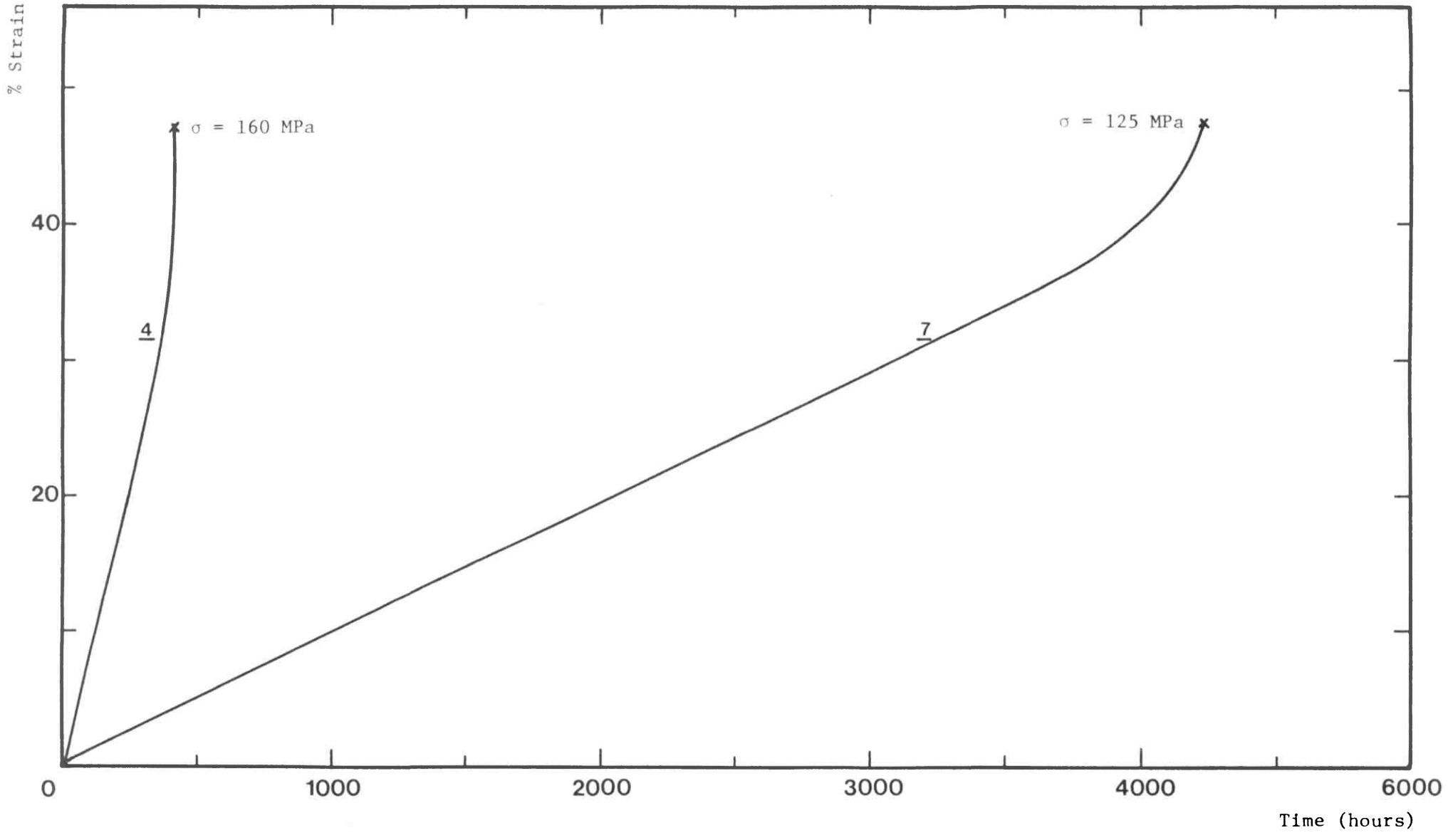

Figure 6.8: Uni-axial constant stress strain-time creep curve at 538°C for some 2¼%Cr 1%Mo steel specimens

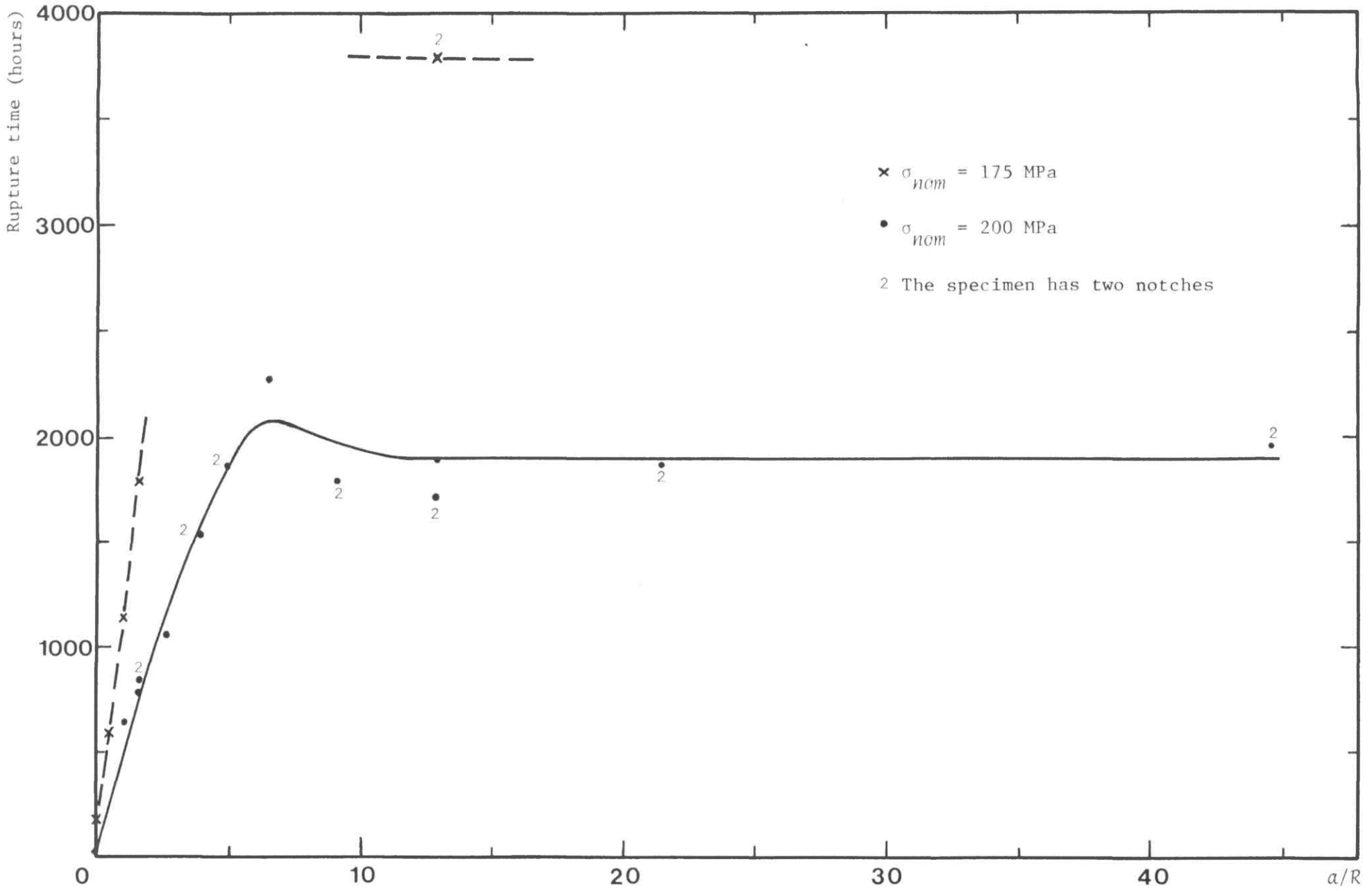

Figure 6.9: Rupture life versus notch sharpness for the 2¼%Cr 1%Mo steel specimens tested at 538°C

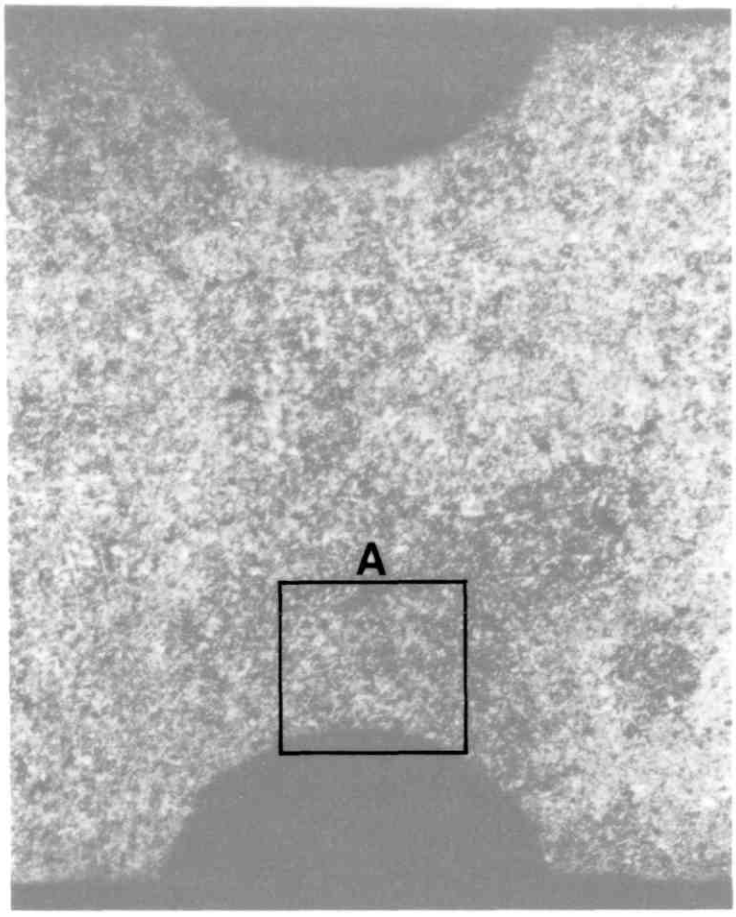

X 11

b/a : 1.46
a/R : 1.67

Area - A

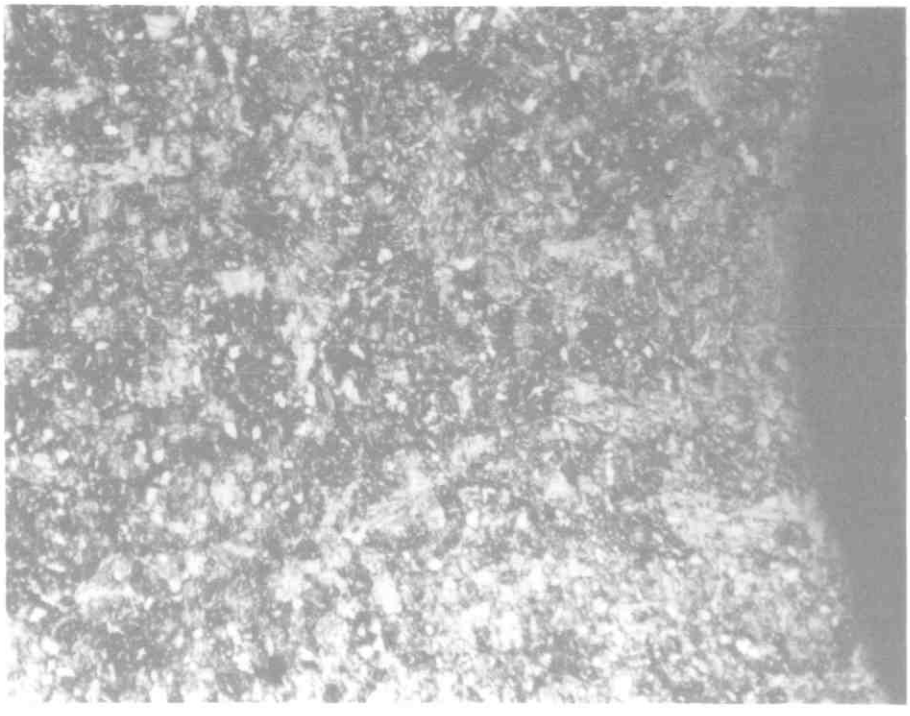

X 48

Figure 6.10: Longitudinal section of unfractured notch of a 2¼%Cr 1%Mo double notched round bar specimen with b/a=1.46 and a/R=1.67 .

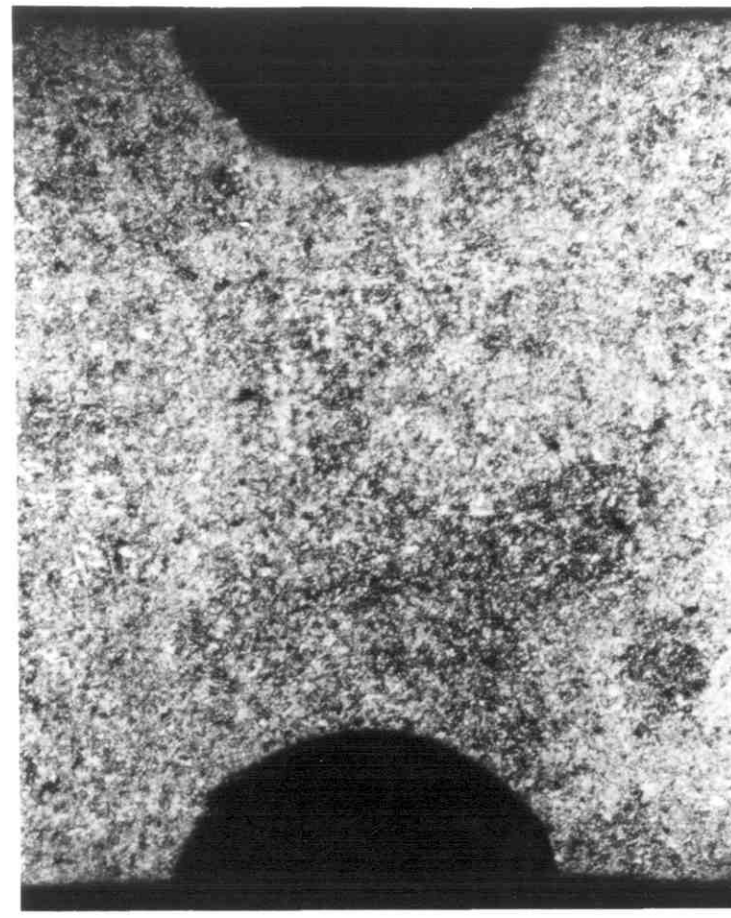

X 11

b/a : 1.46

a/R : 1.67

Area - A

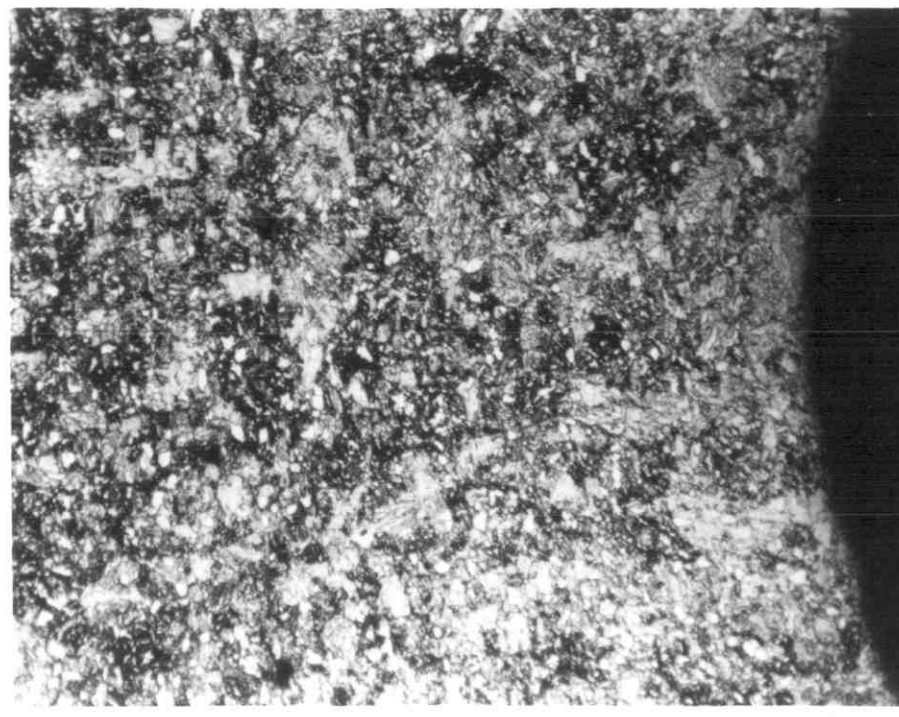

X 48

Figure 6.10: Longitudinal section of unfractured notch of a 2¼%Cr 1%Mo double notched round bar specimen with b/a=1.46 and a/R=1.67 .

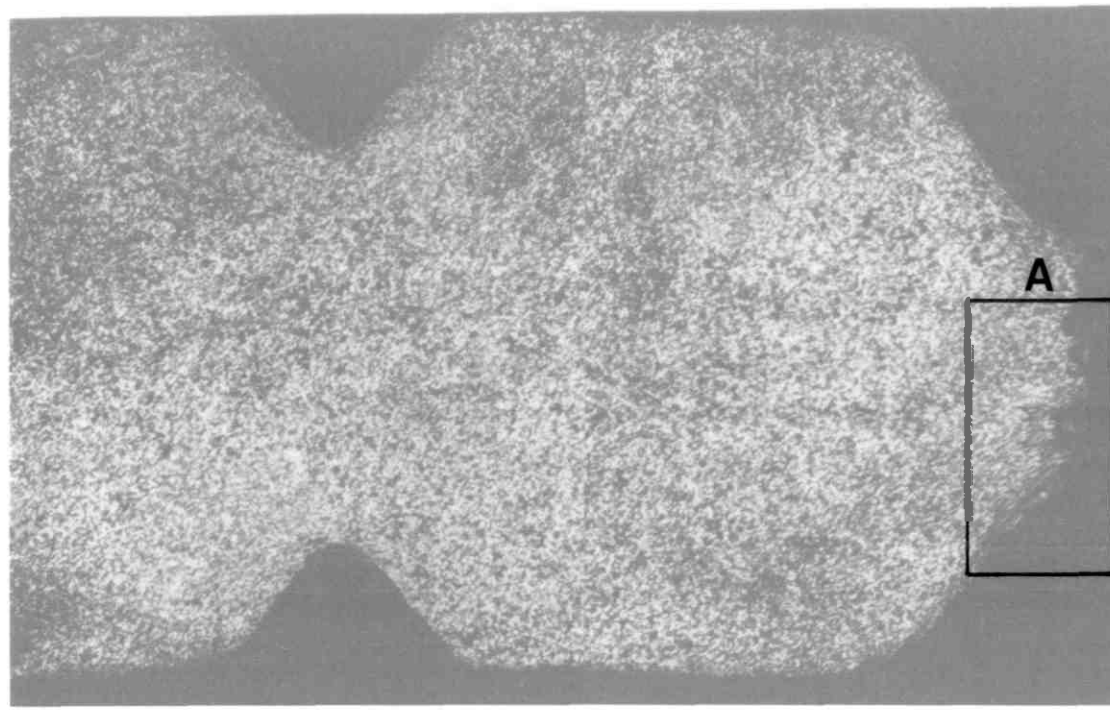

X11

b/a = 1.46

a/R = 13

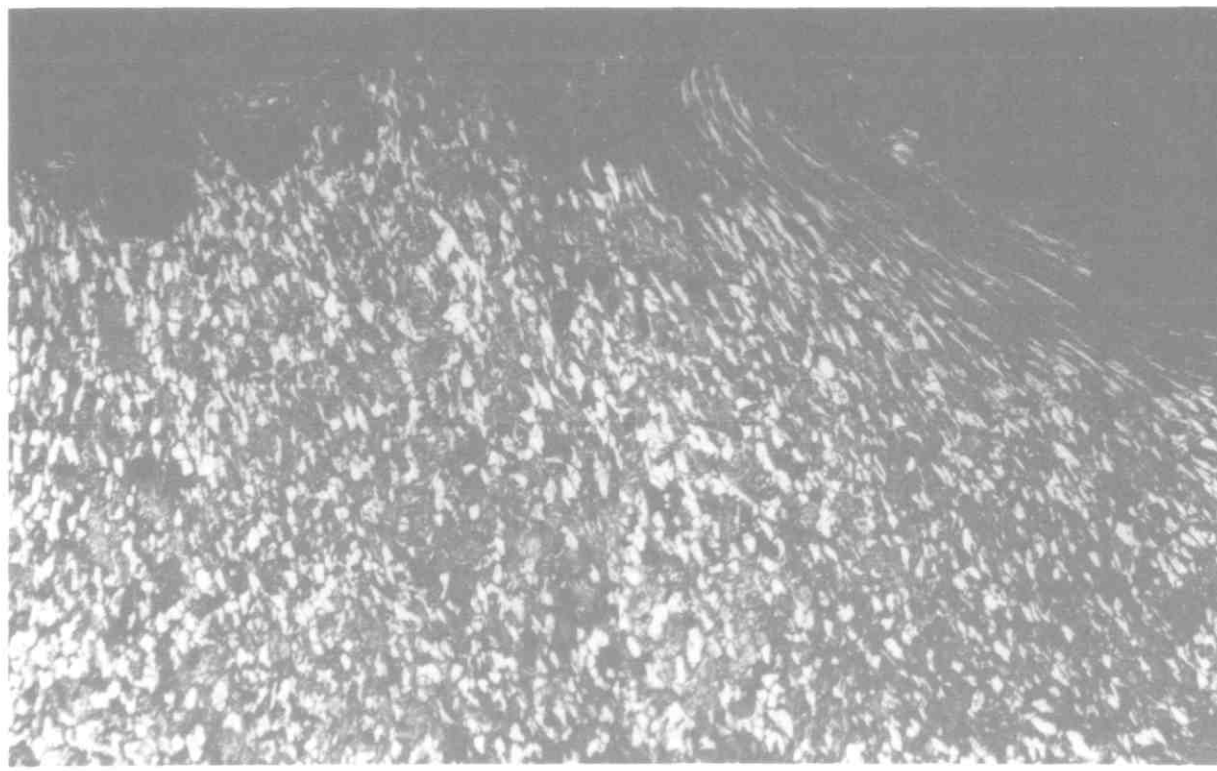

Area - A

X48

Figure 6.11: Longitudinal section of a double notched 2¼%Cr 1%Mo round bar with b/a=1.46 and a/R=13 .

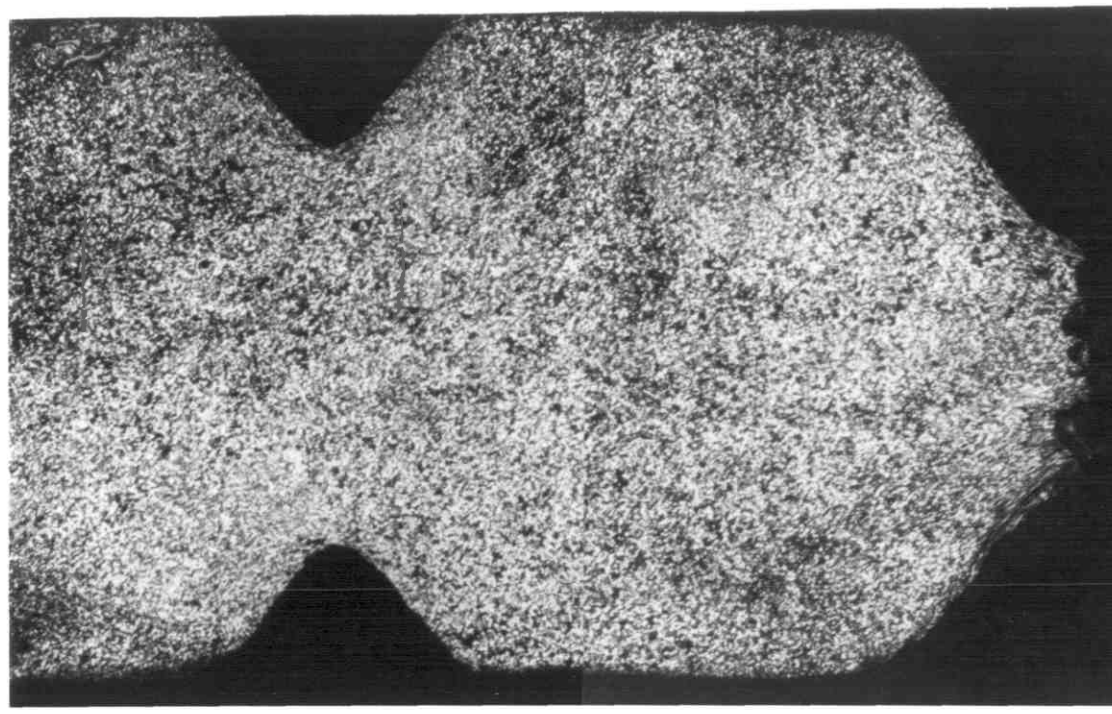

X11

b/a = 1.46

a/R = 13

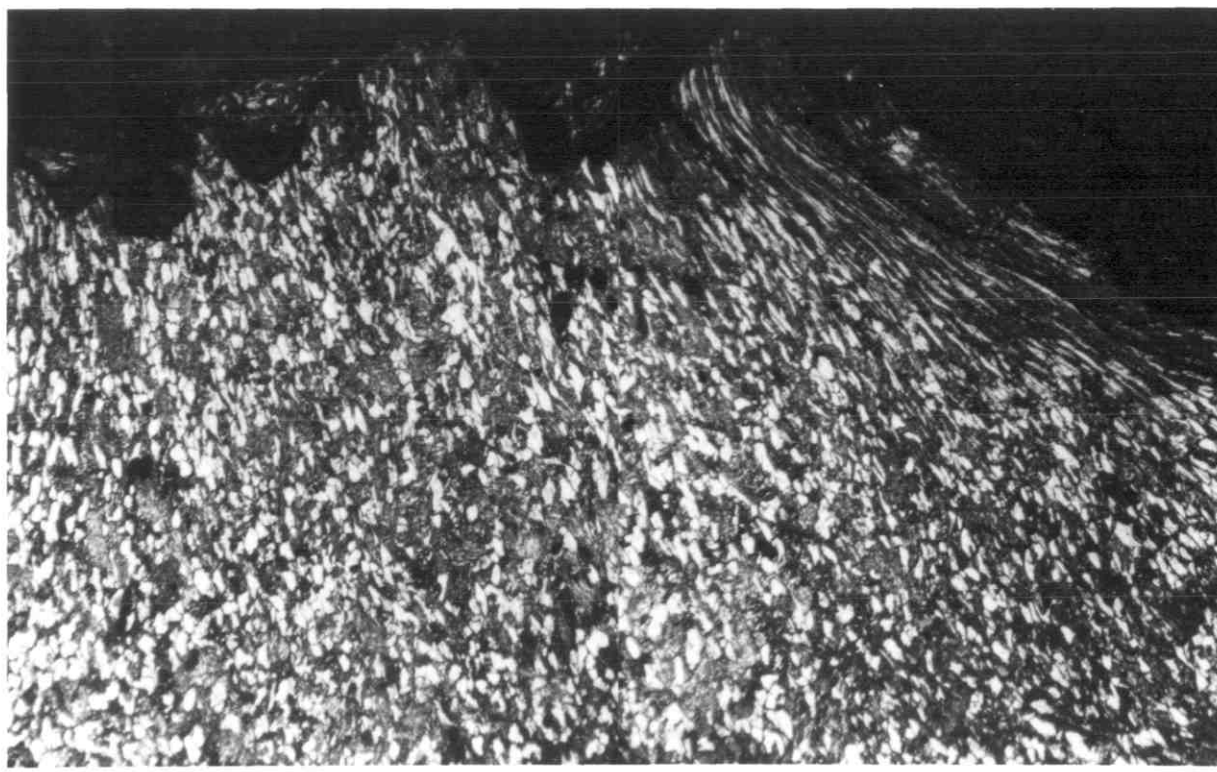

Area - A

X48

Figure 6.11: Longitudinal section of a double notched 2¼%Cr 1%Mo round bar with b/a=1.46 and a/R=13 .

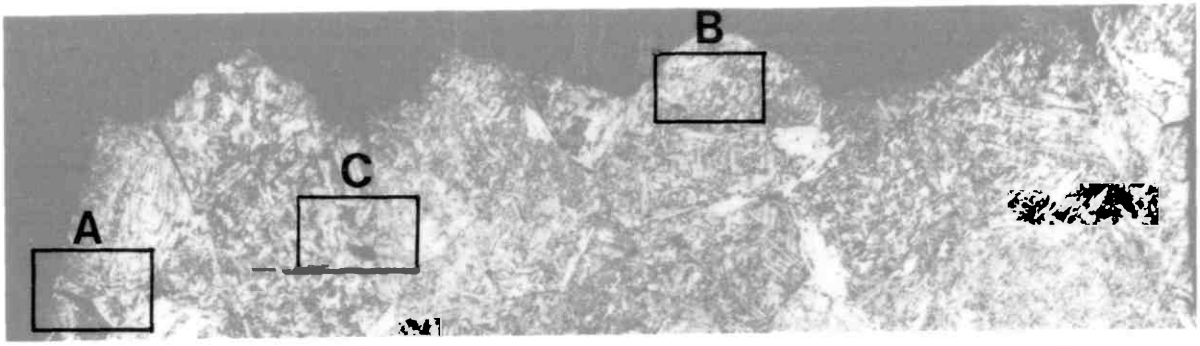

X30

b/a : 1.67
a/R : 0.297

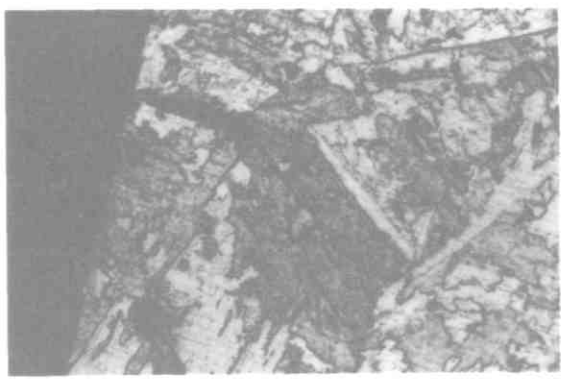

Area - A x148

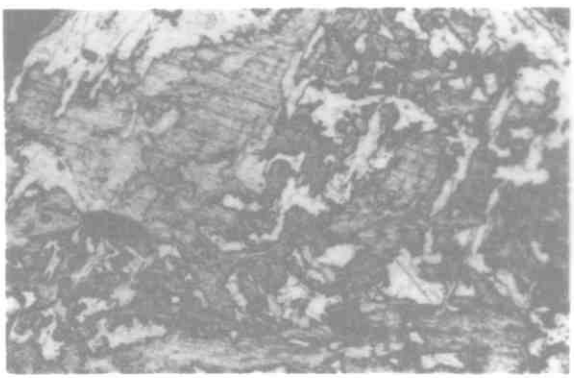

Area - B x128

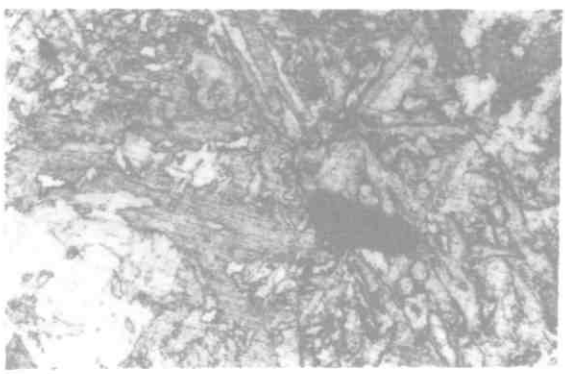

Area - C x128

Figure 6.12: Longitudinal section of a fractured ½%Cr ½%Mo ¼%V notched bar specimen with a/R=0.297 and b/a=1.67

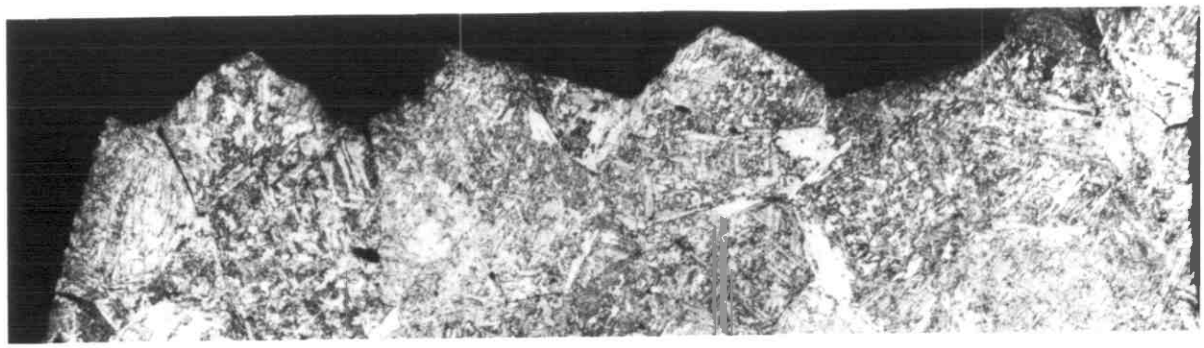

X30

b/a : 1.67

a/R : 0.297

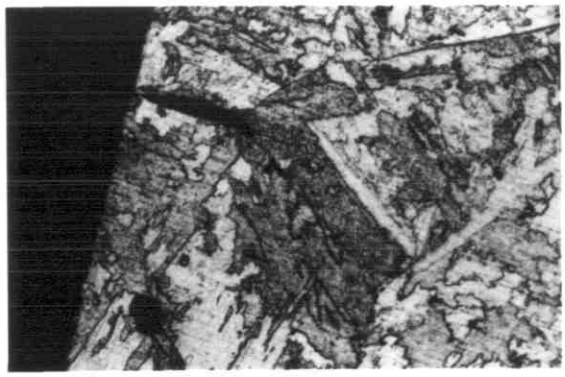

Area - A x148

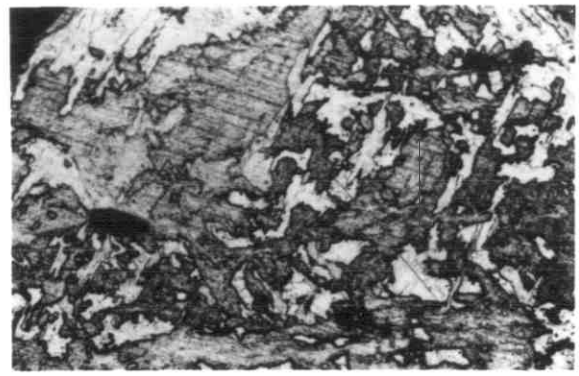

Area - B x128

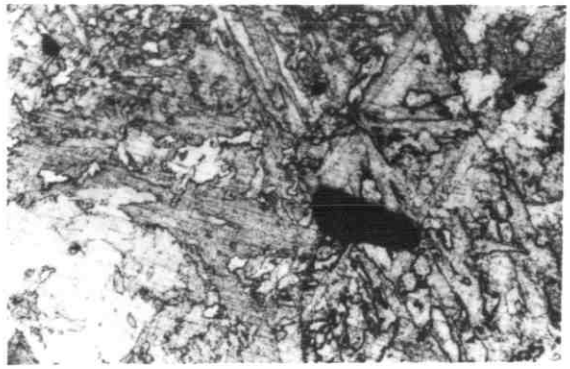

Area - C x128

Figure 6.12: Longitudinal section of a fractured ½%Cr ½%Mo ¼%V notched bar specimen with a/R=0.297 and b/a=1.67 .

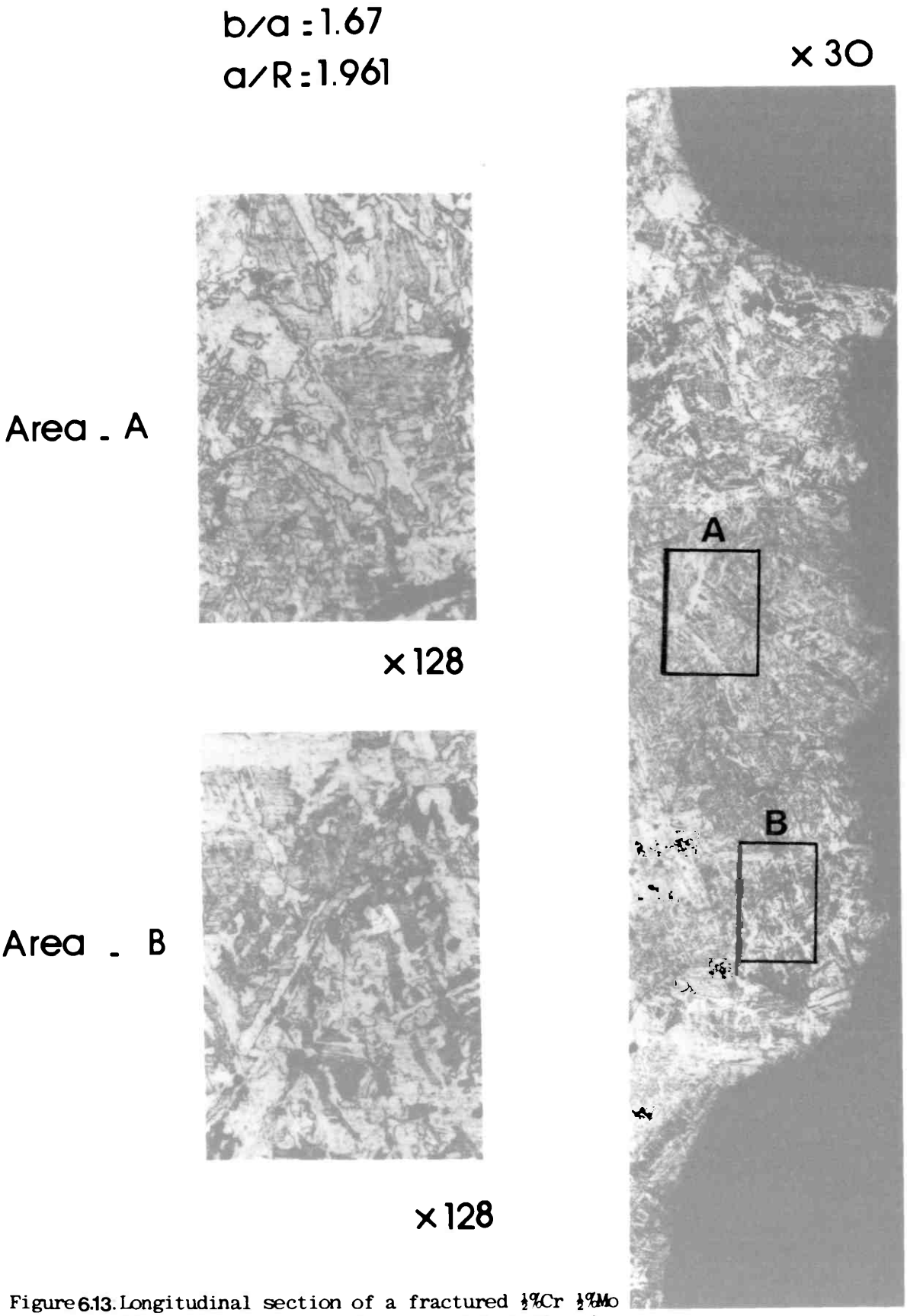

Figure 6.13. Longitudinal section of a fractured ½%Cr ½%Mo 1%V notched bar specimen with b/a=1.67 and a/R=1.961 .

b/a : 1.67

a/R : 1.961

× 30

Area - A

× 128

Area - B

× 128

Figure 6.13. Longitudinal section of a fractured ½%Cr ½%Mo 1%V notched bar specimen with b/a=1.67 and a/R=1.961 .

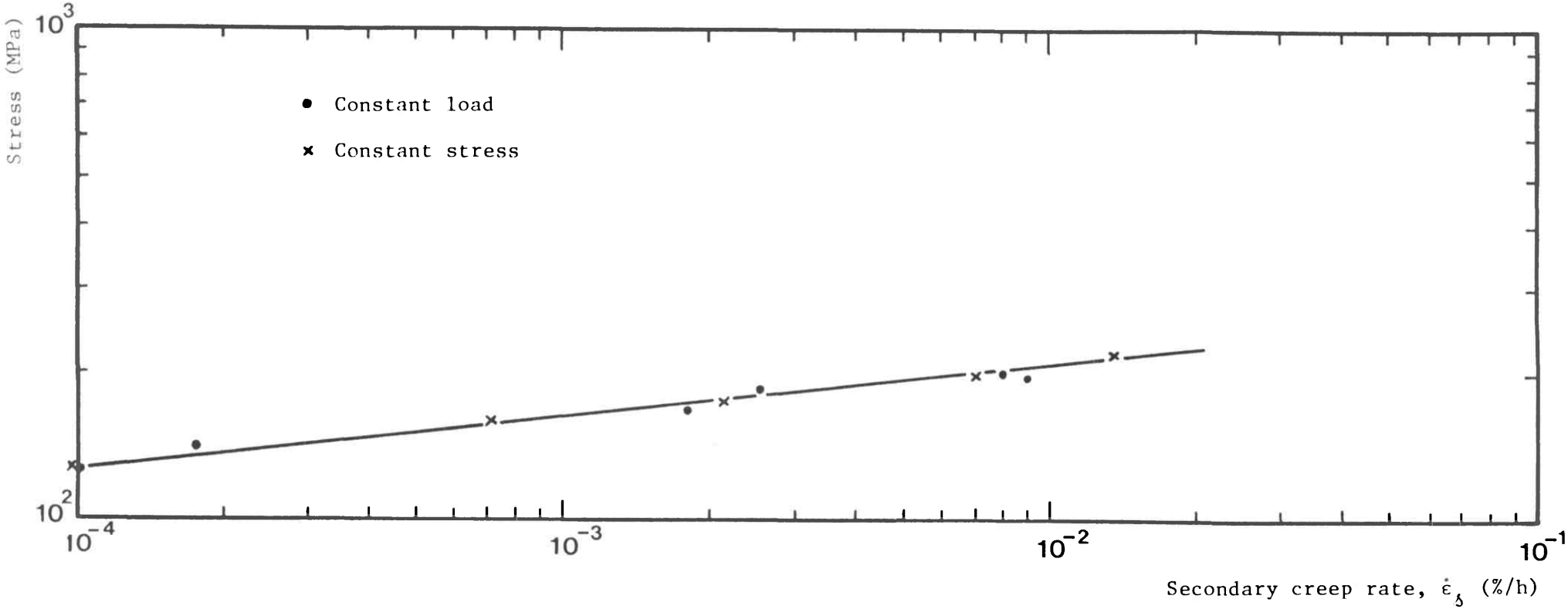

Figure 6.14: Secondary creep rate as a function of stress for the $2\frac{1}{4}$%Cr 1%Mo steel tested at 538°C

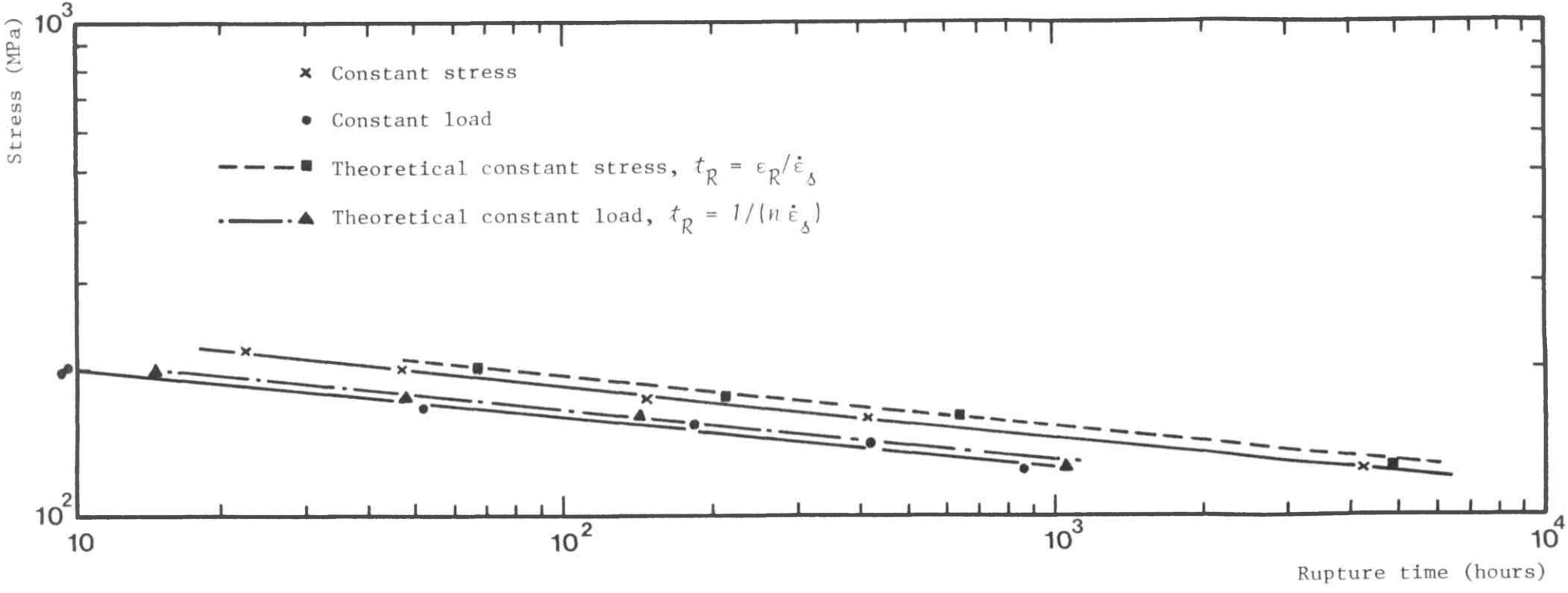

Figure 6.15: Experimental and theoretical stress-rupture time curves for the 2¼%Cr 1%Mo steel tested at 538°C

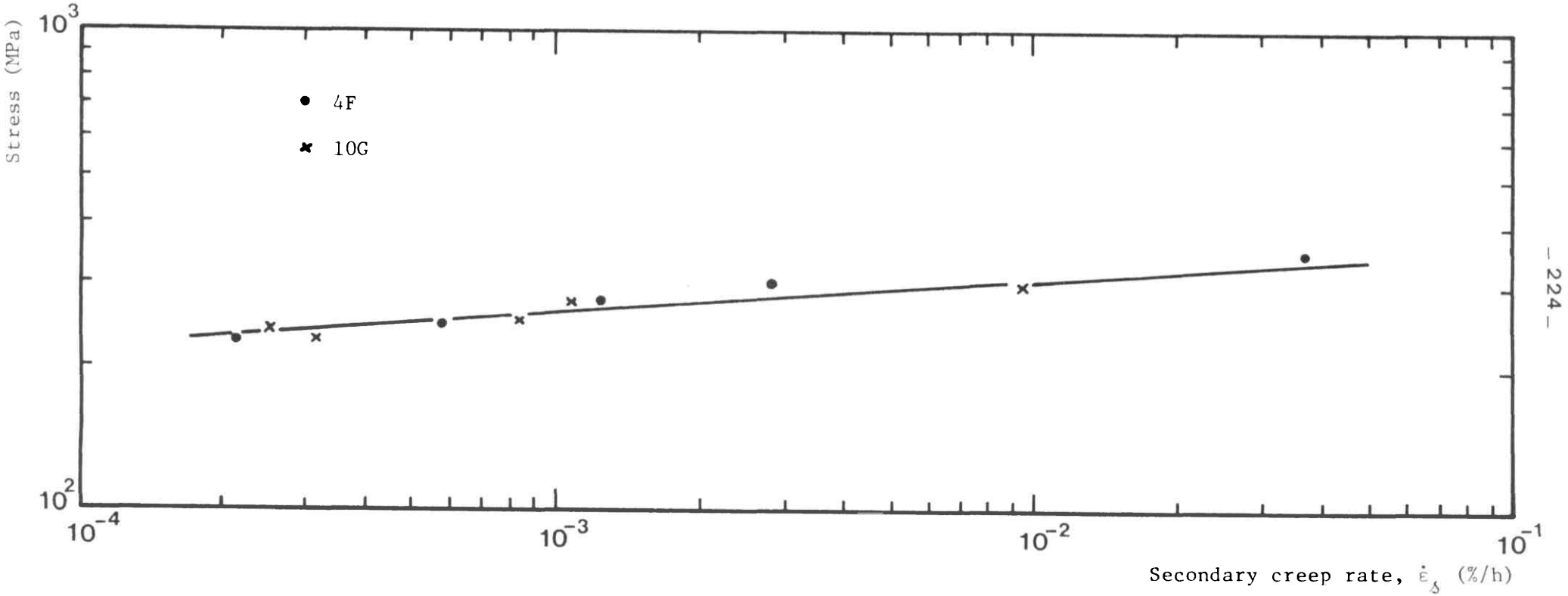

Figure 6.16: Secondary creep rate as a function of stress for the ½%Cr ½%Mo ¼%V steel tested at 565°C

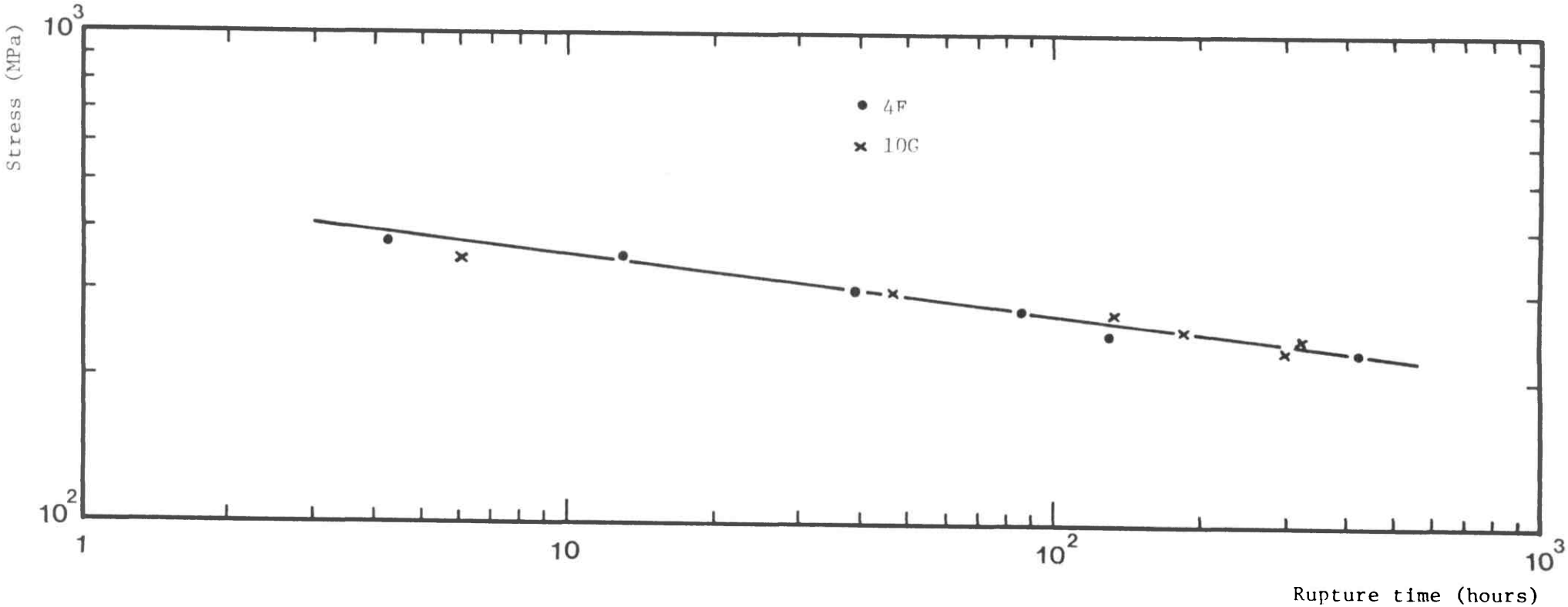

Figure 6.17: Stress-rupture time curve for the ½%Cr ½%Mo ¼%V steel tested at 565°C

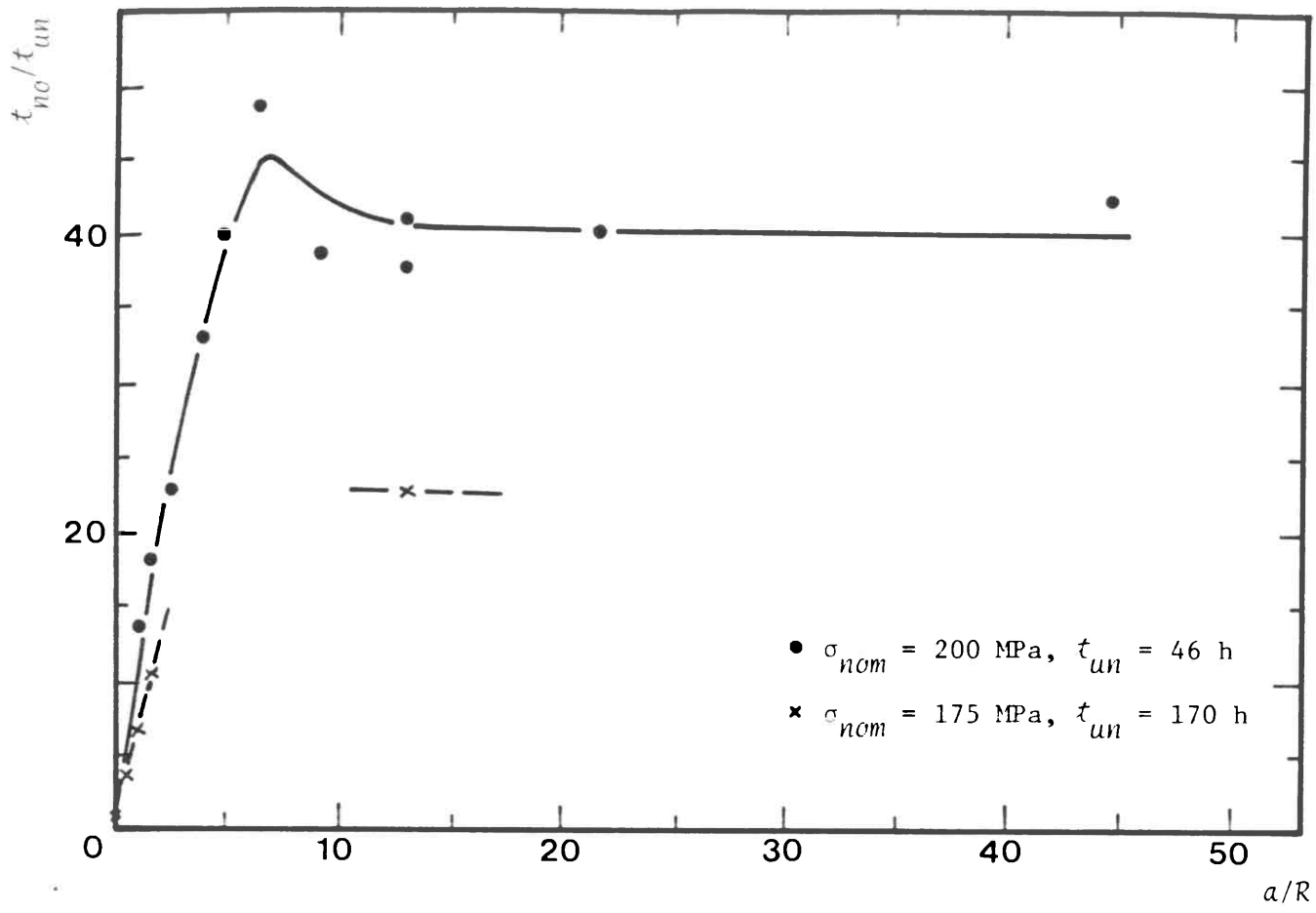

Figure 6.18: Dependence of notched to unnotched time strength ratios on notch shape for the 2¼%Cr 1%Mo steel

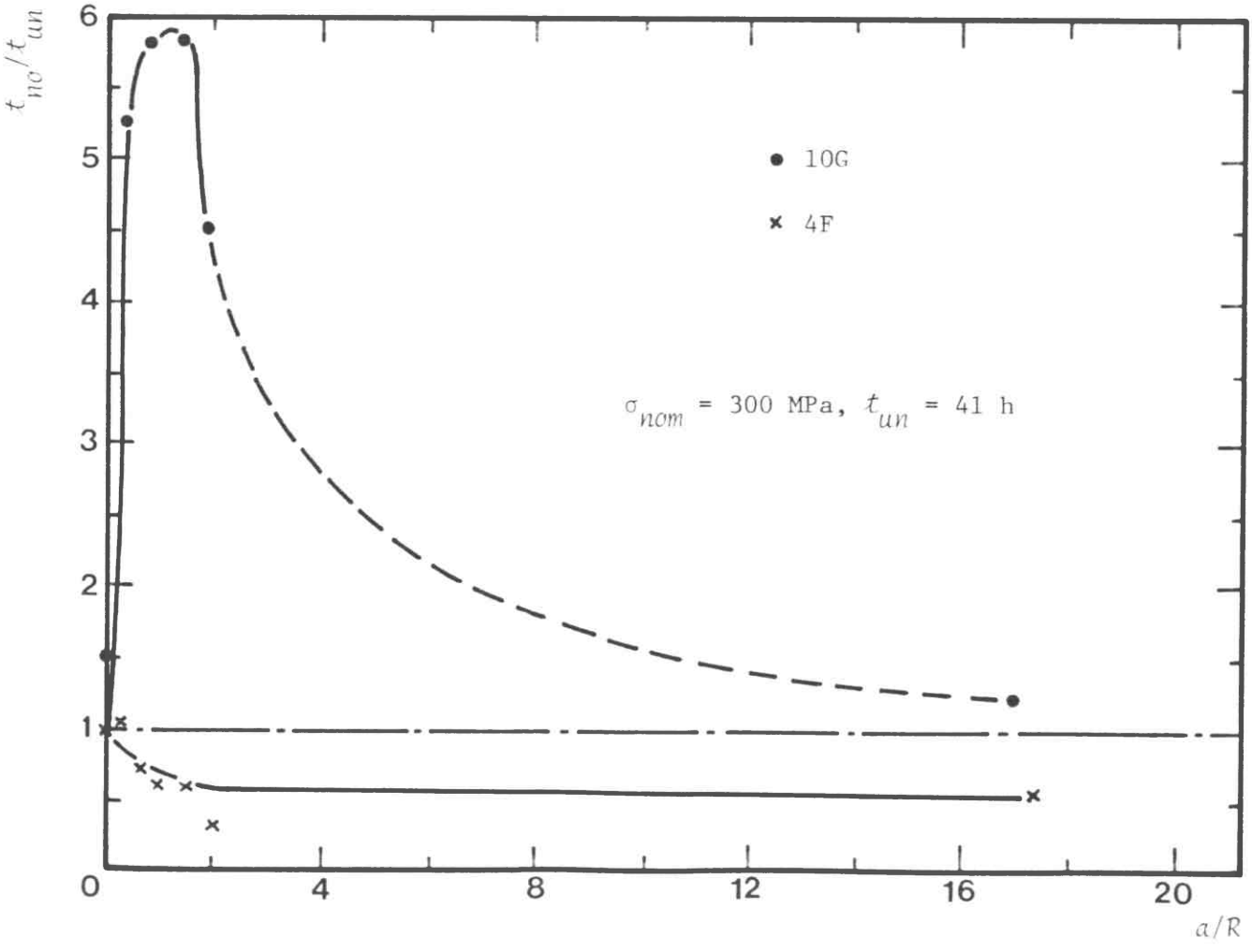

Figure 6.19: Dependence of notched to unnotched time strength ratios on notch shape for the ½%Cr ½%Mo ¼%V steel

CHAPTER 7

APPLICATION OF CREEP RUPTURE MODELS TO EXPERIMENTAL DATA

7.1 INTRODUCTION

The continuum mechanics and void growth models derived in Chapter 5 to predict notch strengthening and weakening are applied in this chapter to the experimental data presented in Chapter 6 on the 2¼%Cr 1%Mo and ½%Cr ½%Mo ¼%V steels. Some data available in the literature on a range of high temperature alloys tested by Davis and Manjoine [1953] are also used in these applications.

7.2 ESTIMATES OF STRESS REDISTRIBUTION TIMES DUE TO CREEP

Rupture time predictions, based on steady-state analysis, are expected to be valid only if the stresses redistribute relatively early in life. The theoretical notch strengthening and weakening models proposed in Chapter 5 were all based on the steady-state finite element predictions at the skeletal point, given in Chapter 4. The numerical approach used in the calculations cannot determine the time taken to reach steady-state. However, an approximate method has been proposed in Section 5.2.2 for calculating stress redistribution times due to creep, based on the assumption that the overall behaviour of structures is dominated by the redistribution of the peak stress (Calladine [1969]). This approach has been used in this section to estimate steady-state times for various notched bar geometries using the experimental data given in the previous chapter on both the 2¼CM and ½CMV steels. Comparisons between Calladine's approximate time-scale predictions and computed times to steady-state, based on Hayhurst, et al.'s [1977a,b] incremental finite element calculations, are also given.

7.2.1 Analysis

A general expression for calculating the time taken for stress relaxation to be 90% complete was derived previously in Section 5.2.2 for structures in which $\bar{\sigma}_{max}$ dominates the overall behaviour during creep deformation. The constitutive creep law used was:

$$\dot{\bar{\varepsilon}} = C\,\bar{\sigma}^{n}\,G(t) \tag{7.1}$$

and for secondary creep, the result was:

$$f(t_s) = \frac{2.3}{C\,n\,E\,\bar{\sigma}_{max}^{(n-1)}} \tag{7.2}$$

The steady-state finite element calculations performed in Chapter 4 on various notched bar geometries showed that the effective stress is always a maximum at the notch root and equivalent to:

$$\bar{\sigma}_{max} = F\,k\,\sigma_o^{\infty} = F\,k\,\sigma_{nom}\left(\frac{a}{b}\right)^2 \tag{7.3}$$

where F is the relative stress concentration factor based on the effective stress values at the notch root (equation (5.1)), k is the elastic effective stress concentration factor, σ_{nom} is the nominal stress across the minimum section of the notched bar specimen, and a and b are the notch throat and bar radii as before. Substituting equation (7.3) into equation (7.2) gives:

$$f(t_s) = \frac{2.3}{C\,n\,E\,[F\,k\,\sigma_{nom}\,(a/b)^2]^{(n-1)}} \tag{7.4}$$

For materials in which the maximum principal stress, $\sigma_{1_{max}}$, controls failure (Johnson, et al. [1962], Hayhurst [1972], Cane[1980]), equation (7.2) can now be written as:

$$f(t_s) = \frac{2.3}{C\,n\,E\,\sigma_{1_{max}}^{(n-1)}} \tag{7.5}$$

Although a skeletal point for the steady-state stress distributions given in Chapter 4 for various notched geometries was not reported, a zone where the axial stress is nearly independent of n exists at the position of the effective stress skeletal stress. Using the skeletal values of $\sigma_1^*/\sigma_o^{\infty}$ as a reference stress that controls failure in maximum principal stress materials, equation (7.5) can now be written as:

$$f(t_s) = \frac{2.3}{\bar{C}\,n\,\bar{E}\,\sigma_1^{*(n-1)}} \tag{7.6}$$

From the finite element prediction:

$$\sigma_1^* = (K_n \sigma_{nom})^* \tag{7.7}$$

where K_n varies with the notch sharpness, as shown previously in Figure 5.6. Substituting equation (7.7) into equation (7.6) results in:

$$\delta(t_\delta) = \frac{2.3}{C\ n\ E\ [K_n\ \sigma_{nom}]^{*(n-1)}} \tag{7.8}$$

A similar equation to (7.8) can be derived when the maximum axial stress, $\sigma_{1_{max}}$, is used in the calculations. The only difference is that the term $(K_n \sigma_{nom})^*$ in equation (7.8) is replaced by $(K_n \sigma_{nom})_{max}$ which, in this case, is dependent on n and has a different position to that of the skeletal effective stress, as shown by the stress distributions in Appendix A and Chapter 4.

The time incremental finite element method adopted by Hayhurst, et al. [1977a,b] to calculate the steady-state stress distributions across the throat of various notched geometries (Section 3.3.1) differs from the present finite element method by its ability to predict times to steady-state. A normalised time-scale, $\tau_{\delta\delta}$, was set to allow the stresses to redistribute from the elastic to steady-state, such as:

$$\tau = \int_0^t C\ E\ \sigma_o^{(n-1)}\ G(t)\ dt \tag{7.9}$$

where C and n are material constants, E is Young's modulus, σ_o is the applied stress and equal to $\sigma_{nom}\,(a/b)^2$, and $G(t)$ is a general function of time. For secondary creep, equation (7.5) gives:

$$\delta(t_\delta) = \frac{\tau_{\delta\delta}}{C\ E\ [\sigma_{nom}\ (a/b)^2]^{(n-1)}} \tag{7.10}$$

The ratio between Hayhurst's and Calladine's estimates of steady-state times for notched geometries in which $\bar{\sigma}_{max}$ dominates the overall behaviour can be found by dividing equation (7.10) by equation (7.4). The result is:

$$\frac{\delta(t_s)_{Hayhurst}}{\delta(t_s)_{Calladine}} = \frac{n}{2.3}\,[F\,k]^{(n-1)}\,\tau_{ss} \qquad (7.11)$$

7.2.2 Results

Comparisons have been made between Calladine's approximate estimates of steady-state times for $\bar{\sigma}$ and σ_1 materials (equations (7.4) and (7.8)), and Hayhurst's finite element predictions (equation (7.11)) using available information on four different notched bar geometries. The two materials used in the investigations were the 2¼CM and ½CMV steels for which C, n and E are known (Chapter 6). The values of $\bar{\sigma}_{max}/\sigma_o^{\infty}$, which is also equal to $F\,k$, and $K_n\,\sigma_{nom}$ (the maximum value in this case) needed in Calladine's equations, were taken from the stress distributions calculated by the present finite element method (Chapter 4). The dimensionless time to stationary state, τ_{ss}, required in equation (7.10) was taken from Hayhurst, et al. [1977a,b], and τ_{ss} versus n diagrams of the geometries investigated. The ½CMV has an n value of 16.66 which is outside the range of these diagrams (n = 0 to 10), therefore τ_{ss} for this material was found by linear extrapolation. The results of these comparisons are listed in Table 7.1. It is observed that the times predicted by Hayhurst are always greater than those of Calladine by between 2 and 9 orders of magnitude.

Calculations have also been made to predict steady-state times for the notch rupture data available on the 2¼CM and ½CMV steels (Chapter 6), using Calladine's approximate method. The results of these

calculations are listed in Table 7.2 for both materials. The value of Fk, which is also equal to $\bar{\sigma}/\sigma_{nom}$, used to calculate $\delta(t_s)$ in equation (7.4) was taken from the finite element solutions (Chapter 4) at both the maximum and the skeletal effective stress points. Results of some calculations, using equation (7.8), for materials in which the skeletal $\sigma_1^*/\sigma_o^\infty$ controls creep deformation and rupture are also listed in Table 7.2. Calladine's theoretical predictions suggest, when compared with the $2\frac{1}{4}$CM steel notch rupture data, that steady-states have been achieved relatively early in life when both $\bar{\sigma}$ and σ_1 controls failure (the latter being too conservative). However, for the $\frac{1}{2}$CMV steel when either the maximum or the skeletal $\bar{\sigma}/\sigma_o^\infty$ are used in the calculations, steady-state has not been achieved. This implies that creep failure for this material is controlled by σ_1 or a combination of both σ_1 and $\bar{\sigma}$ (Hayhurst, et al. [1978], Cane [1980]).

7.2.3 Discussion

When creep rupture is the prime design consideration, Calladine's approximate approach for calculating the stress redistribution times seems appropriate to check the validity of using steady-state conditions to predict rupture in complex structures. For the material in question, the uni-axial creep coefficients required in the analysis are easy to find. This leaves the only unknown to be the state of stress parameter which controls creep deformation and rupture ($\bar{\sigma}/\sigma_o^\infty$ or σ_1/σ_o^∞). These parameters are very difficult to measure experimentally, especially in complex geometries, therefore they have to be found analytically. For notched bar geometries, the Bridgman analysis given in Section 4.2 can be used to estimate the required state of stress parameters for fully plastic conditions; i.e. $n = \infty$. The other alternative is to use the finite element method to calculate the steady-state stress distributions for any

value of n.

The results of several calculations performed on various notched bar geometries were previously given in Chapter 4. This section focuses the attention on two types of diagram which can be used as a useful design tool. Firstly, the relative stress concentration factor, F, versus $1/n$ diagrams (Figures 5.1 to 5.3). If $\bar{\sigma}_{max}$ controls creep deformation and failure, F, in Calladine's equation (7.4) becomes as easy to find for the appropriate value of n as the elastic stress concentration factors, K, usually presented in charts in any standard design book. The second type of diagram is one which shows the change in the state of stress parameters at the skeletal point with increase in notch sharpness, a/R (Figures 4.8, 4.14 and 4.20). In this case, the parameters of interest are the skeletal $\bar{\sigma}$ and σ_1.

Hayhurst's predictions of the stress redistribution times listed in Table 7.2 show that notches manufactured from ductile materials have shorter times to stationary-state than those manufactured from brittle materials. They also suggest that stress redistribution is never complete except for the BS V-notch manufactured from the 2¼CM steel. The stress redistribution time for this notch, according to Hayhurst, is 300 hours which is also questionable because, if n is taken to be 9 and not 9.77, then the time to stationary-state will be approximately 10^4 hours, which is outside the experimental rupture time.

Calladine's estimates of the stress redistribution times listed in Table 7.2 were based on either $\bar{\sigma}$ (maximum and skeletal) or σ_1. The results show that for the ductile 2¼CM steel, the predictions are more realistic when $\bar{\sigma}$ is used in the calculations. When σ_1 is used, the results are too conservative. However, for the brittle ½CMV steel, Calladine's estimates suggest that the creep behaviour of this material is dominated by the axial stress, σ_1. When $\bar{\sigma}$ is used in the calculations, complete stress redistribution is not achieved.

7.3 INTERPRETATION OF NOTCH RUPTURE DATA

Notch rupture data are usually interpreted and presented in terms of notched to unnotched lives or stress strength ratios. The conditions applied when time or strength ratios are used in the presentation were previously given and discussed in Chapter 1, Section 1.4.1. In this section, the implications of applying these conditions to experimental creep data are discussed.

One of the most extensive experimental investigations undertaken on a series of materials to collect uni-axial and notch rupture data was carried out by Davis and Manjoine in 1953. They creep tested in tension a number of uni-axial and notched bar specimens with different notch profiles under a constant temperature and various nominal stresses. The results of their investigation were presented in several logarithmic stress versus rupture time diagrams. It is observed that the uni-axial and the notch rupture data for some of the materials investigated are parallel to each other but in most cases they are not. The σ-t_R lines of the notched specimens diverge from the uni-axial line with no systematic trends. This author believes that this point should have been taken into consideration when McLean, et al. [1977] and Cocks [1980] compared the Davis and Manjoine data, plotted in terms of notch rupture strength, with their proposed theoretical bounds and models. The schematic diagrams in Figure 7.1 explain why. If the uni-axial and notched data lines are parallel, as shown in Figure 7.1(a), then the notched to unnotched time or stress strength ratios will be the same at any reference rupture time or stress (the horizontal and vertical lines). However, the values of these ratios become very sensitive to the position of the reference time or stress when the data lines are not parallel (Figure 7.1(b) and (c)). If the data lines do not cross over at any applied nominal stress (which is very likely), then the position at which the switch from notch

strengthening to notch weakening takes place remains the same. At different reference times or stresses, the numerical value of the notched to unnotched ratios will be the only variable (Figure 7.1(d)).

7.4 APPLICATION OF THE PROPOSED NOTCH STRENGTHENING AND WEAKENING MODELS TO CREEP DATA

In Chapter 5, several theoretical models have been proposed, based on either continuum mechanics or microstructural approaches, to predict notch strengthening and weakening. In this section, these models are applied to the experimental creep data available on the 2¼%Cr 1%Mo and ¼%Cr ½%Mo ¼%V steels (Chapter 6) and also to the Davis and Manjoine [1953] data. The assumptions associated with using either the time or stress strength ratios to present and compare these data with the proposed models are fully discussed.

7.4.1 Summary of Analytical Expressions of the Models

The steps which have been followed in applying the proposed continuum mechanics and microstructural models, discussed in detail in Chapter 5, to the experimental data are summarised in this section. The first step is to present the equations describing these models in terms of normalised rupture time, $t_R \dot{\varepsilon}_o$. The continuum mechanics approach for materials in which the effective stress controls failure (equation (5.9)) gives:

$$t_R \dot{\varepsilon}_o = \varepsilon_R \left(\frac{\sigma_{nom}}{\bar{\sigma}}\right)^n \tag{7.12}$$

and for σ_1 materials, the result is:

$$t_R \dot{\varepsilon}_o = \varepsilon_R \left(\frac{\sigma_{nom}}{\sigma_1}\right)^n \tag{7.13}$$

where $\sigma_{nom} = \sigma_o$ in equation (5.9), and $\dot{\varepsilon}_o$ is the minimum creep rate which corresponds to the applied nominal stress, σ_{nom}.

From Ashby's theory of creep rupture by void growth, equation (5.14) for boundary diffusion becomes:

$$t_R \dot{\varepsilon}_o \simeq \frac{0.17}{\phi_o} \left(\frac{\sigma_{nom}}{\sigma_1}\right) \tag{7.14}$$

and for surface diffusion, equation (5.16), when $\delta_i < 0.01$ gives:

$$t_R \dot{\varepsilon}_o \simeq \frac{1}{\psi_o} \left(\frac{\sigma_{nom}}{\sigma_1}\right)^3 \tag{7.15}$$

For materials in which voids grow by power-law creep, the general constant stress rupture time equation (2.30), when the nucleation time, $t_n = 0$, reduces to:

$$t_R \dot{\varepsilon}_o = \frac{\alpha}{(n+1)} \ln \left[\frac{1}{(n+1)\delta_i}\right] \left(\frac{\sigma_{nom}}{\bar{\sigma}}\right)^n \tag{7.16}$$

and when the rupture strain equation (2.34) for power-law creep is used, with the assumption that the term $0.2\ell/d$ is negligible, the result is identical to the continuum mechanics equation (7.12) for $\bar{\sigma}$ materials.

Equations describing the theoretical models in terms of time strength ratios were also derived in Chapter 5. The continuum mechanics constant ductility models for either $\bar{\sigma}$ or σ_1 materials are:

$$\frac{t_{no}}{t_{un}} = \left(\frac{\sigma_{nom}}{\bar{\sigma}}\right)^n \tag{7.17}$$

and:

$$\frac{t_{no}}{t_{un}} = \left(\frac{\sigma_{nom}}{\sigma_1}\right)^n \tag{7.18}$$

If the Bridgman values of $\sigma_{nom}/\bar{\sigma}$ (equation (4.5)) are used in equation (7.17), the result is:

$$\left(\frac{t_{no}}{t_{un}}\right)_{Bridgman} = \left[\left(1 + \frac{2R}{a}\right) \ln \left(1 + \frac{a}{2R}\right)\right]^n \tag{7.19}$$

Ashby's theory for materials in which voids grow by boundary diffusion (Section 5.4.1) gave:

$$\frac{t_{no}}{t_{un}} = \frac{\sigma_{nom}}{\sigma_1} \tag{7.20}$$

Equation (7.20) is similar to the continuum mechanics equation (7.18) when $n = 1$.

For surface diffusion, the result was:

$$\frac{t_{no}}{t_{un}} = \left(\frac{\sigma_{nom}}{\sigma_1}\right)^3 \tag{7.21}$$

When δ_i was assumed to remain constant under both uni-axial and multi-axial conditions, the power-law creep expression was:

$$\frac{t_{no}}{t_{un}} = \left(\frac{\alpha}{\alpha_o}\right) \left(\frac{\sigma_{nom}}{\bar{\sigma}}\right)^n \tag{7.22}$$

Similar expressions to the continuum mechanics equation (7.17) can be derived from the reduced power-law rupture strain equation (5.24), assuming that ductility at failure is constant for both uni-axial and notched bar specimens.

When the stress strength ratios are used to model notch strengthening and weakening, the continuum mechanics approach for either $\bar{\sigma}$ or σ_1 materials gave:

$$\frac{\sigma_n}{\sigma_{un}} = \frac{\sigma_{nom}}{\bar{\sigma}} \tag{7.23}$$

and:

$$\frac{\sigma_n}{\sigma_{un}} = \frac{\sigma_{nom}}{\sigma_1} \tag{7.24}$$

The Bridgman values of $\sigma_{nom}/\bar{\sigma}$ were previously derived in Section 4.2 as:

$$\left(\frac{\sigma_n}{\sigma_{un}}\right)_{Bridgman} = \frac{\sigma_{nom}}{\bar{\sigma}} = \left[\left(1 + \frac{2R}{a}\right) \ln \left(1 + \frac{a}{2R}\right)\right] \tag{7.25}$$

Ashby's theory for materials in which voids grow by either boundary diffusion or surface diffusion gave a similar expression to that of equation (7.24). However, for materials in which voids grow by power-law alone, three equations were given. The first equation was derived from the constant stress rupture time equation (2.30) with the assumption that δ_i is constant. The result was:

$$S_\delta = \left(\frac{\alpha}{\alpha_o}\right)^{1/n} \frac{\sigma_{nom}}{\bar{\sigma}} \tag{7.26}$$

The second equation was derived using the assumption that the rupture strain is constant for uni-axial and multi-axial specimens. The results gave an identical expression to that of the continuum mechanics for $\bar{\sigma}$ materials (equation (7.23)). The third expression given was that derived by Cocks [1980]:

$$S_\delta = N \left\{\frac{\sinh\left[\frac{2}{3}\left(\frac{n - \frac{1}{2}}{n + \frac{1}{2}}\right)\right]}{\sinh\left[2\left(\frac{n - \frac{1}{2}}{n + \frac{1}{2}}\right)\left(N - \frac{2}{3}\right)\right]}\right\}^{1/n} \tag{7.27}$$

where:

$$N = \sigma_n/\bar{\sigma} \tag{7.28}$$

σ_n and $\bar{\sigma}$ are the slip-line field predictions of the average axial and equivalent stress in the minimum section of a notched bar.

Before applying these models to the experimental data, it is necessary to summarise the assumptions used in their derivation. They were:

(a) Nucleation time is negligible.

(b) Failure mechanisms are controlled by void growth only with no intervention due to mechanical instability (necking).

(c) Either the strain to failure or δ_i remain constant.

Finally, it has to be pointed out that only one curve of time or stress strength ratio versus constraint for a particular value of n can be predicted. This implies that the logarithmic notched and uni-axial stress-time lines are assumed to be parallel (Figure 7.1(a)).

7.4.2 The 2¼%Cr 1%Mo Steel Creep Data

In this section, the proposed models are applied to the experimental data available on the 2¼%Cr 1%Mo steel (Chapter 6, Tables 6.3 to 6.5). The first step followed was to plot the experimental rupture times, expressed in terms of $t_R \dot{\varepsilon}_o$, versus constraint, as shown in Figure 7.2. Three models were also plotted in the same figure; these were the continuum mechanics (equation (7.12)), boundary diffusion (equation (7.14)), and power-law creep (equation (7.16)) models. The stress index, n, for this material was approximated to 9 and the uni-axial rupture strain, ε_R, used in equation (7.12) was taken from Table 6.4 as equivalent to approximately 40% at σ_{nom} = 200 MPa. The state of stress parameters required in the calculation, such as $\sigma_{nom}/\bar{\sigma}$, σ_{nom}/σ_1 and α, were taken from the finite element predictions for the notched geometries with b/a = 1.46 (Figures 4.14 and 5.8). Estimates of the material property, ϕ_o, which appear in the boundary diffusion equation (7.14) are given in Table 7.3. The material coefficients used to calculate ϕ_o (equation (2.18)) were given by Dyson [1982] at 565°C, which is slightly higher than the creep test temperature of 538°C. No information could be obtained in order to calculate the surface diffusion material parameter, ψ_o, required in equation (7.15), and this model was therefore excluded.

It is observed from Figure 7.2 that the uni-axial and all the notched bar specimens have failed by power-law creep and not by diffusion. This is indicated by the fact that the boundary diffusion model always predicts longer lives than were measured in practice. It is also observed that the continuum mechanics constant ductility model represented by equation (7.12) over-estimates the experimental lives for $a/R > 3.0$. The power-law creep model gave a good fit to the rupture times of the specimens with high constraint with $\delta_i = 5 \times 10^{-6}$. The uni-axial ductility predicted using this value of δ_i in equation (5.23) is equal to 157%, which is much higher than the measured ductility of 90% (Table 6.4, σ_{nom} = 200 MPa).

It has been stated in Section 7.4.1 that Ashby's model for uni-axial behaviour is only applicable prior to the onset of necking. Therefore, the difference between the experimental and predicted ductilities indicates that plastic instability was the final cause of failure, and not creep. If the material is allowed to deform uniformly, then the uni-axial rupture time is expected to be much higher than the experimentally measured value. This is illustrated in Figure 7.3 for the plain bar specimen tested at a constant stress of 200 MPa. The predicted rupture time, t'_{un}, using the experimental secondary creep rate which corresponds to 200 MPa and a ductility of 157% is about 225 hours. This predicted time is about 4.85 higher than that measured experimentally.

Finally, the proposed models expressed in terms of notched to unnotched lives and stress strength ratios are shown plotted against the experimental data in Figures 7.4 to 7.6. In Figure 7.4, the measured uni-axial rupture time, equivalent to 46 hours, was used to normalise the experimental data. It is observed that both the Bridgman and the constant ductility models (equation (7.17)) agree with the experimental data up to approximately $a/R = 3$. This is expected since the Bridgman analysis is only valid for blunt notches of small constraint and the

continuum mechanics constant ductility model does not take into account any drop in ductility due to increase in tri-axiality with increase in notch sharpness. These two models can therefore be regarded as upper bounds. The estimates of t_{no}/t_{un} shown in Figure 7.4 when δ_i was assumed constant (equation (7.22)) are about 4 or 5 times smaller than the experimental ratios. This is approximately the same difference as between the predicted uni-axial rupture time and that measured experimentally (Figure 7.3). When the true uni-axial rupture time, t'_{un} = 225 hours, was therefore used in Figure 7.5, the constant δ_i model fits the normalised data almost perfectly. Similar trends are observed when the data are plotted in terms of stress strength ratios using the corrected uni-axial rupture time (t'_{un}), as shown in Figure 7.6.

7.4.3 The ½%Cr ½%Mo ¼%V Steel Creep Data

Two blocks of this material, labelled as 10G and 4F, were creep tested in 1980 by Ng, Webster and Dyson at 565°C. The information made available by their research was previously listed and discussed in Chapter 6, Tables 6.7 and 6.8. Metallurgical investigations on fractured surfaces of some notched specimens revealed that a clear intergranular type of failure was the cause of fracture. It also showed that damage in the form of small cracks and voids was observed around the area of the fractured surfaces (Figures 6.12 and 6.13), which is expected from a material in which the uni-axial ductility, measured over the gauge length, is between approximately 4% and 0.2%.

It is evident from the metallurgical observations and the absence of necking in all plain bar specimens that damage accumulation and not plastic instability was the cause of failure. For this material, no information could be obtained in order to calculate the boundary or surface diffusion parameters, ϕ_o and ψ_o. Therefore, it was not possible to plot

the data in terms of the normalised time, $t_R \dot{\varepsilon}_o$, in order to assess whether the formation and linkage of voids was caused by power-law creep or by diffusion. However, there is a clear indication that the models in which the axial component σ_1 is the dominant parameter gave a reasonable fit to some of the data when plotted in terms of notched to unnotched life strength ratios (Figure 7.7). It is observed from this figure that the continuum mechanics, boundary and surface diffusion models all predict notch weakening which is consistent with the 4F material behaviour. The only difference between these three models is the power to which the normalised axial component σ_{nom}/σ_1 is raised (n = 1, 3 or 16). It is also observed that the constant ductility and constant δ_i models gave a good fit up to about a/R = 0.5 for the 10G material which was more ductile than the 4F material. However, no agreement with any of the models is obtained for the sharpest notches for the 10G material.

7.4.4 Davis and Manjoine's [1953] Creep Data

The uni-axial and notched rupture data reported by Davis and Manjoine in 1953 on a range of high temperature alloys with different grain size, hardness, ductility and heat-treatment have been used by several investigators to provide some understanding of notch behaviour. The creep data on four different alloys are shown plotted in Figure 7.8 as a ratio of 1000 hours notched to unnotched rupture strength. Previous models proposed by McLean, et al. [1977] and Cocks [1980], together with the continuum mechanics and microstructural models suggested by the present author are also given in the same figure. McLean, et al. [1977] used the Bridgman equation (7.2) which gave good agreement with the initial notch strengthening behaviour of three of the four alloys. They also suggested two bounds to notch strengthening dictated by the geometrical ratio, b/a. The first was an upper bound due to the onset of gross section creep caused

by the notch constraint $(b/a)^2$ and the second was a lower bound due to the loss of localised deformation caused by the ratio b/a being insufficient to sustain constraint beyond a critical value of r/a. These two bounds are shown in Figure 7.8 as two horizontal lines.

Cocks [1980] used equation (7.27) with $n = 9$ to model the behaviour of alloy A. He suggested that the deviation between his model and the experimental data in the region of high constraint was probably due to the drop in failure strains which can cause a drop in stress redistribution times.

In Figure 7.8, the present models of constant ductility, constant δ_i, diffusion and continuum mechanics for σ_1 materials are shown plotted as a function of constraint. The state of stress parameters, such as $\sigma_{nom}/\bar{\sigma}$, σ_{nom}/σ_1 and α, were taken from the finite element predictions given in Chapter 4 for the notched geometries with $b/a = 1.33$. The stress index for alloys A and B were approximated to $n = 7$ and D and C to $n = 12$. It is observed that the constant ductility line gave an excellent fit to alloy A data and the σ_{nom}/σ_1 model (diffusion and continuum mechanics for σ_1 materials) can be regarded as a good lower bound. It must be noted that the data presented in this figure were normalised with respect to the constant load and not constant stress uni-axial line, due to the lack of information on the latter. It is therefore expected that the experimental data on alloy D, which has approximately the same ductility and n values as the $2\frac{1}{4}$%Cr 1%Mo steel, will drop by a factor of 1.2 to 1.3 if the true uni-axial rupture life is used. This is the factor required to bring the data line nearer to the constant δ_i line shown in Figure 7.8 for $n = 12$. The other alloys are less ductile than alloy D. Therefore, it is expected that the effects of plastic instability have a smaller influence on the measured uni-axial rupture lives. Nevertheless, a factor of up to 1.1 will bring the data

of alloys C and B nearer to the σ_{nom}/σ_1 model and improve the fit of the blunt notched data of alloy A with the constant δ_i line for $n = 7$.

7.5 GENERAL COMMENTS ON THE PROPOSED MODELS

It was necessary, before applying the proposed models to the experimental data, to check the validity of using the state of stress parameters at the skeletal point to predict rupture times. The results, based on Calladine's approximate time-scale predictions, showed that stress redistribution was achieved relatively early in life for all the notched geometries investigated. If these predictions were opposite to those which have been already reported in Section 7.2, i.e. no stress redistribution was achieved early in life, then the theoretical lifetime predictions would have been invalid.

A factor which has been highlighted prior to the application of the proposed models to experimental data is the importance of having an efficient method for estimating the required state of stress parameters in the notch throat. The limitation of the approximate plasticity solutions, such as the Bridgman method, makes the present rapid finite element method very attractive in providing the necessary information.

The good agreement between the proposed models and the experimental data suggest that the assumption that nucleation time is negligible is not a bad approximation. However, the results point out very strongly that if plastic instability causes early failure, then this factor has to be taken into consideration. The proposed microstructural models using the assumption that ductility is constant seem to provide a useful fit to the data in the region of low constraint. It is believed that the deviation of this model from the data is due to the drop in ductility as the constraint increases. The best fit observed between any of the proposed models and the experimental data was obtained using the constant δ_i lines. The strength of this model lies in its ability to include both the increase in the hydrostatic and the decrease in the effective stress components as the constraint increases, through the state of stress

parameter α which is also dependent on n. However, if plastic instability intervenes, then this model will under-estimate the measured strength ratios.

7.6 CONCLUSIONS

Estimates of stress redistribution times due to creep have been given for a range of notch geometries using Calladine's approximate method and the Hayhurst finite element predictions. Comparison with the experimental lifetimes of some of these geometries indicate that stress redistribution can be achieved, provided that the right stresses are used in the calculations. The results also confirm the validity of using the state of stress parameters at the skeletal point to predict notch bar behaviour and their lifetimes.

The continuum mechanics and microstructural models derived in Chapter 5 have been applied to several experimental creep data, some of which are reported in Chapter 6 and the others in the literature. The model in which the ductility is assumed constant provides a good fit to the data in the region of low constraint. It was found that for materials which fail by damage accumulation and not plastic instability, agreement is obtained with the models which predict notch weakening only through the normalised axial component raised to the power 1, 3 or n. The best fit was provided by the model which assumes δ_i remains constant with increase in constraint if the effects of plastic instability were taken into consideration.

TABLE 7.1

Estimates of Steady-State Times for Some Notched Bar Geometries

(a) $2\frac{1}{4}$%Cr 1%Mo steel: $n = 9.77$, $C = 2.5156 \times 10^{-25}$, $\sigma_{nom} = 200$ MPa, $E = 152$ GPa

Notch	b/a	a/R	$\bar{\sigma}_{max}/\sigma_o^{\infty}$	$\sigma_{1_{max}}/\sigma_o^{\infty}$	τ_{ss}	Calladine $\delta(t_s)$ (h)		Hayhurst $\delta(t_s)$ (h)	Experimental t_R (h)
						$\bar{\sigma}_{max}$	$\sigma_{1_{max}}$		
Semi-circular notch	1.67	1.5	2.1	3.05	2×10^{-2}	0.49	0.18	27.8	-
BS V-notch	1.41	18.18	1.5	3.05	4.2	0.48	9.3×10^{-3}	300.0	≃ 1800
Deep notch, DN1	1.9	2.0	2.5	4.15	1.1×10^{-2}	1.02	0.11	147.0	-
Deep notch, DN2	2.25	5.0	3.2	5.8	4×10^{-3}	2.27	0.12	1040.0	-

TABLE 7.1 (continued)

(b) ½%Cr ½%Mo ¼%V steel: $n = 16.66$, $C = 2.2 \times 10^{-46}$, $\sigma_{nom} = 300$ MPa, $E = 176$ GPa

Notch	b/a	a/R	$\bar{\sigma}_{max}/\sigma_o^{\infty}$	$\sigma_{1_{max}}/\sigma_o^{\infty}$	$\tau_{\delta\delta}$	Calladine $\delta(t_\delta)$ (h)		Hayhurst $\delta(t_\delta)$ (h)	Experimental t_R (h)
						$\bar{\sigma}_{max}$	$\sigma_{1_{max}}$		
Semi-circular notch	1.67	1.5	2.05	3.18	7×10^{-4}	437.0	0.434	2.76×10^{-5}	24 (4F) 240 (10G)
BS V-notch	1.41	18.18	2.4	3.1	2.0	0.176	3.13×10^{-3}	3.93×10^{-6}	-
Deep notch, DN1	1.9	2.0	2.45	4.2	2×10^{-4}	1536.0	0.316	4.48×10^{-6}	-
Deep notch, DN2	2.25	5.0	2.8	5.9	4×10^{-5}	3.8×10^{4}	0.31	1.79×10^{-8}	-

TABLE 7.2

Estimates of Steady-State Times for Two Low Alloy Steel Notched Specimens

(a) 2¼%Cr 1%Mo steel: b/a = 1.46, n = 9.77

a/R	σ_{nom} = 200 MPa						
	$\bar{\sigma}_{max}/\sigma_o^\infty$	$\bar{\sigma}^*/\sigma_o^\infty$	$\sigma_1^*/\sigma_o^\infty$	$t_s(t_s)_{max}$ (h)	$t_s(t_s)^*$ (h)	$t_s(t_s)_1^*$ (h)	Experimental t_R (h)
0.0	2.136	2.136	2.136	0.041	0.041	0.041	46.9
1.0	1.75	1.72	2.24	0.233	0.272	0.0173	639.4
1.67	1.69	1.58	2.23	0.317	0.572	0.018	779.8
2.6	1.62	1.48	2.225	0.459	1.015	0.0279	1064.5
5.0	1.625	1.375	2.42	0.447	1.936	0.0133	1860.5
8.125	1.65	1.33	2.44	0.39	2.592	0.01	–
13.0	1.8	1.32	2.625	0.182	2.77	0.0065	1885.2
21.66	–	1.318	–	–	2.8	–	187.0
32.5	1.45	1.315	2.8	1.215	2.86	0.0037	–
44.7	–	1.31	–	–	2.96	–	1960.4
a/R	σ_{nom} = 175 MPa						
0.0	2.136	2.136	2.136	0.131	0.131	0.131	148.7
1.0	1.75	1.72	2.24	0.753	0.876	0.055	1146.5
1.67	1.69	1.58	2.23	1.023	1.846	0.058	1788.4
13.0	1.8	1.32	2.625	0.588	8.93	0.021	3799.4

(b) ½%Cr ½%Mo ¼%V steel: b/a = 1.67, n = 16. , σ_{nom} = 300 MPa

a/R	$\bar{\sigma}_{max}/\sigma_o^\infty$	$\bar{\sigma}^*/\sigma_o^\infty$	$\sigma_1^*/\sigma_o^\infty$	$t_s(t_s)_{max}$ (h)	$t_s(t_s)^*$ (h)	$t_s(t_s)_1^*$ (h)	Experimental t_R (h)	
							4F	10G
0.0	2.78	2.78	2.78	3.43	3.43	3.43	41.0	41.0
0.75	2.35	2.35	2.77	50.86	50.86	3.63	30.1	–
1.5	2.15	2.1	2.9	206.4	299.0	1.76	24.0	239.9
2.0	1.95	1.9	2.92	960.8	1446.5	1.585	13.2	185.5
17.0	–	–	–	–	–	–	–	49.4
18.0	–	–	–	–	–	–	23.2	–
20.0	1.9	1.55	3.27	1446.5	3.5×10^4	0.266	–	–

TABLE 7.3

Estimates of the Material Property ϕ_o for the 2¼%Cr 1%Mo Steel at 565°C

The equation for ϕ_o is:

$$\dot{\phi}_o = \frac{2\, D_b\, \delta_b\, \Omega}{k\, T\, \ell^3} \frac{\sigma_o}{\varepsilon_o}$$

where (source: Dyson [1982]):

$$D_b = 4.4 \times 10^{-14}\ m^2/s$$

$$\delta_b = 5 \times 10^{-10}\ m$$

$$\Omega = 1.7 \times 10^{-29}\ m^3$$

$$k = 1.4 \times 10^{-23}\ J/K$$

$$\ell \simeq 10\ \mu m$$

$$\sigma_o = 2 \times 10^{8}\ Pa$$

The test conditions were:

$\sigma_o = 2 \times 10^8$ Pa , $\dot{\varepsilon}_o = 7.07 \times 10^{-3}$ 1/h = 1.964×10^{-6} 1/s

and:

$\sigma_o = 1.75 \times 10^8$ Pa , $\dot{\varepsilon}_o = 2.1 \times 10^{-3}$ 1/h = 5.83×10^{-7} 1/s

The calculations gave:

$\phi_o = 6.5 \times 10^{-3}$ at 2×10^8 Pa

and: $\phi_o = 1.92 \times 10^{-4}$ at 1.75×10^8 Pa

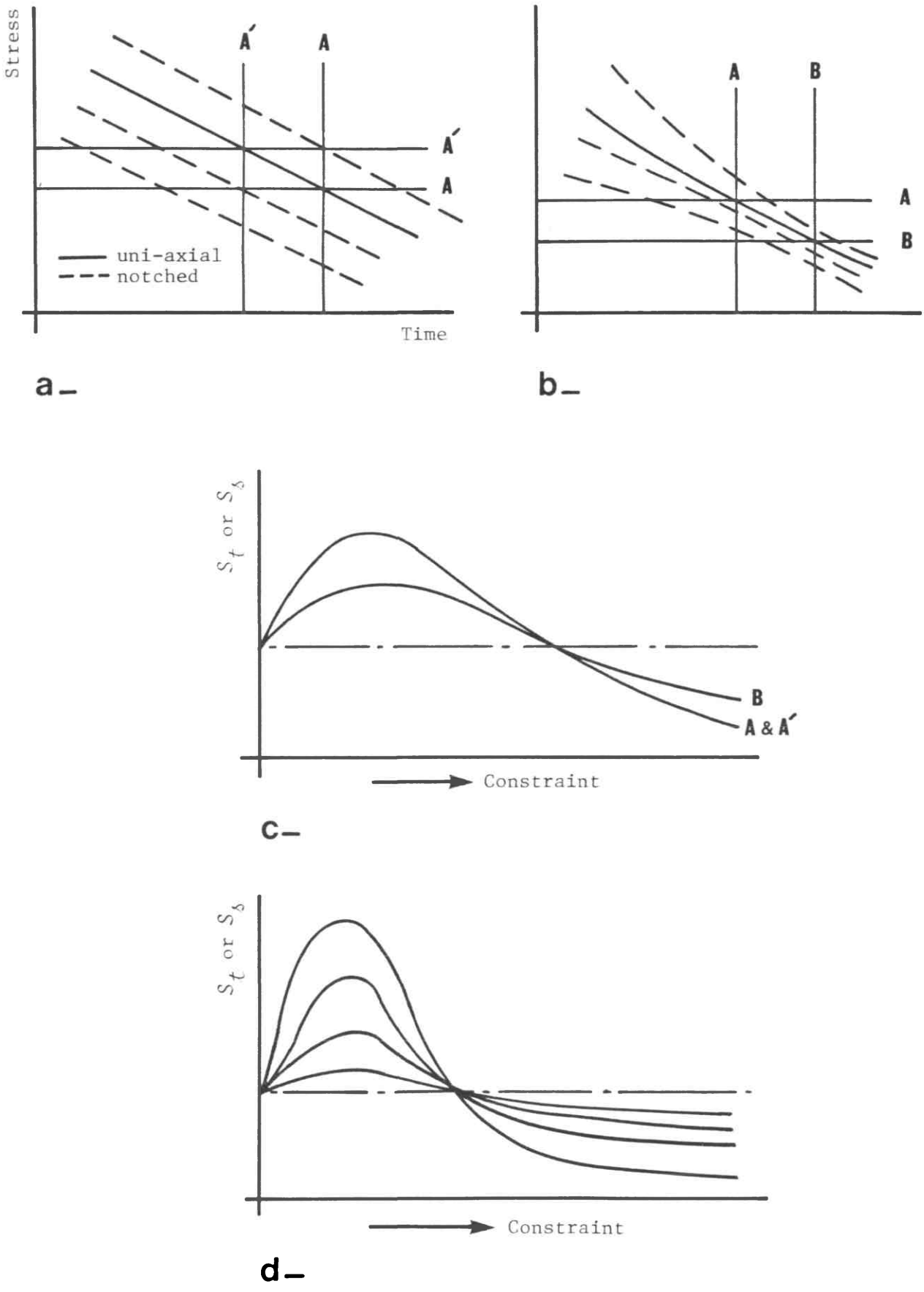

Figure 7.1: The different ways of interpreting creep data

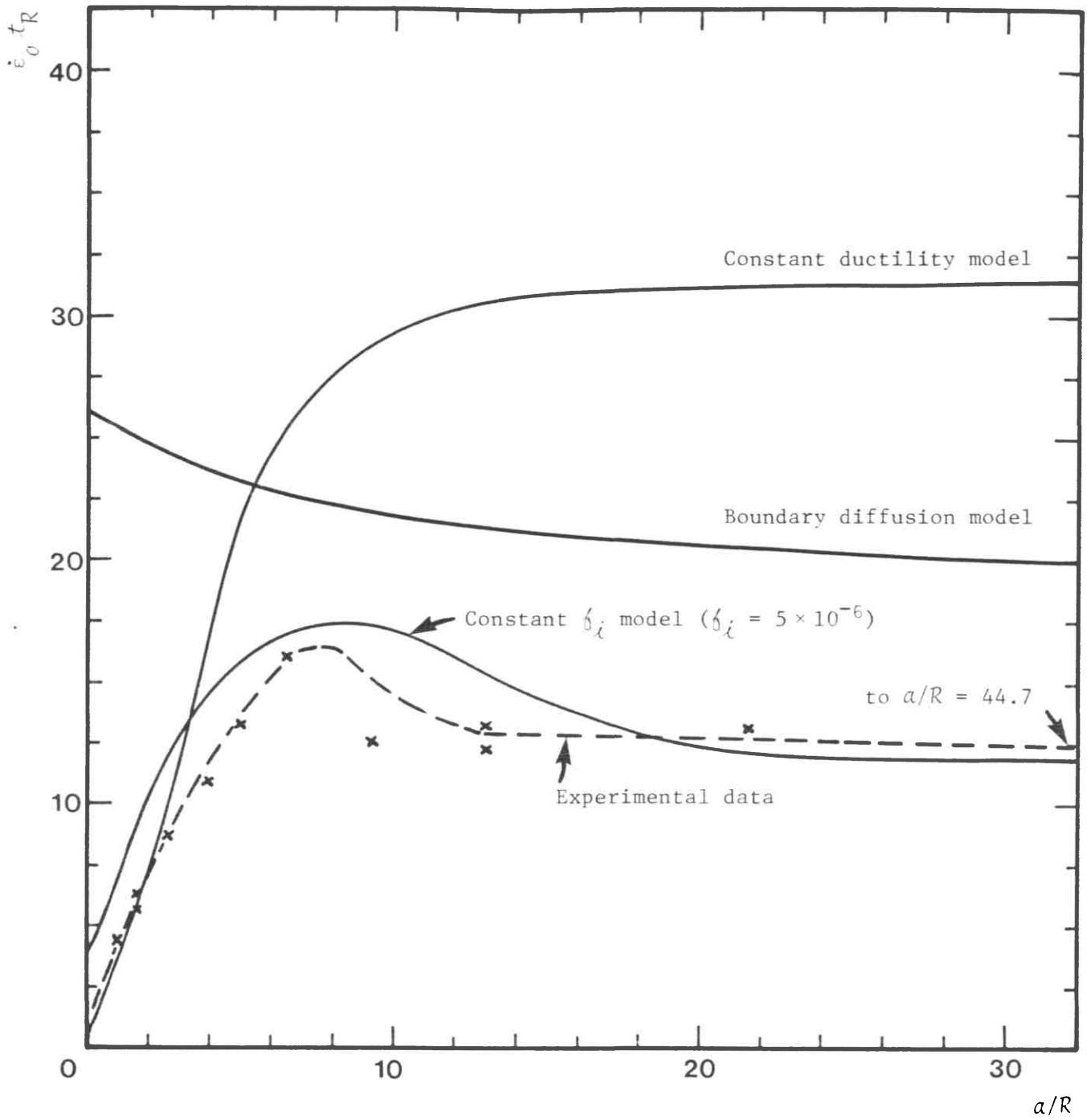

Figure 7.2: Application of the proposed models in terms of rupture time, $\dot{\varepsilon}_o t_R$, to the 2¼%Cr 1%Mo steel data

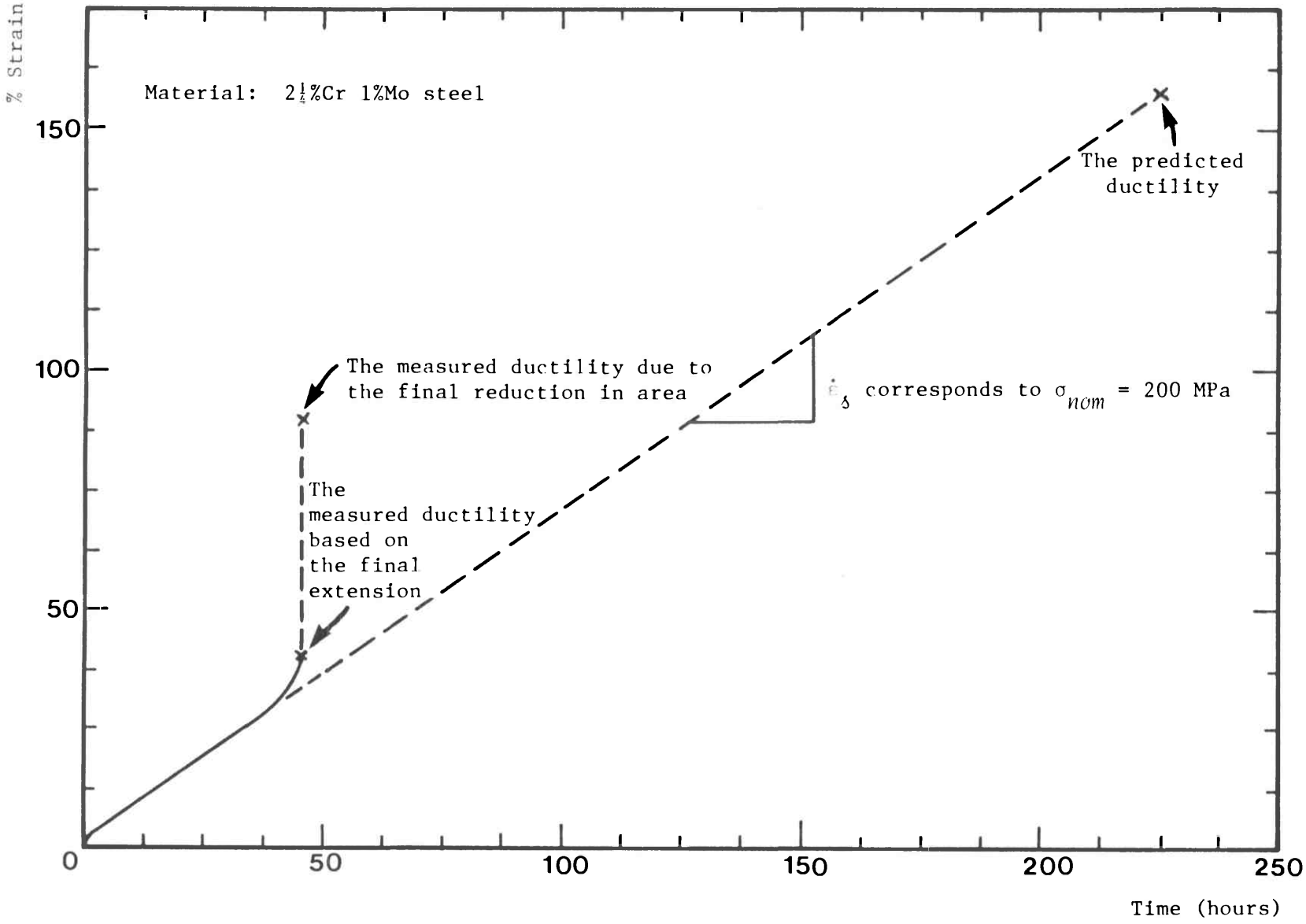

Figure 7.3: Comparison between the experimentally measured and the true rupture time for a uni-axial specimen creep tested at 538°C under a constant stress of 200 MPa

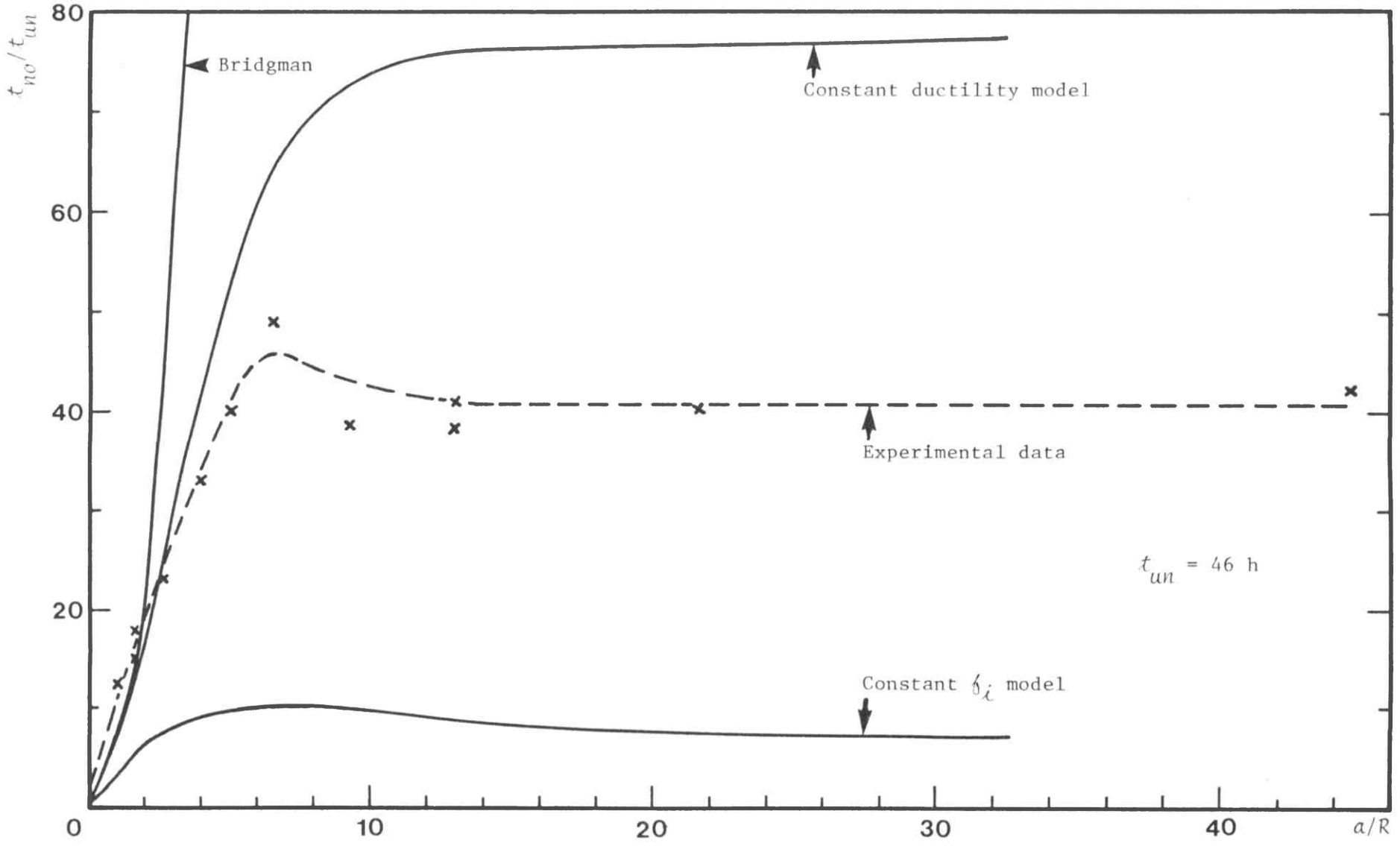

Figure 7.4: Application of the proposed models in terms of notched to unnotched lifetimes to the 2¼%Cr 1%Mo steel data using the experimentally measured uni-axial rupture time, t_{un}

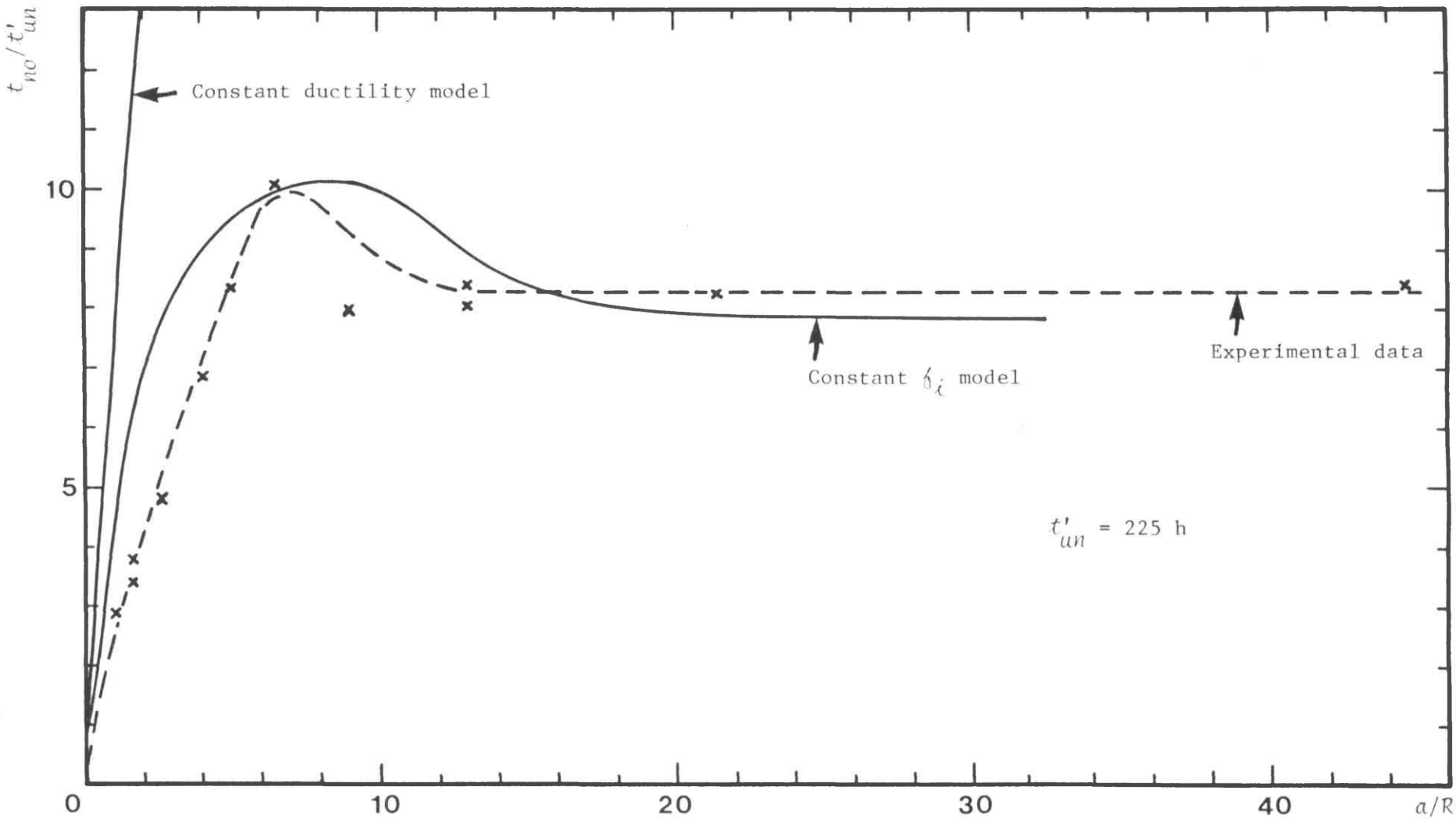

Figure 7.5: Application of the proposed models in terms of notched to unnotched lifetimes to the 2¼%Cr 1%Mo steel data using the true uni-axial rupture time, t'_{un}

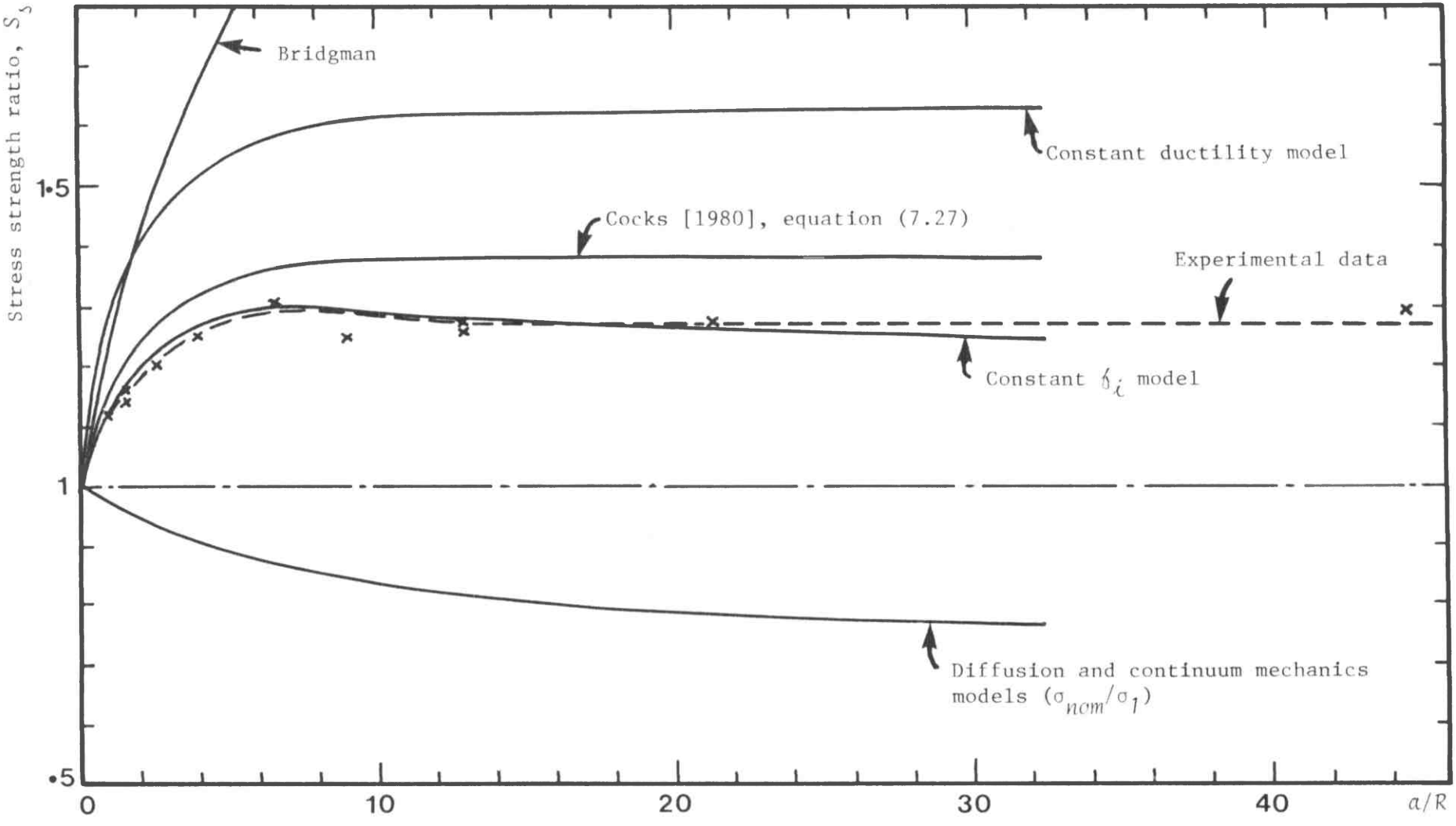

Figure 7.6: Application of the proposed models in terms of stress strength ratios to the $2\frac{1}{4}$%Cr 1%Mo steel data

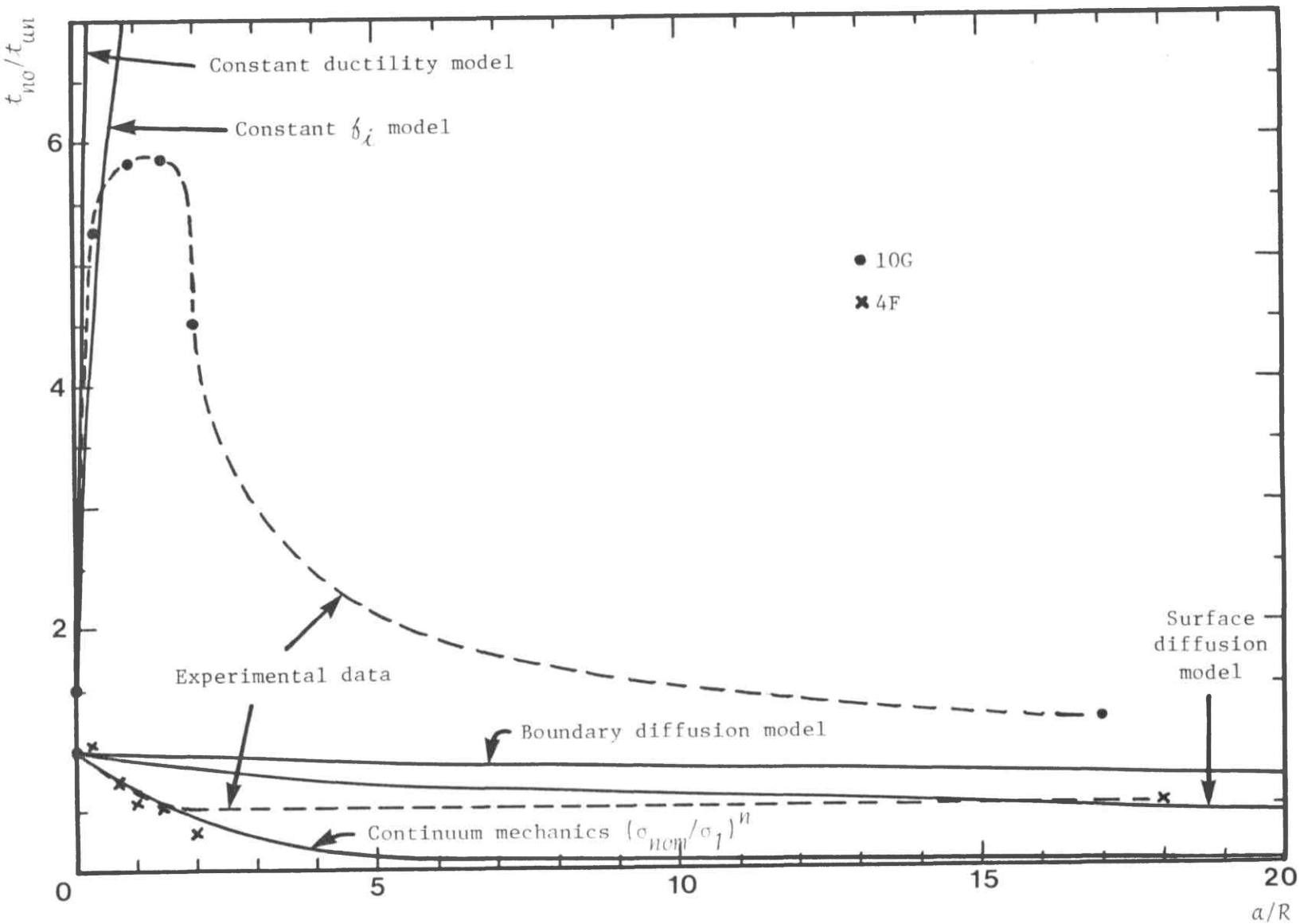

Figure 7.7: Application of the proposed models in terms of notched to unnotched lifetimes to the ½%Cr ½%Mo ¼%V steel data

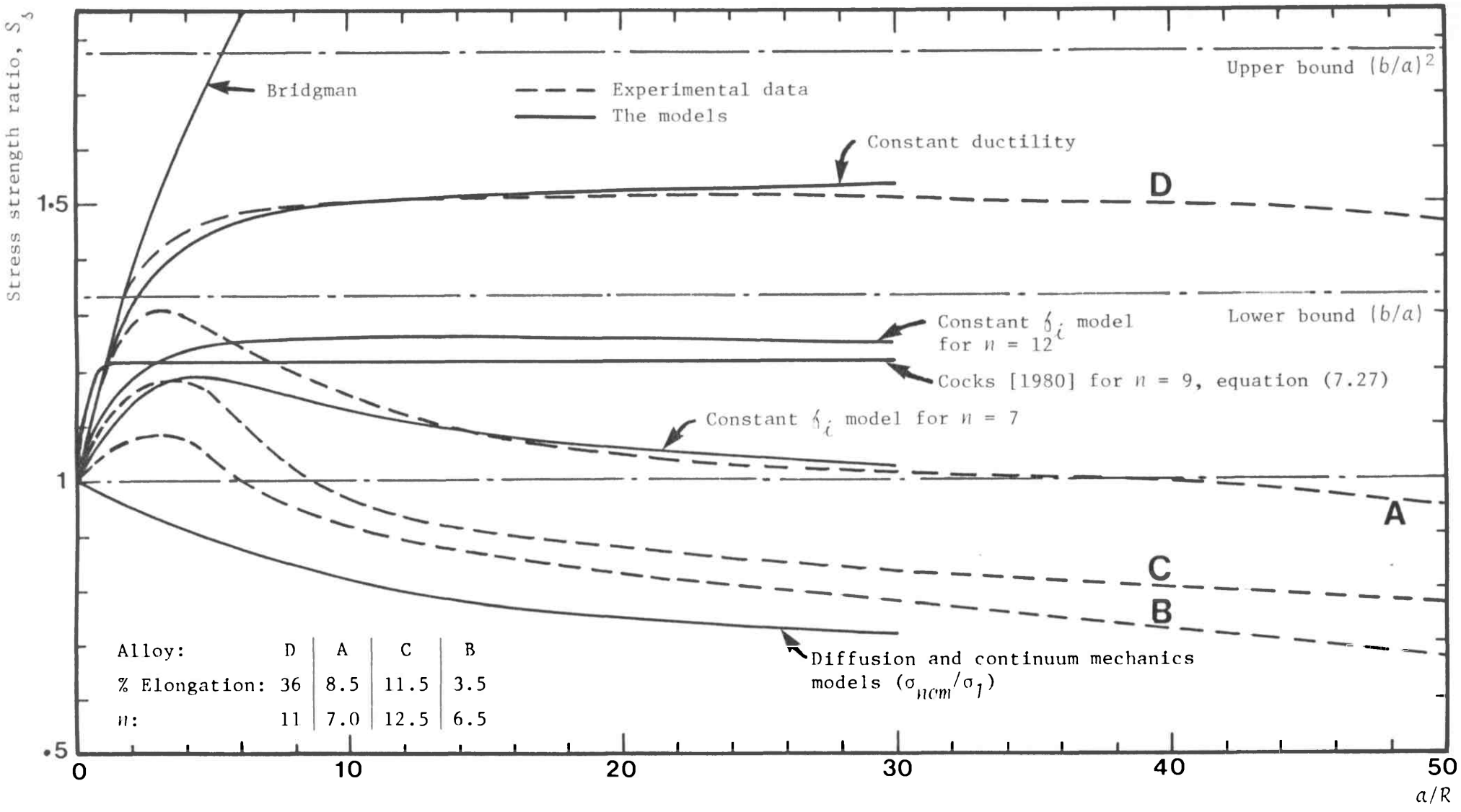

Figure 7.8: Application of the proposed and other models in terms of stress strength ratios to Davis and Manjoine's [1953] creep data

CHAPTER 8

CONCLUSIONS AND RECOMMENDATIONS

8.1 CONCLUSIONS

The object of the work presented in this thesis was to investigate the influence of state of stress on creep failure. The procedure followed in order to fulfil these objectives was to think of a possible method in which the state of stress can be systematically varied and then investigate their influence on the prediction of component lifetimes. Previous experimental and theoretical investigations have shown that by changing the notch profile in round bars pulled in tension, the state of stress parameters in the throat will vary accordingly. The research procedure after adopting this method branched into the following main lines:

(a) To develop an efficient numerical technique based on the finite element method in order to assess how the state of stress parameters vary in the throat with notch shape.

(b) To conduct a series of experimental creep tests on plain and notched bar specimens made of a material of practical relevance. The results of the experimental investigation would provide a knowledge of some material creep coefficients and lifetimes needed in the analysis.

(c) To use the finite element predictions of the state of stress parameters in the notch throat in some theoretical models to predict the lifetimes of the notched specimens.

Prior to presenting any theoretical or experimental results, a detailed literature review of continuum mechanics and microstructural laws

which describe the behaviour of components undergoing creep deformation were given in Chapters 1 and 2. In particular, attention was focused on the Ashby and co-workers theory for modelling the growth of voids by mechanisms controlled by diffusion, power-law creep and by any combination of these two.

Discussions of (a) were given in Chapters 3 and 4, (b) in Chapter 6, and (c) in Chapters 5 and 7. The conclusions reached were as follows:

(i) Two finite element programs have been developed and used successfully to calculate the steady-state stress distributions in axi-symmetric and two-dimensional bodies subjected to creep. The iterative numerical method adopted in which the elastic material properties are up-dated after each iteration until the final steady-state is achieved, have been found to be economical in terms of cost and accurate in comparison with exact and other finite element solutions.

(ii) Solutions have been obtained for a range of circumferentially-notched bar geometries and different values of stress index, n. Other geometries have also been investigated; these were blunt and sharp double notches under remote uniform tension, and compact tension specimens with different hole sizes machined into their crack plane.

(iii) It has been found that for all the notch geometries investigated and for values of $n > 1$, a skeletal point at which the effective stress remained constant, independent of n, was observed.

(iv) Several theoretical models have been derived using either a continuum mechanics approach or Ashby's void growth theory to predict notched bar behaviour. These models were used in a

detailed calculation using hypothetical material constants, ductilities and area fraction of holes. The state of stress parameters required in these calculations were taken from the finite element prediction at the skeletal point. It was found that if the ductility is assumed constant, the models always predict notch strengthening for $\bar{\sigma}$ materials and notch weakening for σ_1 materials. When the area fraction of holes was assumed constant, both notch strengthening and weakening can be predicted, depending on the value of n and the tri-axial state of stress.

(v) Creep tests at 538°C have been carried out on several plain and notched bar specimens pulled in tension. The material tested was the 2¼%Cr 1%Mo steel used in the electric power generation industries. The creep data obtained have been analysed and compared with the brittle ½%Cr ½%Mo ¼%V steel. It has been found that no matter how severe the notch sharpness is, the 2¼%Cr 1%Mo steel will always notch strengthen.

(vi) Some indication of the time taken to reach the steady-state conditions have been included using Calladine's approximate method and the creep coefficients obtained in the experimental part of this investigation. The approximate time-scale predictions based on the state of stress parameters at the skeletal point showed that rapid stress redistribution is achieved.

(vii) The continuum mechanics and microstructural models have been applied to the experimental data obtained on the 2¼%Cr 1%Mo steel and other creep data available in the literature. It has been found that a constant ductility model gave a good fit to the data in the region of low constraint. If the material notch weakens, i.e. fails by damage accumulation and not by

necking, then the diffusion models provided a good fit to these type of data, with the continuum mechanics model for σ_1 materials being the lower weakening bound. It has also been found that if the material fails by plastic instability, then the proposed model which assumes σ_i constant gave an excellent fit to the data, provided a corrected and not a measured lifetime is used.

8.2 RECOMMENDATIONS

In a research programme of this scope, it is inevitable that all aspects of the problem could not have been covered. During the course of the investigation and the writing of this thesis, a number of suggestions have arisen which could lead to further work. Some of these are now offered:

(1) Modify the present finite element method so that solutions at intermediate time steps can be estimated, together with the final stress redistribution time. This involves adding routines which calculate an optimum time step and over-relaxation factor after each iteration. Extra arrays may be required to store the previous, new and the calculated strains and stresses. Prior to this, a suitable time function has to be chosen.

(2) There are some grounds for improving the performance of the present finite element method if, for example, quadratic types of elements are used instead of the present constant strain triangular elements. This means that accurate estimates of the stress distributions in the presence of very sharp notches or cracks could be made possible. This suggestion requires some time to be spent in adopting a new method for storing and solving the dimension and stiffness matrices, respectively.

(3) The influence of anisotropy in material properties is another possibility which can be incorporated into the present finite element method. This involves adding some logic statements to modify the homogeneous material properties after each iteration.

(4) Quantitative measurements of voids and their growth rate in the present material could be made using, possibly, electron

microscopy techniques. This means a series of interrupted tests at successive times prior to failure to determine the development of damage throughout life. In this way, the assumptions of the microstructural models can be checked.

REFERENCES

AL-FADDAGH, K.D., FENNER, R.T., and WEBSTER, G.A. [1982]
J. Strain Analysis, 17 (3), 123.

ASHBY, M.F., GANDHI, C., and TAPLIN, D.M.R. [1979]
Acta Met., 27, 699.

BAILEY, R.W. [1929]
The Engineer, 148, 528.

BAILEY, R.W. [1951]
Proc. Instn. Mech. Engrs., 164, 425.

BATES, R.C., and SANTHANAM, A.T. [1978]
Int. J. Fracture, 14 (5), 501.

BEERE, W., and SPEIGHT, M.V. [1978]
Met. Sci., 4, 172.

BRIDGMAN, P.W. [1952]
Studies in Large Plastic Flow and Fracture,
McGraw-Hill, New York.

CALLADINE, C.R. [1963]
Proc. Instn. Mech. Engrs., 178 (3A), 2.

CALLADINE, C.R. [1964]
Proc. Instn. Mech. Engrs., 178, 198.

CALLADINE, C.R. [1966]
J. Appl. Mech., 33, 322.

CALLADINE, C.R. [1967]
J. Mech. Engng. Sci., 9, 198.

CALLADINE, C.R. [1969]
Proc. R. Soc. Lond., A309, 363.

CANE, B.J. [1980]
ICF5 in Advances in Fracture Research (edited by Francois, D., et al.),
Pergamon Press, Oxford/New York.

CANE, B.J. [1981]

Central Electricity Research Laboratories, Report No. RD/L/2101 N 81, Job No. VH071, VH052, VH589.

CHEVENARD, P.C.R. [1919]

Acad. Sci. Paris, 69, 712.

CHUANG, T-J., KAGAWA, K.I., RICE, J.R., and SILLS, L.B. [1979]

Acta Met., 27, 265.

COCKS, A.C.F. [1980]

PhD Thesis, Cambridge University.

COCKS, A.C.F., and ASHBY, M.F. [1980a]

Proc. IUTAM Symposium on Creep in Structures, Leicester, England (edited by Ponter, A.R.S., and Hayhurst, D.R.).

COCKS, A.C.F., and ASHBY, M.F. [1980b]

Met. Sci., 14, 395.

COCKS, A.C.F., and ASHBY, M.F. [1982a]

Prog. Mater. Sci., 27, 189.

COCKS, A.C.F., and ASHBY, M.F. [1982b]

Met. Sci., 16, 465.

COOK, G., and ROBERTSON, A. [1911]

Engineering, 92, 786.

COX, A.P.D. [1981]

PhD Thesis, Imperial College, London University.

DA COSTA ANDRADE, E.N. [1910]

Phil. Mag., 9, 513.

DAVIS, E.A. [1945]

J. Appl. Mech., 12, A13.

DAVIS, E.A., and MANJOINE, J.J. [1953]

ASTM STP 128, 67.

DAWSON, R.J., FESSLER, H., HYDE, T.H., and WEBSTER, J.J. [1981]

J. Strain Analysis, 15 (1), 21.

DICKENSON, J.H.S. [1922]

J. Iron Steel Inst., 106, 103.

DYSON, B.F. [1976]

Met. Sci., 10, 349.

DYSON, B.F., and TAPLIN, D.M.R. [1976]

Proc. Instn. Metallurgists Meeting, Jersey, E13.

DYSON, B.F., and McLEAN, D. [1977]

Met. Sci., 11, 37.

DYSON, B.F., and LOVEDAY, M.S. [1980]

Proc. IUTAM Symposium on Creep in Structures, Leicester, England (edited by Ponter, A.R.S., and Hayhurst, D.R.).

DYSON, B.F. [1982]

Private communications.

EDWARD, C.H., and ASHBY, M.F. [1979]

Acta Met., 27, 1505.

EWING, D.J.F., and HILL, R. [1967]

J. Mech. Phys. Solids, 15, 115.

EWING, D.J.F. [1968]

J. Mech. Phys. Solids, 16, 81.

FENNER, R.T. [1975]

Finite Element Methods for Engineers,

Macmillan, London.

FORD, H. [1963]

Advanced Mechanics of Materials,

Longmans, London.

FURSE, J.E., and LOVEDAY, M.S. [1981]

British Patent 8131641.JX5782.

GREENBAUM, G.A., and RUBENSTEIN, M.F. [1968]

Nucl. Engng. Design, 7, 379.

GREENWOOD, J.N., MILLER, R.R., and SUITER, J.W. [1954]

Acta Met., 2, 256.

HANCOCK, J.W., and MACKENZIE, A.C. [1976]

J. Mech. Phys. Solids, 14, 107.

HAYHURST, D.R. [1972]

J. Mech. Phys. Solids, 20, 381.

HAYHURST, D.R. [1973a]

J. Appl. Mech., 40, 244.

HAYHURST, D.R. [1973b]

J. Appl. Mech., 40, 915.

HAYHURST, D.R., and LECKIE, F.A. [1973]

J. Mech. Phys. Solids, 21, 431.

HAYHURST, D.R., DIMMER, P.R., and CHERNUKA, M.W. [1975]

J. Mech. Phys. Solids, 23, 335.

HAYHURST, D.R., and HENDERSON, J.T. [1977a]

Int. J. Mech. Sci., 19, 133.

HAYHURST, D.R., LECKIE, F.A., and HENDERSON, J.T. [1977b]

Int. J. Mech. Sci., 19, 147.

HAYHURST, D.R., LECKIE, F.A., and MORRISON, C.J. [1978]

Proc. R. Soc. Lond., A360, 243.

HELLAN, K. [1975]

Int. J. Mech. Sci., 17, 369.

HOFF, N.J. [1953]

J. Appl. Mech., 20, 105.

HOLLOWAY, G., and SHELTON, A. [1979]

J. Mech. Engng. Sci., 21 (4), 221.

HULL, D., and RIMMER, D.E. [1959]

Phil. Mag., 4, 673.

HYDE, T.H., WEBSTER, J.J., and FESSLER, H. [1980]

4th Int. Conf. on Pressure Vessel Technology, London.

JOHNSON, A.E. [1951]

Proc. Instn. Mech. Engrs., 164, 432.

JOHNSON, A.E., HENDERSON, J., and KHAN, B. [1962]

HMSO, Edinburgh.

JOHNSON, W., and MELLOR, P.B. [1975]

Engineering Plasticity,

Van Nostrand Reinhold Company, London.

KACHANOV, L.M. [1958]

Izv. A.N. USSR, OTN, No. 8, 26.

KUMAR, V., GERMAN, M.A., and SHIH, C.F. [1980]

Contract RP123-1 for Electric Power Research Institute, Palo Alto, California 94303, USA.

LECKIE, F.A., and HAYHURST, D.R. [1974]

Proc. R. Soc. Lond., A340, 323.

LIANIS, G., and FORD, H. [1957]

J. Mech. Phys. Solids, 5, 215.

LINDBORG, U. [1968]

J. Mech. Phys. Solids, 16, 328.

LINDBORG, U. [1969]

Acta Met., 17, 521.

LODE, W. [1926]

Zeit. Physik, 36, 913.

LOVEDAY, M.S., and DYSON, B.F. [1979]

Proc. ICM3, 2, 213 (edited by Miller, K.J., and Smith, R.F.), Pergamon Press.

MACKENZIE, A.C., HANCOCK, J.W., and BROWN, D.K. [1977]

Engng. Fract. Mech., 9, 167.

MARRIOT, D.L., and LECKIE, F.A. [1964]

Proc. Instn. Mech. Engrs., 178 (3L), 115.

MARTIN, J.B., and LECKIE, F.A. [1972]

J. Mech. Phys. Solids, 20, 223.

McLEAN, D., DYSON, B.F., and TAPLIN, D.M.R. [1977]

ICF4 on Fracture, 1, Waterloo, Canada.

McCLINTOCK, F.A. [1961]

Weld. Res. Suppl.,

McCLINTOCK, F.A. [1968]

J. Appl. Mech., 35, 363.

MORRISON, J.L.M. [1940]

Proc. Instn. Mech. Engrs., 142, 193.

MORRISON, J.L.M. [1948]

Proc. Instn. Mech. Engrs., 159, 81.

MORZERIA, A.M. [1979]

Third Year Project Report, Imperial College, London University.

NADAI, A. [1937]

J. Appl. Phys., 8, 418.

NADAI, A. [1950]

Theory of Flow and Fracture of Solids,

Volume 1, McGraw-Hill.

NAGHDI, P.M., ESSENBURG, F., and KOFF, W. [1958]

J. Appl. Mech., 25, 201.

NEEDLEMAN, A., and SHIH, C.F. [1978]

Comp. Meths. Appl. Mech. Engng., 15, 223.

NEEDLEMAN, A., and RICE, J.R. [1980]

Acta Met., 28, 1315.

NG, S.E., WEBSTER, G.A., and DYSON, B.F. [1980]

ICF5 on Advances in Fracture Research (edited by Francois, D., et al.), Pergamon Press, Oxford/New York.

NEIMARK, J.E. [1968]

J. Appl. Mech., 35, 111.

NEWMAN, D.P., JONES, M.H., and BROWN, W.F. [1953]

Proc. ASTM, 53, 677.

NORTON, F.H. [1929]

Creep of Steel at High Temperatures,

McGraw-Hill, New York.

ODQVIST, F.K.G. [1935]

Int. Congr. Appl. Mech., Cambridge 1934, Proc. Cambridge University Press.

ODQVIST, F.K.G. [1953]

Trans. R. Int. Tech., Stockholm, 66, 1.

PENNY, R.K. [1967]

Int. J. Mech. Sci., 9, 373.

PENNY, R.K., and MARRIOT, D.L. [1971]

Design for Creep,

McGraw-Hill, London.

PENNY, R.K. [1974]

Metals and Materials, 8 (2), 124.

PHILLIPS, F. [1905]

Phil. Mag., 9, 513.

PRAGER, W. [1945]

J. Appl. Phys., 16, 837.

RAJ, R., and ASHBY, M.F. [1975]

Acta Met., 23, 653.

RICE, J.R., and TRACEY, D.M. [1969]

J. Mech. Phys. Solids, 17, 201.

RICHARDS, K. [1955]

Mitteilungen, Verein Grossdampfkessel-Besitzer (in German), 39, 836.

ROBINSON, E.L. [1952]

Trans. Amer. Soc. Mech. Engrs., 74, 777.

ROBOTNOV, Y.N. [1969]

Creep Problems in Structural Members,

North-Holland Publishing Company, London.

ROGAN, J., and SHELTON, A. [1969]

J. Strain Analysis, 4, 127.

SANTHANAM, A.T., and BATES, R.C. [1979]

Mat. Sci. Engng., 41, 243.

SCZCZEPINSKI, W., DIETRICH, L., DRESCHER, E., and MIASTKOWSKI, J. [1966]

Int. J. Solids Structures, 2, 543.

SEGERLIND, L.J. [1976]

Applied Finite Element Analysis,

Wiley, New York.

SIEBEL, M.P.L. [1953]

J. Mech. Phys. Solids, 1, 189.

SODERBERG, C.R. [1936]

Trans. Amer. Soc. Mech. Engrs., 58, 733.

SPEIGHT, M.V., and HARRIS, J.E. [1967]

Met. Sci., 1, 83.

SPEIGHT, M.V., and BEERE, W. [1975]

Met Sci., 9, 190.

SUTHERLAND, W.H. [1970]

Nucl. Engng. Design, 11, 269.

SVENSSON, L.E., and DUNLOP, G.L. [1980]

Proc. IUTAM Symposium on Creep in Structures, Leicester, England (edited by Ponter, A.R.S., and Hayhurst, D.R.).

TAPSELL, H.J., and JOHNSON, A.E. [1940]

Engineering, 150, 24.

TAYLOR, G.I., and QUINNEY, H. [1931]

Phil. Trans. R. Soc., A230, 323.

WEBSTER, G.A., and NIKBIN, K.M. [1981]

Progress Report No. 3, Agreement No. 2037/0205 XR/NGTE(P), Imperial College, London University.

WEERTMAN, J. [1974]

Met. Trans., 5, 1743.

ZIENKIEWICZ, O.C. [1977]

The Finite Element Method,

3rd edition, McGraw-Hill, London.

APPENDIX A

STEADY-STATE STRESS DISTRIBUTIONS IN CIRCUMFERENTIALLY NOTCHED BARS SUBJECTED TO CREEP

Paper by:

K.D. Al-Faddagh, R.T. Fenner and G.A. Webster

Published in:

Journal of Strain Analysis, Vol. 17, No. 3, 1982, pp. 123-132

STEADY-STATE STRESS DISTRIBUTIONS IN CIRCUMFERENTIALLY NOTCHED BARS SUBJECTED TO CREEP

K. D. AL-FADDAGH *Imperial College of Science and Technology, London.*

R. T. FENNER *Imperial College of Science and Technology, London. Member of the Institution.*

G. A. WEBSTER *Imperial College of Science and Technology, London. Member of the Institution.*

The paper describes a procedure, based on a finite element method, for calculating directly the steady-state stress distribution in circumferentially notched bars subjected to creep without the need for obtaining solutions at intermediate time intervals. Good agreement is obtained with relevant approximate plasticity solutions and with numerical calculations which approach the steady-state over a period of time from the initial elastic stress distribution. Also, the procedure is equally applicable to primary, secondary, and tertiary creep, provided the variables of stress and time are separable in the creep law.

Results obtained for a range of notch geometries and values of the stress index, n, are reported. It is found for each profile that a region of approximately constant effective stress, $\bar{\sigma}$, independent of n, is obtained which can be used to characterise the overall behaviour of the notch throat region when a steady-state is reached sufficiently early in life. An approximate method for estimating the maximum equivalent steady-state stress across the notch throat is also presented which does not require a computer solution.

1 INTRODUCTION

Failure by excessive creep deformation or fracture is an important design consideration in structures required to operate at elevated temperatures over long periods of time. Often these components are subjected to triaxial states of stress resulting from the applied loading or sharp changes in section. In order to determine useful component lives in such circumstances, laws governing creep behaviour under multi-axial stressing are needed (1)(2)†.

A uniform state of triaxial stress is difficult to produce in laboratory experiments. The most frequent method of introducing a three-dimensional state of stress into a test piece is to subject circumferentially notched bars to an axial tensile load. The constraint of the shank produces a state of triaxial tension in the notch region which depends upon the notch geometry and creep properties of the material. In tests carried out by a number of investigators (3)–(5), both notch strengthening and notch weakening have been observed, depending upon the notch dimensions and material examined. Some knowledge of the stress distribution across the notch throat is needed if this behaviour is to be explained.

The stress distribution within a notch region can be determined in a number of ways, depending upon the assumptions made. Initially, in the absence of plastic deformation on loading, an elastic stress distribution will be obtained. As time progresses, stress redistribution will take place due to the high sensitivity of creep deformation to stress. When secondary creep dominates, creep strain rate can often be written in the form

$$\dot{\bar{\varepsilon}} = C\bar{\sigma}^n \tag{1}$$

where C and n are constants at constant temperature, and $\bar{\sigma}$ and $\dot{\bar{\varepsilon}}$ are the corresponding equivalent stress and creep strain rates appropriate to multiaxial states of stress. Several calculations, relevant to circumferentially notched bars, have been made using finite element techniques and equation (1) (6)–(11). An incremental procedure is adopted and solutions obtained by iteration for successive time intervals. These are, however, often expensive and time-consuming to produce. The calculations, nevertheless, show that frequently a steady-state (or stationary) stress distribution is achieved across the notch throat after a sufficiently long period of time. If this stress distribution occurs early enough in the specimen life, it may be possible to use it to characterise the test piece behaviour.

Several methods of determining steady-state stress distributions directly have been proposed (12)–(17). Most (12)–(15) make use of non-work hardening plasticity solutions and are, therefore, strictly only relevant to values of $n \to \infty$. This paper presents a numerical method for determining the steady-state stress distribution in axisymmetric problems, rapidly, for any value of n, without the need for calculating how stress redistribution occurs with time. Results are included for a range of values of n and notch geometries, and comparisons made with the incremental time step solutions of Hayhurst and co-workers (8)–(11). An approximate procedure for providing conservative estimates of the maximum steady-state equivalent stress,

The MS. of this paper was received at the Institution on 5th October 1981 and accepted for publication on 18th January 1982.

† *References are given in the Appendix.*

0309–3247/82/0700–0123 $02.00

$\bar{\sigma}_{max}$, in the notch throat is outlined. Also, some indication of the time taken to reach a steady-state is included.

1.1 Notation

a	Notch throat radius
a_i, a_j, a_k	Dimensions of a triangular element
b	Bar radius
b_i, b_j, b_k	Dimensions of a triangular element
$[\mathbf{B}]$	Element dimension matrix
C	Material constant in creep law
$C_1 \cdots C_6$	Displacement coefficients
$[\mathbf{D}]$	Element elastic property matrix
$[\mathbf{d}]$	Element dimension matrix
E	Young's modulus
F	Relative stress concentration factor
$[F]$	Vector of overall externally applied forces
$[\mathbf{K}]$	Overall stiffness matrix
k	Elastic effective stress concentration factor
$[\mathbf{k}]_m$	Element stiffness matrix
n	Stress index in creep law
P	Pressure
R, $\bar{R}_m$	Notch profile radius, element radial coordinate
R_1, R_2	Internal and external radii
R_i, R_j, R_k	Element radial distance from the axis of symmetry
u_i, u_j, u_k	Element radial displacement component
w_i, w_j, w_k	Element axial displacement component
Δ_m	Element area
$[\delta]$, $[\delta]_m$	Overall and element vector of displacement components
ε, $\bar{\varepsilon}$	Strain, effective strain
$\dot{\varepsilon}$, $\dot{\bar{\varepsilon}}$	Creep strain rate, effective creep strain rate
ν	Poisson's ratio
σ, $\bar{\sigma}$	Stress, effective stress
χ	Total potential energy
λ	Convergence tolerance

Subscripts

zz, $\theta\theta$, rr	Refer to axial, hoop and radial directions
m	Refers to triangular element m
ss	Refers to steady-state
∞	Refers to remote boundary
o	Refers to initial or reference conditions

2 AXI-SYMMETRIC FINITE ELEMENT ANALYSIS

Axi-symmetric problems can be solved by considering a two-dimensional solution domain lying in a radial plane through the axis of symmetry of the body concerned, as shown in Fig. 1. The solution procedure adopted is first to calculate the elastic stress and strain distributions. These are then modified with the aid of equation (1). To obtain the steady-state stress distribution, it is assumed that elastic strains are negligible compared with the creep strains so that equation (1) can be used to determine total strains.

2.1 Finite element formulation for small strain linear elasticity

Figure 1 shows a typical triangular finite element, numbered m, in the axial-radial plane, r and z being local

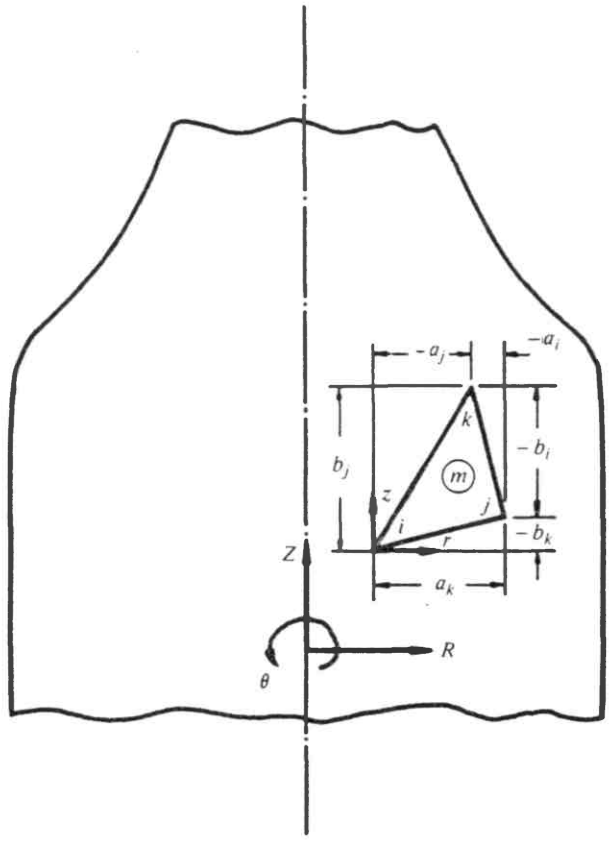

Fig. 1. Triangular finite element in a radial plane of an axisymmetric body

coordinates parallel to the global coordinates R and Z. The element has three nodes, numbered i, j, and k, located at its corners. Although more sophisticated higher-order elements are often to be preferred for linearly elastic problems, simple triangular elements offer a number of advantages for non-linear problems.

The radial and axial displacement components are assumed to vary linearly over the typical element, so that

$$u = C_1 + C_2 r + C_3 z \tag{2}$$

$$w = C_4 + C_5 r + C_6 z \tag{3}$$

where the six constants may be found in terms of the six nodal point displacements from

$$C_1 = u_i; \quad [C_2\, C_3]^T = \frac{1}{2\Delta_m}[\mathbf{d}][u_i\, u_j\, u_k]^T \tag{4}$$

$$C_4 = w_i; \quad [C_5\, C_6]^T = \frac{1}{2\Delta_m}[\mathbf{d}][w_i\, w_j\, w_k]^T \tag{5}$$

where

$$[\mathbf{d}] = \begin{bmatrix} b_i & b_j & b_k \\ a_i & a_j & a_k \end{bmatrix}$$

and $\Delta_m = \frac{1}{2}(a_k b_j - a_j b_k)$ is the area of the element. Hence, most of the non-zero strains are constant over the element and

$$\varepsilon_{rr} = \frac{\partial u}{\partial r} = C_2; \quad \varepsilon_{zz} = \frac{\partial w}{\partial z} = C_6;$$

$$\varepsilon_{rz} = \frac{\partial u}{\partial z} + \frac{\partial w}{\partial r} = C_3 + C_5 \tag{6}$$

Although the hoop strain does vary over the element, it is reasonable to assume it to be constant (**18**) to give

$$\varepsilon_{\theta\theta} = \frac{u}{R} \simeq \frac{\bar{u}}{\bar{R}_m} \tag{7}$$

where $\bar{u}$ and $\bar{R}_m$ are the mean values over the element of the radial displacement and radial distance from the axis of symmetry

$$\bar{u} = \tfrac{1}{3}(u_i + u_j + u_k); \quad \bar{R}_m = \tfrac{1}{3}(R_i + R_j + R_k)$$

Combining equations (4)–(7), the element strain components can be expressed in terms of nodal point displacements by

$$[\varepsilon] = [\varepsilon_{rr}\, \varepsilon_{zz}\, \varepsilon_{\theta\theta}\, \varepsilon_{rz}]^T = \frac{1}{2\Delta_m}[\mathbf{B}][\delta]_m \tag{8}$$

where

$$[\delta]_m = [u_i\, w_i\, u_j\, w_j\, u_k\, w_k]^T$$

and

$$[\mathbf{B}] = \begin{bmatrix} b_i & 0 & b_j & 0 & b_k & 0 \\ 0 & a_i & 0 & a_j & 0 & a_k \\ 2\Delta_m/3\bar{R}_m & 0 & 2\Delta_m/3\bar{R}_m & 0 & 2\Delta_m/3\bar{R}_m & 0 \\ a_i & b_i & a_j & b_j & a_k & b_k \end{bmatrix}$$

The relationship between element stresses and strains can be derived from Hooke's law as

$$[\sigma] = [\sigma_{rr}\, \sigma_{zz}\, \sigma_{\theta\theta}\, \sigma_{rz}]^T = [\mathbf{D}][\varepsilon] \tag{9}$$

where the elastic property matrix is given by

$$[\mathbf{D}] = \frac{E^*}{1 - \nu^{*2}} \begin{bmatrix} 1 & \nu^* & \nu^* & 0 \\ \nu^* & 1 & \nu^* & 0 \\ \nu^* & \nu^* & 1 & 0 \\ 0 & 0 & 0 & \tfrac{1}{2}(1 - \nu^*) \end{bmatrix}$$

E^* and ν^* being the Young's modulus and Poisson's ratio modified as for plane strain conditions (**18**)

$$E^* = \frac{E}{1 - \nu^2}; \quad \nu^* = \frac{\nu}{1 - \nu}$$

Equilibrium conditions for the entire mesh of elements can be obtained by requiring the total potential energy, χ, to be stationary for small changes in the displacements (**18**). Hence

$$d\chi = 2\pi \sum_m \bar{R}_m \Delta_m [\sigma]^T\, d[\varepsilon] - [F]^T\, d[\delta] = 0 \tag{10}$$

where $[\delta]$ is a vector containing all the nodal point displacement components, while $[F]$ contains the corresponding forces, uniformly distributed around the circumferences through the nodes at which they are applied. Introducing equations (8) and (9), this result becomes

$$2\pi \sum_m \frac{\bar{R}_m}{4\Delta_m} [\mathbf{B}]^T[\mathbf{D}][\mathbf{B}][\delta]_m = \sum_m [\mathbf{k}]_m[\delta]_m = [\mathbf{K}][\delta] = [F] \tag{11}$$

where the $[\mathbf{k}]_m$ are element stiffness matrices, which are assembled to form the overall stiffness matrix, $[\mathbf{K}]$. Solution of the overall linear equations, which is equivalent to inverting this matrix, yields the nodal point displacements and hence stresses. An important consequence of using constant strain triangular (CST) finite elements is that the method of solution can be either a direct elimination type technique, which is the approach most commonly used in finite element methods, or an iterative technique such as Gauss–Seidel. The latter can be particularly useful when dealing with non-linear problems.

2.2 Treatment of non-linear problems

Non-linearities in material behaviour, such as creep and plastic deformation, which cause the effective elastic properties E and ν to vary with, for example, time or the local state of strain, can be dealt with in different ways. One approach is to solve a series of linear problems corresponding to small increments of the relevant independent variable, such as time or loading. For example, in the present context, equation (1) can be used to obtain solutions at a series of time intervals, Δt. An advantage of this approach is that solutions are obtained not only at the final time required but also at a number of intermediate times. This is the procedure adopted in references (**6**)–(**11**). The main disadvantage is that if the time increment, Δt, is made too large, the computed solutions will diverge from their true values. On the other hand, if Δt is made very small, the amount of computing required becomes excessive as a large number of complete solutions of linear equations in the form of equation (11) are required.

A second approach, and the one which is used here, is to treat the elastic properties as variables, thereby making the [**D**] matrix for each element, its stiffness matrix, and the overall stiffness matrix into variables. Thus, equation (11) is no longer linear. Nevertheless, it is possible to solve it using the iterative Gauss–Seidel technique, provided the elastic properties and stiffness matrices are up-dated during the iterative process. Although the amount of computing involved in a typical non-linear solution of this type is more than that required for the corresponding linear solution, it is generally only greater by a factor of some two or three. Therefore, this non-linear stiffness approach is more economical than the incremental time step approach, and it is generally much easier to ensure correct convergence of the solution. On the other hand, the many intermediate solutions associated with the incremental approach are not available, the partially converged results of intermediate iterations having no physical significance.

A difficulty is experienced with the present finite element formulation when the material concerned is incompressible. Setting $\nu = \frac{1}{2}$ makes the element [**D**] matrix singular. Although a complete reformulation of the method can overcome this difficulty, at least for the types of physical problems considered here, it is adequate to use a value of $\nu = 0.49$. It is close enough to incompressibility to avoid significant errors, while at the same time avoiding the numerical instabilities associated with values much closer to 0.5.

Since the present finite element formulation uses displacement as the nodal point variables, the elastic modulus needs to be expressed as a function of the local state of strain. Using the constitutive equation (1), therefore, the strain at time t is given by

$$\bar{\varepsilon} = C\bar{\sigma}^n t \tag{12}$$

which may be inverted to give

$$\bar{\sigma} = \left(\frac{\bar{\varepsilon}}{Ct}\right)^{1/n} \tag{13}$$

An apparent or effective modulus, E', can now be defined such that

$$E' = \bar{\sigma}/\bar{\varepsilon}$$

Substituting in equation (13) gives

$$E' = \frac{1}{\bar{\varepsilon}}\left(\frac{\bar{\varepsilon}}{Ct}\right)^{1/n} = E_o(\bar{\varepsilon}/\bar{\varepsilon}_o)^{(1/n)-1} \tag{14}$$

where E_o is the effective modulus at some convenient reference strain, ε_o. Setting $n = 1$ gives a constant modulus $E' = E_o$, whereas for $n > 1$, E' will be a function of strain. Before calculations can be made, it is necessary to define the appropriate equivalent stress $\bar{\sigma}$ and strain $\bar{\varepsilon}$. In this presentation, the Von Mises criterion has been adopted throughout, giving

$$\bar{\varepsilon} = \left[\frac{2}{3}(\varepsilon_{rr}^2 + \varepsilon_{zz}^2 + \varepsilon_{\theta\theta}^2 + \tfrac{1}{2}\varepsilon_{rz}^2)\right]^{1/2} \tag{15}$$

An advantage of using CST elements is that the strains, and hence $\bar{\varepsilon}$ and E', are constant over each element. The general procedure for the non-linear analysis can be summarized in the following steps.

(i) Taking ν and E' to be constant everywhere initially, and equal to, say, 0.3 and E_o, the overall stiffness matrix [**K**] is assembled using equation (11).
(ii) The elastic strains and stresses are calculated using the Gauss–Seidel iterative technique.
(iii) New moduli E', which will vary from element to element, are computed using equation (14) and (15) and a modified [**K**] matrix is reassembled with $\nu = 0.49$.
(iv) A few cycles of Gauss–Seidel iteration are carried out. These may be termed inner iterations.
(v) From the partially converged displacement solutions, new moduli E' are determined as in (iii).
(vi) Steps (iii)–(v) are repeated until satisfactory convergence is achieved. These repetitions may be termed outer iterations.

Convergence is achieved when the displacements computed after successive outer iterations differ by only a small amount

$$\frac{\sum_i \{|\Delta u_i| + |\Delta v_i|\}}{\sum_i \{|u_i| + |v_i|\}} < \lambda \tag{16}$$

where the summations are carried out over all the nodes in the mesh, and Δu_i and Δv_i are the changes in the computed displacements between successive outer iterations. The small tolerance, λ, was taken as 10^{-6}, a value which was found to give very satisfactory convergence. The choice of the number of inner iterations performed in step (iv) has an important bearing on the cost of computation: making this number too small results in unnecessarily frequent up-dating of [**K**], while making it too large results in unnecessarily complete convergence of the solutions to the linearised equations between each modification of [**K**]. A series of tests showed that, at least for the types of problems considered here, about four inner iterations for each outer iteration was the best choice. The number of outer iterations required for convergence depends on both the level of mesh refinement and the magnitude of the exponent n, and increases with the number of elements and with the value of n.

2.3 Comparison with an exact solution

In order to test the finite element method, an example was chosen where the exact linear elastic and non-linear creep solutions are known. This was the case of a thick-walled cylinder subjected to an internal pressure, P. If R_1 and R_2 are the internal and external radii of the cylinder, the distributions of hoop and radial stresses for plane strain conditions are given by (**19**)

$$\sigma_{\theta\theta} = \frac{P}{1-(R_1/R_2)^{2/n}}\left\{\left(\frac{R_1}{R_2}\right)^{2/n} + \left(\frac{2}{n} - 1\right)\left(\frac{R_1}{r}\right)^{2/n}\right\} \tag{17}$$

$$\sigma_{rr} = -\frac{P}{1-(R_1/R_2)^{2/n}}\left\{\left(\frac{R_1}{r}\right)^{2/n} - \left(\frac{R_1}{R_2}\right)^{2/n}\right\} \tag{18}$$

where r is the radial coordinate measured from the axis of symmetry. For the linear elastic case of $n = 1$, these reduce to the familiar Lamé equations.

Figure 2 shows the finite element mesh used for this example, consisting of 34 right-angled triangles arranged in a radial row. The case of $R_2 = 2R_1$ was treated. The displacement constraints allowed the nodes to move only in the radial direction, thereby imposing the required plane strain condition. Results were obtained for $n = 1$, 2, 3, 9, and 100. In all cases, the computed stresses agreed with the above analytical solutions to within 0.3 per cent. This very satisfactory level of agreement is similar to that achieved by Needleman and Shih (**16**), who treated the equivalent problem of a thick-walled cylinder undergoing power-law hardening plastic deformation, although in their finite element computations complete incompressibility was assumed. Provided the stress dependence of creep and plastic deformation can be written in the same form as equation (1), the stress distributions indicated by equations (17) and (18) will be representative of both plastically deforming and creeping tubes. Although the analysis presented here has been applied to creep situations, equations (14) and (15) could equally well be used to determine stress distributions for power-law hardening plastic deformation when the

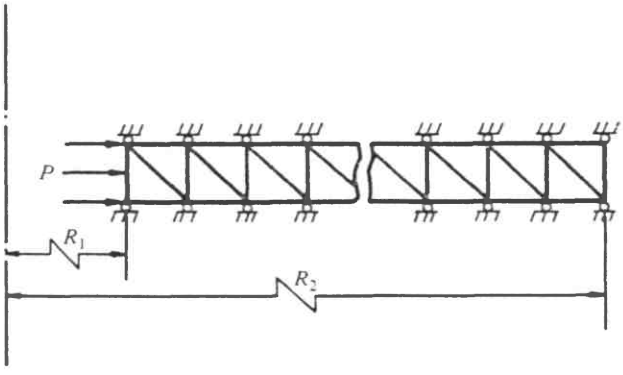

Fig. 2. Simple finite element mesh for thick-walled cylinder problem: $R_2/R_1 = 2$

plastic strains are large compared with the elastic strains. Similarly, attention need not be restricted to secondary creep deformation provided the creep law can be written in the form

$$\bar{\varepsilon} = C\bar{\sigma}^n F(t) \tag{19}$$

where $F(t)$ is an appropriate time function which can describe primary, secondary, and tertiary creep as appropriate. In this case, equation (13) becomes modified to

$$\bar{\sigma} = \left\{\frac{\bar{\varepsilon}}{CF(t)}\right\}^{1/n} \tag{20}$$

but E' can still be written, from equation (14), as

$$E' = E_o(\bar{\varepsilon}/\bar{\varepsilon}_o)^{(1/n)-1}$$

The only restrictions, therefore, on a steady-state stress distribution being achieved for a given geometry and applied loading condition, are that the creep strains must be large in relation to the elastic strains, and the variables of stress and time be separable. It does not matter whether the material is undergoing primary, secondary, or tertiary creep, the same steady-state stress distribution will be achieved, provided each stage of creep can be described by the same value of n. If a different n is needed for each stage, then a true steady-state will not be achieved unless one stage dominates.

In the next section, the numerical technique outlined above is used to calculate the steady-state stress distribution across the throat of circumferentially notched round tensile bars. Some of the notch dimensions have been chosen to enable comparisons to be made with previous (9)(10) finite element calculations which established this stress distribution by extrapolation from solutions obtained over a large number of time intervals. In addition, comparisons are made with an approximate analytical solution by Bridgman (9) for a rigid–plastic material having $n = \infty$.

3 NUMERICAL ESTIMATES FOR NOTCHED BARS

Since a selection of notch geometries needing broadly similar finite element mesh distributions were to be examined, it was worth seeking a method of generating the required grid automatically from a small number of geometric parameters. A similar technique to that reported by Segerlind (20) was used and found to be satisfactory.

3.1 Mesh design

Typical finite element mesh distributions for three notch profiles corresponding to those investigated by Hayhurst *et al.* (13)(14) are shown in Fig. 3. The automatic mesh generation routine developed enabled each cross-section to be divided into regions and the mesh size to be graded so that it was finest where the stress gradient and geometrical changes were greatest. Care was taken to ensure that triangles having obtuse angles were avoided, the ideal shape being an equilateral triangle (18). Experimentation with progressively finer grid sizes has shown that satisfactory accuracy is achieved with approximately 450–500 elements and the notch throat divided into a row of 28 elements, as shown in Fig. 3.

3.2 Calculations

Calculations have been made for values of $n = 1, 3, 5, 9,$ and 20, and 17 notch dimensions. Figure 3 shows a representative range of the notch shapes investigated. In all instances, a uniform axial stress, σ_o^∞, was applied at the specimen remote boundaries, as illustrated in

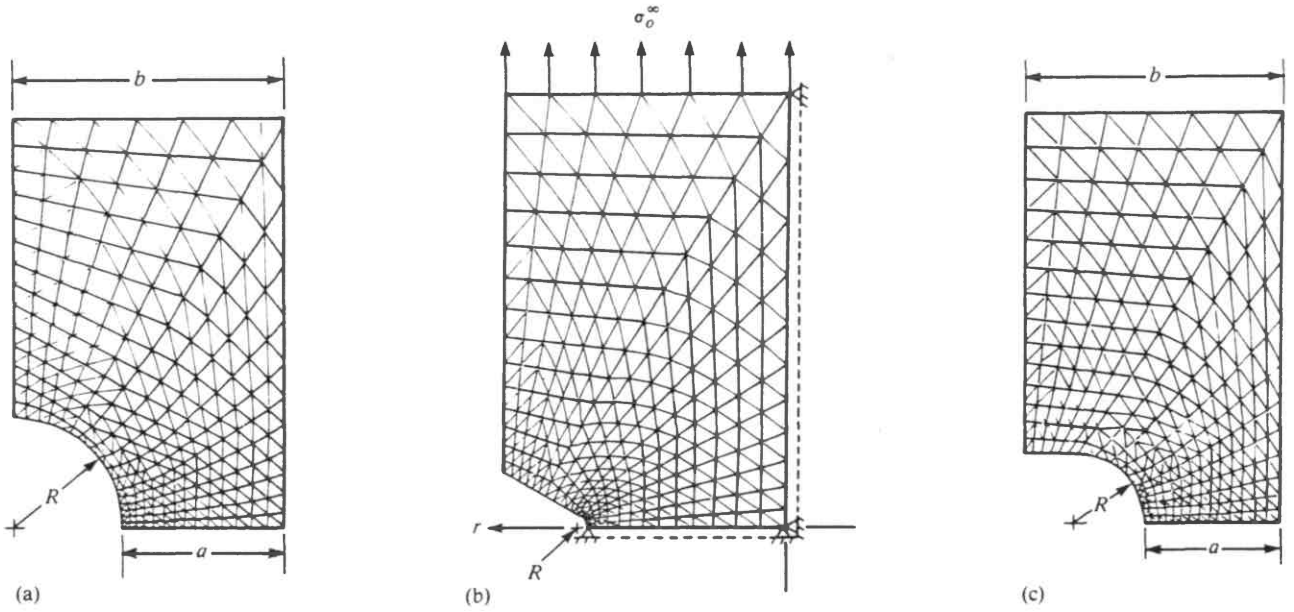

Fig. 3. Finite element meshes and their boundary conditions for the notch geometries: (a) Semi-circular notch; $a/R = 1.5$, $b/a = 1.67$; (b) British Standard V-notch; $a/R = 18.18$, $b/a = 1.41$; (c) Deep notch; $a/R = 2$, $b/a = 1.9$

Fig. 3(b). Also, the specimen axis was constrained to move only in a vertical direction while the notch throat was prevented from moving vertically, again as indicated in Fig. 3(b).

The stress components in each element were calculated for each value of n by the procedure previously described. The results of all the calculations are summarized in Figs 4–12 and compared with previous work (9)(10)(15)(17) where appropriate. Only stress distributions across the minimum diameter of the throat region have been presented, since this section is the most critically loaded, and may, therefore, be expected to determine the deformation and fracture characteristics of such samples.

4 DISCUSSION

Stress distributions have been presented in some detail in Figs 4–9 for the notch geometries shown in Fig. 3 for comparison with previous calculations made on these notch dimensions (9)(10)(15)(17). Figures 4–6 show data for a rather blunt semi-circular notch having $b/a = 1.67$ and $a/R = 1.5$ (Fig. 3(a)); Fig. 4 compares the relative axial stress distributions, $\sigma_{zz}/\sigma_o^\infty$, across the notch throat for $n = 1$, 3, 5, and 9. The $n = 1$ solution corresponds to the elastic distribution. It is clear, for this geometry, that as n increases, the maximum axial stress moves from the notch root, $r = a$, towards the specimen centre line, $r = 0$. The results show good agreement with the steady-state solutions of Kumar *et al.* (17) made for an incompressible material having $\nu = 0.5$. The adoption, therefore, of $\nu = 0.49$ in the present calculations to avoid matrix [D] becoming singular (equation (9)) would seem to be acceptable. Initially, at time zero on first loading, and in the absence of plastic deformation, the stress distribution will be elastic. As creep takes place, regions of high stress shed load onto the lower stress regions because of the high sensitivity to stress of creep deformation. The extent of the stress redistribution that takes place in order to achieve the steady-state condition increases with increase in the value of n (Fig. 4).

Figure 5 presents data for all the stress components for the extreme values of $n = 1$ and 20 used. Figure 6 shows the corresponding results for intermediate values of $n = 3$ and 9. The same trends are observed for the radial, σ_{rr}, and hoop, $\sigma_{\theta\theta}$, stress components as were observed in Fig. 4 for the axial stress. As n increases, load is redistributed from the notch root region, $r = a$, towards the specimen axis, $r = 0$, to compensate for the relative amounts of creep strain accumulated in each region. Comparisons of the axial stresses for $n = 9$ and 20 with the Bridgman (15) rigid plastic solution ($n = \infty$) in Figs 5 and 6 shows close agreement, indicating that the Bridgman approximation can be used to determine σ_{zz} with reasonable precision for $n > 9$. The Bridgman solution gives $\sigma_{rr} = \sigma_{\theta\theta}$ and under-estimates both these stresses for all values of n.

Comparison is also made in Fig. 5 with the steady-state solutions obtained asymptotically by Hayhurst *et al.* (9) from incremented time-step

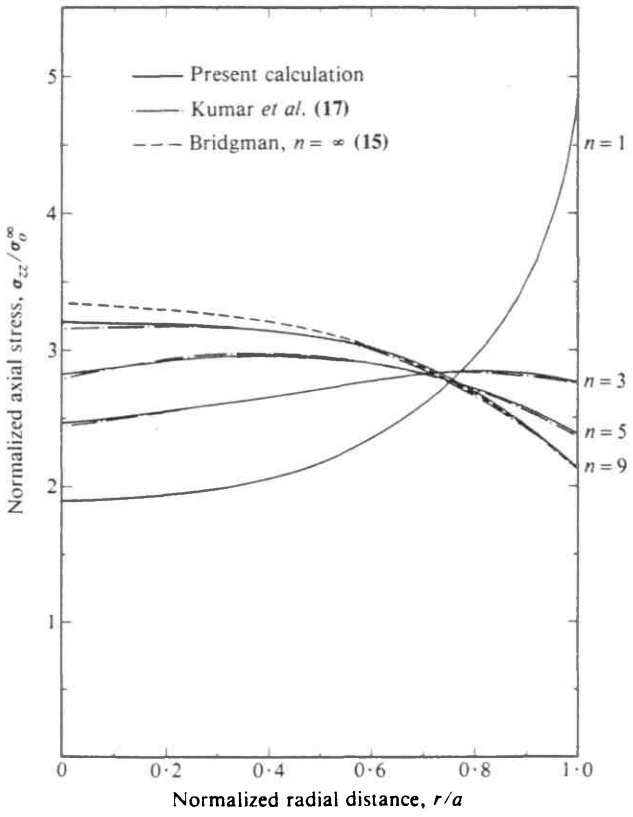

Fig. 4. Axial stress distribution at steady state across the throat of a semi-circular notch ($a/R = 1.5$)

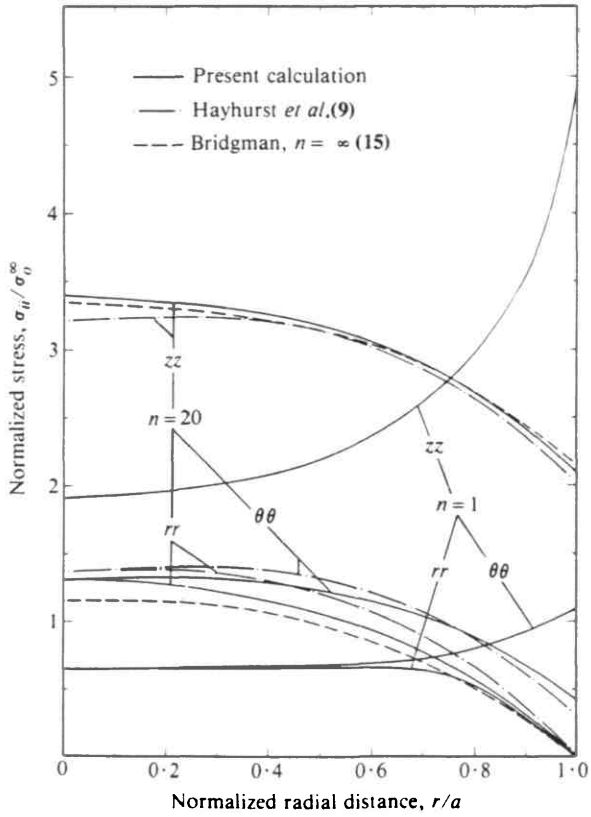

Fig. 5. Stress distribution at steady state across the throat of a semi-circular notch ($a/R = 1.5$) for $n = 1$ and $n = 20$

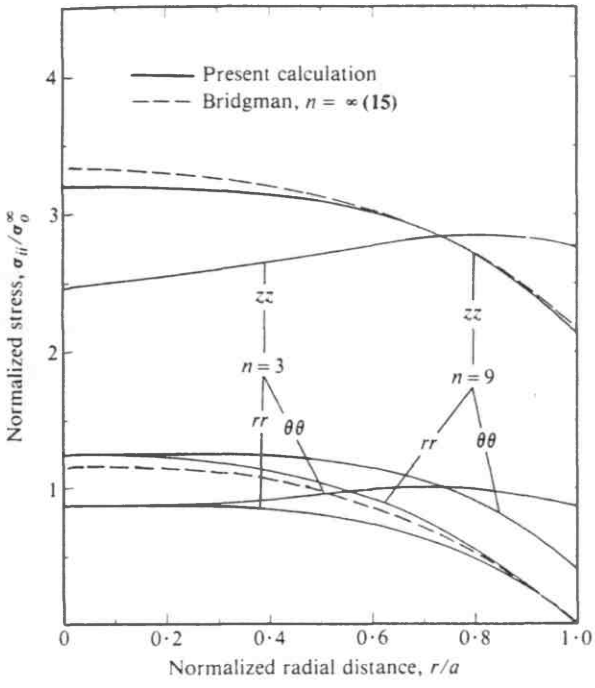

Fig. 6. Stress distribution at steady state across the throat of a semi-circular notch (a/r = 1.5 for n = 3 and n = 9)

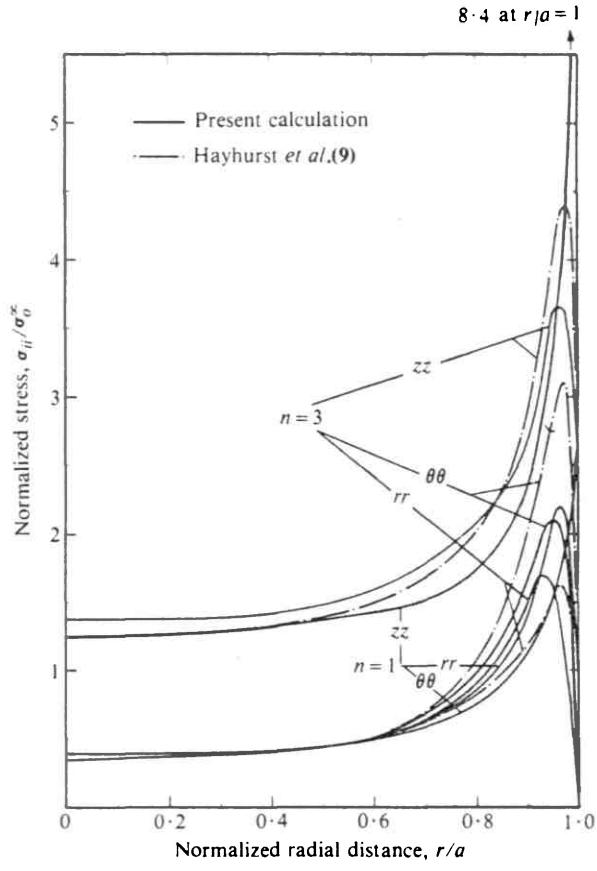

Fig. 7. Stress distribution at steady state across the throat of a BS V-notch for n = 1 and n = 3

computations. Generally, closer agreement is obtained between the two finite element calculations than with the Bridgman approximation. The axial stress distribution of Hayhurst *et al.* (9) is between the elastic and steady-state solutions for n = 20 of the present solutions, suggesting that a true steady-state had possibly not quite been achieved from the Hayhurst *et al.* (9) calculations.

Figures 7 and 8 show the corresponding steady-state stress distributions across the throat of a British Standard V-notch specimen (Fig. 3(b)). Figure 7 presents the data for the n = 1 (elastic) and n = 3 cases, whereas Fig. 8 shows results for n = 5 and 20. Although there are detailed differences between the sharp notch and blunt notch situations, the same general features are apparent. The highest axial and hoop elastic stresses are again at the notch root. However, unlike the blunt notch case, as n increases for the sharp notch, the maximum values of σ_{zz} and $\sigma_{\theta\theta}$ remain close to the notch root, even for n = 20. Figure 7 also shows the predictions of the incremental time-step approach of Hayhurst *et al.* (9), who indicate the same qualitative trends. Greater quantitative differences are apparent than were obtained with the blunt notch geometry (Fig. 5), suggesting that the incremental approach may not have achieved a true steady-state. This is consistent with the comments of Hayhurst *et al.* (9) that correspondingly longer times are required to achieve complete stress redistribution for the British Standard V-notch geometry than for the semi-circular notch. Although comparisons have been shown for only one value of $n(=3)$ with Hayhurst *et al.* (9), similar differences were noted at all values of n.

Figure 9 shows corresponding results for a specimen having a deep, relatively blunt notch with b/a = 1.9 and

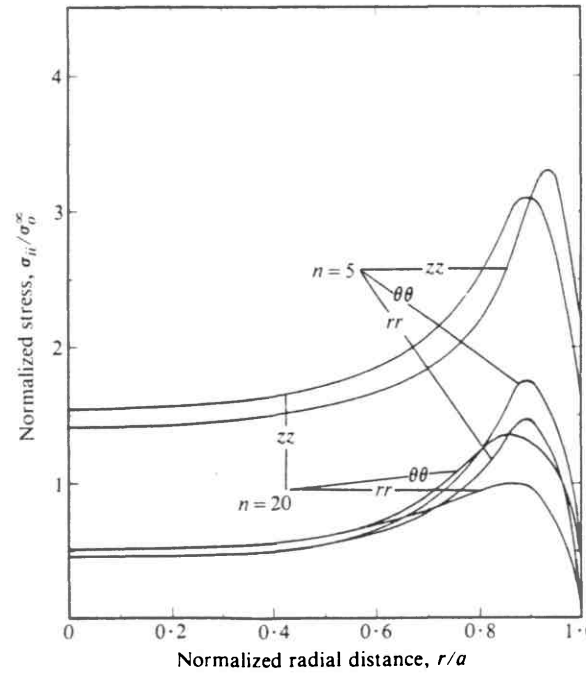

Fig. 8. Stress distribution at steady state across the throat of a BS V-notch for n = 5 and n = 20

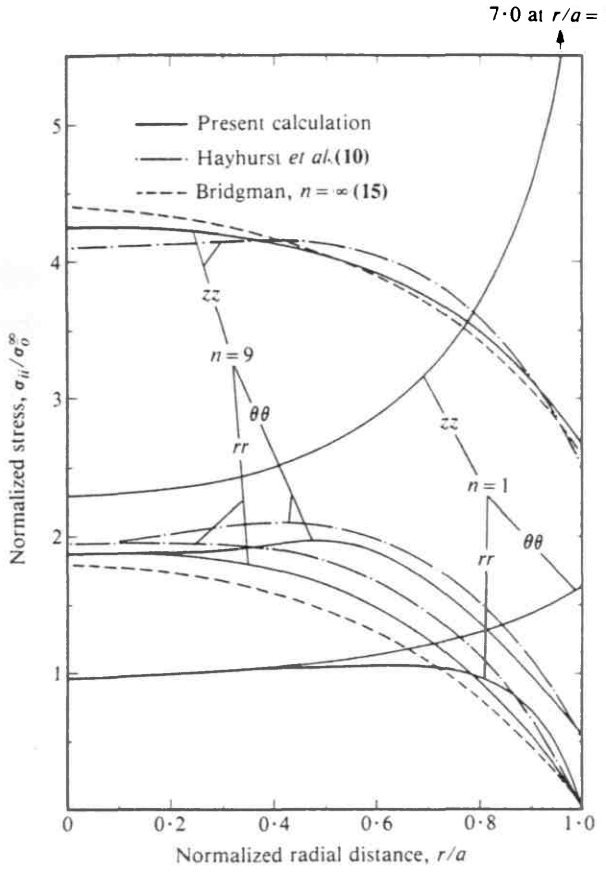

Fig. 9. Stress distribution at steady state across the throat of a notch with $a/R = 2$ and for $n = 1$ and $n = 9$

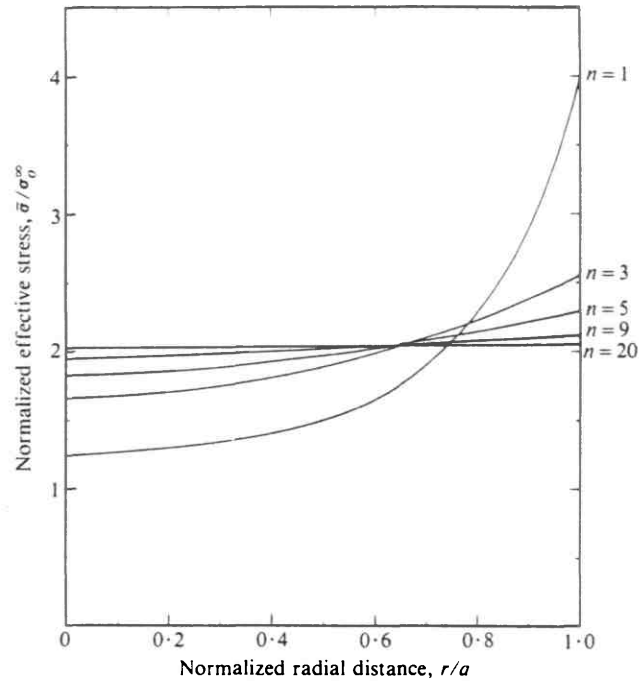

Fig. 10. Effective stress distribution at steady state across the throat of a semi-circular notch ($a/R = 1.5$)

$a/R = 2$ (Fig. 3(c)). Results for $n = 1$ (elastic) and $n = 9$ only are presented, since intermediate features to those observed on the previous two geometries were obtained. Comparisons with the Bridgman (**15**) and Hayhurst *et al.* (**10**) solutions indicate similar agreement to those reported for the semi-circular notch (Fig. 5). For the deep notch geometry, an approximately uniform state of stress is achieved in the region $r < 0.4a$ at steady-state.

It is apparent from Figs 4–9 that the present rapid method of estimating the steady-state stress distribution directly by means of an effective modulus, E', is consistent with the other methods (**9**)(**10**)(**11**)(**17**) of determining this stress distribution. It has the appreciable attraction over the incremental time-step approach that solutions at intermediate time intervals need not be calculated. It is also not necessary, with this approach, to postulate an equation of state for creep since it has not been necessary to write equation (19) in incremental form. Consequently, provided equation (19) gives a satisfactory description of primary, secondary, and/or tertiary creep, the same steady-state stress distribution will be obtained for a given notch geometry and value of n, irrespective of whether, for example, the time-hardening or strain-hardening equations of state for creep (**2**) were adopted. For a creep law of the form of equation (19), therefore, the choice of a particular equation of state will only affect how the steady-state stresses are achieved and not their final distribution. This could have useful design implications.

The creep analysis used assumes that the deformation behaviour of a component subjected to a complex state of stress is governed by an effective (or equivalent) stress criterion. The Von Mises or Tresca definitions could have been used. In the present paper, the Von Mises criterion was applied and Figs 10 and 11 show the distributions of the normalized effective stress, $\bar{\sigma}/\sigma_o^\infty$,

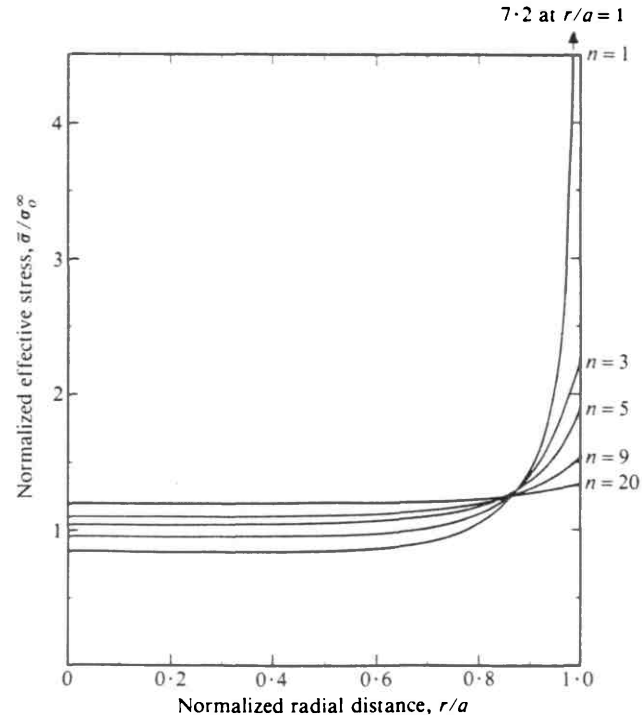

Fig. 11. Effective stress distribution at steady state across the throat of a BS V-notch

across the notch throat for the semi-circular and V-notch specimens, respectively, for $n = 1$, 3, 5, 9, and 20. For both geometries, the effective stress is a maximum at the notch root for all values of n. The magnitude of the maximum effective stress, $\bar{\sigma}_{max}$, decreases with increase in n, and the whole stress distribution levels out. For both geometries for $n > 3$, there is a tendency for the stress distributions to cross at almost the same value of r/a, implying an approximate point of constant stress, often called a skeletal point (**2**). For the semi-circular notch, the skeletal point occurs at about $r/a = 0.65$ and for the sharp V-notch at $r/a = 0.85$. For the other notch geometries, it occurred at an intermediate radius. The presence of a skeletal point may enable the stress there to be used as a reference stress to characterise the overall deformation behaviour of the notched bars. Such an approach will only be relevant, however, provided an approximate steady-state stress distribution is achieved relatively early in life and the high local stresses close to the notch root (particularly in the sharp notch samples) do not cause premature failure.

The results of further computations made by the present technique to evaluate $\bar{\sigma}_{max}$ for notch dimensions having values of b/a of 1.67 and 1.46, and notch root profiles ranging from a/R of 0.5–16.25, are summarized in Fig. 12. This figure presents the maximum effective stress normalized with respect to its corresponding elastic value, that is

$$F = \frac{\bar{\sigma}_{max}}{k\sigma_o^{\infty}} \tag{21}$$

where k is the elastic effective stress concentration factor. For all the geometries, the maximum effective stress always occurred at the notch root. The figure indicates that $\bar{\sigma}_{max}$ decreases with increase in n in an approximately linear fashion for a fixed notch geometry when plotted against $1/n$. The decrease is greatest for the sharpest notches (that is, those with the largest values of a/R). Similar trends have been observed previously by Calladine (**21**) for other types of components undergoing a variety of loading conditions involving bending, plane stress and plane strain situations. It is apparent that graphs of the form of Figs 12(a) and 12(b) can be used to provide rapid estimates of the maximum steady-state effective stress, $\bar{\sigma}_{max}$, for any value of n in notched bars. Depending upon the factors governing the mode of fracture, this stress may then be used to investigate the risk of failure locally.

Comparison is also made in Fig. 12 with the Bridgman (**15**) prediction of the effective stress across a notch throat for a rigid plastic material having $n = \infty$. The Bridgman analysis gives a constant effective stress across the notch throat of

$$\bar{\sigma} = \bar{\sigma}_{max} = \frac{(b/a)^2\sigma_o^{\infty}}{\{(1 + 2R/a)\ln(1 + a/2R)\}} \tag{22}$$

The values of F determined from this equation are shown on the vertical axes of Figs 12(a) and 12(b). The equation gives somewhat higher values than those predicted from the computer calculations. This is due to the fact that the Bridgman analysis results in lower values of σ_{rr} and $\sigma_{\theta\theta}$ than the computer estimates, and hence a greater effective stress. Nevertheless, conservative estimates of F

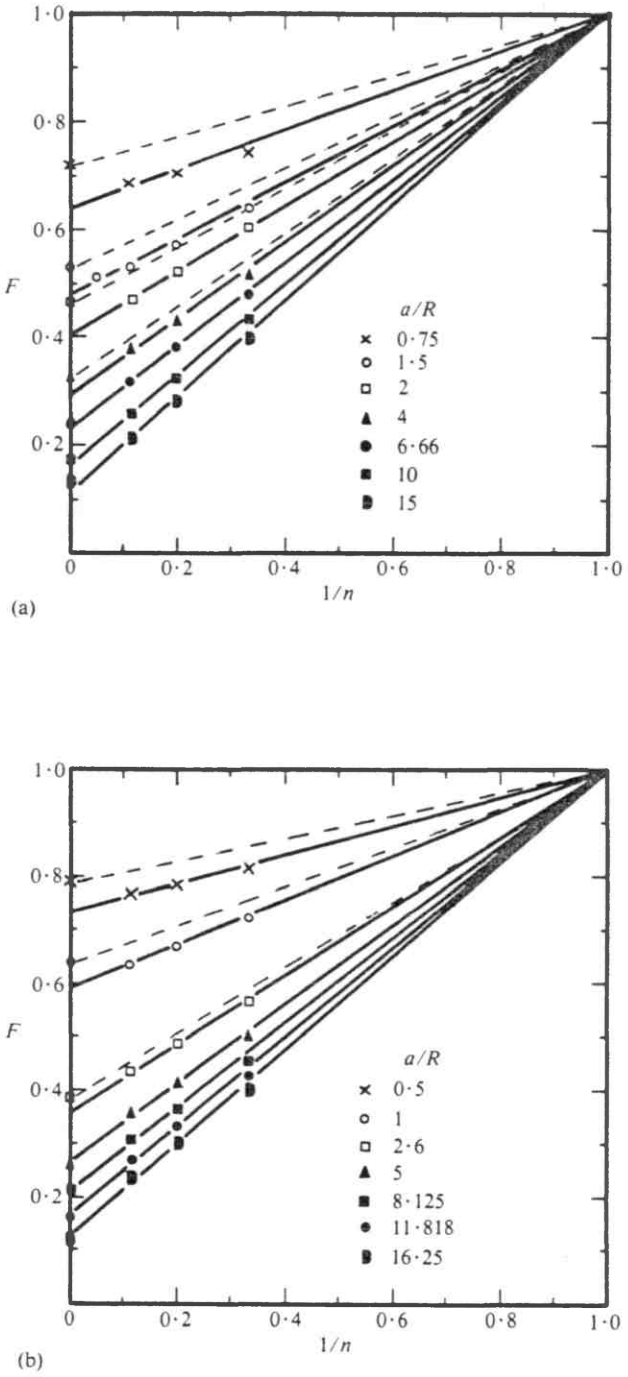

Fig. 12. Relative maximum stress concentration factor, F, as a function of $1/n$ for (a) $b/a = 1.67$, and (b) $b/a = 1.46$

by this approach are possible by making reference to the dotted lines in Fig. 12 which are drawn through the Bridgman solutions for $n = \infty$. By combining equations (21) and (22)

$$F = \frac{1}{n} + \frac{(1 - 1/n)(b/a)^2}{k(1 + 2R/a)\ln(1 + a/2R)} \tag{23}$$

For sharp notches, this expression gives good agreement with computer estimates, even though the stress distributions are very different (see, for example, Fig. 8) to those predicted by the Bridgman analysis. For progressively blunter notches, the equation gives increasingly conservative predictions.

Before it is possible to know whether predictions of component behaviour based on a steady-state stress distribution are justified, it is necessary to establish the time taken to reach this stress distribution. Lifetimes based on a steady-state analysis can only be expected to be reliable if this stress distribution is achieved rapidly.

Since the present numerical approach calculates the steady-state stress distribution directly, the time taken to reach this state is not determined. An approximate procedure has, however, been proposed by Calladine (22) for giving realistic estimates. For a material which creeps according to equation (19), Calladine shows that the time taken for the stress to relax from its initial elastic value, $\bar{\sigma}_o$, to some value, $\bar{\sigma}$, is approximately

$$F(t) = \frac{1}{CnE\bar{\sigma}_{ss}^{(n-1)}} \ln\left(\frac{\bar{\sigma}_o - \bar{\sigma}_{ss}}{\bar{\sigma} - \bar{\sigma}_{ss}}\right) \tag{24}$$

where $\bar{\sigma}_{ss}$ is the effective stress at the steady-state. Comparisons with numerical calculations have shown that satisfactory estimates of the time to achieve a steady-state, t_{ss}, can be obtained from equation (24) by calculating the time taken for stress relaxation to be 90 per cent complete, and by substituting $\bar{\sigma}_{max}$ for $\bar{\sigma}_{ss}$ so that

$$F(t_{ss}) = \frac{2.3}{CnE\bar{\sigma}_{max}^{(n-1)}} \tag{25}$$

Use of this equation with the procedures presented here will, therefore, indicate whether the adoption of a steady-state stress distribution for characterising component behaviour and predicting creep lives is acceptable.

For n typically in the range 5–10, it can be shown from equation (25) that the time to steady-state, t_{ss}, is approached when the maximum equivalent creep strain, $\bar{\varepsilon}_{max}$, is between, respectively, about $\frac{1}{2}$ and $\frac{1}{4}$ of the corresponding maximum elastic strain. It is not necessary, therefore, to assume in the analysis that the creep strain is large everywhere compared to the elastic strain for an approximate steady-state stress distribution to be achieved.

5 CONCLUSIONS

A finite element iterative procedure has been presented for calculating steady-state stress distributions in axi-symmetric bodies subjected to creep. It has been shown to be economical in terms of computing costs and to give results which indicate satisfactory agreement with approximate non-work hardening plasticity solutions and numerical procedures which approach steady-state incrementally from a series of solutions at successively longer times.

It has been found that the method proposed is not restricted to the assumption of secondary creep. Provided the variables of stress and time are separable in the creep law, the same steady-state stress distribution is obtained, for a given creep stress index, n, for primary, secondary, and tertiary creep. It is also shown that this stress distribution is not dependent upon the choice of an equation of state for creep.

Calculations have been made for a range of circumferential notch geometries and values of n to determine the steady-state effective stress across the notch throat region. A skeletal point at which the stress remained approximately constant, independent of n, was observed for each notch dimension. In all cases, the maximum effective stress occurred at the notch root. Some indication of the time taken to reach the steady-state condition has also been included and used to indicate when these stresses may be used to provide acceptable approximate predictions of notched bar behaviour and lifetimes.

APPENDIX

REFERENCES

(1) F. K. G. ODQVIST, *Mathematical theory of creep and creep rupture*, 1966 (Oxford Mathematical Monographs).
(2) PENNY, R. K. and MARRIOT, D. L., Design for creep, 1971 (McGraw-Hill, London).
(3) DAVIS, E. A. and MANJOINE, J. J., 'Effect of notch geometry on rupture strength at elevated temperatures', *ASTM STP 128*, (1953) 67.
(4) NEWMAN, D. P., JONES, M. H., and BROWN, W. F., 'Time-temperature dependence of the notch effect and influence of notch depth in stress rupture tests on a Cr–Mo–V steel', *Proc. ASTM*, 1953, **53**, 677–689.
(5) NG, S. E., WEBSTER, G. A., and DYSON, B. F., 'Notch weakening and strengthening in creep of ¼Cr.½Mo ¼V steel', in Advances in fracture research (ed. D. Francois *et al.*), 1980 (Pergamon Press, Oxford/New York).
(6) GREENBAUM, G. A. and RUBENSTEIN, M. F., 'Creep analysis of axisymmetric bodies using finite elements', *Nucl. Engng Design*, 1968, 7, 379–397.
(7) SUTHERLAND, W. H., 'AXICRP–Finite element computer code for creep analysis of plane stress, plane strain and axisymmetric bodies', *Nucl. Engng Design*, 1970, 11, 269–285.
(8) HAYHURST, D. R., DIMMER, P. R., and CHERNUKA, M. W., 'Estimates of the creep rupture lifetime of structures using finite element method', *J. Mech. Phys Solids*, 1975, **23**, 335–355.
(9) HAYHURST, D. R. and HENDERSON, J. T., 'Creep stress redistribution in notched bars', *Int. J. mech. Sci.*, 1977, 19, 133–146.
(10) HAYHURST, D. R., LECKIE, F. A., and HENDERSON, J. T., 'Design of notched bars for creep rupture testing under triaxial stresses', *Int. J. mech. Sci.*, 1977, 19, 147–159.
(11) HAYHURST, D. R., LECKIE, F. A., and MORRISON, C. J., 'Continuum damage study of notch strengthening and weakening in creep rupture', *Proc. R. Soc. Lond.*, 1978, **A360**, 243–264.
(12) SCZCZEPINSKI, W., DIETRICH, L., DRESCHER, E., and MIASTKOWSKI, J., 'Plastic flow of axially-symmetric notched bars pulled in tension', *Int. J. Solids Structures*, 1966, **2**, 543–554.
(13) NEIMARK, J. E., 'The fully plastic, plane strain tension of notched bar', *J. appl. Mech.*, 1968, **35**, 111–116.
(14) SANTHANAM, A. T., and BATES, R. C., 'The influence of notch-tip geometry on the distribution of stress and strain', *Mat. Sci. Engng*, 1979, 41, 243–250.
(15) BRIDGMAN, P. W., *Studies in large plastic flow and fracture*, 1952 (McGraw-Hill, New York).
(16) NEEDLEMAN, A. and SHIH, C. F., 'Finite element method for plane strain deformation of incompressible solids', *Comp. Meths appl. mech. Engng*, 1978, **15**, 223–240.
(17) KUMAR, V., GERMAN, M. A., and SHIH, C. F., 'Estimation technique for the prediction of elastic-plastic fracture of structural components of nuclear systems', Contract RP123-1, 1 June 1980, for Electric Power Research Institute, Palo Alto, California 94303, USA.
(18) FENNER, R. T., *Finite element methods for engineers*, 1975 (Macmillan, London).
(19) BAILEY, R. W., 'Creep relationships and their application to pipes, tubes and cylindrical parts under internal pressure', *Proc. Instn mech. Engrs*, 1951, **164**, 425–447.
(20) SEGERLIND, L. J., *Applied finite element analysis*, 1976 (Wiley, New York).
(21) CALLADINE, C. R., 'A rapid method for estimating the greatest stress in a structure subjected to creep', *Proc. Instn mech. Engrs*, 1964, **178**, 198–206.
(22) CALLADINE, C. R., 'Time-scales for redistribution of stress in creep of structures', *Proc. R. Soc. Lond.*, 1969, **A309**, 363–375.

APPENDIX B

LISTING OF THE AXI-SYMMETRIC FINITE ELEMENT PROGRAM USED FOR SOLVING ELASTIC AND NON-LINEAR PROBLEMS

```
      PROGRAM AXISYM(INPUT,OUTPUT,TAPE1,TAPE2,TAPE5=INPUT,TAPE6=OUTPUT)
C
C  AXI-SYMMETRIC FINITE ELEMENT PROGRAM FOR SOLVING ELASTIC AND
C  NON-LINEAR PROBLEMS.
C
      DIMENSION NOB(40)
      COMMON NEL,NNP,X(300),Y(300),AI(500),AJ(500),AK(500),BI(500),
     1  BJ(500),BK(500),AREA(500),NPI(500),NPJ(500),NPK(500),NXPT,NYPT,
     2  MOUT,NBP,NPB(40),XAXIS,RBAR(500),OKXX(300,9),OKXY(300,9),
     3  OKYX(300,9),OKYY(300,9),U(300),V(300),FX(300),FY(300),
     4  FXMOD(300),FYMOD(300),SFXX(300),SFXY(300),SFYX(300),SFYY(300),
     5  NPA(300,9),NAP(300),NMAT,E(5),NU(5),ALPHA(5),RHO(5),MATM(500),
     6  DELTAT(500),XBAR(500),YBAR(500),SU(500),SV(500),PX,PY,
     7  NCOND(40),TANG(40),UPRES(40),VPRES(40),NBC3P
C
      REAL  NU
C
      DIMENSION  TITLE(6),B(4,6),D(4,4),BTD(6,4),ESTIFF(6,6),IJK(3),
     1           ET(4),THETAM(6)
      DATA  BLANK  /  10H           /
C
C  INPUT THE PROBLEM TITLE AND TYPE - STOP IF BLANK CARD ENCOUNTERED.
 1    READ(5,51) TITLE
 51   FORMAT(6A10)
      IF(TITLE(1).EQ.BLANK) STOP
      WRITE(6,61) TITLE
 61   FORMAT(54H0CST FINITE ELEMENT SOLUTION FOR AXI-SYMMETRIC PROBLEM
     1       //  6A10)
C
C  INPUT OR GENERATE THE MESH DATA, MATERIAL PROPERTIES, TEMPERATURE
C  CHANGES AND BODY FORCES.
      CALL MESH1
      CALL  MODIFY
      CALL  AXIS
      CALL  MATLS
      CALL  TEMPS
      CALL  BODYF
C
C  COMPUTE THE ELEMENT GEOMETRIES.
      DO 2 M=1,NEL
      I=NPI(M)
      J=NPJ(M)
      K=NPK(M)
      AI(M)=-X(J)+X(K)
      AJ(M)=-X(K)+X(I)
      AK(M)=-X(I)+X(J)
      BI(M)=Y(J)-Y(K)
      BJ(M)=Y(K)-Y(I)
      BK(M)=Y(I)-Y(J)
      AREA(M)=0.5*(AK(M)*BJ(M)-AJ(M)*BK(M))
      IF(AREA(M).GT.0.) GO TO 2
      WRITE(6,62) M
 62   FORMAT(15H0ELEMENT NUMBER,I5,25H HAS NEGATIVE AREA - STOP)
      STOP
 2    CONTINUE
C
C  OUTPUT THE MESH DATA.
      CALL  MSHOUT
C
C  INPUT THE REQUIRED NUMBER OF OUTER ITERATIONS.
```

```
      READ(5,52) NITER
 52   FORMAT(I3)
      DO 201 IITER=1,NITER
C  SET INITIAL VALUES OF STIFFNESSES, EXTERNAL FORCES AND UNKNOWNS.
      DO 4 IROW=1,NNP
      DO 3 IC=1,9
      OKXX(IROW,IC)=0.
      OKXY(IROW,IC)=0.
      OKYX(IROW,IC)=0.
      OKYY(IROW,IC)=0.
 3    NPA(IROW,IC)=0
      NPA(IROW,1)=IROW
      FXMOD(IROW)=0.
      FYMOD(IROW)=0.
      IF(IITER.GT.1) GO TO 4
      U(IROW)=0.
      V(IROW)=0.
   4  CONTINUE
C
C  MODIFY MATERIAL PROPERTIES FOR (AXI-SYMMETRIC) PLANE STRAIN.
      IF(IITER.GT.1) GO TO 6
      DO 5 MAT=1,NMAT
      E(MAT)=E(MAT)/(1.-NU(MAT)**2)
 5    NU(MAT)=NU(MAT)/(1.-NU(MAT))
C
C  SET UP THE OVERALL ASSEMBLY LOOP.
  6   DO 19 M=1,NEL
C
C  STORE THE ELEMENT NODE NUMBERS IN ORDER IN ARRAY IJK.
      IJK(1)=NPI(M)
      IJK(2)=NPJ(M)
      IJK(3)=NPK(M)
C
C  COMPUTE THE BODY FORCE COMPONENTS ON EACH NODE OF THE ELEMENT.
      GXM=XBAR(M)*AREA(M)/3.*RBAR(M)
      GYM=YBAR(M)*AREA(M)/3.*RBAR(M)
C
C  FORM THE ELEMENT DIMENSION MATRIX.
      DO 7 IRE=1,3
      DO 7 ICE=1,6
 7    B(IRE,ICE)=0.
      B(1,1)=BI(M)
      B(1,3)=BJ(M)
      B(1,5)=BK(M)
      B(2,2)=AI(M)
      B(2,4)=AJ(M)
      B(2,6)=AK(M)
      FACT=2.*AREA(M)/(3.*RBAR(M))
      DO 8 ICE=1,6
      IF(MOD(ICE,2).EQ.1) B(3,ICE)=FACT
      IF(MOD(ICE,2).EQ.0) B(4,ICE)=B(1,ICE-1)
 8    IF(MOD(ICE,2).EQ.1) B(4,ICE)=B(2,ICE+1)
C
C  FORM THE ELASTIC PROPERTY MATRIX.
      DO 9 IRE=1,4
      DO 9 ICE=1,4
 9    D(IRE,ICE)=0.
      MAT=MATM(M)
      EFACT=1.
      IF(IITER.GT.1) CALL NONLIN (M,EFACT,IITER)
```

```
      IF(IITER.GT.1) NU(MAT)=Ø.95
      SU(M)=EFACT
      FACT=EFACT*E(MAT)/(1.-NU(MAT)**2)
      DO 91 IRE=1,3
      DO 91 ICE=1,3
      D(IRE,ICE)=1.
      IF(IRE.NE.ICE) D(IRE,ICE)=NU(MAT)
 91   D(IRE,ICE)=D(IRE,ICE)*FACT
      D(4,4)=FACT*Ø.5*(1.-NU(MAT))
C
C  MULTIPLY THE TRANSPOSE OF MATRIX B BY MATRIX D.
      DO 1Ø IRE=1,6
      DO 1Ø ICE=1,4
      BTD(IRE,ICE)=Ø.
      DO 1Ø ISUM=1,4
 1Ø   BTD(IRE,ICE)=BTD(IRE,ICE)+B(ISUM,IRE)*D(ISUM,ICE)
C
C  FORM THE THERMAL STRAIN AND THERMAL FORCE VECTORS.
      ET(1)=ALPHA(MAT)*DELTAT(M)
      ET(2)=ET(1)
      ET(3)=ET(1)
      ET(4)=Ø.
      DO 12 IRE=1,6
      SUM=Ø.
      DO 11 ISUM=1,4
 11   SUM=SUM+BTD(IRE,ISUM)*ET(ISUM)
 12   THETAM(IRE)=Ø.5*SUM*RBAR(M)
C
C  FORM THE ELEMENT STIFFNESS MATRIX.
      DO 14 IRE=1,6
      DO 14 ICE=1,6
      SUM=Ø.
      DO 13 ISUM=1,4
 13   SUM=SUM+BTD(IRE,ISUM)*B(ISUM,ICE)
 14   ESTIFF(IRE,ICE)=Ø.25*SUM/AREA(M)*RBAR(M)
C
C  ADD ELEMENT STIFFNESS TO OVERALL STIFFNESS.
      DO 18 IRE=1,3
      DO 18 ICE=1,3
      IROW=IJK(IRE)
      ICOL=IJK(ICE)
C
C  STORE STIFFNESS COEFFICIENTS IN RECTANGULAR FORM OF OVERALL MATRICES.
      DO 15 IC=1,9
      IF(NPA(IROW,IC).EQ.ICOL) GO TO 17
      IF(NPA(IROW,IC).EQ.Ø) GO TO 16
 15   CONTINUE
      WRITE(6,63) IROW
 63   FORMAT(5HØNODE,I5,38H HAS MORE THAN 8 ADJACENT NODES - STOP)
      STOP
 16   NPA(IROW,IC)=ICOL
      NAP(IROW)=IC
 17   OKXX(IROW,IC)=OKXX(IROW,IC)+ESTIFF(2*IRE-1,2*ICE-1)
      OKXY(IROW,IC)=OKXY(IROW,IC)+ESTIFF(2*IRE-1,2*ICE)
      OKYX(IROW,IC)=OKYX(IROW,IC)+ESTIFF(2*IRE,2*ICE-1)
 18   OKYY(IROW,IC)=OKYY(IROW,IC)+ESTIFF(2*IRE,2*ICE)
C
C  ASSEMBLE THE EXTERNAL FORCES ON THE NODES.
      DO 19 IRE=1,3
      IROW=IJK(IRE)
```

```
      FXMOD(IROW)=FXMOD(IROW)+GXM+THETAM(2*IRE-1)
 19   FYMOD(IROW)=FYMOD(IROW)+GYM+THETAM(2*IRE)
C
C  COMPUTE THE SELF-FLEXIBILITY SUBMATRICES.
      DO 20 I=1,NNP
      DENOM=OKXX(I,1)*OKYY(I,1)-OKXY(I,1)*OKYX(I,1)
      SFXX(I)=OKYY(I,1)/DENOM
      SFXY(I)=-OKXY(I,1)/DENOM
      SFYX(I)=-OKYX(I,1)/DENOM
 20   SFYY(I)=OKXX(I,1)/DENOM
C
C  APPLY THE BOUNDARY CONDITIONS.
      CALL BCS(IITER)
C
C  SOLVE THE LINEAR EQUATIONS.
      CALL SOLVE2(IITER)
C
C  OUTPUT THE REQUIRED RESULTS.
C
      CALL OUTPUT(IITER,NITER)
 201  CONTINUE
      GO TO 1
      END
      SUBROUTINE  MESH1
C
C  SUBPROGRAM TO READ OR GENERATE A MESH OF TRIANGULAR FINITE ELEMENTS.
C  THIS VERSION READS IN THE NECESSARY DATA.
C
      COMMON NEL,NNP,X(300),Y(300),AI(500),AJ(500),AK(500),BI(500),
     1  BJ(500),BK(500),AREA(500),NPI(500),NPJ(500),NPK(500),NXPT,NYPT,
     2  MOUT,NBP,NPB(40),XAXIS,RBAR(500),OKXX(300,9),OKXY(300,9),
     3  OKYX(300,9),OKYY(300,9),U(300),V(300),FX(300),FY(300),
     4  FXMOD(300),FYMOD(300),SFXX(300),SFXY(300),SFYX(300),SFYY(300),
     5  NPA(300,9),NAP(300),NMAT,E(5),NU(5),ALPHA(5),RHO(5),MATM(500),
     6  DELTAT(500),XBAR(500),YBAR(500),SU(500),SV(500),PX,PY,
     7  NCOND(40),TANG(40),UPRES(40),VPRES(40),NBC3P
C
      REAL  NU
C
      READ(1,51) NNP,NEL,MOUT
 51   FORMAT(3I5)
C
      READ(1,52) (I,X(I),Y(I),N=1,NNP)
 52   FORMAT(I5,2E15.5)
C
      READ(1,53) (M,NPI(M),NPJ(M),NPK(M),N=1,NEL)
  53  FORMAT(4I5)
      RETURN
      END
      SUBROUTINE  MATLS
C
C  SUBPROGRAM FOR DEFINING THE MATERIAL PROPERTIES OF THE ELEMENTS.
C
      COMMON NEL,NNP,X(300),Y(300),AI(500),AJ(500),AK(500),BI(500),
     1  BJ(500),BK(500),AREA(500),NPI(500),NPJ(500),NPK(500),NXPT,NYPT,
     2  MOUT,NBP,NPB(40),XAXIS,RBAR(500),OKXX(300,9),OKXY(300,9),
     3  OKYX(300,9),OKYY(300,9),U(300),V(300),FX(300),FY(300),
     4  FXMOD(300),FYMOD(300),SFXX(300),SFXY(300),SFYX(300),SFYY(300),
     5  NPA(300,9),NAP(300),NMAT,E(5),NU(5),ALPHA(5),RHO(5),MATM(500),
     6  DELTAT(500),XBAR(500),YBAR(500),SU(500),SV(500),PX,PY,
```

```
     7  NCOND(40),TANG(40),UPRES(40),VPRES(40),NBC3P
C
      REAL  NU
C
C  INPUT THE MATERIAL PROPERTIES - MAXIMUM 5 DIFFERENT MATERIALS.
      READ(5,51) NMAT
 51   FORMAT(I5)
      IF(NMAT.LE.5) GO TO 1
      WRITE(6,61) NMAT
 61   FORMAT(28H0TOO MANY MATERIALS - NMAT =,I5)
      STOP
 1    READ(5,52) (MAT,E(MAT),NU(MAT),ALPHA(MAT),RHO(MAT),N=1,NMAT)
 52   FORMAT(I5,4E15.5)
      WRITE(6,62) (MAT,E(MAT),NU(MAT),ALPHA(MAT),RHO(MAT),MAT=1,NMAT)
 62   FORMAT(20H0MATERIAL PROPERTIES //
     1 50H   MATL    E           NU      ALPHA        RHO      /
     2      (1X,I5,E12.4,F8.3,2E12.4))
C
C  DEFINE THE MATERIAL FOR EACH ELEMENT.
C  THIS VERSION ASSUMES ALL ELEMENTS ARE OF FIRST MATERIAL.
      DO 2 M=1,NEL
 2    MATM(M)=1
      RETURN
      END
      SUBROUTINE  AXIS
C
C  SUBPROGRAM TO DEFINE THE POSITION OF THE AXIS OF SYMMETRY AND MEAN
C  RADIUS FROM THIS AXIS OF EACH ELEMENT.
C
      COMMON NEL,NNP,X(300),Y(300),AI(500),AJ(500),AK(500),BI(500),
     1  BJ(500),BK(500),AREA(500),NPI(500),NPJ(500),NPK(500),NXPT,NYPT,
     2  MOUT,NBP,NPB(40),XAXIS,RBAR(500),OKXX(300,9),OKXY(300,9),
     3  OKYX(300,9),OKYY(300,9),U(300),V(300),FX(300),FY(300),
     4  FXMOD(300),FYMOD(300),SFXX(300),SFXY(300),SFYX(300),SFYY(300),
     5  NPA(300,9),NAP(300),NMAT,E(5),NU(5),ALPHA(5),RHO(5),MATM(500),
     6  DELTAT(500),XBAR(500),YBAR(500),SU(500),SV(500),PX,PY,
     7  NCOND(40),TANG(40),UPRES(40),VPRES(40),NBC3P
C
      REAL  NU
C
C  INPUT THE X-COORDINATE OF THE AXIS OF SYMMETRY.
      READ(5,51) XAXIS
 51   FORMAT(F10.0)
C
C  DEFINE THE MEAN RADII OF THE ELEMENTS.
      DO 1 M=1,NEL
      I=NPI(M)
      J=NPJ(M)
      K=NPK(M)
 1    RBAR(M)=(X(I)+X(J)+X(K))/3.-XAXIS
      RETURN
      END
      SUBROUTINE  TEMPS
      COMMON NEL,NNP,X(300),Y(300),AI(500),AJ(500),AK(500),BI(500),
     1  BJ(500),BK(500),AREA(500),NPI(500),NPJ(500),NPK(500),NXPT,NYPT,
     2  MOUT,NBP,NPB(40),XAXIS,RBAR(500),OKXX(300,9),OKXY(300,9),
     3  OKYX(300,9),OKYY(300,9),U(300),V(300),FX(300),FY(300),
     4  FXMOD(300),FYMOD(300),SFXX(300),SFXY(300),SFYX(300),SFYY(300),
     5  NPA(300,9),NAP(300),NMAT,E(5),NU(5),ALPHA(5),RHO(5),MATM(500),
     6  DELTAT(500),XBAR(500),YBAR(500),SU(500),SV(500),PX,PY,
```

```
     7  NCOND(40),TANG(40),UPRES(40),VPRES(40),NBC3P
C
      REAL  NU
C
C
C  SUBPROGRAM FOR DEFINING MEAN TEMPERATURE CHANGES FOR THE ELEMENTS.
C  THIS VERSION READS AND ASSIGNS A UNIFORM CHANGE.
C
      READ(5,51) TEMP
 51   FORMAT(F10.0)
      DO 1 M=1,NEL
 1    DELTAT(M)=TEMP
      RETURN
      END
      SUBROUTINE  BODYF
C
C  SUBPROGRAM FOR DEFINING THE BODY FORCE COMPONENTS (PER UNIT VOLUME)
C  FOR THE ELEMENTS.
C  THIS VERSION ASSUMES GRAVITY ACTS IN THE NEGATIVE Y-DIRECTION.
C
      COMMON NEL,NNP,X(300),Y(300),AI(500),AJ(500),AK(500),BI(500),
     1  BJ(500),BK(500),AREA(500),NPI(500),NPJ(500),NPK(500),NXPT,NYPT,
     2  MOUT,NBP,NPB(40),XAXIS,RBAR(500),OKXX(300,9),OKXY(300,9),
     3  OKYX(300,9),OKYY(300,9),U(300),V(300),FX(300),FY(300),
     4  FXMOD(300),FYMOD(300),SFXX(300),SFXY(300),SFYX(300),SFYY(300),
     5  NPA(300,9),NAP(300),NMAT,E(5),NU(5),ALPHA(5),RHO(5),MATM(500),
     6  DELTAT(500),XBAR(500),YBAR(500),SU(500),SV(500),PX,PY,
     7  NCOND(40),TANG(40),UPRES(40),VPRES(40),NBC3P
C
      REAL  NU
C
      DO 1 M=1,NEL
      XBAR(M)=0.
      MAT=MATM(M)
 1    YBAR(M)=-RHO(MAT)
      RETURN
      END
      SUBROUTINE  MSHOUT
C
C  SUBPROGRAM TO WRITE OUT THE MESH DATA.
C
      COMMON NEL,NNP,X(300),Y(300),AI(500),AJ(500),AK(500),BI(500),
     1  BJ(500),BK(500),AREA(500),NPI(500),NPJ(500),NPK(500),NXPT,NYPT,
     2  MOUT,NBP,NPB(40),XAXIS,RBAR(500),OKXX(300,9),OKXY(300,9),
     3  OKYX(300,9),OKYY(300,9),U(300),V(300),FX(300),FY(300),
     4  FXMOD(300),FYMOD(300),SFXX(300),SFXY(300),SFYX(300),SFYY(300),
     5  NPA(300,9),NAP(300),NMAT,E(5),NU(5),ALPHA(5),RHO(5),MATM(500),
     6  DELTAT(500),XBAR(500),YBAR(500),SU(500),SV(500),PX,PY,
     7  NCOND(40),TANG(40),UPRES(40),VPRES(40),NBC3P
C
      REAL  NU
C
      IF(MOUT.EQ.0) RETURN
C
C  OUTPUT THE NUMBER OF ELEMENTS AND NODES, AND THE NODE CO-ORDINATES.
      WRITE(6,61) NEL,NNP,(I,X(I),Y(I),I=1,NNP)
 61   FORMAT(28H0GEOMETRIC DATA FOR THE MESH //
     1   10X,21H NUMBER OF ELEMENTS =,I4 //
     2   10X,25H NUMBER OF NODAL POINTS =,I4 //
     3        25H NODAL POINT CO-ORDINATES //
```

```
     4       72H    I      X        Y       I      X        Y       I
     5   X        Y     / (3(1X,I5,2F9.4)))
C
C  OUTPUT X-COORDINATE OF AXIS OF SYMMETRY.
      WRITE(6,63) XAXIS
 63   FORMAT(/// 39H X-COORDINATE OF THE AXIS OF SYMMETRY =,E12.4)
C
C  OUTPUT THE ELEMENT NODE AND MATERIAL NUMBERS, AREAS, TEMPERATURE
C  CHANGES, BODY FORCE COMPONENTS AND MEAN RADII.
      WRITE(6,62) (M,NPI(M),NPJ(M),NPK(M),MATM(M),AREA(M),DELTAT(M),
     1            XBAR(M),YBAR(M),RBAR(M),M=1,NEL)
 62   FORMAT(13HØELEMENT DATA // 84H    M    I    J    K  MAT    AREA
     1    DELTAT       XBAR         YBAR        RADIUS    /
     2                                    (1X,4I5,I3,5E12.4))
      RETURN
      END
      SUBROUTINE BCS(IITER)
C
C  SUBPROGRAM TO APPLY THE BOUNDARY CONDITIONS.
C
      COMMON NEL,NNP,X(3ØØ),Y(3ØØ),AI(5ØØ),AJ(5ØØ),AK(5ØØ),BI(5ØØ),
     1  BJ(5ØØ),BK(5ØØ),AREA(5ØØ),NPI(5ØØ),NPJ(5ØØ),NPK(5ØØ),NXPT,NYPT,
     2  MOUT,NBP,NPB(4Ø),XAXIS,RBAR(5ØØ),OKXX(3ØØ,9),OKXY(3ØØ,9),
     3  OKYX(3ØØ,9),OKYY(3ØØ,9),U(3ØØ),V(3ØØ),FX(3ØØ),FY(3ØØ),
     4  FXMOD(3ØØ),FYMOD(3ØØ),SFXX(3ØØ),SFXY(3ØØ),SFYX(3ØØ),SFYY(3ØØ),
     5  NPA(3ØØ,9),NAP(3ØØ),NMAT,E(5),NU(5),ALPHA(5),RHO(5),MATM(5ØØ),
     6  DELTAT(5ØØ),XBAR(5ØØ),YBAR(5ØØ),SU(5ØØ),SV(5ØØ),PX,PY,
     7  NCOND(4Ø),TANG(4Ø),UPRES(4Ø),VPRES(4Ø),NBC3P
C
      REAL  NU
C
      IF(IITER.GT.1) GO TO 4
      DO 1 I=1,NNP
      FX(I)=Ø.
 1    FY(I)=Ø.
C
C  INPUT THE NUMBERS OF SETS OF DATA FOR EACH TYPE OF BOUNDARY CONDITION
      READ(5,51) NBC1P,NBC2F,NBC3P
 51   FORMAT(14I5)
C
C  INPUT AND APPLY POINT FORCE (PER RADIAN) DATA.
      IF(NBC1P.EQ.Ø) GO TO 2
      READ(5,52) (I,FX(I),FY(I),N=1,NBC1P)
 52   FORMAT(3(I4,2F1Ø.Ø))
C
C  INPUT AND APPLY DISTRIBUTED FORCE DATA.
 2    IF(NBC2F.EQ.Ø) GO TO 4
      DO 3 IF=1,NBC2F
      READ(5,52) NBP,PX,PY
      READ(5,51) (NPB(N),N=1,NBP)
      NS=NBP-1
      DO 3 IS=1,NS
      I1=NPB(IS)
      I2=NPB(IS+1)
      R=Ø.5*(X(I1)+X(I2))-XAXIS
      SIDE=SQRT((X(I1)-X(I2))**2+(Y(I1)-Y(I2))**2)
      FXM=Ø.5*PX*SIDE*R
      FX(I1)=FX(I1)+FXM
      FX(I2)=FX(I2)+FXM
      FYM=Ø.5*PY*SIDE*R
```

```
      FY(I1)=FY(I1)+FYM
 3    FY(I2)=FY(I2)+FYM
C
C  DEFINE FINAL MODIFIED EXTERNAL FORCES ON THE NODES.
 4    DO 5 I=1,NNP
      FXMOD(I)=FXMOD(I)+FX(I)
 5    FYMOD(I)=FYMOD(I)+FY(I)
C
C  INPUT AND APPLY THE RESTRAINED NODE DATA.
      IF(IITER.GT.1) GO TO 15
      READ(5,53) (NPB(N),NCOND(N),TANG(N),UPRES(N),VPRES(N),N=1,NBC3P)
 53   FORMAT(2(I4,I2,3F10.0))
 15   DO 10 N=1,NBC3P
      I=NPB(N)
      IF(NCOND(N)-1) 8,7,6
C
C  NODE RESTRAINED TO MOVE IN DIRECTION WHOSE SLOPE IS GIVEN BY TANG.
 6    SFXX(I)=(SFXX(I)*SFYY(I)-SFXY(I)*SFYX(I))/
     1        (SFXX(I)*TANG(N)**2-(SFXY(I)+SFYX(I))*TANG(N)+SFYY(I))
      SFXY(I)=SFXX(I)*TANG(N)
      SFYX(I)=SFXY(I)
      SFYY(I)=SFXY(I)*TANG(N)
      GO TO 10
C
C  NODE RESTRAINED TO MOVE IN Y-DIRECTION ONLY.
 7    SFYY(I)=SFYY(I)-SFYX(I)*SFXY(I)/SFXX(I)
      GO TO 9
C
C  NODAL POINT DISPLACEMENTS PRESCRIBED.
 8    SFYY(I)=0.
      U(I)=UPRES(N)
      V(I)=VPRES(N)
 9    SFXX(I)=0.
      SFXY(I)=0.
      SFYX(I)=0.
 10   CONTINUE
      RETURN
      END
      SUBROUTINE SOLVE2(IITER)
C
C  SUBPROGRAM FOR SOLVING BY GAUSS-SEIDEL METHOD THE LINEAR EQUATIONS
C  OBTAINED FROM THE FINITE ELEMENT FORMULATION OF BIHARMONIC PROBLEMS.
C
      COMMON NEL,NNP,X(300),Y(300),AI(500),AJ(500),AK(500),BI(500),
     1  BJ(500),BK(500),AREA(500),NPI(500),NPJ(500),NPK(500),NXPT,NYPT,
     2  MOUT,NBP,NPB(40),XAXIS,RBAR(500),OKXX(300,9),OKXY(300,9),
     3  OKYX(300,9),OKYY(300,9),U(300),V(300),FX(300),FY(300),
     4  FXMOD(300),FYMOD(300),SFXX(300),SFXY(300),SFYX(300),SFYY(300),
     5  NPA(300,9),NAP(300),NMAT,E(5),NU(5),ALPHA(5),RHO(5),MATM(500),
     6  DELTAT(500),XBAR(500),YBAR(500),SU(500),SV(500),PX,PY,
     7  NCOND(40),TANG(40),UPRES(40),VPRES(40),NBC3P
C
      REAL  NU
C
      NPEQN=NNP
C
      IF(IITER.GT.1) GO TO 6
C  INPUT THE SOLUTION PARAMETERS.
      READ(5,51) NCYCLE,IFREQ,ORELAX,TOLER
 51   FORMAT(2I5,2F10.0)
```

```
      WRITE(6,61) ORELAX
 61   FORMAT(48H0SOLUTION OF EQUATIONS BY GAUSS-SEIDEL ITERATION //
     1       25H OVER-RELAXATION FACTOR =,F6.3)
C
C  SET UP ITERATION LOOP.
      IF(IFREQ.NE.0) WRITE(6,62)
 62   FORMAT(21H  ITER       ERROR    )
C
C  INPUT THE REQUIRED NUMBER OF INNER ITERATIONS.
      IF(IITER.EQ.1) GO TO 6
      READ(5,52) NOII
 52   FORMAT(I3)
 6    DO 20 K=1,NOII
      DO 3 ITER=1,NCYCLE
      SUMD=0.
      SUMDD=0.
C
C  OBTAIN NEW ESTIMATE FOR EACH UNKNOWN IN TURN.
      DO 2 IROW=1,NPEQN
      IF(SFXX(IROW)+SFYY(IROW).EQ.0.) GO TO 2
      SUMX=FXMOD(IROW)
      SUMY=FYMOD(IROW)
      ICMAX=NAP(IROW)
      DO 1 IC=1,ICMAX
      ICOL=NPA(IROW,IC)
      SUMX=SUMX-OKXX(IROW,IC)*U(ICOL)-OKXY(IROW,IC)*V(ICOL)
 1    SUMY=SUMY-OKYX(IROW,IC)*U(ICOL)-OKYY(IROW,IC)*V(ICOL)
      DELU=SFXX(IROW)*SUMX+SFXY(IROW)*SUMY
      DELV=SFYX(IROW)*SUMX+SFYY(IROW)*SUMY
      SUMDD=SUMDD+ABS(DELU)+ABS(DELV)
      U(IROW)=U(IROW)+ORELAX*DELU
      V(IROW)=V(IROW)+ORELAX*DELV
      SUMD=SUMD+ABS(U(IROW))+ABS(V(IROW))
 2    CONTINUE
C
C  TEST FOR CONVERGENCE.
      ERROR=SUMDD/SUMD
      IF(ERROR.LT.TOLER) GO TO 4
C
C  OUTPUT PROGRESS INFORMATION EVERY IFREQ CYCLES, UNLESS IFREQ=0.
      IF(IFREQ.EQ.0) GO TO 3
      IF(MOD(ITER,IFREQ).EQ.0) WRITE(6,63) ITER,ERROR
 63   FORMAT(1X,15,E15.4)
 3    CONTINUE
C
C  NORMAL EXIT FROM ITERATION LOOP INDICATES FAILURE TO CONVERGE.
      WRITE(6,64) NCYCLE
 64   FORMAT(21H0NO CONVERGENCE AFTER,I5,7H CYCLES)
      RETURN
C
C  OUTPUT NUMBER OF ITERATIONS AND TOLERANCE FOR CONVERGED SOLUTION.
 4    WRITE(6,65) TOLER,ITER
 65   FORMAT(38H0ITERATION CONVERGED TO A TOLERANCE OF,E12.4,
     1       6H AFTER,I5,7H CYCLES)
C
  20  CONTINUE
      RETURN
      END
      SUBROUTINE OUTPUT(IITER,NITER)
C
```

```
C  SUBPROGRAM TO OUTPUT THE FINAL RESULTS.
C  THIS PROGRAM IS ONLY APPLICABLE FOR NOTCHED BAR GEOMETRIES UNDER
C  REMOT STRESS. IT HAS BEEN DESIGNED TO PRINT THE RESULTS IN THE
C  NOTCH THROAT REAGION ONLY.
C
      DIMENSION NOB(40)
      COMMON NEL,NNP,X(300),Y(300),AI(500),AJ(500),AK(500),BI(500),
     1  BJ(500),BK(500),AREA(500),NPI(500),NPJ(500),NPK(500),NXPT,NYPT,
     2  MOUT,NBP,NPB(40),XAXIS,RBAR(500),OKXX(300,9),OKXY(300,9),
     3  OKYX(300,9),OKYY(300,9),U(300),V(300),FX(300),FY(300),
     4  FXMOD(300),FYMOD(300),SFXX(300),SFXY(300),SFYX(300),SFYY(300),
     5  NPA(300,9),NAP(300),NMAT,E(5),NU(5),ALPHA(5),RHO(5),MATM(500),
     6  DELTAT(500),XBAR(500),YBAR(500),SU(500),SV(500),PX,PY,
     7  NCOND(40),TANG(40),UPRES(40),VPRES(40),NBC3P
C
      REAL  NU
C
      IF(IITER.GT.1) GO TO 6
C  OUTPUT THE DISPLACEMENT BOUNDARY CONDITIONS.
      WRITE(6,61) (NPB(IB),NCOND(IB),TANG(IB),IB=1,NBC3P)
 61   FORMAT(33H0DISPLACEMENT BOUNDARY CONDITIONS //
     1       60H  NODE  COND    TANG  NODE  COND    TANG  NODE  COND
     2TANG / (3(1X,I4,I5,F10.4)))
C
C  OUTPUT THE NODAL POINT FORCES AND DISPLACEMENTS.
      WRITE(6,62) (I,FX(I),FY(I),FXMOD(I),FYMOD(I),U(I),V(I),I=1,NNP)
 62   FORMAT(37H0NODAL POINT FORCES AND DISPLACEMENTS //
     1       78H   NODE   FX          FY          FXMOD       FYMOD
     2   U           V       / (1X,I5,6E12.4))
C
C  COMPUTE AND OUTPUT THE ELEMENT STRAIN AND STRESS COMPONENTS.
      WRITE(6,63)
 63   FORMAT(114H0    M    EXX         EYY         EHP         EXY
     1   ET         SIGXX       SIGYY       SIGHP       SIGXY      )
C
C  INPUT THE NOTCH THROAT RADUIS, A ,AND THE APPLIED REMOT STRESS, PNT.
      READ(5,51)A,PNT
  51  FORMAT(2F10.0)
 6    NXB=0
      TINY=0.0001
      DO 3 I=1,NNP
      IF(Y(I).GT.TINY) GO TO 3
      NXB=NXB+1
      NOB(NXB)=I
  3   CONTINUE
      DO 1 M=1,NEL
      DO 4 K=1,NXB
      IF(NPI(M).EQ.NOB(K)) GO TO 2
      IF(NPJ(M).EQ.NOB(K)) GO TO 2
      IF(NPK(M).EQ.NOB(K)) GO TO 2
  4   CONTINUE
      GO TO 1
  2   I=NPI(M)
      J=NPJ(M)
      K=NPK(M)
      EXX=0.5*(BI(M)*U(I)+BJ(M)*U(J)+BK(M)*U(K))/AREA(M)
      EYY=0.5*(AI(M)*V(I)+AJ(M)*V(J)+AK(M)*V(K))/AREA(M)
      EHP=(U(I)+U(J)+U(K))/(3.*RBAR(M))
      EXY=0.5*(AI(M)*U(I)+BI(M)*V(I)+AJ(M)*U(J)+BJ(M)*V(J)+AK(M)*U(K)
     1        +BK(M)*V(K))/AREA(M)
```

```
      MAT=MATM(M)
      ET=ALPHA(MAT)*DELTAT(M)
      FACT=SU(M)*E(MAT)/(1.-NU(MAT)**2)
      SIGXX=FACT*(EXX-ET+NU(MAT)*(EYY-ET)+NU(MAT)*(EHP-ET))
      SIGXX=SIGXX/PNT
      SIGYY=FACT*(NU(MAT)*(EXX-ET)+EYY-ET+NU(MAT)*(EHP-ET))
      SIGYY=SIGYY/PNT
      SIGHP=FACT*(NU(MAT)*(EXX-ET)+NU(MAT)*(EYY-ET)+EHP-ET)
      SIGHP=SIGHP/PNT
      SIGXY=FACT*0.5*(1.-NU(MAT))*EXY
      SIGXY=SIGXY/PNT
      SIGEFEC=SQRT(.5*((SIGYY-SIGXX)**2+(SIGXX-SIGHP)**2+(SIGHP-SIGYY)**
     12+6.*SIGXY**2))
      RN=-RBAR(M)/A
      SIH=(SIGXX+SIGYY+SIGHP)/3.
      WRITE(6,64)M,EXX,EYY,EHP,SIH,SIGEFEC,SIGXX,SIGYY,SIGHP,SIGXY
      IF(IITER.LT.NITER) GO TO 1
      WRITE(2,65)RN,SIGXX,SIGYY,SIGHP,SIGEFEC
  1   CONTINUE
 64   FORMAT(1X,I5,9E12.4)
 65   FORMAT(5F12.4)
      RETURN
      END
      SUBROUTINE NONLIN (M,EFACT,IITER)
C
C  SUBPROGRAM TO COMPUTE THE NONLINEAR MODULUS OF AN ELEMENT
C
      COMMON NEL,NNP,X(300),Y(300),AI(500),AJ(500),AK(500),BI(500),
     1  BJ(500),BK(500),AREA(500),NPI(500),NPJ(500),NPK(500),NXPT,NYPT,
     2  MOUT,NBP,NPB(40),XAXIS,RBAR(500),OKXX(300,9),OKXY(300,9),
     3  OKYX(300,9),OKYY(300,9),U(300),V(300),FX(300),FY(300),
     4  FXMOD(300),FYMOD(300),SFXX(300),SFXY(300),SFYX(300),SFYY(300),
     5  NPA(300,9),NAP(300),NMAT,E(5),NU(5),ALPHA(5),RHO(5),MATM(500),
     6  DELTAT(500),XBAR(500),YBAR(500),SU(500),SV(500),PX,PY,
     7  NCOND(40),TANG(40),UPRES(40),VPRES(40),NBC3P
C
      REAL  NU
C
C  INPUT THE REQUIRED CREEP INDEX, N
      IF(IITER.GT.2) GO TO 1
      READ(5,51) EN
 51   FORMAT(I3)
  1   I=NPI(M)
      J=NPJ(M)
      K=NPK(M)
      EXX=0.5*(BI(M)*U(I)+BJ(M)*U(J)+BK(M)*U(K))/AREA(M)
      EYY=0.5*(AI(M)*V(I)+AJ(M)*V(J)+AK(M)*V(K))/AREA(M)
      EHP=(U(I)+U(J)+U(K))/(3.*RBAR(M))
      EXY=0.5*(AI(M)*U(I)+BI(M)*V(I)+AJ(M)*U(J)+BJ(M)*V(J)+AK(M)*U(K)
     1         +BK(M)*V(K))/AREA(M)
      ESTRAIN=SQRT((2./3.)*(EXX**2+EYY**2+EHP**2+.5*EXY**2))
      EFACT=ESTRAIN**((1.-EN)/EN)
      RETURN
      END
```

APPENDIX C

LISTING OF THE TWO-DIMENSIONAL FINITE ELEMENT PROGRAM USED FOR SOLVING ELASTIC AND NON-LINEAR PROBLEMS OF THE PLANE STRAIN OR PLANE STRESS TYPE

```
      PROGRAM NPLAIN(INPUT,OUTPUT,TAPE1,TAPE2,TAPE5=INPUT,TAPE6=OUTPUT)
C
C  TWO-DIMENSIONAL FINITE ELEMENT PROGRAM FOR SOLVING ELASTIC AND
C  NON-LINEAR PLAIN STRAIN OR PLAIN STRESS  PROBLEMS.
C
      DIMENSION NOB(40)
      DIMENSION TITLE(6),B(3,6),D(3,3),BTD(6,3),ESTIFF(6,6),
     1  IJK(3),ET(3),THETAM(6)
      COMMON NEL,NNP,X(300),Y(300),AI(500),AJ(500),AK(500),BI(500),
     1  BJ(500),BK(500),AREA(500),NPI(500),NPJ(500),NPK(500),
     2  MOUT,NBP,NPB(40),XAXIS,RBAR(500),OKXX(300,9),OKXY(300,9),
     3  OKYX(300,9),OKYY(300,9),U(300),V(300),FX(300),FY(300),
     4  FXMOD(300),FYMOD(300),SFXX(300),SFXY(300),SFYX(300),SFYY(300),
     5  NPA(300,9),NAP(300),NMAT,E(5),NU(5),ALPHA(5),RHO(5),MATM(500),
     6  DELTAT(500),XBAR(500),YBAR(500),PX,PY,SU(500),
     7  NCOND(40),TANG(40),UPRES(40),VPRES(40),NBC3P
C
      REAL  NU
C
      DATA  BLANK,STRESS,STRAIN / 10H          ,6HSTRESS,6HSTRAIN /
C
C  INPUT THE PROBLEM TITLE AND TYPE - STOP IF BLANK CARD ENCOUNTERED.
 1    READ(5,51) TITLE,CASE
 51   FORMAT(6A10,A6)
      IF(TITLE(1).EQ.BLANK) STOP
      WRITE(6,61) CASE,TITLE
 61   FORMAT(39H0CST FINITE ELEMENT SOLUTION FOR PLANE ,A6,8H PROBLEM
     1       //  6A10)
C
C  INPUT OR GENERATE THE MESH DATA, MATERIAL PROPERTIES, TEMPERATURE
C  CHANGES AND BODY FORCES.
      CALL    MESH1
      CALL MATLS
      CALL TEMPS
      CALL BODYF
C
C  COMPUTE THE ELEMENT GEOMETRIES.
      DO 2 M=1,NEL
      I=NPI(M)
      J=NPJ(M)
      K=NPK(M)
      AI(M)=-X(J)+X(K)
      AJ(M)=-X(K)+X(I)
      AK(M)=-X(I)+X(J)
      BI(M)=Y(J)-Y(K)
      BJ(M)=Y(K)-Y(I)
      BK(M)=Y(I)-Y(J)
      AREA(M)=0.5*(AK(M)*BJ(M)-AJ(M)*BK(M))
      IF(AREA(M).GT.0.) GO TO 2
      WRITE(6,62) M
 62   FORMAT(15H0ELEMENT NUMBER,I5,25H HAS NEGATIVE AREA - STOP)
      STOP
 2    CONTINUE
C
C  INPUT THE REQUIRED NUMBER OF OUTER ITERATIONS.
      READ(5,52) NITER
 52   FORMAT(I3)
      DO 201 IITER=1,NITER
C  SET INITIAL VALUES OF STIFFNESSES, EXTERNAL FORCES AND UNKNOWNS.
      DO 4 IROW=1,NNP
```

```
      DO 3 IC=1,9
      OKXX(IROW,IC)=0.
      OKXY(IROW,IC)=0.
      OKYX(IROW,IC)=0.
      OKYY(IROW,IC)=0.
 3    NPA(IROW,IC)=0
      NPA(IROW,1)=IROW
      FXMOD(IROW)=0.
      FYMOD(IROW)=0.
      IF(IITER.GT.1) GO TO 4
      U(IROW)=0.
      V(IROW)=0.
 4    CONTINUE
C
C  MODIFY MATERIAL PROPERTIES IF CASE IS ONE OF PLANE STRAIN.
      IF(IITER.GT.1) GO TO 6
      IF(CASE.EQ.STRESS) GO TO 6
      DO 5 MAT=1,NMAT
      E(MAT)=E(MAT)/(1.-NU(MAT)**2)
      ALPHA(MAT)=ALPHA(MAT)*(1.+NU(MAT))
 5    NU(MAT)=NU(MAT)/(1.-NU(MAT))
C
C  SET UP THE OVERALL ASSEMBLY LOOP.
 6    DO 19 M=1,NEL
C
C  STORE THE ELEMENT NODE NUMBERS IN ORDER IN ARRAY IJK.
      IJK(1)=NPI(M)
      IJK(2)=NPJ(M)
      IJK(3)=NPK(M)
C
C  COMPUTE THE BODY FORCE COMPONENTS ON EACH NODE OF THE ELEMENT.
      GXM=XBAR(M)*AREA(M)/3.
      GYM=YBAR(M)*AREA(M)/3.
C
C  FORM THE ELEMENT DIMENSION MATRIX.
      DO 7 IRE=1,2
      DO 7 ICE=1,6
 7    B(IRE,ICE)=0.
      B(1,1)=BI(M)
      B(1,3)=BJ(M)
      B(1,5)=BK(M)
      B(2,2)=AI(M)
      B(2,4)=AJ(M)
      B(2,6)=AK(M)
      DO 8 ICE=1,6
      IF(MOD(ICE,2).EQ.0) B(3,ICE)=B(1,ICE-1)
 8    IF(MOD(ICE,2).EQ.1) B(3,ICE)=B(2,ICE+1)
C
C  FORM THE ELASTIC PROPERTY MATRIX.
      DO 9 IRE=1,3
      DO 9 ICE=1,3
 9    D(IRE,ICE)=0.
      MAT=MATM(M)
      EFACT=1.
      IF(IITER.GT.1) CALL NONLIN(M,EFACT)
      IF(IITER.GT.1) NU(MAT)=0.5
      FACT=EFACT*E(MAT)/(1.-NU(MAT)**2)
      SU(M)=EFACT
      D(1,1)=FACT
      D(2,2)=FACT
```

```
      D(1,2)=FACT*NU(MAT)
      D(2,1)=D(1,2)
      D(3,3)=FACT*Ø.5*(1.-NU(MAT))
C
C  MULTIPLY THE TRANSPOSE OF MATRIX B BY MATRIX D.
      DO 1Ø IRE=1,6
      DO 1Ø ICE=1,3
      BTD(IRE,ICE)=Ø.
      DO 1Ø ISUM=1,3
 1Ø   BTD(IRE,ICE)=BTD(IRE,ICE)+B(ISUM,IRE)*D(ISUM,ICE)
C
C  FORM THE THERMAL STRAIN AND THERMAL FORCE VECTORS.
      ET(1)=ALPHA(MAT)*DELTAT(M)
      ET(2)=ET(1)
      ET(3)=Ø.
      DO 12 IRE=1,6
      SUM=Ø.
      DO 11 ISUM=1,3
 11   SUM=SUM+BTD(IRE,ISUM)*ET(ISUM)
 12   THETAM(IRE)=Ø.5*SUM
C
C  FORM THE ELEMENT STIFFNESS MATRIX.
      DO 14 IRE=1,6
      DO 14 ICE=1,6
      SUM=Ø.
      DO 13 ISUM=1,3
 13   SUM=SUM+BTD(IRE,ISUM)*B(ISUM,ICE)
 14   ESTIFF(IRE,ICE)=Ø.25*SUM/AREA(M)
C
C  ADD ELEMENT STIFFNESS TO OVERALL STIFFNESS.
      DO 18 IRE=1,3
      DO 18 ICE=1,3
      IROW=IJK(IRE)
      ICOL=IJK(ICE)
C
C  STORE STIFFNESS COEFFICIENTS IN RECTANGULAR FORM OF OVERALL MATRICES.
      DO 15 IC=1,9
      IF(NPA(IROW,IC).EQ.ICOL) GO TO 17
      IF(NPA(IROW,IC).EQ.Ø) GO TO 16
 15   CONTINUE
      WRITE(6,63) IROW
 63   FORMAT(5HØNODE,I5,38H HAS MORE THAN 8 ADJACENT NODES - STOP)
      STOP
 16   NPA(IROW,IC)=ICOL
      NAP(IROW)=IC
 17   OKXX(IROW,IC)=OKXX(IROW,IC)+ESTIFF(2*IRE-1,2*ICE-1)
      OKXY(IROW,IC)=OKXY(IROW,IC)+ESTIFF(2*IRE-1,2*ICE)
      OKYX(IROW,IC)=OKYX(IROW,IC)+ESTIFF(2*IRE,2*ICE-1)
 18   OKYY(IROW,IC)=OKYY(IROW,IC)+ESTIFF(2*IRE,2*ICE)
C
C  ASSEMBLE THE EXTERNAL FORCES ON THE NODES.
      DO 19 IRE=1,3
      IROW=IJK(IRE)
      FXMOD(IROW)=FXMOD(IROW)+GXM+THETAM(2*IRE-1)
 19   FYMOD(IROW)=FYMOD(IROW)+GYM+THETAM(2*IRE)
C
C  COMPUTE THE SELF-FLEXIBILITY SUBMATRICES.
      DO 2Ø I=1,NNP
      DENOM=OKXX(I,1)*OKYY(I,1)-OKXY(I,1)*OKYX(I,1)
      SFXX(I)=OKYY(I,1)/DENOM
```

```
      SFXY(I)=-OKXY(I,1)/DENOM
      SFYX(I)=-OKYX(I,1)/DENOM
 20   SFYY(I)=OKXX(I,1)/DENOM
C
C  APPLY THE BOUNDARY CONDITIONS.
      CALL BCS(IITER)
C
C  SOLVE THE LINEAR EQUATIONS.
      CALL SOLVE2(IITER)
C
C  OUTPUT THE REQUIRED RESULTS.
      CALL OUTPUT(IITER)
 201  CONTINUE
      GO TO 1
      END
      SUBROUTINE  MESH1
      COMMON NEL,NNP,X(300),Y(300),AI(500),AJ(500),AK(500),BI(500),
     1  BJ(500),BK(500),AREA(500),NPI(500),NPJ(500),NPK(500),
     2  MOUT,NBP,NPB(40),XAXIS,RBAR(500),OKXX(300,9),OKXY(300,9),
     3  OKYX(300,9),OKYY(300,9),U(300),V(300),FX(300),FY(300),
     4  FXMOD(300),FYMOD(300),SFXX(300),SFXY(300),SFYX(300),SFYY(300),
     5  NPA(300,9),NAP(300),NMAT,E(5),NU(5),ALPHA(5),RHO(5),MATM(500),
     6  DELTAT(500),XBAR(500),YBAR(500),PX,PY,SU(500),
     7  NCOND(40),TANG(40),UPRES(40),VPRES(40),NBC3P
C
      REAL  NU
C
C   SUBPROGRAM TO READ DATA FROM TAPE1 .
      READ(1,51) NNP,NEL,MOUT
 51   FORMAT(3I5)
      READ(1,52) (I,X(I),Y(I),N=1,NNP)
 52   FORMAT(I5,2E15.5)
      READ(1,53) (M,NPI(M),NPJ(M),NPK(M),N=1,NEL)
 53   FORMAT(4I5)
      RETURN
      END
       SUBROUTINE  MATLS
      COMMON NEL,NNP,X(300),Y(300),AI(500),AJ(500),AK(500),BI(500),
     1  BJ(500),BK(500),AREA(500),NPI(500),NPJ(500),NPK(500),
     2  MOUT,NBP,NPB(40),XAXIS,RBAR(500),OKXX(300,9),OKXY(300,9),
     3  OKYX(300,9),OKYY(300,9),U(300),V(300),FX(300),FY(300),
     4  FXMOD(300),FYMOD(300),SFXX(300),SFXY(300),SFYX(300),SFYY(300),
     5  NPA(300,9),NAP(300),NMAT,E(5),NU(5),ALPHA(5),RHO(5),MATM(500),
     6  DELTAT(500),XBAR(500),YBAR(500),PX,PY,SU(500),
     7  NCOND(40),TANG(40),UPRES(40),VPRES(40),NBC3P
C
      REAL  NU
C
C  SUBPROGRAM FOR DEFINING THE MATERIAL PROPERTIES OF THE ELEMENTS.
C
C  INPUT THE MATERIAL PROPERTIES - MAXIMUM 5 DIFFERENT MATERIALS.
      READ(5,51) NMAT
 51   FORMAT(I5)
      IF(NMAT.LE.5) GO TO 1
      WRITE(6,61) NMAT
 61   FORMAT(28HØTOO MANY MATERIALS - NMAT =,I5)
      STOP
 1    READ(5,52) (MAT,E(MAT),NU(MAT),ALPHA(MAT),RHO(MAT),N=1,NMAT)
 52   FORMAT(I5,4E15.5)
      WRITE(6,62) (MAT,E(MAT),NU(MAT),ALPHA(MAT),RHO(MAT),MAT=1,NMAT)
```

```
 62   FORMAT(20HØMATERIAL PROPERTIES //
     1 50H   MATL    E           NU      ALPHA       RHO      /
     2       (1X,I5,E12.4,F8.3,2E12.4))
C
C  DEFINE THE MATERIAL FOR EACH ELEMENT.
C  THIS VERSION ASSUMES ALL ELEMENTS ARE OF FIRST MATERIAL.
      DO 2 M=1,NEL
 2    MATM(M)=1
      RETURN
      END
       SUBROUTINE  TEMPS
      COMMON NEL,NNP,X(3ØØ),Y(3ØØ),AI(5ØØ),AJ(5ØØ),AK(5ØØ),BI(5ØØ),
     1  BJ(5ØØ),BK(5ØØ),AREA(5ØØ),NPI(5ØØ),NPJ(5ØØ),NPK(5ØØ),
     2  MOUT,NBP,NPB(4Ø),XAXIS,RBAR(5ØØ),OKXX(3ØØ,9),OKXY(3ØØ,9),
     3  OKYX(3ØØ,9),OKYY(3ØØ,9),U(3ØØ),V(3ØØ),FX(3ØØ),FY(3ØØ),
     4  FXMOD(3ØØ),FYMOD(3ØØ),SFXX(3ØØ),SFXY(3ØØ),SFYX(3ØØ),SFYY(3ØØ),
     5  NPA(3ØØ,9),NAP(3ØØ),NMAT,E(5),NU(5),ALPHA(5),RHO(5),MATM(5ØØ),
     6  DELTAT(5ØØ),XBAR(5ØØ),YBAR(5ØØ),PX,PY,SU(5ØØ),
     7  NCOND(4Ø),TANG(4Ø),UPRES(4Ø),VPRES(4Ø),NBC3P
C
      REAL  NU
C
C  SUBPROGRAM FOR DEFINING MEAN TEMPERATURE CHANGES FOR THE ELEMENTS.
C  THIS VERSION READS AND ASSIGNS A UNIFORM CHANGE.
      READ(5,51) TEMP
 51   FORMAT(F1Ø.Ø)
      DO 1 M=1,NEL
 1    DELTAT(M)=TEMP
      RETURN
      END
       SUBROUTINE  BODYF
      COMMON NEL,NNP,X(3ØØ),Y(3ØØ),AI(5ØØ),AJ(5ØØ),AK(5ØØ),BI(5ØØ),
     1  BJ(5ØØ),BK(5ØØ),AREA(5ØØ),NPI(5ØØ),NPJ(5ØØ),NPK(5ØØ),
     2  MOUT,NBP,NPB(4Ø),XAXIS,RBAR(5ØØ),OKXX(3ØØ,9),OKXY(3ØØ,9),
     3  OKYX(3ØØ,9),OKYY(3ØØ,9),U(3ØØ),V(3ØØ),FX(3ØØ),FY(3ØØ),
     4  FXMOD(3ØØ),FYMOD(3ØØ),SFXX(3ØØ),SFXY(3ØØ),SFYX(3ØØ),SFYY(3ØØ),
     5  NPA(3ØØ,9),NAP(3ØØ),NMAT,E(5),NU(5),ALPHA(5),RHO(5),MATM(5ØØ),
     6  DELTAT(5ØØ),XBAR(5ØØ),YBAR(5ØØ),PX,PY,SU(5ØØ),
     7  NCOND(4Ø),TANG(4Ø),UPRES(4Ø),VPRES(4Ø),NBC3P
C
      REAL  NU
C
C  SUBPROGRAM FOR DEFINING THE BODY FORCE COMPONENTS (PER UNIT VOLUME)
C  FOR THE ELEMENTS.
C  THIS VERSION ASSUMES GRAVITY ACTS IN THE NEGATIVE Y-DIRECTION.
      DO 1 M=1,NEL
      XBAR(M)=Ø.
      MAT=MATM(M)
 1    YBAR(M)=-RHO(MAT)
      RETURN
      END
      SUBROUTINE BCS(IITER)
      COMMON NEL,NNP,X(3ØØ),Y(3ØØ),AI(5ØØ),AJ(5ØØ),AK(5ØØ),BI(5ØØ),
     1  BJ(5ØØ),BK(5ØØ),AREA(5ØØ),NPI(5ØØ),NPJ(5ØØ),NPK(5ØØ),
     2  MOUT,NBP,NPB(4Ø),XAXIS,RBAR(5ØØ),OKXX(3ØØ,9),OKXY(3ØØ,9),
     3  OKYX(3ØØ,9),OKYY(3ØØ,9),U(3ØØ),V(3ØØ),FX(3ØØ),FY(3ØØ),
     4  FXMOD(3ØØ),FYMOD(3ØØ),SFXX(3ØØ),SFXY(3ØØ),SFYX(3ØØ),SFYY(3ØØ),
     5  NPA(3ØØ,9),NAP(3ØØ),NMAT,E(5),NU(5),ALPHA(5),RHO(5),MATM(5ØØ),
     6  DELTAT(5ØØ),XBAR(5ØØ),YBAR(5ØØ),PX,PY,SU(5ØØ),
     7  NCOND(4Ø),TANG(4Ø),UPRES(4Ø),VPRES(4Ø),NBC3P
```

```
C
      REAL  NU
C
C  SUBPROGRAM TO APPLY THE BOUNDARY CONDITIONS.
      IF (IITER.GT.1) GO TO 4
      DO 1 I=1,NNP
      FX(I)=0.
 1    FY(I)=0.
C
C  INPUT THE NUMBERS OF SETS OF DATA FOR EACH TYPE OF BOUNDARY CONDITION
      READ(5,51) NBC1P,NBC2F,NBC3P
 51   FORMAT(14I5)
C
C  INPUT AND APPLY POINT FORCE DATA.
      IF(NBC1P.EQ.0) GO TO 2
      READ(5,52) (I,FX(I),FY(I),N=1,NBC1P)
 52   FORMAT(3(I4,2F10.0))
C
C  INPUT AND APPLY DISTRIBUTED FORCE DATA.
 2    IF(NBC2F.EQ.0) GO TO 4
      DO 3 IF=1,NBC2F
      READ(5,52) NBP,PX,PY
      READ(5,51) (NPB(N),N=1,NBP)
      NS=NBP-1
      DO 3 IS=1,NS
      I1=NPB(IS)
      I2=NPB(IS+1)
      SIDE=SQRT((X(I1)-X(I2))**2+(Y(I1)-Y(I2))**2)
      FXM=0.5*PX*SIDE
      FX(I1)=FX(I1)+FXM
      FX(I2)=FX(I2)+FXM
      FYM=0.5*PY*SIDE
      FY(I1)=FY(I1)+FYM
 3    FY(I2)=FY(I2)+FYM
C
C  DEFINE FINAL MODIFIED EXTERNAL FORCES ON THE NODES.
 4    DO 5 I=1,NNP
      FXMOD(I)=FXMOD(I)+FX(I)
 5    FYMOD(I)=FYMOD(I)+FY(I)
C
C  INPUT AND APPLY THE RESTRAINED NODE DATA.
      IF(IITER.GT.1) GO TO 15
      READ(5,53) (NPB(N),NCOND(N),TANG(N),UPRES(N),VPRES(N),N=1,NBC3P)
 53   FORMAT(2(I4,I2,3F10.0))
 15   DO 10 N=1,NBC3P
      I=NPB(N)
      IF(NCOND(N)-1) 8,7,6
C
C  NODE RESTRAINED TO MOVE IN DIRECTION WHOSE SLOPE IS GIVEN BY TANG.
 6    SFXX(I)=(SFXX(I)*SFYY(I)-SFXY(I)*SFYX(I))/
     1        (SFXX(I)*TANG(N)**2-(SFXY(I)+SFYX(I))*TANG(N)+SFYY(I))
      SFXY(I)=SFXX(I)*TANG(N)
      SFYX(I)=SFXY(I)
      SFYY(I)=SFXY(I)*TANG(N)
      GO TO 10
C
C  NODE RESTRAINED TO MOVE IN Y-DIRECTION ONLY.
 7    SFYY(I)=SFYY(I)-SFYX(I)*SFXY(I)/SFXX(I)
      GO TO 9
C
```

```
C  NODAL POINT DISPLACEMENTS PRESCRIBED.
 8     SFYY(I)=Ø.
       U(I)=UPRES(N)
       V(I)=VPRES(N)
 9     SFXX(I)=Ø.
       SFXY(I)=Ø.
       SFYX(I)=Ø.
 1Ø    CONTINUE
       RETURN
       END
       SUBROUTINE SOLVE2(IITER)
       COMMON NEL,NNP,X(3ØØ),Y(3ØØ),AI(5ØØ),AJ(5ØØ),AK(5ØØ),BI(5ØØ),
      1  BJ(5ØØ),BK(5ØØ),AREA(5ØØ),NPI(5ØØ),NPJ(5ØØ),NPK(5ØØ),
      2  MOUT,NBP,NPB(4Ø),XAXIS,RBAR(5ØØ),OKXX(3ØØ,9),OKXY(3ØØ,9),
      3  OKYX(3ØØ,9),OKYY(3ØØ,9),U(3ØØ),V(3ØØ),FX(3ØØ),FY(3ØØ),
      4  FXMOD(3ØØ),FYMOD(3ØØ),SFXX(3ØØ),SFXY(3ØØ),SFYX(3ØØ),SFYY(3ØØ),
      5  NPA(3ØØ,9),NAP(3ØØ),NMAT,E(5),NU(5),ALPHA(5),RHO(5),MATM(5ØØ),
      6  DELTAT(5ØØ),XBAR(5ØØ),YBAR(5ØØ),PX,PY,SU(5ØØ),
      7  NCOND(4Ø),TANG(4Ø),UPRES(4Ø),VPRES(4Ø),NBC3P
C
       REAL  NU
C
C  SUBPROGRAM FOR SOLVING BY GAUSS-SEIDEL METHOD THE LINEAR EQUATIONS
C  OBTAINED FROM THE FINITE ELEMENT FORMULATION OF BIHARMONIC PROBLEMS.
       NPEQN=NNP
       IF(IITER.GT.1) GO TO 6
C
C  INPUT THE SOLUTION PARAMETERS.
       READ(5,51) NCYCLE,IFREQ,ORELAX,TOLER
 51    FORMAT(2I5,2F1Ø.Ø)
       WRITE(6,61) ORELAX
 61    FORMAT(48HØSOLUTION OF EQUATIONS BY GAUSS-SEIDEL ITERATION //
      1       25H OVER-RELAXATION FACTOR =,F6.3)
C
C  SET UP ITERATION LOOP.
       IF(IFREQ.NE.Ø) WRITE(6,62)
 62    FORMAT(21H  ITER       ERROR    )
C
C  INPUT THE REQUIRED NUMBER OF INNER ITERATIONS.
       READ(5,52) NOII
 6     DO 2Ø K=1,NOII
       DO 3 ITER=1,NCYCLE
       SUMD=Ø.
       SUMDD=Ø.
C
C  OBTAIN NEW ESTIMATE FOR EACH UNKNOWN IN TURN.
       DO 2 IROW=1,NPEQN
       IF(SFXX(IROW)+SFYY(IROW).EQ.Ø.) GO TO 2
       SUMX=FXMOD(IROW)
       SUMY=FYMOD(IROW)
       ICMAX=NAP(IROW)
       DO 1 IC=1,ICMAX
       ICOL=NPA(IROW,IC)
       SUMX=SUMX-OKXX(IROW,IC)*U(ICOL)-OKXY(IROW,IC)*V(ICOL)
 1     SUMY=SUMY-OKYX(IROW,IC)*U(ICOL)-OKYY(IROW,IC)*V(ICOL)
       DELU=SFXX(IROW)*SUMX+SFXY(IROW)*SUMY
       DELV=SFYX(IROW)*SUMX+SFYY(IROW)*SUMY
       SUMDD=SUMDD+ABS(DELU)+ABS(DELV)
       U(IROW)=U(IROW)+ORELAX*DELU
       V(IROW)=V(IROW)+ORELAX*DELV
```

```
      SUMD=SUMD+ABS(U(IROW))+ABS(V(IROW))
 2    CONTINUE
C
C  TEST FOR CONVERGENCE.
      ERROR=SUMDD/SUMD
      IF(ERROR.LT.TOLER) GO TO 4
C
C  OUTPUT PROGRESS INFORMATION EVERY IFREQ CYCLES, UNLESS IFREQ=0.
      IF(IFREQ.EQ.0) GO TO 3
      IF(MOD(ITER,IFREQ).EQ.0) WRITE(6,63) ITER,ERROR
 63   FORMAT(1X,I5,E15.4)
 3    CONTINUE
C
C  NORMAL EXIT FROM ITERATION LOOP INDICATES FAILURE TO CONVERGE.
      WRITE(6,64) NCYCLE
 64   FORMAT(21H0NO CONVERGENCE AFTER,I5,7H CYCLES)
      RETURN
C
C  OUTPUT NUMBER OF ITERATIONS AND TOLERANCE FOR CONVERGED SOLUTION.
 4    WRITE(6,65) TOLER,ITER
 65   FORMAT(38H0ITERATION CONVERGED TO A TOLERANCE OF,E12.4,
     1       6H AFTER,I5,7H CYCLES)
 20   CONTINUE
      RETURN
      END
      SUBROUTINE OUTPUT(IITER)
      DIMENSION NOB(40)
      COMMON NEL,NNP,X(300),Y(300),AI(500),AJ(500),AK(500),BI(500),
     1  BJ(500),BK(500),AREA(500),NPI(500),NPJ(500),NPK(500),
     2  MOUT,NBP,NPB(40),XAXIS,RBAR(500),OKXX(300,9),OKXY(300,9),
     3  OKYX(300,9),OKYY(300,9),U(300),V(300),FX(300),FY(300),
     4  FXMOD(300),FYMOD(300),SFXX(300),SFXY(300),SFYX(300),SFYY(300),
     5  NPA(300,9),NAP(300),NMAT,E(5),NU(5),ALPHA(5),RHO(5),MATM(500),
     6  DELTAT(500),XBAR(500),YBAR(500),PX,PY,SU(500),
     7  NCOND(40),TANG(40),UPRES(40),VPRES(40),NBC3P
C
      REAL  NU
C
C  SUBPROGRAM TO OUTPUT THE FINAL RESULTS.
      IF(IITER.GT.1) GO TO 6
C  OUTPUT THE DISPLACEMENT BOUNDARY CONDITIONS.
      WRITE(6,61) (NPB(IB),NCOND(IB),TANG(IB),IB=1,NBC3P)
 61   FORMAT(33H0DISPLACEMENT BOUNDARY CONDITIONS //
     1       60H  NODE  COND    TANG  NODE  COND    TANG  NODE  COND
     2TANG / (3(1X,I4,I5,F10.4)))
C
C  OUTPUT THE NODAL POINT FORCES AND DISPLACEMENTS.
      WRITE(6,62) (I,FX(I),FY(I),FXMOD(I),FYMOD(I),U(I),V(I),I=1,NNP)
 62   FORMAT(37H0NODAL POINT FORCES AND DISPLACEMENTS //
     1       78H   NODE   FX          FY          FXMOD       FYMOD
     2   U           V       / (1X,I5,6E12.4))
C
C  COMPUTE AND OUTPUT THE ELEMENT STRAIN AND STRESS COMPONENTS.
      WRITE(6,63)
 63   FORMAT(90H0    M    EXX         EYY         EXY         ET
     1  SIGXX       SIGYY       SIGXY    )
 6    NXB=0
      TINY=0.0001
      DO 3 I=1,NNP
      IF(Y(I).GT.TINY) GO TO 3
```

```
      NXB=NXB+1
      NOB(NXB)=I
 3    CONTINUE
      DO 1 M=1,NEL
      DO 4 K=1,NXB
      IF(NPI(M).EQ.NOB(K)) GO TO 2
      IF(NPJ(M).EQ.NOB(K)) GO TO 2
      IF(NPK(M).EQ.NOB(K)) GO TO 2
 4    CONTINUE
      GO TO 1
 2    I=NPI(M)
      J=NPJ(M)
      K=NPK(M)
      EXX=0.5*(BI(M)*U(I)+BJ(M)*U(J)+BK(M)*U(K))/AREA(M)
      EYY=0.5*(AI(M)*V(I)+AJ(M)*V(J)+AK(M)*V(K))/AREA(M)
      EXY=0.5*(AI(M)*U(I)+BI(M)*V(I)+AJ(M)*U(J)+BJ(M)*V(J)+AK(M)*U(K)
     1        +BK(M)*V(K))/AREA(M)
      MAT=MATM(M)
      ET=ALPHA(MAT)*DELTAT(M)
      FACT=SU(M)*E(MAT)/(1.-NU(MAT)**2)
      SIGXX=FACT*((EXX-ET)+NU(MAT)*(EYY-ET))
      SIGYY=FACT*(NU(MAT)*(EXX-ET)+(EYY-ET))
      SIGXY=FACT*0.5*(1.-NU(MAT))*EXY
      SIGEFC=SQRT(SIGXX**2.+SIGYY**2.-SIGXX*SIGYY+3.*SIGXY**2.)
      WRITE(6,64) M,EXX,EYY,EXY,SIGEFC,SIGXX,SIGYY,SIGXY
 1    CONTINUE
 64   FORMAT(1X,I5,7E12.4)
      RETURN
      END
      SUBROUTINE NONLIN(M,EFACT)
      COMMON NEL,NNP,X(300),Y(300),AI(500),AJ(500),AK(500),BI(500),
     1  BJ(500),BK(500),AREA(500),NPI(500),NPJ(500),NPK(500),
     2  MOUT,NBP,NPB(40),XAXIS,RBAR(500),OKXX(300,9),OKXY(300,9),
     3  OKYX(300,9),OKYY(300,9),U(300),V(300),FX(300),FY(300),
     4  FXMOD(300),FYMOD(300),SFXX(300),SFXY(300),SFYX(300),SFYY(300),
     5  NPA(300,9),NAP(300),NMAT,E(5),NU(5),ALPHA(5),RHO(5),MATM(500),
     6  DELTAT(500),XBAR(500),YBAR(500),PX,PY,SU(500),
     7  NCOND(40),TANG(40),UPRES(40),VPRES(40),NBC3P
C
      REAL  NU
C
C  SUBPROGRAM TO COMPUTE THE NONLINEAR MODULUS OF AN ELEMENT
C
C  INPUT THE REQUIRED CREEP INDEX, N .
      IF(IITER.GT.2) GO TO 1
      READ(5,51) EN
 51   FORMAT(I3)
  1   I=NPI(M)
      J=NPJ(M)
      K=NPK(M)
      EXX=0.5*(BI(M)*U(I)+BJ(M)*U(J)+BK(M)*U(K))/AREA(M)
      EYY=0.5*(AI(M)*V(I)+AJ(M)*V(J)+AK(M)*V(K))/AREA(M)
      EXY=0.5*(AI(M)*U(I)+BI(M)*V(I)+AJ(M)*U(J)+BJ(M)*V(J)+AK(M)*U(K)
     1       +BK(M)*V(K))/AREA(M)
      ESTRAIN=SQRT((2./3.)*(EXX**2.+EYY**2.+0.5*EXY**2.))
C
      EFACT=ESTRAIN**((1./EN)-1.)
      RETURN
      END
```